LOW-ASPECT-RATIO TOKAMAK START-UP AND OPERATIONAL CURRENT LIMITS IN CDX-U

Theodore George Jones

A DISSERTATION
PRESENTED TO THE FACULTY
OF PRINCETON UNIVERSITY
IN CANDIDACY FOR THE DEGREE
OF DOCTOR OF PHILOSOPHY

RECOMMENDED FOR ACCEPTANCE
BY THE DEPARTMENT OF
ASTROPHYSICAL SCIENCES

November 1995

©Copyright by Theodore G. Jones, 1995. All rights reserved.

Abstract

A new, small, low-aspect-ratio tokamak (LART), named the Current Drive Experiment - Upgrade (CDX-U), has been designed and built for the investigation and development of the LART configuration, as well as for the investigation of novel current drive methods. Recently, an inductive ohmic heating and current drive (OH) system, including a compact high-field OH transformer coil, was designed and installed in CDX-U, enabling the study of LART plasmas with higher plasma currents and temperatures.

Electron cyclotron resonance heating (ECH) was used in CDX-U to assist plasma breakdown, allowing breakdown with low initial induced voltage. Plasma start-up was achieved with transmitted ECH power of approximately 1% of the maximum coupled OH power, at loop voltages as low as 1 Volt, and in toroidal magnetic fields ranging by a factor of 2.5 in strength. The reduction in loop voltage necessary for start-up minimized large, induced eddy currents in the toroidally continuous vessel walls common to LARTs. Plasma start-up and control in the presence of these significant vessel eddy currents was demonstrated, an important achievement for LART operation. Calculated ohmic efficiency, in terms of the Ejima coefficient, C_E, compared favorably with that found in other tokamaks, yielding $C_E \geq 0.3$–0.4.

An operational current limit was found during extensive CDX-U ohmic operation, corresponding to an MHD safety factor, $q(a)$, of approximately 3.5, a new low demonstrated q-limit for an aspect ratio, A, of 1.6. Studies of magnetic fluctuations in a range of plasma current from 15 kA to 40 kA revealed a coherent, saturating, 10–15 kHz frequency mode, with a toroidal mode number of n=1 and a poloidal mode number ranging from m=1 to m=3. Numerical stability analysis of a magnetic reconstruction of a typical discharge exibiting this mode indicated ideal stability. Previous studies of this mode at the lower plasma currents showed the amplitude increasing dramatically as the safety factor approached the operational current limit of $q(a) = 3.5$, and a radial mode structure consistent with magnetic island formation. These n=1, low m, resistive modes are a good candidate for an MHD instability causing the observed operational current limit.

Contents

Abstract - iv

List of Figures - viii

List of Tables - xi

1 Introduction - 1

1.1 Magnetically Confined Fusion and the Tokamak - - - - - - - - - - 2

1.1.1 Economic Considerations - - - - - - - - - - - - - - - - - - - 3

1.1.2 Engineering Considerations - - - - - - - - - - - - - - - - - - 5

1.2 Review of Low-aspect-ratio Tokamak Experiments - - - - - - - - 8

1.3 Outline - 8

2 Theory - 10

2.1 Review of the Tokamak Equilibrium - - - - - - - - - - - - - - - - 10

2.1.1 Toroidal Confinement - 10

2.1.2 The Tokamak - 13

2.2 The Low-aspect-ratio Tokamak - - - - - - - - - - - - - - - - - - 17

2.2.1 Current and Pressure Limits in Low-aspect-ratio - - - - - - 18

3 The CDX-U Device - 24

3.1 The CDX-U Vacuum Vessel - 25

3.1.1 Diagnostic Ports - 32

3.1.2 Ohmic Heating Upgrade - Vessel Changes - - - - - - - - - - 32

3.1.3 Vacuum System - - - 34
3.2 Magnetic Field Systems - - - 37
3.2.1 Toroidal Field System - - - 37
3.2.2 Poloidal Field System - - - 38
3.2.3 Ohmic Heating System - - - 41
3.3 Plasma Formation and Control Hardware - - - 46
3.3.1 Electron Cyclotron RF Heating System - - - 46
3.3.2 LaB_6 Electron Beam Injection Cathode - - - 47
3.3.3 Timing and Control Systems - - - 49
3.4 Diagnostics - - - 51
3.4.1 Magnetics - - - 51
3.4.2 Electrostatic Probes - - - 55
3.4.3 Segmented Limiter Array - - - 58
3.4.4 Microwave Interferometer - - - 60
3.4.5 Spectroscopy - - - 63
3.5 Data Acquisition System - - - 63

4 Low-aspect-ratio Start-up - - - 65
4.1 The CDX-U Ohmic Start-up Sequence - - - 66
4.2 ECH Preionization - - - 69
4.2.1 Electron Cyclotron Resonance Heating - - - 69
4.2.2 Optimal Parameters for ECH Breakdown in CDX-U - - - 70
4.2.3 Heated Emissive Cathode - - - 75
4.3 Plasma Current Ramp-up and Control - - - 76
4.3.1 OH-Induced Wall Eddy Current - - - 77
4.3.2 PF Programming - - - 78
4.4 Start-up Results - - - 81
4.4.1 Low V_{loop} Start-up - - - 81
4.4.2 Volt-second Consumption and Ohmic Efficiency - - - 83
4.4.3 Start-up at Low B_T - - - 88

4.4.4 Plasma-Limiter Interaction - - - - - - - - - - - - - - - 88

5 MHD Behavior - 92

5.1 Ohmic Operations - 92

5.2 Operational Current Limit - - - - - - - - - - - - - - - - - - - 93

5.3 36 kA Discharge - Equilibrium Reconstruction - - - - - - - - - 98

5.3.1 Magnetics Data - 98

5.3.2 Density Profiles - 99

5.3.3 Equilibrium Reconstruction - - - - - - - - - - - - - - - - 102

5.4 36 kA Discharge Stability Analysis - PEST2 - - - - - - - - - - 105

5.4.1 Stability at Peak Current - - - - - - - - - - - - - - - - 106

5.4.2 Stability During Current Decay - - - - - - - - - - - - - - 106

5.5 Fluctuation Studies - 107

5.5.1 Toroidal and Poloidal Mode Structure - - - - - - - - - - - 107

5.6 Low-I_p, Low-q_a MHD Activity - - - - - - - - - - - - - - - - 115

5.7 Summary - 117

6 Conclusions - 119

6.1 Future Work - 121

6.1.1 Low-aspect-ratio Start-up - - - - - - - - - - - - - - - - 121

6.1.2 Low-aspect-ratio MHD - - - - - - - - - - - - - - - - - - 122

6.1.3 ULART Experiments in CDX-ST and NSTX - - - - - - - - - 123

6.1.4 Confinement Studies - - - - - - - - - - - - - - - - - - - 124

A PPPL-TM-396: OH System - - - - - - - - - - - - - - - - - - - 125

I Introduction and Motivation - - - - - - - - - - - - - - - - - - 131

II Housing - 132

III Toroidal Field Conductors - - - - - - - - - - - - - - - - - - 134

IV Ohmic Heating Solenoid - 136

Appendix: Supporting Calculations for OH System - - - - - - - - - 142

Bibliography 182

Figures

2.1 Toroidal magnetic configuration - 11
2.2 Geometric parameters for the tokamak - - - - - - - - - - - - - - - - - - 14
2.3 Large and small aspect-ratios - 18
2.4 I_p limit in low and high aspect ratios - - - - - - - - - - - - - - - - - - 21

3.1 A photograph of the CDX-U device - - - - - - - - - - - - - - - - - - 26
3.2 The outer wall of the CDX-U vacuum vessel - - - - - - - - - - - - - - 27
3.3 The CDX-U top flange - 28
3.4 The CDX-U vessel - 29
3.5 CDX-U device assembly drawing - - - - - - - - - - - - - - - - - - - 30
3.6 A photograph of the inside of the vacuum vessel - - - - - - - - - - - 31
3.7 Cross-sectional view of outer wall toroidal break - - - - - - - - - - - 33
3.8 The CDX-U vacuum system - 35
3.9 The poloidal field coil set - 39
3.10 Schematic of a typical PF coil power supply - - - - - - - - - - - - - - 41
3.11 Poloidal flux contours from OH coils - - - - - - - - - - - - - - - - - 43
3.12 Schematic of the OH power supply - - - - - - - - - - - - - - - - - - 45
3.13 The ECH system and rf antenna positions - - - - - - - - - - - - - - - 48
3.14 The cathode pulsing circuit - 49
3.15 CDX-U internal hardware - 50
3.16 Magnetic diagnostics - 54
3.17 Schematic of Langmuir probe controls - - - - - - - - - - - - - - - - 58

3.18 CDX-U limiter array - 59
3.19 The 2-mm interferometer system - - - - - - - - - - - - - - - - - - - 62

4.1 Typical CDX-U ohmic start-up sequence - - - - - - - - - - - - - - - 67
4.2 Flux contours at start-up - 72
4.3 Error fields at start-up - 73
4.4 Programmed PF currents - 79
4.5 CDX-U ohmic volt-second consumption - - - - - - - - - - - - - - - - 83
4.6 Calculated volt-second consumption - - - - - - - - - - - - - - - - - 87
4.7 CDX-U operational q(a) limit - 89
4.8 Plasma-limiter interaction - 91

5.1 B_{T0} scan showing disruptive q_a limit - - - - - - - - - - - - - - - - 94
5.2 CDX-U operational q_a limit with disruptions - - - - - - - - - - - - 96
5.3 Measured and calculated magnetic field evolution - - - - - - - - - - 98
5.4 36 kA discharge – line-integrated density, vertical view - - - - - - - 100
5.5 36 kA discharge – line-integrated density, horizontal view - - - - - - 101
5.6 EFIT equilibrium reconstruction of 36 kA discharge near $I_{p,max}$ - - - - 103
5.7 EFIT equilibrium reconstruction of 36 kA discharge during 13 kHz mode 104
5.8 PEST2 equal arclength coordinate system - - - - - - - - - - - - - - - 105
5.9 10–15 kHz mode magnetic signal - - - - - - - - - - - - - - - - - - - 108
5.10 10–15 kHz mode – typical cross power and cross-phase - - - - - - - 110
5.11 10–15 kHz mode – toroidal structure - - - - - - - - - - - - - - - - - 111
5.12 PEST-θ mapping for t= 11 ms equlibrium - - - - - - - - - - - - - 113
5.13 10–15 kHz mode – poloidal structure - - - - - - - - - - - - - - - - - 114
5.14 Low I_p, 10–15 kHz MHD mode amplitude vs. q_{cyl} - - - - - - - - - 116

A.1 Cross section of CDX-U device - 150
A.2 Vertical Cross section of OH Center Stack - - - - - - - - - - - - - - 151
A.3 Center Stack Housing - 152
A.4 9 1/2" Flange - 153

A.5 Housing Gusset - 154
A.6 14" Flange with O-ring - 155
A.7 14" Flange without O-ring - 156
A.8 Full size Assembly Section - 157
A.9 Cross section of OH Center Stack Showing OH Connections - - - - - - 158
A.10 Cross section of OH Center Stack Showing TF Connections - - - - - - 159
A.11 Cross section of OH Center Stack Showing TF Conductors - - - - - - 160
A.12 Vertical Cross section of Top of OH Center Stack-45° - - - - - - - - 161
A.13 Vertical Cross section of Top of OH Center Stack-68° - - - - - - - - 162
A.14 Vertical Cross section of Top of OH Center Stack-110° - - - - - - - 163
A.15 Phenolic Casing - Layer 6 - 164
A.16 Phenolic Casing - 165
A.17 OH Solenoid Clamp (Side View) - - - - - - - - - - - - - - - - - - - 166
A.18 OH Solenoid Clamp (Top View) - - - - - - - - - - - - - - - - - - - 167
A.19 OH Solenoid Clamp Brace - 168
A.20 OH Solenoid Clamping Shoe (Top) - - - - - - - - - - - - - - - - - - 169
A.21 OH Solenoid Clamping Shoe (Bottom) - - - - - - - - - - - - - - - - 170
A.22 G-10 for Clamping Shoe - 171
A.23 G-10 for Clamp Brace - 172
A.24 Phenolic Clamp Hold-Down - 173
A.25 OH Return Conductor with Slots (flat) - - - - - - - - - - - - - - - 174
A.26 OH Return Conductor (rolled) - - - - - - - - - - - - - - - - - - - 175
A.27 OH Solenoid Inner Connector - 176
A.28 OH Return Inner Connector - 177
A.29 Details of TF Joints - 178
A.30 OH Jumper Bus - 179
A.31 OH Return Bus Connector - 180
A.32 OH Solenoid Bus Connector - 181

Tables

3.1 Vacuum vessel geometric parameters - - - - - - - - - - - - - - - - - - 29
3.2 Poloidal field coil data - 40
3.3 Data for magnetic pick-up coils - 53

Acknowledgements

Experimental plasma physics, and tokamak fusion research in particular, are by nature collaborative efforts. Therefore many thanks are due to a large number of people who helped with this thesis work.

First I want to thank my thesis advisor, Prof. Masayuki Ono, whose vision and creativity as a physicist are an inspiration to me. His valuable advice and continuous support throughout my studies at Princeton have been instrumental to this work.

Thanks go to all my present and former colleagues in the CDX-U group. Special thanks go to Dr. Douglass Darrow, who introduced me to the CDX laboratory during my first year here, who joined me in the initial design of the OH system, and who finally went above and beyond the call of duty by serving as a thesis reader. Much credit is due to Dr. Yong-Seok Hwang, who joined me in a large part of the ohmic experiments presented here, and performed the magnetic reconstructions presented in Chapter 5. Wonho Choe has provided untold help to everyone involved in the project, from computer drawings, many of which are used here, to helping design the CDX-U TF system and building electronics. Dr. Cary Forest provided many useful suggestions for study and many improvements to the CDX-U laboratory during his time in the group, as well as loaning some of the figures shown in this thesis. Jon Menard spent many late nights designing and fabricating the correction coils for the OH system, then later, many more running the PEST2 stability code for the MHD analysis herein. Thanks go to Ernest Lo for double-checking the analysis presented in Fig. 5.13. The able technical help of Jim Taylor and Bill Kineyko have helped keep CDX-U, and generations of devices before it, productive. Jim was especially helpful in obtaining many important material resources available at PPPL, sometimes even during the day. I will never forget the monumental effort of the group in reassembling the CDX-U tokamak after the OH upgrade. CDX-U went from being empty floorspace

to a working tokamak in only three weeks during October 1993.

Many teachers at Princeton deserve credit for imparting some of their plasma physics knowledge to me. Thanks go to Prof. Nat Fisch, Prof. Bill Tang, Prof. Charles Karney, Prof. Steve Cowley, Prof. Rip Perkins, and Prof. Sam Cohen. Prof. Steve Jardin has earned special appreciation for reading this thesis, and for providing valuable suggestions for analysis in this work. Support from Prof. Tom Stix, as director of graduate studies, encouraged me during trying early years at Princeton.

Special thanks goes to Barbara Sarfaty, who as Program secretary helped us students over many of the bureaucratic hurdles encountered at PPPL and the University, at the same time serving as a friend to many of us.

Alex MacAulay, Karl Krushelnick, Sherrie Preische, and Dave Coster were good friends as well as good compatriots during the academic challenges of the Program. Thanks also go to Mike Beer, Jon Menard, Kevin Ilcisin, and other friends in the program for joining in some fun among all the work. Bill Dorland and Hans Hermann deserve special mention for their skills in organizing and providing entertainment during conferences.

Thanks go to Princeton friends outside of plasma physics, including members of the Sunday dinner club, Miléna, Anne, Uwe, and others.

Many thanks go to my parents, Martha and Richard Jones, for their unwavering support in my graduate studies.

Finally, immeasurable thanks go to my fiancée, Adele Morris, without whose love, understanding, and constant support this thesis work would have weighed inordinately heavily on me. I recognize Adele as, easily, my greatest discovery while at Princeton.

Ted G. Jones

July, 1995 [1]

[1] This work supported by DoE contract No. DE–AC02–76–CHO–3073.

Chapter 1

Introduction

SEVERAL reasons for reducing our dependence on fossil fuels as a primary energy source have become evident in the past few decades. The goal of fusion energy research is to provide a technologically and economically viable alternative energy source by controlling nuclear fusion reactions. The fusion reaction with the largest cross section, $\sigma_{fus}(v)$, at low energies is the deuterium-tritium (d-t) reaction [DUANE, 1972; MILEY *et al.*, 1974]:

$$d + t \rightarrow \alpha(3.5\ MeV) + n(14.1\ MeV).$$

In addition to being the easiest fusion reaction to initiate, vast supplies of the fuels are available. Deuterium is extremely abundant in sea water and tritium can be obtained in virtually unlimited quantities by transmutation of lithium.

The fusion reaction rate per unit volume is

$$R = n_d n_t \left\langle \sigma_{fus}(v) v \right\rangle_v ,$$

where the subscript v denotes that the average is performed over the relative velocity and depends on the velocity distribution of the reactants. The fusion power density is then given by

$$P_{fus} = R E_{fus}, \tag{1.1}$$

where E_{fus} is the energy released per reaction. For a thermal (Maxwellian) distribution, $\langle \sigma_{fus}(v) v \rangle_v$ is maximized when the reactant densities are equal, $n_d = n_t$, and $T_i \approx 70$ keV. Other fusion reactions have reaction rates that have a much slower peak

rate, or peak at much higher temperatures, or both. Energy in a confined plasma is continuously being lost, either by diffusion and convection to the plasma boundaries or by radiative processes such as bremsstrahlung and cyclotron radiation. The criterion for a self-sustaining d-t reaction is that plasma heating from the alpha particles, $\frac{1}{4}n_i^2 \langle \sigma v \rangle E_\alpha$, exceed the power lost from the plasma, $\frac{3nT}{\tau_E}$, where E_α is the deposited energy per alpha particle and τ_E is the characteristic time for the plasma to lose its thermal energy. This criterion yields [Wesson, 1987]:

$$n\tau_E > \frac{12\ T}{E_\alpha \langle \sigma v \rangle}. \tag{1.2}$$

The right-hand side is a function of temperature and has a minimum of 1.5×10^{14} cm^{-3} s at $T \approx 30$ keV. Still, this criterion is optimistic for a fusion reactor since it ignores the power necessary to confine the plasma (e.g. magnetic field, plasma current drive, etc. in a tokamak). Clearly, maintaining the d-t fuel at a temperature of several tens of keV at sufficient density is critical to successful thermonuclear fusion. Achieving these necessary conditions for a power-producing fusion reaction has proven to be a much greater challenge than envisioned at the start of fusion energy research, nearly 45 years ago.

1.1 Magnetically Confined Fusion and the Tokamak

Among fusion schemes, magnetically confined thermonuclear plasmas have come closest to producing net power at commercially viable levels. To lowest order, charged particle orbits follow the magnetic field lines. With an appropriate field configuration, the hot plasma may be kept insulated from vessel walls. The most experimentally successful magnetic fusion device in terms of fusion triple product, $n_i\tau_E T_i$, and the configuration upon which the most developmental effort has been focused, is the tokamak. The tokamak's toroidal configuration allows all field lines within the plasma volume to close on themselves or stay within the plasma volume. Some components of the confining field are generated by external coils, and some by toroidal current flowing in the plasma. The tokamak equilibrium is reviewed in Sec. (2.1). *The purpose of this work is to investigate and develop possible improvements on the tokamak concept, specifically the low-aspect-ratio tokamak (LART).*

1.1.1 Economic Considerations

As presently envisioned, and given present energy costs, a tokamak reactor would be too complicated and costly to be economically attractive. Estimates of the cost of fusion power have been made, e.g. in the ARIES-I reactor design studies [MILLER and THE ARIES TEAM, 1989]. These studies have found that the cost of fusion energy (COE) will scale strongly with several factors: size of the reactor, magnetic field strength, net power produced and factors which affect it such as the ratio of plasma pressure to field strength (β) and the energy confinement time (τ_E). These factors comprise a useful set of parameters for judging the improvement an alternative tokamak design may offer in terms of the "bottom line", the cost of fusion energy.

One major factor in the COE is the initial capital investment necessary to build a tokamak reactor. Perhaps the most important factor in the reactor cost is its size. The scaling of the reactor cost with its mass is probably even stronger than linear, and highlights the advantage of designing a smaller tokamak reactor. Largely because of the enormous capital expense of building present reactor designs, reactor sizes producing several GW (10^9 W) of power would be necessary in order to achieve sufficient economy of scale to make the COE competitive. Any tokamak reactor design that can produce significant fusion power, or even achieve ignition, with a smaller size than conventional designs would constitute a great improvement by reducing the capital cost. Clearly, the ratio of the power-producing plasma volume to the reactor hardware volume, ($\frac{V_P}{V_R}$), should be maximized. An issue that is related to reactor size is the complexity of the reactor. Any simplification of the tokamak design is likely to increase its reliability as a power plant, and can also help reduce the COE.

Confinement time τ_E, is found to scale strongly with plasma current, I_p in many L-mode scaling laws. For example, ITER89-P scaling has $\tau_E \sim I_p^{0.85}$ [YUSHMANOV *et al.*, 1990]. A more recent fit by the ITER group to an expanded database gives $\tau_E \sim I_p^{0.73}$ [KAYE *et al.*, 1994]. While the aspect ratios for the databases used for these scaling laws were large ($2.4 < A < 7$), the aspect ratio dependence was rather weak within that range [KAYE *et al.*, 1994]. It seems likely that τ_E will at least exhibit a similarly favorable scaling with I_p in low-aspect-ratio . Other factors in the total fusion power, n and T, are also generally found to increase with I_p. Increasing τ_E reduces the size of the reactor necessary to achieve fusion plasma parameters, as well as the heating power needed for ignition. τ_E has a strong influence on reactor

cost and COE.

Confinement times used to compile the above scalings were based on tokamak operation with conventional geometry since data on confinement performance in low-aspect-ratio configurations is extremely limited. A strong motivation for investigating low-aspect-ratio tokamak performance is to explore τ_E scaling as aspect ratio is decreased. Preliminary measurements have been reported [APPEL *et al.*, 1992; SYKES *et al.*, 1994], and are discussed in Sec. (2.2.1). Recent kinetic calculations suggest that confinement scaling at low-aspect-ratio may be favorable due to stabilization of trapped electron microinstabilities, which have been postulated to dominate transport in core regions of large tokamaks with reactor-like parameters [REWOLDT and TANG, 1989; REWOLDT *et al.*, 1994].

Another major factor in the cost of a tokamak reactor is the magnetic field needed to support a given plasma current. One measure of how well the field is utilized is the ratio of the total toroidal field (TF) current to the plasma current, ($\frac{I_{TF}}{I_p}$). Magnetic field strength is costly in terms of power needed to energize field coils, even for superconducting coils which need significant cooling power. Field strength especially affects the cost of the coils themselves and the structure necessary to support them. Mechanical forces on the coils scale as B^2, and most reactor designs use fields producing stresses near the maximum material strength of the coil conductor. Any decrease in ($\frac{I_{TF}}{I_p}$) can significantly reduce the cost of the reactor, as well as the COE.

The maximum β during operation is an important factor in the COE. β is the ratio of the volume averaged plasma pressure, $\overline{p}$, to the magnetic pressure and can be defined as

$$\beta \equiv \frac{2\mu_o \overline{p}}{B_0^2}, \tag{1.3}$$

where B_0 is the vacuum magnetic field strength on axis. By substituting $\overline{p} = n_e T_e + \Sigma_i n_i T_i \approx 2n_e T = 4n_{d,t}T$, the fusion power density can be written in terms of β:

$$P_{fus} = \beta^2 E_{fus} V \frac{\langle \sigma v \rangle}{T^2} \frac{B_0^4}{64\mu_o^2}. \tag{1.4}$$

Therefore, for a given B_0, P_{fus} is maximized when β is a maximum. Alternatively, if β and P_{fus} are held fixed, B_0 can be greatly reduced to reduce costs. Experimentally, β is the most restrictive parameter in this equation. Therefore the quantity $\frac{\langle \sigma v \rangle}{T^2}$ rather than $\langle \sigma v \rangle$ must be optimized as a function of temperature. For d-t fusion this occurs at T $\approx$ 12 keV rather than T $\approx$ 70 keV.

The maximum β achievable during operation is limited by the onset of magnetohydrodynamic (MHD) instabilities. This maximum critical β can be found from numerical ideal MHD stability analysis and scales with the ratio of plasma current to minor radius times toroidal field:

$$\beta_c(\%) = \beta_N \times \frac{I(MA)}{a(m)B_0(T)}, \tag{1.5}$$

where β_N is a dimensionless. For a range of higher aspect ratio numerical equilibria, β_N is calculated to be a constant with a value near 3.5 [TROYON *et al.*, 1984; SYKES *et al.*, 1983]. This has been corroborated by experimental results [STAMBAUGH *et al.*, 1985]. Once again, the advantage of maximizing I_p to maximize P_{fus} and minimize reactor size and cost can be seen. Recent studies, discussed in Sec. (2.2.1), indicate that β_N may be significantly higher at low-aspect-ratio .

1.1.2 Engineering Considerations

Much of the increase in $(\frac{V_p}{V_R})$ in low-aspect-ratio geometry is due to the reduction in the size of the central core volume, inside the torus of the tokamak. This assembly, referred to in CDX-U as the "center stack", typically contains the inside of the toroidal field coils, most of the ohmic heating coils used to drive current inductively in a tokamak, and any necessary support structure for these components. As mentioned before, decreases in $(\frac{I_{TF}}{I_p})$ and increases in β can reduce the required magnetic field. Thus the reduction in center stack volume is compatible with magnetic field requirements in low-aspect-ratio . The low toroidal field requirements and small space may even make copper conductor coil sections an attractive alternative to superconducting coils in the central column of the TF coil set. The use of conventional conductor in part or all of the TF coil set will further simplify a tokamak reactor and reduce its cost.

The ohmic heating (OH) coils are a different story. The total energy available for current drive from the OH system is proportional to the square of the maximum magnetic flux, Φ^2_{max}, of the OH coils. For a solenoid, for example, Φ_{max} is given by [see Sec. (3.2.3)]:

$$\Phi_{max} = \mu_o \frac{N I_{max}}{L} A,$$

where N is the number of turns, L the length and A the area. I_{max} is typically determined by the maximum mechanical stress caused by magnetic forces that can

be supported by the coil. Since the maximum OH energy is proportional to the square of the area of the solenoid, it scales as the center stack radius to the fourth power. Therefore, reducing the center stack size severely limits the OH current drive capability. The overriding goal in low-aspect-ratio design of minimizing the center stack radius makes engineering an OH coil to fit available space very challenging. The LART configuration, therefore, requires optimal use of available ohmic heating power, since a low-aspect-ratio reactor configuration will be even more dependent on non-inductive current drive than will a conventional aspect ratio configuration.

The limitations of inductive current drive go beyond engineering difficulties in low-aspect-ratio . Present day tokamaks' predominant dependence on OH for current drive, as well as for a significant part of the plasma heating, means they are limited to pulsed operation. Ideally, a fusion reactor would be steady-state so that auxiliary heating is only necessary to start up the plasma and achieve ignition. Also, steady-state operation would eliminate the cyclic mechanical and thermal stresses that can shorten the life of a tokamak reactor.

These issues have led to the development of several non-inductive current drive schemes. Several schemes involve radio-frequency (rf) current drive—transferring momentum to electrons from various types of plasma waves launched at the plasma edge. Experimentally, the most successful so far has been to transfer momentum to the plasma electrons by Landau damping of lower hybrid waves launched into the plasma. This scheme, however, suffers from poor power efficiency and inaccessibility of the core regions of the plasma to lower hybrid waves at reactor-level densities. Other types of proposed rf current drive include electron cyclotron current drive (ECCD), and fast-wave current drive (FWCD). Recently FWCD has been proposed for CDX-U [Menard *et al.*, 1995] as well as for a proposed 1 MA-size LART, the National Spherical Tokamak Experiment (NSTX). Other current drive schemes which do not involve rf are being investigated because of their possibly increased efficiency, including DC helicity injection [Ono *et al.*, 1987], spheromak injection [Brown and Bellan, 1990], and neutral beam current drive [Ohkawa, 1970].

Perhaps the most promising means of tokamak current drive is the use of internally generated pressure-driven currents. The dominant pressure-driven current is the bootstrap current, I_{bs}, which has been previously proposed as a means of sustaining the tokamak configuration [Bickerton *et al.*, 1971]. The pressure gradient driven nature of the bootstrap current means that most of the plasma current can be sustained

simply by heating the plasma. Most scenarios for advanced or high-performance tokamaks assume a large fraction of the total plasma current is created as bootstrap current. A fully pressure-driven tokamak configuration was demonstrated on CDX-U [FOREST *et al.*, 1992]. Recent numerical MHD studies by Jon Menard and others in the NSTX team show that somewhat optimized profiles together with passive wall stabilization can yield stable low-aspect-ratio plasmas ($A = 1.25$) which simultaneously have a bootstrap current fraction, $f_{bs} \equiv \frac{I_{bs}}{I_p} \approx 0.8$, $\beta = 44\%$, and $\beta_N = 8.6$ [ONO *et al.*, 1995].

Optimization of the COE with respect to aspect ratio in the ARIES-I design study balanced a tradeoff between several effects favoring low-aspect-ratio, and two predicted disadvantages: a low f_{bs}, and a high ratio of maximum toroidal field (TF) at the coil to that at the plasma, causing mechanical stress problems. Important factors which were optimized at low-aspect-ratio included β, and the ratio of fusion power to total reactor mass, $\frac{P_{fus}}{M_{reactor}}$, both strongly affecting fusion COE. High aspect ratio was found to have a higher predicted f_{bs} and correspondingly lower required current drive power. However, if the class of equilibria found in [ONO *et al.*, 1995] with $f_{bs} \approx 0.8$ turn out to be experimentally obtainable, then current drive requirements will not be as high as those predicted with the scaling in the ARIES-I study. In addition, low-aspect-ratio reactor designs may include copper central conductors for the TF coils, thus eliminating the need for shielding and reducing the maximum toroidal field (TF) at the coil for a given plasma TF. Consequently, the COE minimization may occur at a much lower aspect ratio than the high value of $A = 4.5$ found with the assumptions in the ARIES-I study.

In summary, economic and physics considerations in projecting the COE and practicality of a tokamak reactor design motivate the effort to minimize reactor size and ($\frac{I_{TF}}{I_p}$), and to maximize β and τ_E. Chapter 2 will examine each of these factors in turn, and show how the LART configuration may be an improvement over the conventional tokamak geometry. Engineering the central column of a low-aspect-ratio tokamak will be challenging, and inevitably will result in limited or no inductive current drive capability. Any technique that can increase the efficiency of the conventional inductive start-up and current drive would make the tokamak reactor and especially the LART configuration more attractive. Non-inductive current drive schemes will also be important in low-aspect-ratio , especially the bootstrap current.

1.2 Review of Low-aspect-ratio Tokamak Experiments

Low-aspect-ratio and spherical tokamaks have previously been proposed as a favorable design for an ignition tokamak device [Jassby, 1977; Peng and Dory, 1978; Miller *et al.*, 1986; Ono *et al.*, 1994]. Formal device proposals have been made for LARTs with plasma currents in the 250 kA to 1 MA range [Lazarus *et al.*, 1985; Nascimento *et al.*, 1991; Gusev, 1994], and some proposals are in progress [Ono *et al.*, 1995], though no device of this size has yet been constructed. Only recently have any tokamaks with aspect ratio less than 2.0 actually been in operation including CDX-U, the START device at Culham Laboratory [Sykes *et al.*, 1992], the HIT device at University of Washington [Jarboe *et al.*, 1992], and a small device at the University of Wisconsin [Garstka *et al.*, 1994]. Their equilibrium and confinement characteristics are only beginning to be experimentally investigated. Short duration discharges in spheromaks with a small central conductor were some of the first LART plasmas produced [Bruhns *et al.*, 1987; Hwang *et al.*, 1994].

1.3 Outline

The relatively unexplored low-aspect-ratio tokamak geometry may offer significant advantages over conventional geometries, as well as provide insight into the characteristics of conventional tokamaks. This thesis focuses on techniques to assist OH efficiency in plasma breakdown in low-aspect-ratio and on investigating LART behavior in low ($\frac{I_{TF}}{I_p}$) operation. Electron cyclotron heating was used to preionize the plasma prior to the OH pulse, thus saving valuable Volt-seconds, which are limited by the low-aspect-ratio geometry. Ohmic current drive performance and efficiency in CDX-U are evaluated for a range of parameters. Low-q_a (low $\frac{I_{TF}}{I_p}$) ohmic shots were studied, and MHD behavior characterized.

In Chapter 2 general aspects of the tokamak equilibrium are briefly reviewed, including the existence of trapped particle orbits which have a large effect on kinetic and neoclassical plasma behavior at low-aspect-ratio . The discussion then focuses on MHD limits on parameters important to tokamak reactor performance, especially kink, interchange, and ballooning instabilities which limit current and pressure. The

effects of low-aspect-ratio geometry are examined for the above MHD-limited parameters, ($\frac{I_{TF}}{I_p}$), which is usually expressed in terms of the inverse rotational transform q_a, and β.

Chapter 3 describes the CDX-U device, its power supplies, diagnostics and other supporting equipment in the laboratory. *Much of the experimental hardware, including a large fraction of the CDX-U tokamak itself was designed, built and then significantly upgraded as a part of this thesis work.* The ohmic heating upgrade was instrumental to the experiments performed in this thesis, and has been described in a self-contained report which is added as Appendix A.

Chapter 4 details rf preionization and start-up techniques used to advantage in the CDX-U low-aspect-ratio geometry. The chapter starts with a discussion of the unique challenges of inductive start-up in LARTs, then continues with a description of a typical start-up sequence for ohmic plasma shots in CDX-U. After reviewing basic principles of electron cyclotron resonance heating (ECH), optimal ECH preionization techniques found in CDX-U are discussed. Analysis of ohmic current drive efficiency for ECH-assisted start-up, as well as a breakdown of OH flux consumption is presented. Finally, strong limiter-plasma interactions which often limited ohmic operations in CDX-U are discussed.

Chapter 5 describes observed MHD fluctuations and general MHD stability behavior. This chapter begins with a discussion of the CDX-U low-q_a ohmic shots and the observed operational q_a limit. The focus is then turned to a particular reproducible low-q_a ohmic discharge. After presenting the equilibrium data we review the equilibrium reconstruction for two times during the discharge using the EFIT code. Mapping codes were used to convert one equilibrium solution to a form which was then analyzed by the PEST2 code for ideal MHD stability. A coherent, saturating MHD mode was observed during part of this and similar discharges. Measured mode structure for this instability is presented. Previously presented data for a similar mode at low I_p is reviewed and compared with the present fluctuation data, and possible connection to the observed q_a limit is discussed.

Finally, Chapter 6 summarizes the efficacy of the start-up techniques applied in the CDX-U LART configuration. Results of investigation of the $\frac{I_{TF}}{I_p}$ (q_a) limit in low-aspect-ratio are discussed, as well as its relation to observed MHD activity. Also, suggestions for future studies and the ramifications of the present work on large scale LART operation are discussed.

Chapter 2

Theory

2.1 Review of the Tokamak Equilibrium

2.1.1 Toroidal Confinement

MAGNETIC confinement devices use a magnetic field to confine particles. In a uniform magnetic field without collisions, the particles follow helical trajectories along the field lines, with gyro-radii of $\rho_e = \frac{mv_\perp}{eB}$ perpendicular to the field. In typical reactor parameter ranges, the gyro-radius is much smaller than the dimensions of the device ($\frac{\rho_e}{a} \sim 10^{-4}$, $\frac{\rho_i}{a} \sim 10^{-2}$). Thus the particles are confined in two dimensions, but are free to move parallel to the magnetic field.

A toroidal magnetic confinement device has a magnetic configuration where each field line either closes on itself or otherwise does not intersect the vessel walls. The curvature and field gradients brought about by this toroidal configuration cause deviations in the helical particle orbits, which can be characterized as a set of drifts of the orbit centers (usually referred to as guiding centers) from a field line. To first order in $\frac{\rho}{R_B}$, where R_B is the scale length of the field variation, the perpendicular drift of the guiding center motion can be found to be [Krall and Trivelpiece, 1973]:

$$\vec{v}_d = \frac{m}{e}(\frac{1}{2}v_\perp^2 + v_\parallel^2)\frac{\vec{B} \times \nabla B}{B^3} \; + \; \frac{\vec{E} \times \vec{B}}{B^2}. \tag{2.1}$$

In a purely toroidal field the first term, comprising the ∇B and curvature drifts, is in the vertical direction. Electrons and ions move in opposite directions, causing charge

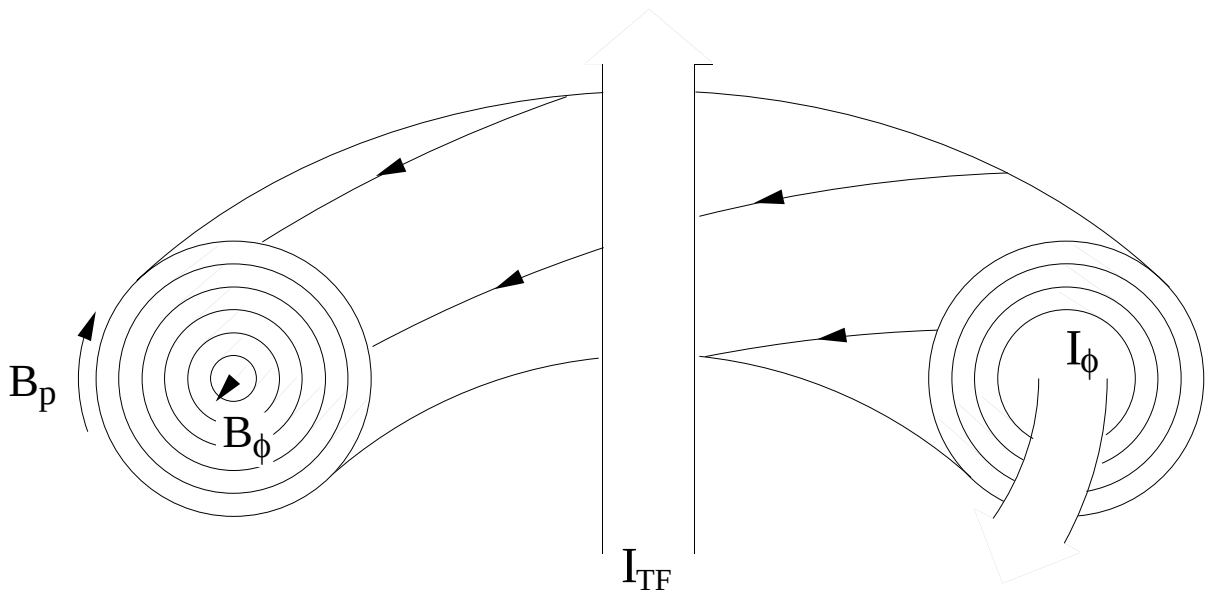

Figure 2.1. A schematic of axisymmetric toroidal magnetic confinement in a tokamak. An axial current generates a toroidal field (B_ϕ), and a toroidal current generates a poloidal field (B_p). The magnetic field lines then lay on concentric toroidal shells known as flux surfaces, as shown schematically above. The poloidal field direction can define a coordinate, θ, orthogonal to the toroidal direction of symmetry, $\hat{\phi}$. The third coordinate, ψ, is $\parallel$ $(\hat{\theta}\times\hat{\phi})$ and proportional to the poloidal flux contained in the surface. ψ, θ, and ϕ are flux coordinates.

separation and creating an electric field which in turn causes another drift via the second term. Perpendicular confinement would be lost.

One way to cancel the effects of the drifts is to add a poloidal rotation to the field line as it makes a circuit around the torus. As a charged particle follows the field line and simultaneously drifts vertically, it spends half its orbit drifting away from the midplane (defined by Z = 0 [1]), and half drifting towards it. The resulting orbit is still confined to the volume around a field line with a small deviation in the $\hat{R}$ direction that averages to zero (see Sec. (2.1.2)). The poloidal field component providing the poloidal rotation must be provided by a toroidal current. This current can be carried in external coils as in a stellarator, or by current flowing in the plasma, as in tokamaks and reversed-field pinches. With the addition of a poloidal field component, each field line is then confined within the surface of a toroidal shell. The final toroidal magnetic configuration consists of field lines residing in a set of nested toroidal shells. These shells are often referred to as flux surfaces since they can be identified by the total

[1]Unless otherwise noted, cylindrical coordinates (R, ϕ, Z) are used.

poloidal magnetic flux contained within.

A quantity describing the average pitch of the field lines on a given flux surface is the safety factor:

$$q_{MHD} \equiv \frac{d\Phi}{d\Psi}, \tag{2.2}$$

where Φ and Ψ are the toroidal and poloidal fluxes, respectively, within the flux surface. The safety factor then is only a function of the flux surface. The safety factor is also related to the rotational transform, ι:

$$q = 2\pi/\iota, \tag{2.3}$$

where ι is equal to the flux surface-average change in the cylindrical poloidal coordinate, θ, in one toroidal circuit along the field line. The safety factor, then, is the flux surface-average number of toroidal rotations along a field line required to make one poloidal circuit. In this context, the safety factor can be approximated by

$$q_{MHD} \approx \left\langle \frac{d\phi}{d\theta} \right\rangle, \tag{2.4}$$

where the brackets denote an average around a poloidal circuit along a field line. If the number q is rational, the field line returns to the the toroidal location at which it began and the surface is called a rational surface. If q is irrational, however, the field line covers a toroidal flux surface.

In describing the total plasma current in comparison to the toroidal field, the expression for q appropriate to circular cylindrical geometry is often used:

$$q_{cyl} = \frac{r}{R_0}\frac{B_\phi}{B_p(r)} \tag{2.5}$$

$$\text{or} \quad q_{cyl}(a) = \frac{a}{R_0}\frac{2\pi a B_0}{\mu_0 I_p}, \tag{2.6}$$

$$\text{using} B_p(r) = \mu_0 \frac{I(r)}{2\pi r}.$$

In toroidal geometries, $q_{MHD} \to q_{cyl}$ as the cross section shape becomes circular and as the aspect ratio becomes infinite, $A = \frac{R_0}{a} \to \infty$. R_0 and a are geometric parameters described below. Unless otherwise noted, all q values quoted in this thesis are the MHD q, defined in Eq. (2.2).

2.1.2 The Tokamak

Various schemes have been described in Sec. (1.1.2) for driving the toroidal plasma current necessary to create a tokamak configuration. Experiments in this thesis used conventional inductive current drive, described in Sec. (3.2.3) with a description of the CDX-U OH system. In this section, a selective review of tokamak equilibrium and stability characteristics are presented, emphasizing differences between low-aspect-ratio geometry and conventional geometry.

Geometric Parameters of the Tokamak

In describing tokamak geometries, several parameters describing shape and size are commonly used. Typically the configuration is characterized by the shape of a poloidal cross section (ϕ=const.) of the outermost closed flux surface (i.e. the plasma boundary). Figure 2.2 shows the minor and major radii, a and R_o, and the elongation, κ, of the plasma. The aspect ratio is defined as $A \equiv \frac{R}{a}$. For the general case of a plasma with a non-circular cross section, these parameters can be defined by:

$$\begin{aligned} R_0 &= \frac{R_{max} + R_{min}}{2}, \\ a &= \frac{R_{max} - R_{min}}{2}, \\ A &= \frac{R_{max} + R_{min}}{R_{max} - R_{min}}, \qquad \text{and} \\ \kappa &= \frac{Z_{max}}{a} \qquad \text{assuming symmetry about Z} = 0, \end{aligned}$$

where R_{min}, R_{max}, and Z_{max} denote the plasma boundary limits. In CDX-U, the plasma boundary is determined by the outermost closed flux surface, which is usually in contact with a limiter. Other parameters can be used to further characterize the plasma shape such as triangularity, indentation, etc. In this thesis, the low-aspect-ratio tokamak (LART) refers to a configuration with $A \leq 2.0$, and the ultra-low-aspect-ratio tokamak (ULART) refers to $A < 1.5$.

Current and Pressure Limits

The limit on plasma current as a function of toroidal field, or ($\frac{I_{TF}}{I_p}$), is known as the Kruskal-Shafranov limit and is due to the onset of the n=1, m=1 ideal MHD

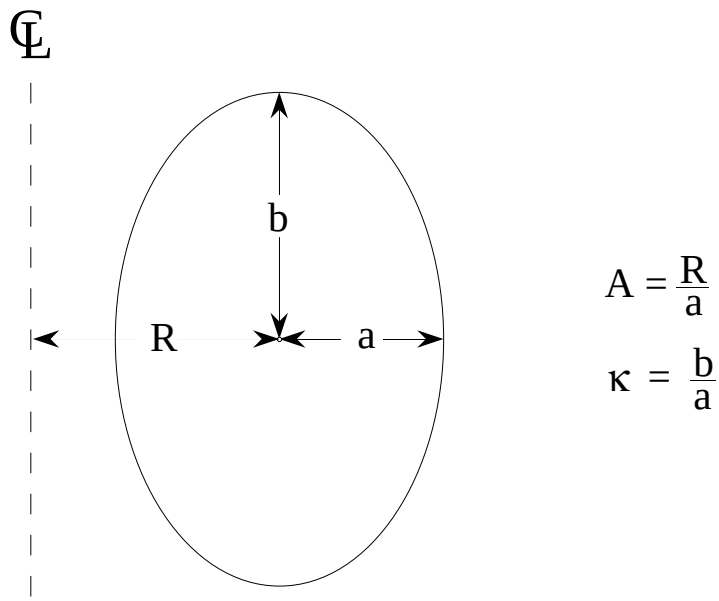

Figure 2.2. A schematic of a poloidal cross section of the plasma shows the geometric parameters for the tokamak: major radius, R_0, minor radius, a, elongation, κ, and aspect ratio, A.

kink instability. This limit is most directly expressed in terms of a limit on q(a), and limits $q_a > 1$ for stability. Using ideal MHD theory at large aspect ratio, numerical analysis of stability of internal kink and interchange modes and external kink modes for a class of current profiles of form $J(r) = J_0(1 - r^2/a^2)^\nu$ has been performed by [Wesson, 1978], yielding a more stringent stability limit of $q_a > 2$. However, with the possibility of magnetic reconnection in a resistive plasma, resistive tearing modes can cause disruptions in the range $q_a \sim 2$–3.

Ideal MHD internal kink and interchange instabilities, as well as high-n ballooning modes appear to limit the plasma β. This maximum β, given in Eq. (1.5) and repeated here for convenience, is:

$$\beta_c(\%) = \beta_N \times \frac{I_{MA}}{aB_0},$$

where stability analysis for large aspect ratio optimized profiles yield $\beta_N \sim 2.8$ for low-n kink modes [Troyon *et al.*, 1984], and $\beta_N \sim 3.5$ for the high-n ballooning modes [Sykes *et al.*, 1983]. This limit is in rough agreement with the onset of disruptions and increased MHD activity in tokamak experiments. A β limit with $\beta_N \sim 3.5$ was found experimentally at $A \sim 3$ with a range of elongation and triangularity [Stambaugh *et al.*, 1985]. Recently, a calculated $\beta_N \sim 5.4$ was predicted for optimized profiles in the proposed TPX experiment, at aspect ratio, $A \approx 4.5$

[GOLDSTON, 1994]. Numerical stability analysis at ultra-low-aspect-ratio, $A = 1.2$ has yielded $\beta_N \sim 8 - 9$, as discussed in Sec. (2.2.1). The plasma β limit remains untested experimentally, however, at aspect ratios below ~ 2.4.

Trapped Particles

The vacuum toroidal field in a tokamak varies as $\frac{1}{R}$:

$$B_T = \frac{\mu_0 I_{TF}}{2\pi R}, \tag{2.7}$$

where I_{TF} is the total toroidal field current and R the major radius. Assuming $B_T \gg B_p$, this $\frac{1}{R}$ scaling produces a strong variation of the field strength at low aspect ratios. This variation goes as

$$\frac{B_{max}}{B_{min}} = \frac{A+1}{A-1}, \tag{2.8}$$

resulting in a variation of a factor of 5 in field for $A = 1.5$.

For tokamak plasmas, $\omega_{transit} \ll \Omega$, where $\omega_{transit} \sim \frac{v_\parallel}{qR}$ is the frequency with which a particle samples regions with significantly different field strengths or curvature (e.g. inboard and outboard regions of the torus), and Ω is the cyclotron frequency. In simple terms, this means that along a particle orbit, the change in B is very small in one gyro-period. In this case, the magnetic moment, μ, which arises from the gyro-motion of the particles, is an adiabatic invariant of the motion. μ is given by

$$\mu = \frac{m v_\perp^2}{2B}. \tag{2.9}$$

More formally, the action integral associated with the gyro-motion (with Larmor radius ρ and gyro-angle θ) is an adiabatic invariant:

$$\begin{aligned} J_\perp &\equiv \oint p_\theta \rho d\theta \approx const \\ &= 2\pi m \frac{v_\perp^2}{\Omega} \\ &= \left(\frac{4\pi m}{q}\right) \frac{\frac{1}{2} m v_\perp^2}{B} \\ &= \left(\frac{4\pi m}{q}\right) \mu. \end{aligned} \tag{2.10}$$

The magnetic moment, μ, can cause particles to be mirror-trapped in the low-field outboard region of the tokamak as can be seen by considering the conservation of energy. The total particle energy, E, is the sum of parallel and perpendicular energy, and can be written as:

$$E = \frac{1}{2}mv_{\|}^2 + \mu B,$$

using Eq. (2.9). Then by conservation of energy the parallel velocity is given by:

$$v_{\|} = \pm\sqrt{\frac{2}{m}(E - \mu B)}. \tag{2.11}$$

If $E = \mu B$ for a particle somewhere on the particle orbit, the particle is at a turning point in its orbit and $v_{\|}$ changes sign. Physically this can be interpreted as the magnetic field of the tokamak exerting a force on the particle given by:

$$F_{\|} = -\mu\frac{\partial B}{\partial \ell},$$

where ℓ is a distance along the field.

The condition that a particle have a turning point, $E < \mu B_{max}$, can be expressed in terms of velocity:

$$\left|\frac{v_{\|}}{v}\right| < \sqrt{1 - \frac{B}{B_{max}}}. \tag{2.12}$$

At B_{min},

$$\left|\frac{v_{\|}}{v_{\perp}}\right| < \sqrt{1 - \frac{B_{min}}{B_{max}}}, \tag{2.13}$$

which can be expressed in terms of A using Eq. (2.8):

$$\left|\frac{v_{\|}}{v_{\perp}}\right| < \sqrt{\frac{2}{A+1}}. \tag{2.14}$$

For an isotropic velocity distribution, the fraction of particles which are trapped is also given by

$$f_T = \sqrt{1 - \frac{B(\vec{x})}{B_{max}}}. \tag{2.15}$$

The maximum of f_T on a flux surface is where $B(\vec{x}) = B_{min}$, giving an upper bound on f_T of:

$$f_T \leq \sqrt{\frac{2}{A+1}}. \tag{2.16}$$

When the toroidal drift in Eq. (2.1) is added to the parallel motion, the resulting orbit is the trapped "banana" orbit, named after its banana-shaped poloidal cross section. Because these particles are not free to circulate toroidally, and because they have a significant deviation from the flux surface, these trapped particles can have a dramatic effect on tokamak behavior.

Electron collisionality, ν_{*e}, is the ratio of the 90-degree collision time to the trapped particle orbit time, and is proportional to $\frac{1}{N_b}$, where N_b is the average number of bounce orbits executed before the particle is scattered, possibly being detrapped. Thus ν_{*e} provides a measure of whether particles are able to execute trapped orbits, with collisionality $\ll 1$ implying existence of trapped particle orbits. For plasma parameters in a typical CDX-U reconstructed plasma [see Sec. (5.3.3) and Fig. 5.6], at a minor radius of $r \approx \frac{a}{2}$, the plasma is in the collisionless regime with $\nu_{*e} \sim 0.1$. At this radius, $A \approx 3$, so that $f_T \sim 0.7$. Therefore in CDX-U (and in low-aspect-ratio in general) there is typically a large fraction of the particle population that is collisionless and mirror-trapped, further increasing the importance of trapped particle effects.

2.2 The Low-aspect-ratio Tokamak

Following the discussion in Sec. (1.1.1), we focus now on the LART configuration and compare some important tokamak figures of merit affecting COE with their values in conventional aspect ratio configurations. In addition, we consider differences that may change the MHD characteristics and transport behavior sufficiently to open new regimes of tokamak operation. These differences may serve to shed light on operation of conventional tokamaks as well as offer an improved alternative.

The extreme toroidicity (see Fig. 2.3) of the LART has inherently high I_p for a given q_a, allowing in turn an inherently high β_c. In addition the LART is a relatively compact [high $(\frac{V_p}{V_R})$], and therefore low-cost approach.

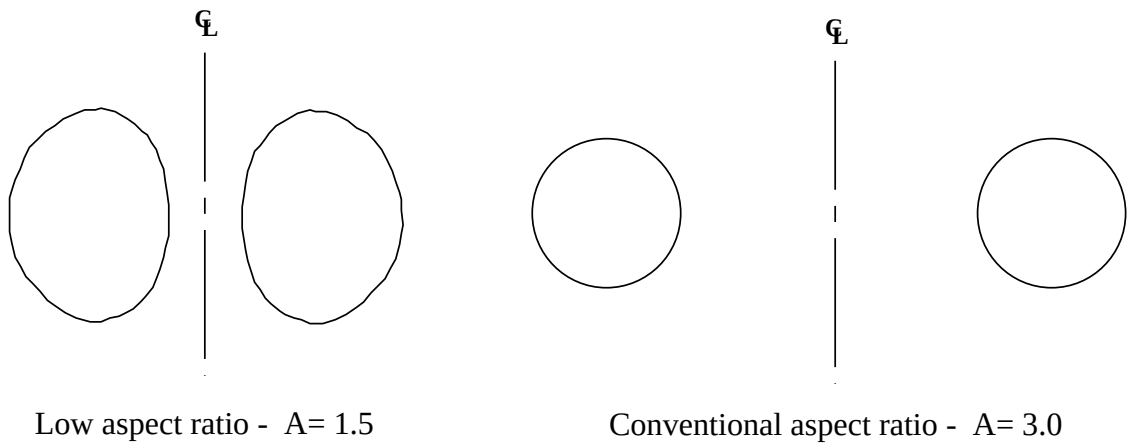

Figure 2.3. A schematic of plasma shape in large and small aspect-ratio tokamaks is shown. Note the "natural" elongation occurring at low-aspect-ratio .

2.2.1 Current and Pressure Limits in Low-aspect-ratio

Toroidicity Effects on q_a

A fundamental characteristic of the LART is the large variation of the vacuum toroidal field within the plasma volume. This large variation causes a large variation in the field line pitch between the outboard and inboard sides of the plasma. As might be expected, this in turn has a big effect on the flux surface averaged field line pitch, expressed in terms of q. The edge q value, $q_a \propto (\frac{I_{TF}}{I_p})$, and is a good measure of how well the costly toroidal field is utilized. Using the MHD q approximation from Eq. (2.4):

$$q_a = \left\langle \frac{aB_T}{RB_p} \right\rangle ,$$

where the brackets denote a flux surface average. A rough approximation of q_a, sufficient for illustrating the effects of low-aspect-ratio on q_a and $(\frac{I_{TF}}{I_p})$ can be made by taking a two-point average of the local q. Following a calculation made by [Peng and Strickler, 1986], we estimate the effect of aspect ratio on q_a by averaging local q on the inside and outside plasma boundaries at the midplane.

$$q_a \approx \frac{1}{2}\left(q_{inner} + q_{outer}\right),$$

The local q is determined by the local value of B_T as well as contributions to B_p from plasma current on both sides of the major axis. B_p is assumed to vary as $\sim \frac{\mu_0 I_p}{2\pi r}$,

giving:

$$\begin{aligned} q_{inner} &= \frac{2\pi a B_{T0} R_0}{\mu_0 I_p \left(R_0 - a\right)^2 \left(\frac{1}{a} - \frac{1}{2R_0 - a}\right)} \\ &= q_{cyl} \frac{1}{2} \frac{(2-\epsilon)}{(1-\epsilon)^3}, \end{aligned}$$

where q_{cyl} is given by Eq. (2.5) and $\epsilon = \frac{a}{R_0}$. Similarly:

$$\begin{aligned} q_{outer} &= \frac{2\pi a B_{T0} R_0}{\mu_0 I_p \left(R_0 + a\right)^2 \left(\frac{1}{a} - \frac{1}{2R_0 + a}\right)} \\ &= q_{cyl} \frac{1}{2} \frac{(2+\epsilon)}{(1+\epsilon)^2}, \end{aligned}$$

Averaging yields:

$$q_a \approx q_{cyl} \frac{1}{\left(1-\epsilon^2\right)^2}. \tag{2.17}$$

Natural Elongation

Low-aspect-ratio tokamaks exhibit a "natural" vertical elongation, i.e. an elongation in a nearly uniform vertical field, due to toroidal effects [Peng and Strickler, 1986]. This elongation ranges between $\kappa = 1$ at high aspect ratio, and $\kappa \approx 2$ as $A \to 1$. The natural elongation is also mildly dependent on current profile. This natural elongation effect is due to a vertical component of the tokamak hoop force. The hoop force, which is a repulsion of the toroidal plasma current on diametrically opposite sides of the major axis, results predominantly in a radially outward force. Due to the proximity of the diametrically opposite currents, the local plasma current near the top and bottom of the poloidal cross section experiences a radial component of the poloidal field contribution from the opposite current. The interaction of this radial field component and the local toroidal current results in a vertical self-force away from the midplane. Since this force is stronger closer to the axis of symmetry, there is a slightly greater elongation on the inboard side of the plasma, resulting in a "D" shape.

The effects of plasma elongation on MHD stability are known to be beneficial. The natural elongation at low aspect ratios means that complicated and power-consuming

poloidal field coils are not necessary to elongate the plasma, at the same time simplifying the machine and reducing the risk of vertical instability compared to a plasma with induced elongation.

As far as q_a is concerned, the effect of plasma elongation is to reduce the average B_p around the flux surface. This, in turn, increases q_a for a given I_p or q_{cyl}. In high aspect ratio, this effect can be approximated as:

$$q_a \approx q_{cyl}\left(\frac{1+\kappa^2}{2}\right). \tag{2.18}$$

Aspect Ratio Scaling of q_a

Finally, an expression for q_a in terms of I_p which includes toroidicity and elongation effects can be pieced together by combining factors. As summarized in [PENG and STRICKLER, 1986], $q_a(\epsilon,\kappa)$ is given by:

$$\begin{aligned} q_a &= q_{cyl}\left(\frac{C_I}{(1-\epsilon^2)^2}\right)\left(\frac{1+\kappa^2}{2}\right) \equiv q_{cyl}\ f(\epsilon,\kappa) \\ &= \frac{2\pi a B_{T0}}{\mu_0 I_p}\ \epsilon\ \left(\frac{C_I}{(1-\epsilon^2)^2}\right)\left(\frac{1+\kappa^2}{2}\right), \end{aligned} \tag{2.19}$$

after substituting for q_{cyl} from Eq. (2.5). $C_I = 1.22 - .68\epsilon$, arising from an empirical fit to numerical results. From Eq. (2.19) we can see that $q_a(I_p)$ or conversely $I_p(q_a)$ increases very rapidly as aspect ratio decreases ($\epsilon \to 1$), and as elongation, κ, increases:

$$\begin{aligned} I_p &= \frac{2\pi a B_{T0}}{\mu_0 q_a}\ \epsilon\ \left(\frac{C_I}{(1-\epsilon^2)^2}\right)\left(\frac{1+\kappa^2}{2}\right) \\ &= I_{p,cyl} f(\epsilon,\kappa), \end{aligned} \tag{2.20}$$

where $I_{p,cyl} = \frac{2\pi a B_{T0}}{\mu_0 q_a}\epsilon$ is the current limit from using q_{cyl} and $f(\epsilon,\kappa)$ is as defined in Eq. (2.19).

This increase in q_a for a given I_p, or equivalently decrease in $(\frac{I_{TF}}{I_p})$ for a given q_a is a result of the strong toroidicity in low-aspect-ratio . As discussed above it is due to two factors: proximity of the plasma current on the diametrically opposite side of the torus affecting the local magnetic field, and the extreme variation in toroidal field strength in low-aspect-ratio . Note the beneficial role of natural elongation in decreasing $(\frac{I_{TF}}{I_p})$. Finally, the extremely high currents allowed by the equilibrium at

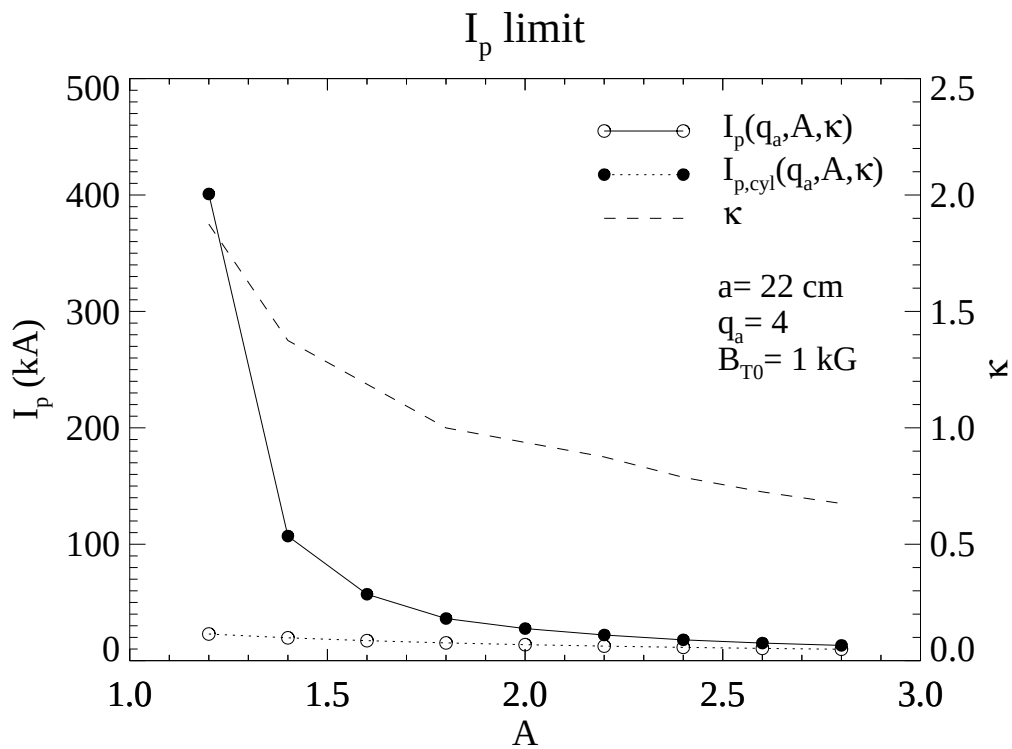

Figure 2.4. The I_p limit from Eq. (2.20) is shown, where the q_a limit is taken to be 4. Plasma elongation, κ, as a function of A is taken from [Sykes, 1994].

low q_a may generate a strongly paramagnetic toroidal field [Peng and Strickler, 1986].

Figure 2.4 shows the scaling with A of I_p in Eq. (2.20) as well as $I_{p,cyl}$. The increase in the I_p limit over that from using q_{cyl}, $(\frac{I_p}{I_{p,cyl}}) = f(\epsilon, \kappa)$. At $A = 1.6$, $f(\epsilon, \kappa) = 3.3$, and at $A = 1.2$ $f(\epsilon, \kappa) = 17.5$. This illustrates the effect of the stronger aspect ratio scaling seen in Eq. (2.20). The ratio of I_p at low-aspect-ratio for a given q_a to that at a relatively high aspect ratio is

$$\frac{I_p(A = 1.6)}{I_p(A = 2.8)} = 4.3, \qquad \text{and}$$
$$\frac{I_p(A = 1.2)}{I_p(A = 2.8)} = 31.$$

Beta Limits in Low-aspect-ratio

This important scaling of $I_p(q_a)$ indicates that low-aspect-ratio makes more efficient use of the costly toroidal field, allowing a larger plasma current for a given edge q_a. Because of this, much higher β values are predicted to be MHD-stable. Recalling β_c from Eq. (1.5) and using the low-aspect-ratio $I_p(q_a)$ scaling in Eq. (2.20), the Troyon β-limit can be recast in terms of ϵ and κ, yielding:

$$\begin{aligned} \beta_c &= \beta_N \frac{I_p}{a B_{T0}} \\ &= \beta_N \frac{1}{q_a} \left(\frac{2\pi}{\mu_0}\right) \left(\frac{\epsilon\, C_I}{(1-\epsilon^2)^2}\right) \left(\frac{1+\kappa^2}{2}\right). \end{aligned} \tag{2.21}$$

This predicted β_c scaling is clearly quite favorable for low-aspect-ratio, especially considering the accompanying natural elongation. For a given q_a and B_{T0}, the Troyon β_c scales the same with aspect ratio as I_p, so that

$$\begin{aligned} \frac{\beta_c(A=1.6)}{\beta_c(A=2.8)} &= \frac{I_p(A=1.6)}{I_p(A=2.8)} = 4.3 \quad \text{and likewise,} \\ \frac{\beta_c(A=1.2)}{\beta_c(A=2.8)} &= 31. \end{aligned}$$

Recent numerical stability studies[ONO *et al.*, 1995] support the above favorable scaling of $I_p(q_a, \epsilon, \kappa)$ as aspect ratio decreases ($\epsilon \to 1$), but indicate an even more favorable scaling of β_c. In these studies, β_N was also found to scale favorably with low-aspect-ratio, increasing to values of 8-9% at $A = 1.2$ with optimized profiles. This exceeds an optimal value of 5.4% at $A = 4.5$ in a recent TPX study case [GOLDSTON, 1994]. Numerical studies of low-aspect-ratio MHD stability by the NSTX team are ongoing.

A critical untested quantity in the above I_p and β_c scaling is the q_a limit at low-aspect-ratio. Extensive experimental tests of the q_a limit at low-aspect-ratio have yet to be done. However, this thesis will show that in ohmic discharges in CDX-U, the q_a limit at $A = 1.6$ is not higher than 4. Even assuming that this q_a value is a hard limit due to MHD instability, and that at high aspect ratios, $q_a \approx 2$ can be reliably achieved, the shift to low-aspect-ratio will still result in a net gain in $I_p(q_a, A)$ and $\beta_c(q_a, A)$. The above scaling predicts a dramatic improvement in $I_p(q_a, A)$ and $\beta_c(q_a, A)$ as $A \to 1.2$.

In addition to the q_a limit, the range of achievable current and pressure profiles for opitimization of β_c needs to be explored experimentally. The strong dependence of the β limit on these profiles means that the practically achievable profiles will play an important role in determining the achievable β in both high and low aspect ratios.

Another unresolved issue is the confinement quality at low-aspect-ratio . The experimental database of confinement quality in terms of confinement time, τ_E, at low-aspect-ratio is extremely limited. However initial measurements of τ_E in the START tokamak at aspect ratios down to $A = 1.4$ have yielded $\tau_E(\text{exper.}) \sim 1$–$2$ ms [Appel *et al.*, 1992] which is comparable to common L-mode scalings:

$$\tau_E(\text{Neo-Alcator}),\ \tau_E(\text{Rebut-Lallia}),\ \tau_E(\text{T-10}) \leq \tau_E(\text{exper.}).$$

More recent START experiments where more detailed profile data was available have also yielded $\tau_E(\text{exper.}) \sim 1$–$2$ ms at aspect ratios down to $A = 1.35$ [Sykes *et al.*, 1994; Walsh, 1994], with the following comparison to common scalings:

$$\begin{aligned}\tau_E(\text{Neo-Alcator}),\ \tau_E(\text{Connor-Lackner-Gottardi}) &< \tau_E(\text{exper.})\\ &< \tau_E(\text{ITER89-P}),\ \tau_E(\text{Rebut-Lallia}),\end{aligned}$$

and where $\tau_E(\text{exper.})$ is within a factor of 2 of all quoted L-mode scalings. Thus far, confinement at low-aspect-ratio seems to be at least as good as that at high aspect ratio, an encouraging, if preliminary, result.

In light of the importance of $(\frac{I_{TF}}{I_p})$ and especially β_c for the fusion power COE, their predicted favorable scaling with aspect ratio constitutes one of the most compelling reasons to further study the LART configuration. Experimental tests of these scalings are urgently needed.

Chapter 3

The CDX-U Device

THE PLANNING stages of this machine and thesis project began in 1987 with the beginning of the Current Drive Experiment-Upgrade (CDX-U) conceptual design. The conceptual experiment that was to become the CDX-U device was initially to be a small, table-top sized proof-of-principle experiment for low-aspect-ratio tokamak operation. As the conceptual design progressed, it became apparent that the research focus of the CDX experiment on non-inductive current drive and the low-aspect-ratio physics research focus of the new experiment were not only compatible but complementary. The decision was then made to make the CDX-U device the replacement for the CDX experiment.[1] The CDX-U experiment proposal[ONO and THE CDX GROUP, 1988] was favorably reviewed by the Department of Energy in January, 1989. The new machine was constructed during 1989, and produced its first plasma in January, 1990. In this first stage of CDX-U operations, there was no ohmic solenoid in the center stack and experiments involved solely non-inductive current drive. This phase of operations produced several new results in the field of non-inductive current drive such as the first fully bootstrap current driven tokamak configuration[FOREST *et al.*, 1992] and direct evidence of anomalous current transport[HWANG, 1993].

In October 1993, the CDX-U device underwent a significant upgrade with the addition of an ohmic heating (OH) system. The CDX-U OH Upgrade was motivated by the desire to explore low-aspect-ratio tokamak physics at higher plasma currents and temperatures, and generally more reactor-relevant plasma parameters. The ohmic

[1] The CDX-U conceptual design was partially described in [JONES *et al.*, 1988].

heating system can deliver several times the heating and current drive power of the non-inductive systems used in the first stage of CDX-U operation: DC Helicity Injection, and Electron Cyclotron Heating (ECH). The CDX-U OH upgrade modifications maintain all previous capabilities for non-inductive current drive and heating.

What are now the CDX-U group and laboratory have been dedicated to investigating advanced concepts for plasma fusion devices. Some of the concepts studied and developed include rf heating, rf current drive, DC helicity injection, pressure-driven currents and the low-aspect-ratio tokamak configuration. The CDX-U experiment itself has been one of the first to explore low-aspect-ratio tokamak physics and operational techniques. The CDX-U device is only the most recent in a long list of machines (CDX, ACT-1, L-4, L-3, etc.) investigating these issues that have operated in the laboratory [Hwang, 1993; Forest, 1992; Darrow, 1988; Skiff, 1985; Goree, 1985; Wurden, 1982; Wilson, 1980; Ono, 1978].

At this point, a bit of reiteration of experiment history and names may help clarify any confusion. The Advanced Concepts Torus-1 (ACT-1) device was a high-aspect-ratio toroidal experiment primarily studying RF plasma heating and current drive physics. In 1985 modifications were made to the ACT-1 device enabling it to operate with DC Helicity Injection current drive, and the experiment was redesignated as the Current Drive Experiment (CDX). CDX-U is the low-aspect-ratio successor to the old CDX experiment and is a *completely new device*, sharing only a few power supplies and diagnostics with the previous experiment. The CDX-U OH Upgrade, often referred to in this chapter, was a significant modification to the CDX-U device enabling ohmic operation.

3.1 The CDX-U Vacuum Vessel

The CDX-U vacuum vessel was designed with four desired attributes in mind: 1) the ability to accommodate low-aspect-ratio plasmas, 2) maximal access to the plasma for diagnostics, 3) modular design, allowing ease of assembly and disassembly for experimental flexibility and repair, and 4) maximal compatibility with CDX device ports, allowing bolt-on use of previously existing diagnostics. A photograph of the CDX-U device is shown in Fig. 3.1.

The vacuum vessel consists of four components assembled into a closed cylinder.

Figure 3.1. A photograph showing the CDX-U device after the ohmic heating upgrade.

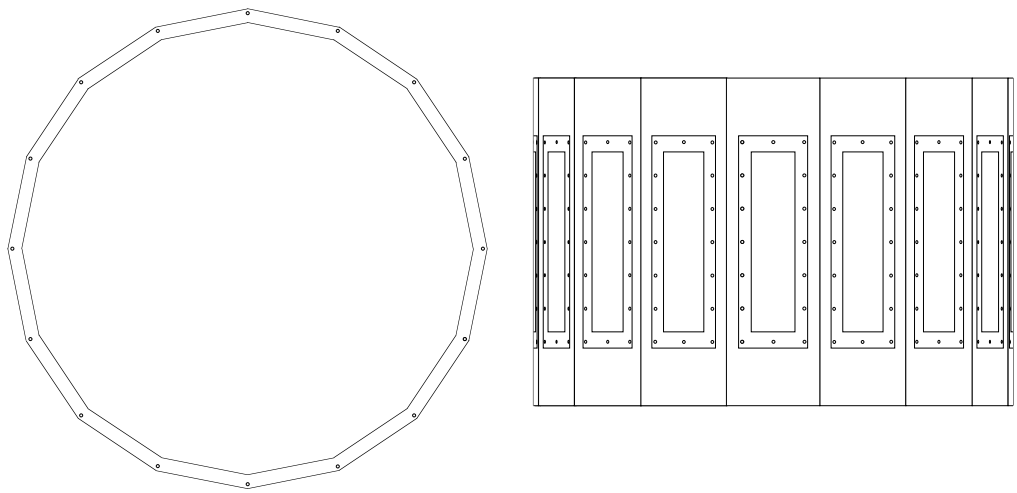

Figure 3.2. Top and side views of the outer wall of the CDX-U vacuum vessel. The wall was formed from flat pieces of 3.8 cm thick soft aluminum bent into a sixteen-sided cylindrical shape.

The outer wall of the cylinder, sometimes referred to as the "tub", is shown in Fig. 3.2. The tub is formed from two sheets of soft (5083, "O" temper), 3.8 cm thick aluminum bent into halves of a sixteen-sided shape (decahexagonal cross section) and then welded together. This outer wall has a 122 cm i.d. at its narrowest point. Sixteen 2.54 cm $\times$ 1.27 cm $\times$ 51 cm aluminum nut-plates with threaded holes at 2.54 cm intervals are welded vertically on the inside of the corners of the outer wall. These nut-plates (see Fig. 3.6) provide convenient mounting points for diagnostics, limiters and other experimental apparatus inside the vessel. The inner column or "center stack" contains the central conductors of the toroidal field (TF) coils. The first center stack used in CDX-U had a tubular stainless steel casing with a 12.7 cm o.d. The center stack used since the OH upgrade contains an OH solenoid in addition to the TF conductors, and has a tubular Inconel casing with a 17.5 cm o.d. This center stack is described in more detail in Sec. 3.2.3 and in Appendix A. Capping the top and bottom of the inner and outer cylindrical walls are two large annular flanges, shown in Fig. 3.3. The original CDX-U top and bottom flanges were machined from 2.54 cm thick aluminum. O-ring grooves were machined into the outer vessel wall and into flanges welded at the ends of the center stack. These O-rings formed vacuum seals against the top and bottom vessel flanges.

The entire vacuum vessel assembly, along with all magnet coils, is supported by four legs attached to the bottom vessel flange. The legs are made of 0.66 cm thick,

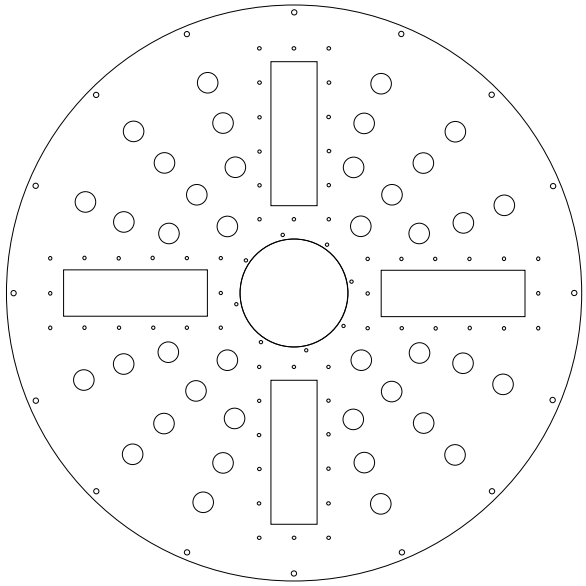

Figure 3.3. The layout of the four rectangular ports and forty circular ports in the top flange of CDX-U is shown schematically. Twenty-four of the circular holes have a 5 cm diameter, and sixteen have 3.8 cm diameter. The flange is 142 cm in diameter. The bottom flange layout is identical with the exception of mounting points for the four supporting legs, which replace four small circular ports.

12.7 cm diameter stainless steel tubing. A cross section of the CDX-U vacuum vessel assembly with support legs is shown in Fig. 3.4. External top and side views of the CDX-U device after the OH Upgrade are shown in Fig. 3.5.

The radius from the tokamak axis of symmetry out to the surface of the original CDX-U center stack was 6.35 cm, and the radius of the new center stack is 8.73 cm. With the inside wall minimum radius of 61 cm, and a maximum vertical height of 90 cm between the insides of the top and bottom flanges, vacuum volume geometry is as summarized in Table 3.1. These dimensions give a rough indication of what kind of aspect ratio and elongation are possible in CDX-U. Of course, the maximum plasma volume will be smaller due to the presence of limiters, nut-plates, and other internal hardware. Section 3.4.3 gives details of limiter locations during experiments in this thesis. The interior of the vacuum vessel with the new center stack is shown in Fig. 3.6. Note the small fraction of the vessel volume occupied by the center stack.

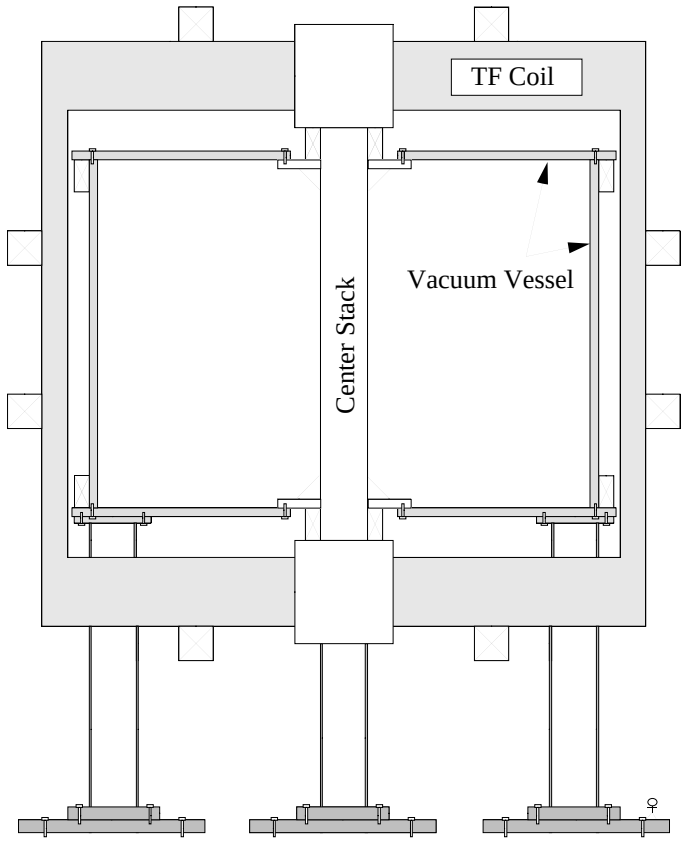

Figure 3.4. A cross section of CDX-U showing the vacuum vessel assembly and positions of the toroidal field (TF) and poloidal field (PF) coils. The vessel consists of a center stack, an outer cylindrical wall, and top and bottom flanges. The TF conductors in the center stack have return windings in 16 detachable "C"-shaped coils which are electrically and mechanically connected to the center stack.

geometric parameter	formula	before OH upgrade	after OH upgrade
$R_{0,vessel}$	$\frac{R_{outer}+R_{inner}}{2}$	34 cm	35 cm
A_v	$\frac{R_{outer}+R_{inner}}{R_{outer}-R_{inner}}$	1.23	1.33
κ_v	$\frac{H}{R_{outer}-R_{inner}}$	1.65	1.72

Table 3.1. Vacuum vessel geometric parameters

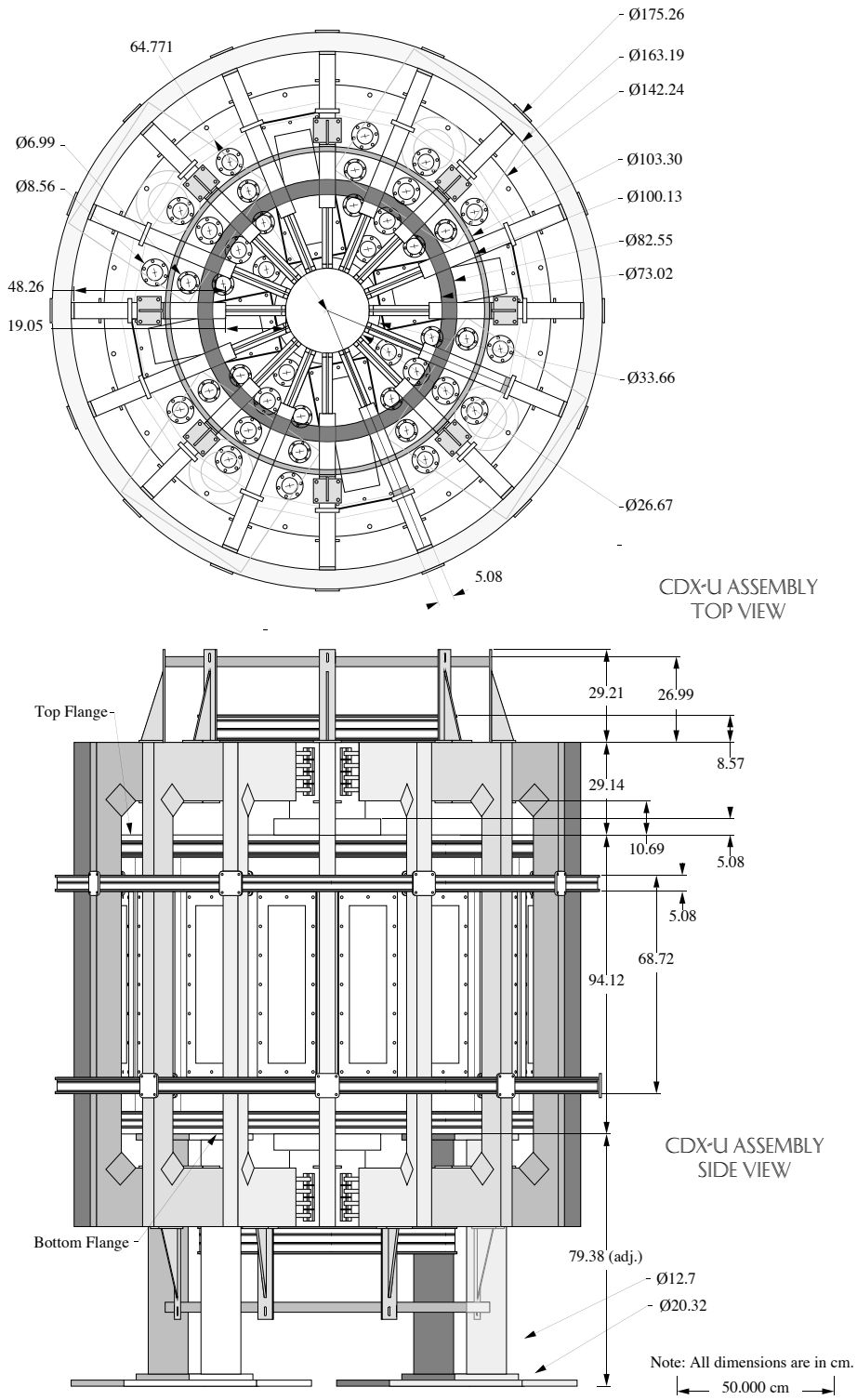

Figure 3.5. Top and side views showing the assembled CDX-U device after the OH Upgrade.

Figure 3.6. A wide angle lens photograph of the inside of the vacuum vessel showing the center stack and nut-plates for mounting internal hardware.

3.1.1 Diagnostic Ports

The CDX-U vacuum vessel allows generous diagnostic access through a set of large rectangular ports and an extensive array of standard Conflat flange circular ports. The outer vessel wall has sixteen 50 cm $\times$ 13 cm rectangular ports. Each outer rectangular window is centered vertically about the midplane in one of the sixteen outer wall faces. These outer ports accept previously manufactured flanges used on the CDX experiment. This compatibility made most diagnostics used on CDX instantly available for use on CDX-U, while saving significant machining costs and initial set-up time. The top and bottom flanges have four 38 cm $\times$ 12.5 cm rectangular ports spaced evenly at 90 degrees. The radial range of these ports is R=20 cm to 58 cm. 24 2-inch nominal size Conflat flanges and 16 1-1/2-inch nominal flanges are arranged as shown in Fig. 3.3 in each of the top and bottom flanges. All ports in the top and bottom flanges are aligned with corresponding ones on the other. This gives extensive access for diagnostic beams (microwave and laser beams - see Sec. 3.4.4) to shine through the plasma. Prior to the OH upgrade all flanges were sealed with Viton rubber gaskets or O-rings. During the OH upgrade all circular port seals were converted to standard circular Conflat flanges using copper gasket seals.

3.1.2 Ohmic Heating Upgrade - Vessel Changes

Most changes to the vacuum vessel were made in an attempt to reduce toroidal eddy currents in the vessel induced by the ohmic heating pulse. Loop voltage during a typical ohmic discharge can be as high as 5 to 10 Volts. In the original CDX-U vessel, toroidal currents generated by this inductive drive would have been much larger than the plasma current, wasting valuable OH Volt-seconds and causing serious equilibrium and plasma control problems.

The housing for the new center stack was made from Inconel 625, a steel alloy with 1.7 times the resistivity of the stainless steel used in the original center stack but with similar strength. The change of material to a thin Inconel housing helped to minimize induced toroidal eddy currents in the center stack. Most changes, however, concentrated on the thick, conductive, aluminum sections of the original CDX-U vacuum vessel: the outer vessel wall, and the top and bottom flanges. Where components of the vessel were replaced, the opportunity was taken to upgrade rubber O-ring vacuum

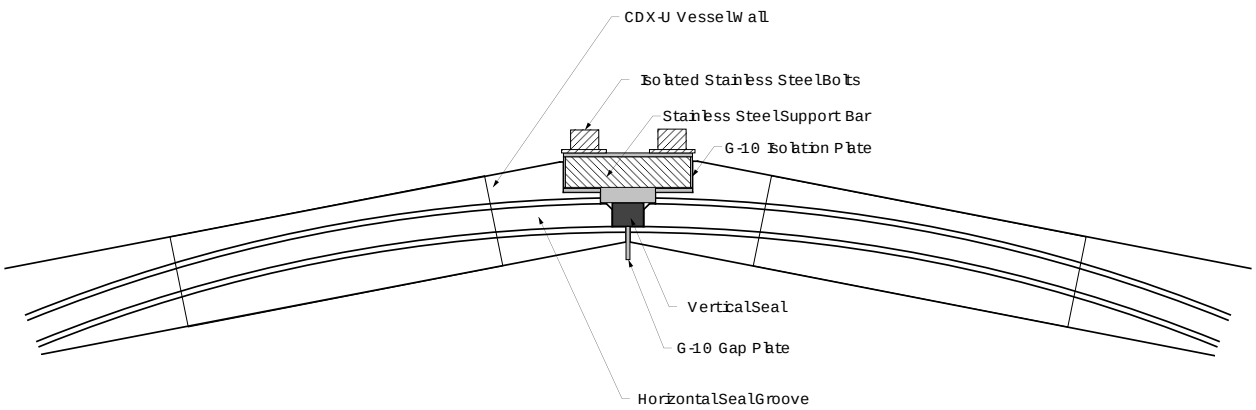

Figure 3.7. A top view of the outer wall toroidal break.

seals to superior copper gasket seals.

Outer Wall Toroidal Break

In order to prevent the flow of any net toroidal currents in the outer vessel wall, an electrical break was made at one of its sixteen corners. A cross sectional view of the toroidal break is shown in Fig. 3.1.2. The break consists of a vertical cut through the 3.8 cm aluminum of the wall. A 1.6 mm thick strip of G-10 insulator was glued into the slot left by the cut. On the outside of the break a vertical 5 cm wide groove was machined into the vessel wall to accommodate a 1.2 cm thick stainless steel reinforcing bar. This bar has two columns of 24 1/4-20 bolts each holding it to the vessel on each side of the break. 1.6 mm thick G-10 insulates the steel bar from either side of the vessel and specially machined G-10 washers insulate the bolts from the steel bar. The result is a complete electrical break in the outer vessel wall that does not compromise the ability of to sustain the 26,000 lbs. of compressive force caused by atmospheric pressure on the outer wall.

In order to prevent induced current in the outer vessel wall from being conducted through the top and bottom flanges around the toroidal break, the joint between the top and bottom rim of the outer wall and the flanges was designed to be electrically isolated. The Viton O-rings forming the vacuum seal between outer wall and top and bottom flanges protruded from its groove, leaving a physical gap and providing

electrical isolation. Bolts attaching the top and bottom flanges to the outer wall, were specially machined so that they would not to contact the sides of the bolt holes in the flanges. G-10 insulating washers were used under the bolt heads.

Stainless Steel Top and Bottom Flanges

New top and bottom vacuum vessel flanges were machined out of 1.6 cm thick stainless steel. The combination of the higher resistivity of stainless steel and the smaller thickness (compared to the original 2.5 cm aluminum flanges), provided for an increase in effective resistivity of the new flanges by a factor of 29. Diagnostic port location and size was kept exactly the same as on the original top and bottom flanges (see Fig. 3.3).

While new top and bottom flanges were being manufactured, the opportunity was taken to upgrade all the circular diagnostic port vacuum seals to copper gasket seals with rotatable Conflat flanges. The two inner main vacuum seals between the top and bottom flanges and their mating flanges on the center stack were also upgraded to copper gasket Conflat flanges. The copper gasket vacuum seals are able to maintain a higher vacuum. Copper gaskets can also withstand much higher vessel temperatures without damage.

3.1.3 Vacuum System

A schematic of the CDX-U vacuum system, which uses several standard high vacuum pumping techniques [Weissler and Carlson, 1979], is shown in Fig. 3.8. A rolling cart was built to support various vacuum diagnostics and a pump box onto which various vacuum pumps are attached. This cart rolls into place to allow the pump box to mate with one of the large rectangular side ports. A rough vacuum of the order of a few milli-Torr is provided by a Leybold-Heraeus D60A mechanical piston pump. This "rough" pump is used as a backing pump for high vacuum pumps connected directly to the pump box.

A Leybold-Heraeus Turbovac NT1500 (1500 Torr-liter/sec air pumping capacity) turbo-molecular pump provides a high vacuum of $\sim 1 \times 10^{-6}$ Torr when used by itself. A turbo-molecular pump consists of a high rotational velocity turbine that mechanically pumps out gas molecules through collisions with the pump turbine vanes.

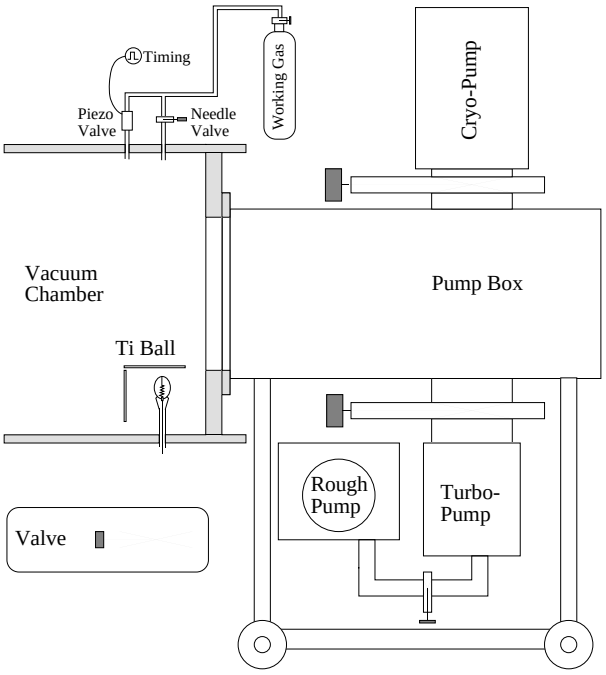

Figure 3.8. A schematic of the CDX-U pump cart and vacuum system. The cart rolls into place and mates with a side port of the vacuum vessel.

Turbo-molecular pumps are effective in removing gases with heavy molecules such as nitrogen, carbon dioxide and argon.

Gases with lighter molecules and thermal velocities of the order of the turbo-pump vane velocity, such as hydrogen and helium, are not effectively removed by the turbo-pump. In order to remove these gases and to assist in removing gases readily adsorbed onto the vessel walls, such as water, a cryogenic pump (CTI-Crygenics Cryo-Torr 8) is used in parallel with the turbo-pump. The cryo-pump works by condensing gas molecules on an array of liquid-helium cooled panels. Surface area on the panels is increased by a coating of granular graphite. When used together, the turbo-pump and cryo-pump provide a vacuum of $\sim 5 \times 10^{-7}$ Torr.

For reactive gases, a pumping technique known as "gettering" is also used. A ball of titanium, an extremely reactive metal, is heated to its sublimation temperature. The sublimated titanium strongly binds to the exposed vessel wall and during a period of several minutes or hours, forms a thin layer over most of the vessel walls. This layer of titanium in turn binds to the reactive gas species during operation. In addition to reducing the base pressure, this technique provides a method of controlling the

wall recycling and therefore neutral pressure and impurity influx during a plasma discharge. During a discharge electrons, ions, and energetic neutrals emitted by the plasma and limiters strike the vessel wall. The titanium coating helps to keep the wall recycling rate (the ratio of particles sputtered or released from the wall to those adsorbed) low and in turn helps to keep the background neutral pressure low.

After opening the vacuum vessel to the laboratory atmosphere, water and other gases often become weakly bound to the surfaces of the limiters and vessel walls in much higher concentrations than under vacuum conditions. These impurities can be freed from the wall by heating and bombardment by energetic particles from the plasma. Several hours of "discharge cleaning" after opening were usually required to achieve a low, stable base pressure.

Finally, wall recycling rates are also kept low by cooling the vacuum vessel during plasma discharges. A series of 2.5 cm-wide copper plates are bolted onto the sides of the rectangular ports. 0.6 cm tubing was brazed onto these plates and carries water from the building water main (usually starting at lower than room temperature). This cooling water flows through four separate cooling circuits, each cooling a different sector of the vacuum vessel. The combination of preliminary discharge cleaning, a turbo-pump, a cryo-pump, Ti gettering, and vacuum vessel cooling provided a vacuum of $\sim$ 8-9 $\times$ 10^{-8} Torr in the absence of any leaks.

The vacuum pressure is monitored by thermocouple gauges (Granville-Phillips Series 275 gauges) at pressures down to a few milli-Torr. Ionization gauges (Kurt Lesker G075P ion gauges with Granville-Phillips Series 275 gauge controllers) are used to monitor pressure from the 10^{-4} Torr range down to the 10^{-8} Torr range. Two ionization gauges were routinely in operation, one at top of the vessel and one at the bottom. They are mounted at the end of tubes extending outside of the TF coils in order to minimize magnetic field interference with ion dynamics critical to ion gauge operation. Absolute pressure measurements displayed by these gauges are subject to various calibration factors depending on the working gas, as well as to instrumental drift, and are only accurate to within a factor of two or so. The relative composition of the constituents of the residual background gas is monitored by a residual gas analyzer (UTi model AGA-100 MUX Quadrupole Gas Analyzer). This gas analyzer is a type of mass spectrometer and displays the concentration of gas species as a function of their charge to mass ratio.

The working gas for experiments in this thesis was typically hydrogen although

helium and deuterium were also used. Gas was usually introduced into the vessel and the plasma by puffing with an electronically controlled, short opening time valve (Veeco PV-10 Piezoelectric valve) located on the outside midplane of the vessel. The controlling voltage signal for the piezoelectric valve was typically a square wave of variable duration. However continuous-feed gas flow with arbitrary waveform was also possible by controlling the piezoelectric valve with a programmable waveform generator (Iotech DAC488HR/4 4-channel digital-analog converter).

3.2 Magnetic Field Systems

In the original CDX-U device, all externally generated magnetic fields and power supplies were steady-state. A significant operational change after the Ohmic Heating Upgrade was that all externally-generated magnetic fields were pulsed, with the exception of the toroidal field. While all poloidal field (PF) coils were unchanged during the OH upgrade, new power supplies based on switched capacitor banks were constructed for each PF coil set. Power supplies and controls described in this section were those in operation after the OH upgrade, during ohmic operation.

3.2.1 Toroidal Field System

The CDX-U toroidal field (TF) coil set consists of a bundle of central conductors housed in the center stack and sixteen detachable outer "C"-shaped coil sections. These outer sections conduct the return TF current around the outside of the vacuum vessel.

The number of turns in the TF coil set and the size of the TF conductors were determined by balancing the total current capability of the TF power supply with the water cooling capacity in each conductor. The TF power supply consists of a 600 kW motor-generator set which provides 2000 A at 300 V, steady-state. In the original CDX-U TF coil set, there was a total of 160 poloidal turns, with 10 windings in each of the sixteen outer TF coil sections. During early CDX-U operations, a few of the conductors in the center stack shorted to each other due to a water leak. The failed conductors were taken out of the TF circuit, along with enough other turns to avoid toroidal asymmetry in the toroidal field. Subsequently, CDX-U operated with a total of 128 turns in the TF coil set, and 8 windings in each outer coil section.

The overriding goal during the design of the CDX-U center stack was to keep its outside diameter, and therefore the achievable plasma aspect ratio, to a minimum. With this goal in mind, the central TF conductors were chosen to be smaller than those in the outer TF coil sections. The central conductor bundle is made from 0.635 cm $\times$ 0.635 cm hollow oxygen-free copper conductors. The central passage of each conductor carries deionized cooling water. Each water cooling circuit in the center conductor bundle consists of two passes, one down and one up.

Cooling water for all field coils, including the TF coils, is supplied by a manifold above the device pressurized to 250 psi. This deionized water flows through a cooling tower outside the CDX-U laboratory building. All water cooling circuits flow through Shur-Flo water flow relays, each of which in turn is connected to a relay panel which controls the toroidal field power supply. If the coolant flow in any relay falls below a preset level, the relay panel is tripped, and the TF power to CDX-U is turned off. This safety relay system helps to ensure adequate cooling during operation.

The removable outer TF coil sections each consist of ten 1.3 cm $\times$ 1.3 cm hollow oxygen-free copper conductors. These are arranged in two columns of five conductors each, with each column a nested set of five "C"-shaped conductors. Each column of five conductors comprises one water-cooling circuit. These coil sections are connected, both electrically and mechanically, to a set of contacts around the top transition section of the center stack. Two 1/4-28 bolts attach each conductor of the outer coil sections to the appropriate center conductor contact.

At the maximum current trip point for the TF circuit breakers of 1950 A, the total TF current through the center stack is 250 kA. This gives a maximum toroidal field at the geometric axis of $B_{T,max}(R_0 = 34\ cm) = 0.15\ T$. Toroidal field strength in terms of the current through the coil set is

$$B_T\ (G) = 25.6\frac{I_{TF}}{R}, \qquad (I_{TF} \text{ in A, and } R \text{ in cm}).$$

Main bus work connections feeding the TF coil set can be quickly changed to reverse the toroidal field direction.

3.2.2 Poloidal Field System

The CDX-U poloidal field (PF) system consists of four pairs of field coils with varying number of turns and mounted at various points around the vessel. Each pair

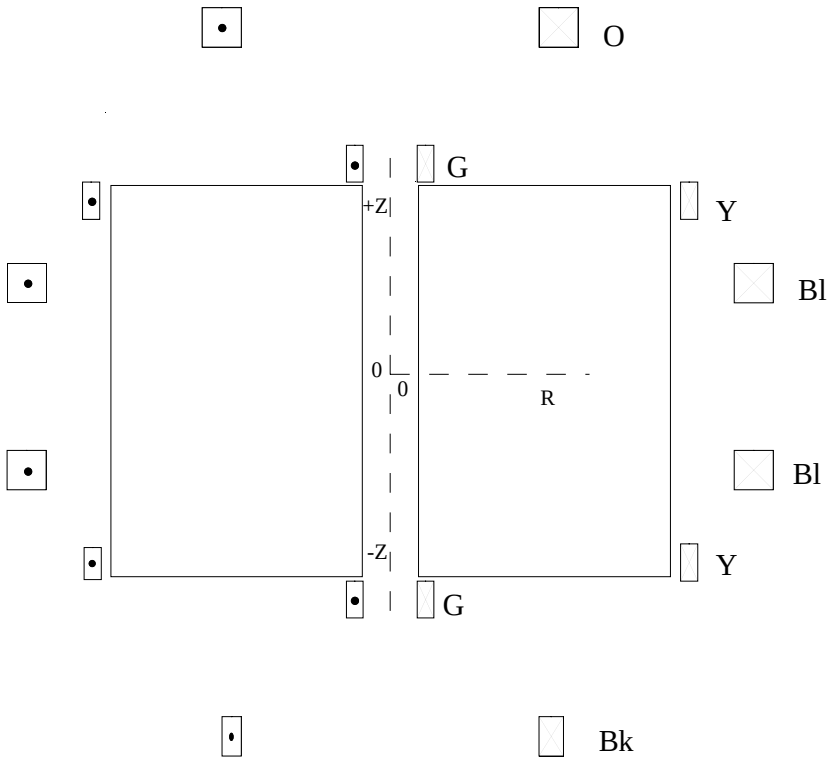

Figure 3.9. The poloidal field coil (PF) set for CDX-U. Each CDX-U PF coil is color-coded for reference. Specific dimensions are given in Table 3.1, corresponding to the coordinate system sketched above.

Coil	R (cm)	Z (cm)	No. of Turns
Green	8.9	49.0	50
Green	8.9	-49.0	50
Orange	40.6	84.0	18 (57 max.)
Black	40.6	-84.0	18
Blue	83.8	36.0	25
Blue	83.8	-36.0	25
Yellow	67.3	40.0	15
Yellow	67.3	-40.0	15

Table 3.2. Poloidal field coil data (dimensions are to the center of each coil).

of PF coils consists of two identical coils at equal distances above and below the midplane. The PF coil set is shown in Figs. 3.4 and 3.9. These coils have supporting frames of aluminum channel bent into hoops. As part of the OH Upgrade, cuts were made in these frames to form a toroidal electrical break in each frame, preventing toroidal current from being induced in them by the OH system. Water cooled 0.635 cm $\times$ 0.635 cm conductor was wound around the channel frames. The channel frames were then mounted to various points on the vacuum vessel or TF coil set via a set of brackets which kept the coil frames electrically isolated from the vessel, and maintaining the integrity of the toroidal electrical breaks in the frames. Placement, dimensions, and number of turns for each PF coil are given in Table 3.2. Each coil pair was color-coded for reference. The orange and black coil pair have unequal total winding numbers, so that the orange coil can be used as a divertor coil. However, an electrical tap is available on the orange coil to allow the use of only 18 turns, providing for a vertically symmetric field with the black coil if desired. Coil pairs were connected in series with each other to ensure equal currents. The blue coil set was often connected so as to produce a predominantly radial field, and then used to control vertical plasma movement.

Poloidal Field Coil Power Supplies

Each poloidal field coil set was powered independently. PF power supplies consisted of capacitor banks switched by silicon controlled rectifiers (SCRs). The PF current waveforms were primarily determined by the OH current. The OH system

induced substantial currents in toroidally continuous sections of the vacuum vessel. These currents produced substantial components of the poloidal field structure. The time dependence of these induced vessel eddy currents roughly followed the loop voltage waveform. In order to maintain a consistent poloidal field structure, the PF power supply must also be able to reproduce roughly the loop voltage waveform. Power supplies for each PF coil consisted of two independently controlled capacitor banks. A schematic of the circuit is shown in Fig. 3.10. PF capacitor banks were triggered by pulses from the CDX-U set of control timers.

3.2.3 Ohmic Heating System

The strongest magnetic field in the device, 4.3 T (actually inside the center stack at maximum design ohmic power), is produced by the ohmic heating solenoid. Flux changes in an OH solenoid inductively drive toroidal plasma current which also heats the plasma by ohmic heat dissipation. The addition of an ohmic heating system in 1993 involved remanufacturing and modifying most major components of the CDX-U device. The OH upgrade included a completely new center stack with an ohmic heating solenoid, new ohmic error field correction coils, and either completely new or significantly modified components in the rest of the vacuum vessel. Additional changes necessary in the course of installing the OH system included designing and constructing an OH power supply, constructing PF power supplies, and electrically isolating all control and data acquisition circuitry to prevent ground loops.

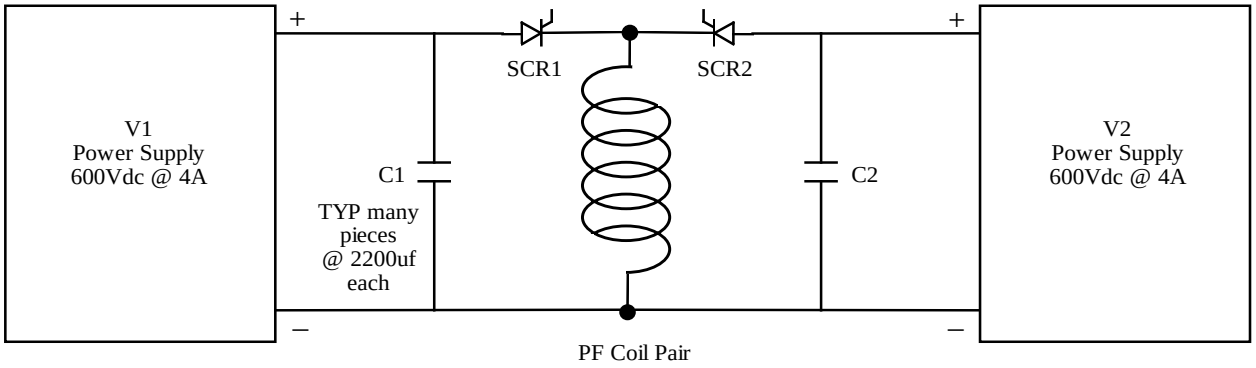

Figure 3.10. A schematic showing a typical double-pulse power supply. Bank 1 (C1) fires first to vertical and poloidal field to support plasma current in the first OH pulse. Bank 2 (C2) is fired to provide additional VF and PF to support the surge in plasma current with the second OH pulse.

The OH system was designed to drive approximately 100 kA of plasma current in the CDX-U device, which is roughly the current limit with the present steady-state TF power supply. Using the TSC time-stepping MHD equilibrium code [Jardin *et al.*, 1986], the OH flux swing necessary to drive this plasma current was estimated to be 100 milli-Volt-seconds (mV·s) given an appropriate target plasma at the start of the ohmic pulse. The designed OH solenoid flux-swing capability was set at 150 mV·s to allow for unforeseen power losses, or a plasma current flat-top capability. In this initial phase of ohmic operation, a power supply capable of driving 30 mV·s was designed and built.

Even with the low-power OH supply used for experiments in this thesis, the total heating and current drive power in CDX-U was drastically increased by the OH upgrade. The 30 mV·s flux swing capability of the OH supply used for experiments in this thesis could deliver up to 200 kW of heating and current drive power over a period of 20 ms. In contrast, the DC Helicity Injection system was capable of around 50 kW of heating and current drive power for a similar duration, and the Electron Cyclotron Heating (ECH) system has a capability of 8 kW of heating power using both magnetron sources. These non-inductive systems have remained fully operational after the OH upgrade and can be used for breakdown assistance and as auxiliary heating and current drive.

New Center Stack with Ohmic Heating Coil

The new center stack with ohmic heating coil installed in the OH upgrade is described in detail in Appendix A. Overall construction of the new center stack is shown in cross-sectional view in Figs. A.2, A.8, and A.11.

In summary, the new center stack housing has an o.d. of 8.73 cm. With optimal limiter placement, the minimum plasma aspect ratio with the new center stack is A=1.45, compared with A=1.40 with the old center stack. The central TF conductor bundle contains 136 water-cooled conductors. 128 of these are used for the toroidal field, and 8 are reserved as spares. The OH solenoid is made from 1.3 cm $\times$ 1.3 cm water-cooled conductor. The conductor chosen for the solenoid was full-hard temper oxygen-free copper in order to support the large magnetic forces (equivalent to 36 atm of outward radial pressure) of the maximum design field of 4.2 T. The OH return current is carried by a cylindrical copper conductor with a toroidal electrical break (to

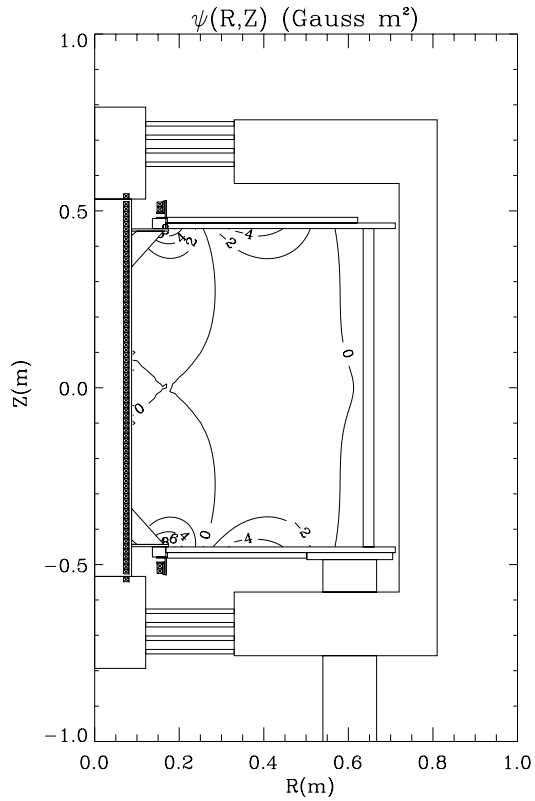

Figure 3.11. Shown above is the poloidal field null in the plasma volume created by the OH solenoid and error-field correction coils. The OH solenoid is the darkened vertical column towards the outside of the center stack. One of the correction coil pairs can be seen mounted just outside the solenoid ends on the top and bottom vacuum flanges. The other pair is mounted at the orange and black coil radius, farther away from the midplane, and can be seen in Fig. 3.1.

avoid toroidal OH-induced eddy current). The OH solenoid, the OH return conductor, and the central TF conductor bundle are all separated by G-10 insulating cylinders. The vacuum housing for the center stack is high resistance, 1.6 mm thick Inconel 625 alloy, minimizing OH-induced currents.

Ohmic Heating Correction Coils

Since the strongest magnetic field in the tokamak is in the OH solenoid, care must be taken to minimize its disturbance of the desired poloidal field configuration. Maintenance of the proper poloidal field configuration is important for equilibrium formation and control, and is especially critical during breakdown and early phases of

current ramp-up. One way to minimize OH solenoid-produced "error field" is to add correction coils near the ends of the OH solenoid which essentially route the return magnetic flux from the solenoid around the plasma volume.

In CDX-U, two matched pairs of correction coils were designed, built and installed as part of the OH Upgrade. Most of the design and construction of the correction coils was performed by Jon Menard of the CDX-U group. The resultant poloidal field structure can be seen in Fig. 3.11. These coils were connected electrically in series with the OH solenoid, so that they did not require separate power supplies. Calculations indicated that the error field throughout most of the plasma volume was reduced by *two orders of magnitude* by addition the of the correction coils. Steady-state field measurements made with a gaussmeter just outside the vacuum vessel outer wall agree with these calculations.

Ohmic Heating Double-Swing Power Supply

For the initial phase of CDX-U ohmic operation, a power supply capable of driving 30 mV·s of flux swing was constructed. Both magnetic forces on OH system components and resistive power losses are greatest at maximum OH current and field. In order to minimize these while maximizing the total flux swing in the OH solenoid, solenoid current is first driven in the direction of desired plasma current, then in the opposite direction. By Faraday's law, the resultant change in magnetic flux in the OH solenoid induces a loop voltage around the plasma volume, which drives plasma current:

$$V_{loop} = \oint \vec{E} \cdot d\vec{l} = -\frac{\partial}{\partial t} \int \vec{B} \cdot d\vec{A} = -\frac{d\Phi}{dt}, \tag{3.1}$$

where the path integral is a toroidal loop around the plasma volume, the surface integral is over a cross section of the solenoid, and Φ is the total magnetic flux through the solenoid. Inside the OH solenoid, the magnetic field at the center is given by:

$$B_{sol} \simeq \mu_0 \frac{N}{L} I_{OH}, \tag{3.2}$$

where N is the number of turns in the solenoid, L is its length, and I_{OH} is the solenoid current. Therefore

$$V_{loop} = -\mu_0 \frac{N}{L} A \frac{dI_{OH}}{dt}, \tag{3.3}$$

where A is the cross sectional area of the solenoid.

Figure 3.12. A schematic showing the double-swing ohmic heating power supply. Bank 1 (C1) fires first, driving OH solenoid current in the positive plasma current direction, banks 2 and 3 (C2,C3) fire subsequently, driving solenoid current in the negative plasma current direction and providing positive loop voltage for plasma current drive. (See Fig. 4.1 for solenoid and plasma current traces.) The commutation circuit is shown in the lower right (C4,SCR4,L4).

The operation and effect of the OH system is illustrated in Fig. 4.1, which includes time traces of I_{OH}, plasma current, I_p, and induced voltage measured at the vessel toroidal break, V_{loop}, during a typical ohmic discharge. All times quoted here refer to Fig. 4.1. The first "positive" OH current swing, beginning at t= -6 ms, is powered by the voltage of OH capacitor bank 1 (as shown in Fig. 3.12). The OH solenoid forms an LCR circuit with each capacitor bank in turn that is fired. The characteristic swing time for the current is $\tau \sim 2\pi\sqrt{L_{OH}C_{bank}}$, and the maximum coil current for each pulse is of the order $I_{max} \sim V_{0,bank}\sqrt{\frac{C_{bank}}{L_{OH}}}$. At t= +4 ms, the second OH capacitor bank is fired, and the OH current is then reduced and driven in the negative direction by the OH bank 2, which is connected to the OH coils with opposite polarity to bank 1.

In some experiments, OH bank 3 was used to drive an even larger negative OH current, lengthening the duration of positive loop voltage. This third pulse was characterized by relatively low loop voltage and long duration, and was useful for maintaining a short plasma current flat-top or lengthening the plasma current decay. In Fig. 4.1 bank 3 is fired at approximately t= +9 ms. The OH power supply configuration shown in Fig. 3.12 had a maximum capacitive stored energy of 80 kJ. The discharge of this energy into the OH system was interlocked with monitors on the OH cooling water supply, as well as with all access panels to the capacitor banks.

A commutation circuit was built to provide more flexibility in changing the OH current waveform, and therefore the loop voltage waveform. The commutation circuit can arbitrarily shut off the SCR for bank 1. This causes the OH solenoid current to ramp down much more quickly (on the order of the LC time of the OH solenoid and the commutation capacitor bank). Consequently, a brief pulse of relatively high loop voltage can be created to assist breakdown, or provide a more rapid plasma current ramp-up.

3.3 Plasma Formation and Control Hardware

3.3.1 Electron Cyclotron RF Heating System

The most important method for plasma breakdown and auxiliary heating for ohmic shots is Electron Cyclotron resonance Heating (ECH). In theory [see Sec. (4.2.1)],

ECH involves transmitting rf power to the plasma which is then absorbed where the transmitted frequency is a multiple of the electron cyclotron frequency,

$$f_{ce}(\mathrm{Hz}) = \frac{eB}{2\pi m_e} = 2.8 \times 10^6 B, \qquad (\mathrm{B\ in\ Gauss}).$$

In the CDX-U plasma volume, f_{ce} typically ranges between 1-10 GHz, depending on major radius and TF current. The ECH system frequency used was 2.45 GHz. This microwave frequency is in common use, and many high-power sources and transmission components for it are readily available.

The CDX-U ECH system is depicted in Fig. 3.13. The rf sources were two Philips YJ1190, 6 kW magnetrons. The rf systems were self-contained in cabinets which included the magnetrons, water cooling for the magnetron resonant cavities, air cooling for the waveguide couplers, circuitry to heat the magnetron cathode filament, high voltage capacitor banks to supply magnetron power, and high voltage modulators to regulate magnetron operation and rf power.

Rf power was introduced into the vacuum vessel through vacuum feed-throughs in the waveguide and into ports in the top and bottom vessel flanges. The launching antennae were simply unterminated WG-283 (S-band) waveguides, protected from the plasma by graphite limiters. Bottom-launched rf power was oriented with O-mode polarization ($\vec{E}_{rf} \parallel \vec{B}_T$). The power launched from the top antenna was polarized in the x-mode orientation ($\vec{E}_{rf} \perp \vec{B}_T$). Transmitted and reflected rf power were sampled by waveguide directional couplers and measured through 57 dB of attenuation by Schottky diode power detectors (Hewlett Packard 8473 B detectors) sensitive to frequencies between 0.01 and 18 GHz.

3.3.2 LaB_6 Electron Beam Injection Cathode

The experiments in this thesis were typically run at the lowest neutral pressure possible. To achieve plasma breakdown, it was sometimes helpful to introduce extra electrons into the vessel by means of a heated emissive cathode.

Certain materials, due to a low surface work function, become copious emitters of electrons when heated to a sufficiently high temperature [Lafferty, 1951]. In particular, a ceramic composed of LaB_6 has proven effective in CDX at providing large thermionic emission currents. One of the technical difficulties overcome by the CDX and ACT-1 groups was to heat this material to the required temperature of

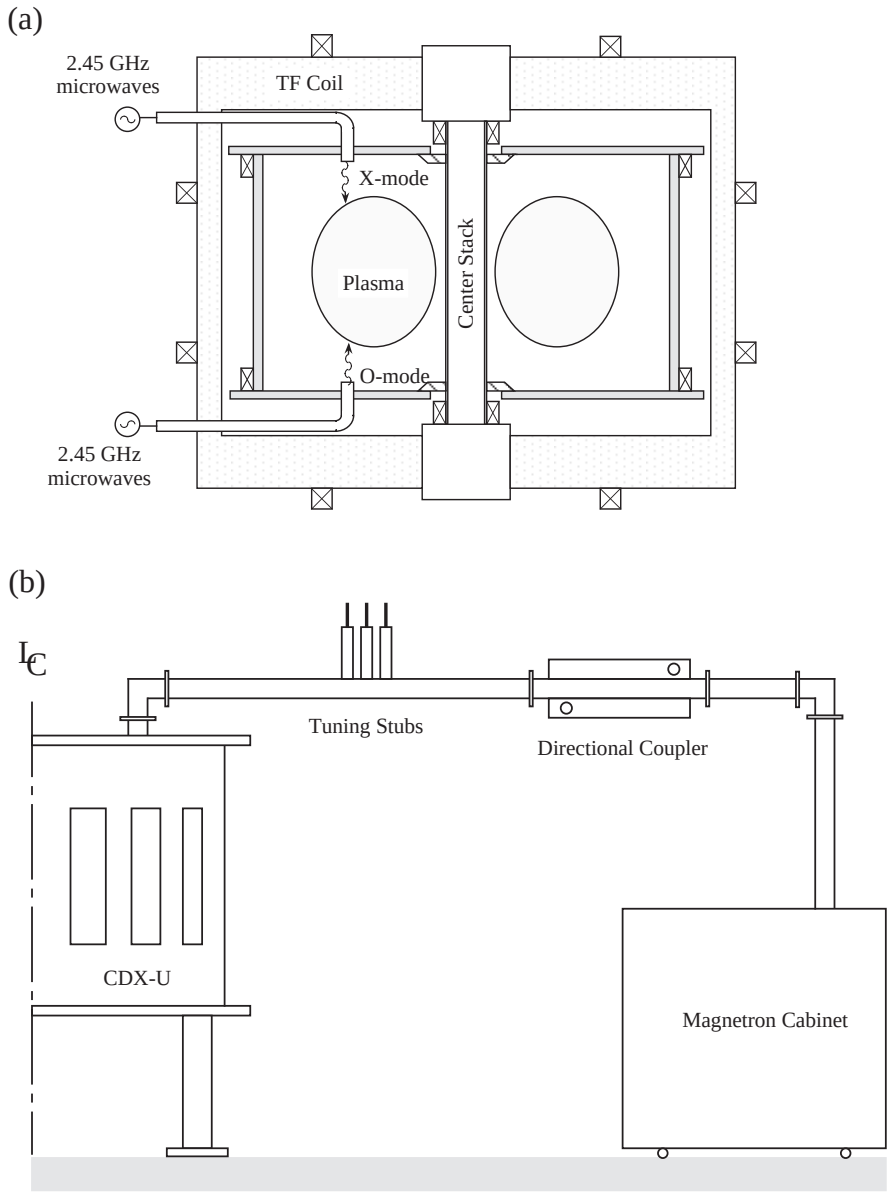

Figure 3.13. (a) A schematic showing where rf power is introduced into the vessel. The antennas are simply unterminated WG-283 waveguides. The top antenna, located at R = 35 cm, Z = 45 cm, is more than 9 cm behind the limiters, and is oriented in the X-mode polarization ($\vec{E}_{rf} \perp \vec{B}$). The bottom antenna is identical except that it is oriented for O-mode polarization ($\vec{E}_{rf} \parallel \vec{B}$). (b) A schematic of the ECH system, showing waveguide run, magnetron cabinet, and vacuum window for the top antenna (the bottom antenna and waveguide are similar).

1400 C [GOREE, 1985]. Beads of LaB_6 were supported by a carbon rod which was heated by large currents (see Fig. 3.15). Plasma breakdown was sometimes aided by the presence of the heated unbiased (with respect to the vacuum vessel) cathode. Low-level thermionic emission may have been possible from the emissive cathode across its sheath to the plasma at positive floating potential. In addition, secondary electron emission caused by high-energy electron bombardment from the plasma may have contributed additional electrons. The cathode was connected to a power supply capable of negatively biasing it for DC Helicity Injection experiments. A schematic of the circuit providing AC heating power, as well as pulsed bias power to the cathode is shown in Fig. 3.14.

3.3.3 Timing and Control Systems

The CDX-U start-up sequence is described in detail in Sec. (4.1). Timing of all events in the plasma shot sequence, including data acquisition, was controlled by a set of Berkeley Nucleonics Corp. model 7010 digital time delay modules. These modules comprise the heart of the CDX-U control console, which is housed in a series of power

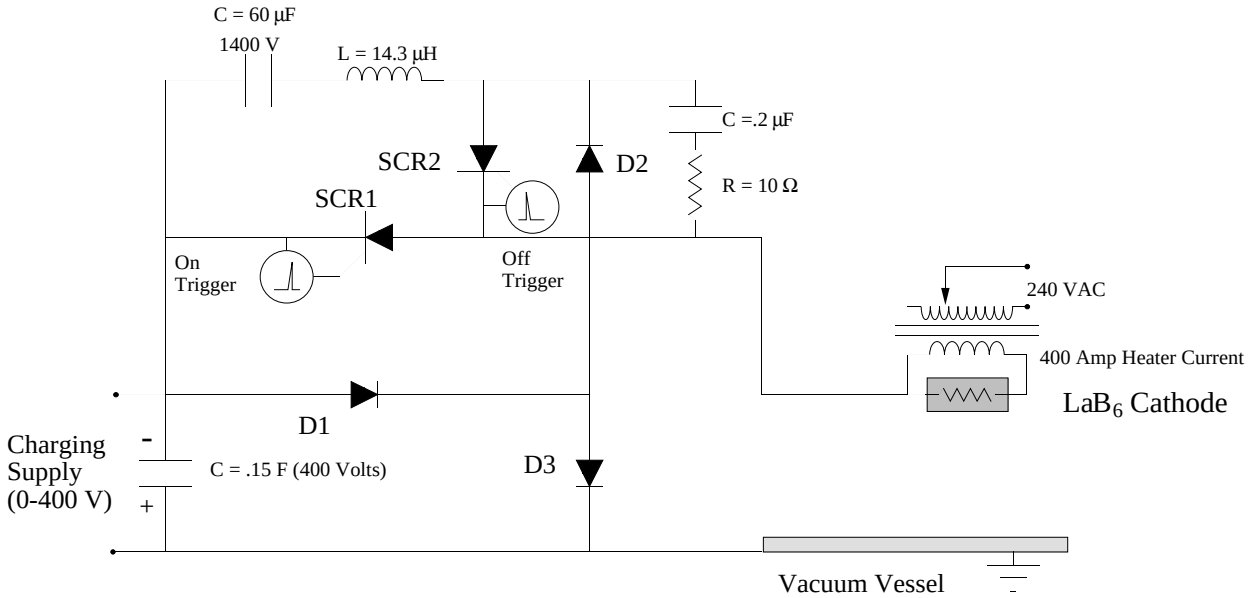

Figure 3.14. A schematic of the high current SCR switch and cathode heating circuit. AC heating current is variable up to 400 A. Bias voltage powered by a capacitor bank is switched on by SCR1 and commutated (switched off) by SCR2. The heated cathode was sometimes used to provide electrons to assist ECH breakdown.

Figure 3.15. A Photograph of the LaB_6 cathode (beads on dual supports shielded by molybdenum plates) and other hardware installed in vessel. The interferometer mirror and inside limiter is shown on the right side of the centerpost.

racks in the room with the CDX-U device. The console also contains CAMAC crates for digitizer equipment, computers for CAMAC control, and oscilloscopes for directly monitoring data signals.

One of the timing modules served as a master timer which started a series of trigger signals controlling gas puffing, energizing of PF and OH field coils, and digitizer triggering. Typically plasma shots were timed every 60 to 90 seconds, with timing determined by charging time for capacitor bank power supplies.

Inductive pickup from ground loops in data and control signal circuits can be a pernicious problem in the presence of pulsed magnetic fields and high-power AC systems. In order to avoid this problem, single-point grounding must be rigorously maintained in every electronic and electrical component in the presence of changing magnetic fields. Each component in the CDX-U laboratory, including the vacuum vessel, was grounded through a single point. Signal lines traveling between components, such as those carrying trigger signals and data, were designed with links providing electrical breaks. In accordance with these procedures, all trigger signals were transmitted via 4N35 optoisolators. Also, all AC electrical power came into the lab through isolation transformers.

3.4 Diagnostics

3.4.1 Magnetics

External Magnetic Diagnostics

By far the most closely monitored diagnostic on CDX-U during ohmic operation was a Rogowski coil measuring total plasma current[HUTCHINSON, 1990]. A Rogowski coil physically performs the path integral in Ampere's law (actually the time derivative of Ampere's law):

$$\frac{\partial}{\partial t}\int \vec{B}\cdot d\vec{l} = \mu_o \frac{\partial I_p}{\partial t}$$

This signal was then electronically integrated over time to provide a voltage proportional to the plasma current, I_p. All integrators in the CDX-U lab were reset before each shot in order to reduce noise from integrated DC bias in the raw signals.

The CDX-U Rogowski coil was constructed in two pieces.[2] The coils consisted of AWG #21 Vespel-coated wire wound around flexible tubing with a density of 30 turns per inch. These windings were housed at atmospheric pressure inside thin walled, 1.27 cm o.d. stainless steel tubes. Each tube of the Rogowski coil passed through a Wilson vacuum seal and was bent to fit against the inside wall of the vacuum vessel. The Rogowski coil, along with all other external magnetics is shielded from the plasma by the segmented limiter array [see Sec. (3.4.3)]. The two halves are shown in Fig. 3.16. The two-circuit construction of the Rogowski coil made it possible to measure the centroid of the plasma current, since the inner half of the loop is more sensitive to currents on the inside of the machine and the outer half is more sensitive to currents on the outside. The difference in the integrated signals can be related to an integrated radial position of the plasma current. This measurement was calibrated using a current-carrying conductor at various radial positions in the vessel.

In addition to the Rogowski coil, a poloidal array of magnetic pick-up coils was installed around the inside of the vacuum vessel to measure the local magnetic field strength on the boundary of the plasma. This array is shown in Fig. 3.16 and details are given in Table 3.3. Eleven sets of coils, three sets on the outer wall and four on the top and bottom flanges, were installed in a poloidal array (at a single toroidal location, $\phi = 0°$). These coils sets measure three orthogonal components of $\vec{B}$, B_R, B_Z, and B_T, on the outer boundary of the vacuum vessel. Another two identical pick-up coil sets were installed at the midplane of the outer wall at different toroidal locations ($\phi = 112.5°$, $202.5°$). The frequency response of these coils was measured from 100 Hz to 100 kHz and found to be within 8% (0.3 dB) of a perfectly flat frequency response, making them a useful diagnostic for MHD fluctuations. These coils gave some resolution of toroidal structure of observed fluctuations. Eight pickup coils sensitive to B_Z were encased in a stainless steel tube and installed along the center stack. For measuring the vertical magnetic flux along the center stack, eleven single-turn flux loops were wound and potted with 10 cm vertical spacing just inside the center stack housing.

[2]The magnetic diagnostics on CDX-U are largely the work of Y. S. Hwang. This diagnostic has been previously reported in [Hwang *et al.*, 1992].

External Magnetic Diagnostics

R (cm)	Z (cm)	Type	Field and Sensitivity
23.2 34.3 45.3 56.3 59.0 59.0 59.0 56.3 45.3 34.3 23.2	41.2 42.5 41.2 41.2 18.3 0.0 -18.3 -41.2 -41.2 -42.5 -41.2	three-element orthogonal sets of pick-up coils	B_R (131 G/V) B_Z, B_T (118 G/V) (sensitivities include integrator gain)
9.0 9.0 9.0 9.0 9.0 9.0 9.0 9.0 9.0	32.0 23.5 15.0 6.5 -2.0 -10.5 -19.0 -27.5 -36.0	single-element pick-up coils	B_Z (130 G/V)
8.5 8.5 8.5 8.5 8.5 8.5 8.5 8.5 8.5 8.5	51.0 40.8 30.6 20.4 10.2 0.0 -10.2 -20.4 -30.6 -40.8 -51.0	ψ loops	$\int B_Z \, dA$ (1×10^{-4} Wb/V)
poloidal plasma boundary		Rogowski coils	total toroidal plasma current 40 kA/V
upper outer corner midplane flange lower outer corner			toroidal eddy current in vacuum vessel 800 A/V

Table 3.3. Data for magnetic pick-up coils.

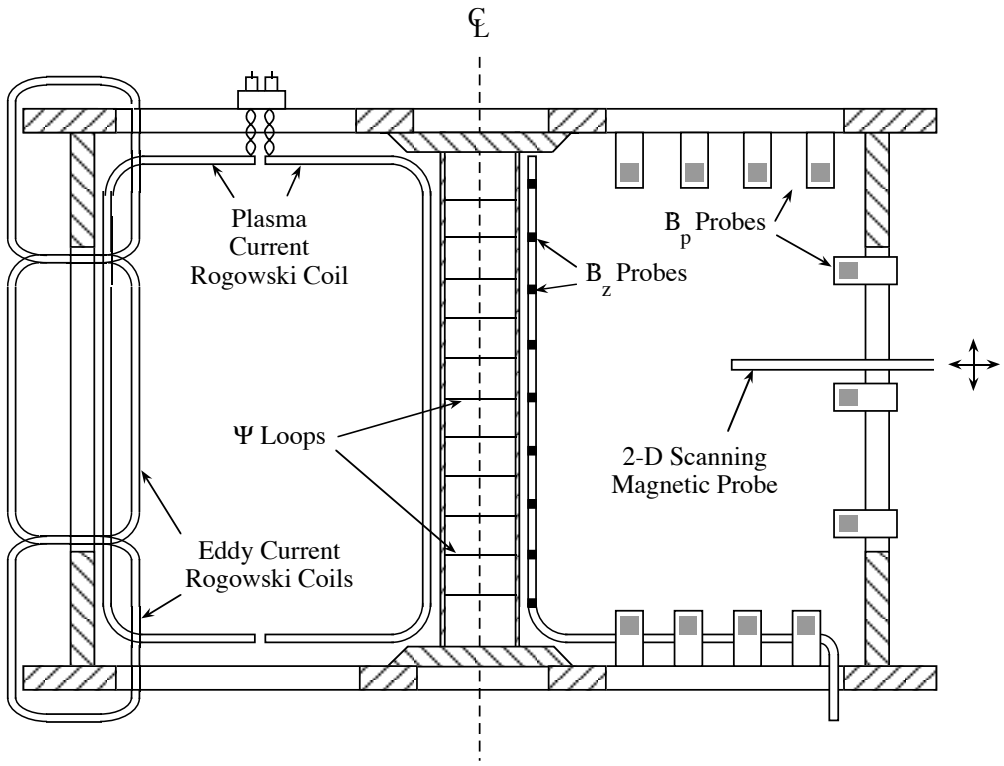

Figure 3.16. The magnetic diagnostic array on CDX-U. Shown here are the poloidal field loops on the outer, top and bottom walls, the Rogowski loop for measuring the plasma current, Ψ or flux loops on the center post, and the probe array for measuring B_z on the inside edge. Also shown are two Rogowski loops measuring eddy currents in sections of the vessel wall. An identical loop, not shown, measured eddy currents in the top corner of the outer wall.

Internal Magnetic Probes

The most versatile magnetic probe on CDX-U is a two-dimensionally scanning probe. This diagnostic is described in [Greene and Ono, 1989]. This probe was capable of measuring two components of $\vec{B}_p$, B_R and B_Z, in the outer half of the vessel volume. The pick-up coils in the probe are sensitive to magnetic fluctuations into the tens of kHz range. Its spatial mobility made it useful for measuring the structure of any strong MHD modes. The spatial scanning range of this probe is:

- R > 28 cm
- -13 cm < Z < 16 cm.

This probe is water cooled, and has a 9.5 mm o.d. boron nitride outer casing protecting it from the plasma. This probe was also used to give an indication of the outer boundary of the plasma, by observing where the probe began to perturb the plasma.

Another internal magnetic probe used during experiments in this thesis was a radially scanning probe with three pairs of pickup coils to measure orthogonal components of $\dot{\vec{B}}_p$, $\dot{B}_R$ and $\dot{B}_Z$. Pickup coil pairs were housed at atmospheric pressure in thin stainless steel tubing which entered the vacuum vessel through a Wilson seal on a 1 m vacuum flange extension. The steel tubing was shielded from the plasma by a 10 mm o.d. fused quartz tube. This probe and vacuum flange extension was mounted at the midplane of the tokamak. Each pair of coils in the probe was separated radially by 5 cm. The radial range of the innermost coil pair is:

- R > 50 cm
- at Z = 0 cm.

This probe was designed primarily to measure magnetic fluctuations, and radial correlations of fluctuations. Signals from this probe were recorded directly without integration.

3.4.2 Electrostatic Probes

Densities, density fluctuations, plasma potential, and electric fields were measured using several types of electrostatic (Langmuir) probes. Traditionally, temperature is often measured by Langmuir probes for plasmas up to $\sim$ 100 eV. However, after the OH Upgrade, sufficiently high temperatures and densities were attained in the CDX-U plasma to preclude use of uncooled probes. In central regions of the plasma, incident power density to an uncooled electrostatic probe was sufficient to destroy it.

CDX-U Langmuir probes were designed to minimize perturbation of the plasma. Towards this end, probes were typically designed to be as small as possible while maintaining sufficient mechanical strength to withstand pulsed magnetic forces on probe currents. Typical Langmuir probes consisted of 0.4 mm diameter tungsten

wire, with 5 mm of exposed area at the probe tip. This wire was surrounded by a 1.0 mm ceramic alumina tubular insulator. Outside this was a 1.5 mm o.d. stainless steel tube, which was grounded during probe operation. This grounded conducting tube provided high-frequency shielding against capacitive pick-up from the plasma around the length of the probe. Outside of everything was a 2.6 mm alumina tubular shield. This provided shielding from incident plasma power. The inner ceramic tube and stainless steel tube were slightly recessed from the probe tip, leaving only the tungsten probe tip and the outer ceramic shield tube exposed to the plasma.

For a conductor in contact with a plasma, the collected current can be characterized as a function of bias voltage with respect to the vacuum chamber. The total current collected by a Langmuir probe is the sum of collected ion and electron currents[HUTCHINSON, 1990]:

$$I = -I_{i,sat} + I_{e,sat}\, exp\left(\left(V - V_p\right)/T_e\right) \qquad V < V_p, \tag{3.4}$$

where:

$$\begin{aligned} V &= \text{probe potential in Volts} \\ V_p &= \text{plasma potential in Volts} \\ I_{e,sat} &\approx \text{probe current at } V = V_p \\ I_{i,sat} &\simeq 0.5 n_e A_{eff} \left(\frac{T_e}{m_i}\right)^{1/2}, \text{ where} \\ A_{eff} &= \text{effective probe collection area, and} \\ T_e &= \text{electron temperature in eV.} \end{aligned}$$

In a magnetic field, A_{eff} can be taken as the projected area of the probe sheath in the direction of the magnetic field. The probe sheath, where the plasma density is significantly perturbed by the probe potential, has some dependence on the probe bias, even in the ion saturation region of the I-V characteristic. The ion saturation region can be defined as:

$$\begin{aligned} V &\leq V_f - few \times T_e(eV), \text{ where} \\ V_f &= V(I = 0). \end{aligned}$$

The above form of the probe characteristic can be derived from models of the plasma sheath at the probe using several strong assumptions. Most of the assumptions

affect the ion current estimation. First, the model assumes that the Debye length is small compared to the probe tip dimensions, so that ion orbit dynamics do not affect collection at the probe. In CDX-U the Debye length was smaller, though of similar order to the probe diameter. This increases the probe sheath size which is typically a few Debye lengths, and therefore increases the collected ion saturation current ($\sim$ factor of two). The sheath size also has some modest dependence on bias voltage in the ion saturation region. Also, $T_i \ll T_e$ is assumed in derivations of the above. Numerical calculations have shown that $T_i \sim T_e$ slightly decreases the ion current[LAFRAMBOISE, 1966] ($\sim$ 20 % effect).

Because Langmuir probes were used primarily for density fluctuation measurements in the plasma edge, corrections to the above ion current formula were ignored. Absolute plasma density derived from the ion saturation current was used as a rough check on measurements with the 2 mm interferometer system [see Sec. (3.4.4)]. Core temperatures were determined primarily from charge-state analysis of spectroscopic data.

Operation of the Langmuir probe is simple: the current collected at the probe tip is measured as a function of probe bias with respect to the vacuum chamber potential. A schematic of the circuit used to control probe bias, and measure probe current is shown in Fig. 3.17. For density measurements, a time-history of the probe current at a fixed voltage was recorded for each shot. For temperature measurements, shot to shot reproducibility was invoked to compile an I-V characteristic from several shots of data, as the fixed probe voltage was changed between shots. This technique provided a time resolved I-V characteristic, and therefore temperature. Frequency bandwidth of density fluctuation measurements was determined by amplifier bandwidth, and digitizer sampling frequency. Plasma potential fluctuations could also be measured by simply recording the probe floating potential (voltage at the probe across a 1 MΩ to ground). Plasma potential and probe floating potential are related by:

$$V_f - V_p = \frac{T_e}{e}\frac{1}{2}\left[ln\left(2\pi\frac{m_e}{m_i}\right) - 1\right]$$

A CAMAC-controlled digital to analog converter (Kinetic Systems 3112 12-bit DAC) provided an input voltage to a Kepco $\pm$200 V, $\pm$1 A, bipolar operational amplifier. The current flowing to the probe was determined by measuring the voltage across a 10 Ω resistor in series with the op-amp. The signal was detected and amplified by a Stanford Research SR560 Low-Noise pre-amp with 1 MHz bandwidth. For

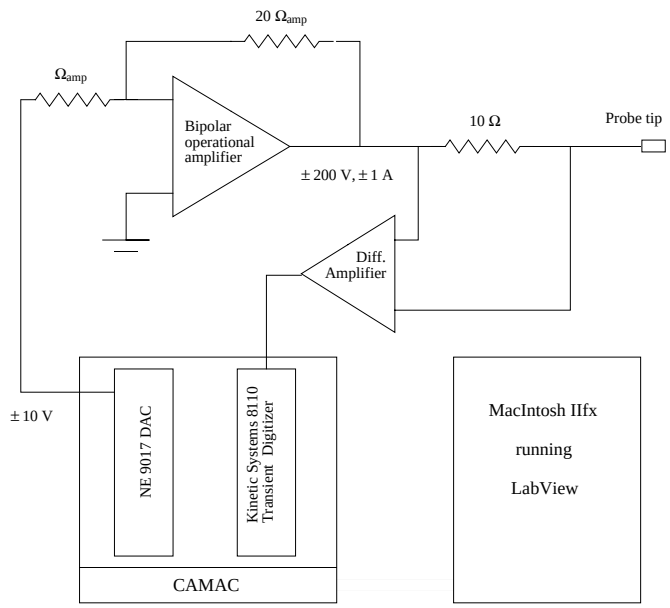

Figure 3.17. A schematic of the Langmuir probe control circuit.

probe fluctuation measurements, the sampling frequency was typically 1 MHz with LP filtering at 300 kHz.

Spectral analysis was usually performed with the digitized data on either the MacIntosh Quadra 800 controlling the data acquisition system, or on a UNIX workstation. However, power measurements could also be made by examining the signal directly on a Hewlett-Packard spectrum analyzer (a 141T display with a 8552B IF section and a 0.01-18 GHz 8555A rf section).

3.4.3 Segmented Limiter Array

All CDX-U ohmic plasmas had boundaries determined by limiters. An array of electrically isolated limiters was installed to measure currents flowing from the periphery of the plasma to various parts of the vessel, sometimes referred to as "halo currents". This limiter array completely surrounded a poloidal cross section of the plasma. The arrangement of the segmented limiter array was as shown in Fig. 3.18. Graphite was used as a limiter material due to its ability to withstand high temperatures. Each of the limiters was mounted on ceramic standoffs which electrically isolated it from the wall. Each limiter was wired to a current-sensing shunt through an electrical feed-through and then grounded outside the vessel.

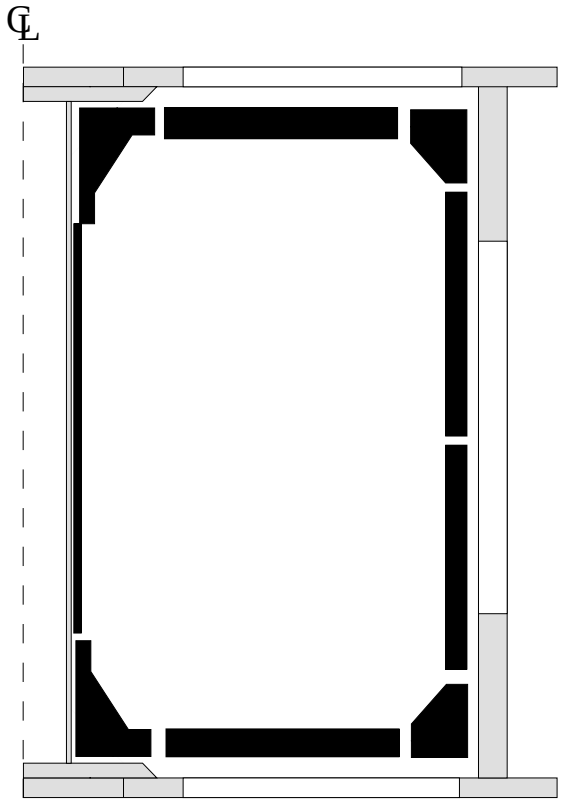

Figure 3.18. The segmented limiter array for CDX-U. These limiters were constructed out of 0.5 cm graphite sheet, and were electrically isolated from the vessel. Each limiter was grounded outside the vessel through current-sensing shunts made from high resistance tungsten wire.

According to Eq. (3.4), for plasma potentials $V_p > 0$ (measured with respect to the vessel ground), a probe will collect mostly ion current. The ion current will be proportional to the plasma density, n_e. For $V_p < 0$, electron current is collected, which again is proportional to n_e as well as a factor depending on electron temperature. Therefore, relatively large absolute values of current to a grounded limiter indicated the proximity of the plasma and/or the opening of a flux surface to it. The set of segmented limiter current signals, with magnetics measurements used as a cross-check, served as accurate and often-used diagnostic of plasma location and movement in CDX-U.

If the current to a particular limiter was non-zero and it was assumed that current was flowing into and not out of the limiters, the sign of the current was an indicator of the charge carrier sign. For example, if a limiter had a net negative current, that

was an indication that electrons were being lost at that location. The limiters restrict the plasma volume to a region defined by

- 11 cm < R < 54 cm
- -34 cm < Z < 35 cm.

3.4.4 Microwave Interferometer

Microwave interferometry provides a non-perturbative way to measure plasma density and profile information, and as such is extremely valuable for characterizing core regions of the plasma. In principle, interferometry consists of measuring the index of refraction of the plasma and relating it to the electron density. This is done by measuring the interference between two beams, a diagnostic beam which is transmitted through the refractive medium, in this case the plasma, and a reference beam which travels through air, which is essentially non-refractive at this frequency.

In the CDX-U interferometer system, microwaves were transmitted with O-mode polarization ($\vec{E}_{\mu-wave} \parallel \vec{B}_T$) for both diagnostic views. For O-mode propagation the index of refraction in plasma is given by

$$n^2 = \frac{c^2 k^2}{\omega_{rf}^2} = 1 - \frac{f_{pe}^2}{f^2},$$

where the plasma frequency is given by

$$f_{pe}^2 = \frac{1}{4\pi^2} \frac{n_e e^2}{m_e \epsilon_0}.$$

and f is the frequency of the transmitted beam. During a plasma discharge, the propagation speed of a microwave beam decreases from the vacuum value. This adds an additional phase shift to the beam. If $f_{pe} \ll f$, the phase shift can be approximated to be

$$\Delta\phi = \frac{e^2}{4\pi f \epsilon_0 m_e} \int n_e(l) dl = \frac{e^2}{4\pi f \epsilon_0 m_e} \overline{n_e} L,$$

where the integral is taken along the beam path. This technique is a non-local measurement in that it measures the chord-averaged value of the density, $\overline{n_e}$. To obtain the local density distribution, an inversion technique must be used in conjunction with the chord-averaged profile measurements. If the geometry is simple (e.g. circular cross-section), standard inversion techniques can be used.

Chord-averaged density profiles were obtained in CDX-U plasmas using a 140 GHz (2.14 mm) microwave interferometer diagnostic. This heterodyne interferometer system had a single diagnostic beam which could be set to pass through either a vertical or a horizontal chord of the plasma. Both vertical and horizontal view optics were mounted on movable tables which could scan horizontally or vertically, respectively. The microwave optics arrangement for this 2-D scanable interferometer system is shown in Fig. 3.19. The diagnostic beam shone through 1.0 cm thick, rectangular fused quartz windows in the top, bottom and side of the device. The range of viewing chords was limited by the windows to:

- 28 cm $\leq$ R $\leq$ 58 cm, and
- |Z| $\leq$ 22 cm.

An 11 cm $\times$ 54 cm graphite mirror was mounted on the center column and acted as a mirror for the horizontal view. This instrument is largely the work of Cary Forest, and has been described in detail in [FOREST *et al.*, 1990].

Stainless steel honeycomb was installed in the windows to prevent 2.45 GHz radiation from the ECH system from escaping the vacuum chamber. This honeycomb had a 0.95 cm cell size and acted as a high-pass rf filter. It provided a cutoff for 2.45 GHz rf, and was over-moded (optically transparent) for 140 GHz rf.

Since the vertical view was only able to provide profiles for $R > 28$ cm, an additional channel was installed inside the vacuum chamber. Two antennas identical with the horizontal view antennas were mounted inside of the vacuum vessel. These antennas provided a single channel at R = 18 cm.

The tables supporting the optics were moved by stepper motors controlled by Superior Electric SP153A indexers. Typically during CDX-U operation, switching between vertical and horizontal viewing, as well as positioning of the optics was performed manually between plasma shots. A logic control unit was also available for CAMAC-controlled movement of the interferometer optics. The vertical and horizontal spatial resolution of this system has been estimated previously to be $\leq$ 2 cm.

This heterodyne interferometer system uses two microwave sources. The transmitter is a fixed-frequency 17 mW Gunn diode oscillator manufactured by the ZAX Millimeter Wave Corp., and operating at a frequency of 137.9 GHz. The local oscillator is a 10 mW, mechanically-tunable Gunn diode tuned to 137.6 GHz, approxi-

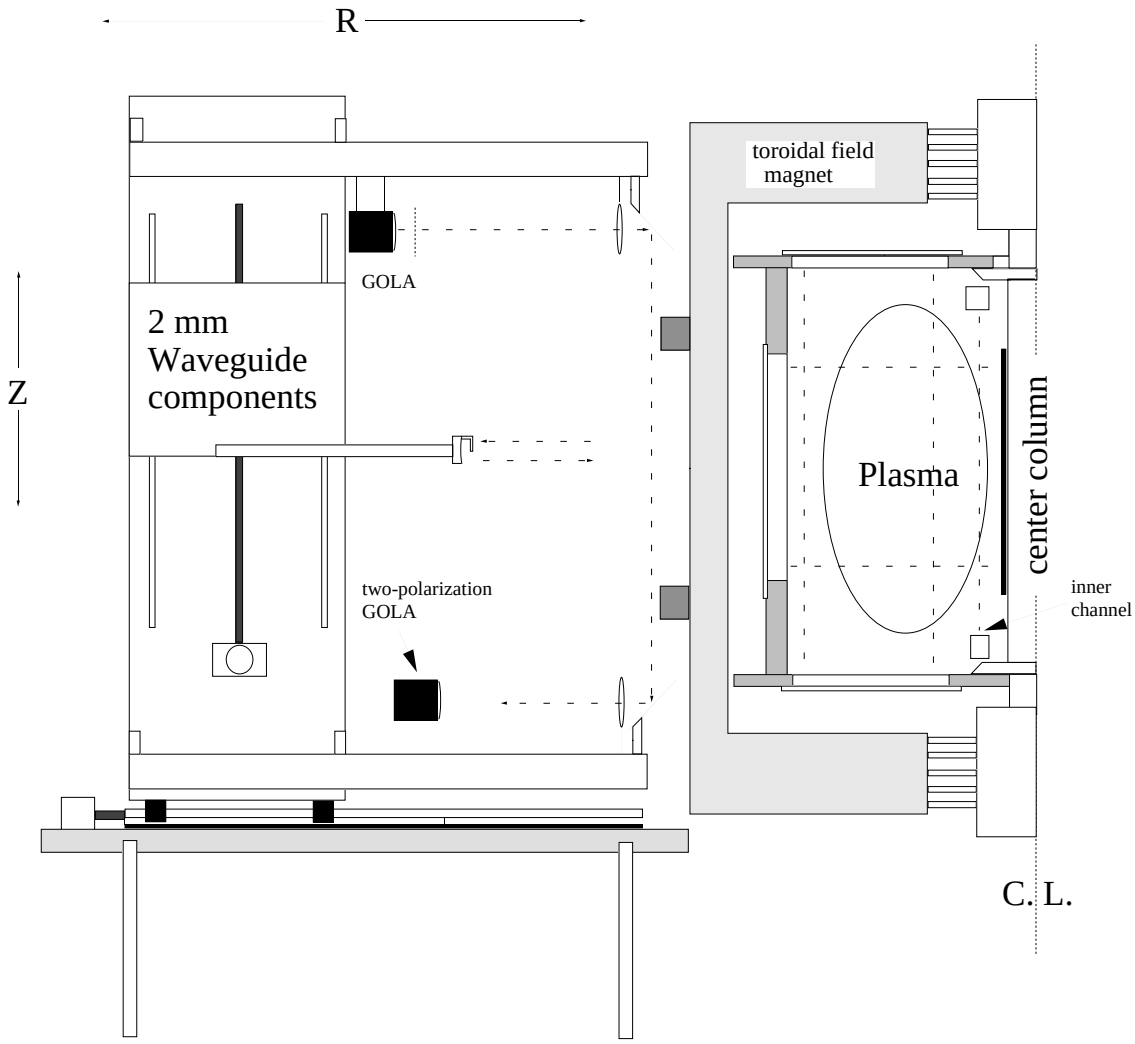

Figure 3.19. A schematic shows the microwave interferometer optics arrangement in relation to the CDX-U vacuum vessel. The vertical view Gaussian Optics Lens Antennas (GOLAs) and the horizontal view Cassegrain-type antennas can be seen attached to their movable support tables. The dotted lines represent the transmission paths for both the horizontal and vertical view. Inside the vessel, the dotted lines demarcate the viewable cross-section of the plasma.

mately 300 MHz from the transmitter. The drifting frequency difference between the transmitter and the local oscillator is canceled by a forward-tracking circuit [DOANE, 1980]. This rf circuit first up-converts the phase information in the reference signal and then mixes it with each of the receiver signals, subtracting out any phase error due to frequency fluctuations in the Gunn oscillators. The receiver channels are then down-converted to an intermediate frequency (IF) of 30 MHz for signal processing. The 30 MHz IF signals were then fed through narrow band-pass filters so that only the phase-modulated carrier signal was transmitted to the phase detector. The phase detector used during experiments in this thesis was an rf (2 - 100 MHz) amplitude and phase detector [CUTSOGEORGE, 1980]. This phase detector could measure up to 4π radians of phase change with an output of 0 - 5 Volts.

3.4.5 Spectroscopy

Some simple spectroscopic diagnostics were available during experiments in this thesis. An amplified photomultiplier tube with a phosphor screen sensitive to soft x-rays was used in line with metal foil filters. Two filters in particular were used during several shots. A Ag 2000 Å foil in series with a Sn 2500 Å foil served as a filter with a bandpass of around 30–80 Å. This filter was chosen to select the C V Helium-like line (2p-1s). A pair of Zr 4000 Å foil filters served as a filter with a bandpass of 100–150 Å. This filter selected the O VI 3d-2p lines. At typical densities found in CDX-U ohmic shots, the C V line would be excited at temperatures above approximately 60 eV, while the O VI lines would be significantly excited at temperatures over 100 eV. The presence of these lines simply indicate a significant population of electrons at energies over those quoted. However, in combination with temperature estimates based on measured neoclassical resistivity, this charge state analysis of oxygen and carbon was used to infer minimum central electron temperatures. These spectroscopic diagnostics are principally the work of Dan Stutman, a post-doc from Hebrew University who is working with the CDX-U group.

3.5 Data Acquisition System

The CDX-U data acquisition system consists of a set of digitizers, CAMAC crates and a MacIntosh computer for crate control contained within the CDX-U control

console. Digitizers and other components in the CAMAC crates were controlled by a MacIntosh Quadra 800 via an 8901 GPIB crate controller. A LeCroy 8210 10-bit, 4-channel, 100 kHz differential input digitizer recorded data into a LeCroy 8800/12 memory module, which was then downloaded to the MacIntosh computer. A LeCroy 8212A/8 12-bit, 8-channel, 25 kHz digitizer stored data in another LeCroy 8800 memory module. Four LeCroy 6810 12-bit 4-channel, 250 kHz, differential input waveform recorders were also available for data recording. All CAMAC control was performed by National Instruments LabVIEW 3.1 programs running on the MacIntosh computer.

Many signals were monitored on oscilloscopes as well as digitizers and LabVIEW routines. The most primitive form of data recording, used as a backup to digitization, was to take Polaroid pictures of oscilloscope waveforms. Signals were typically transmitted to the CAMAC crate by coaxial cable or twinax cable with a grounded shield, and then monitored on a differential input stage of the digitizers to avoid creating ground loops. Fluctuation or other signals recorded for later spectral analysis were filtered at some frequency less than the Nyquist sampling frequency before digitization.

Chapter 4

Low-aspect-ratio Start-up

SEVERAL aspects of the critical start-up phase of a low-aspect-ratio tokamak discharge are unique to the low-aspect-ratio configuration. Operational techniques to deal with these features as well as a solid understanding of their effects are vital to LART operation.

As discussed in Sec. (1.1.2), the limited volume of the center stack in a LART means that the size and flux (volt-second capability) of a central ohmic heating coil are severely limited. For ohmic LART experiments such as NSTX to be viable, optimal use must be made of the limited OH system volt-seconds, in addition to the development of effective, non-inductive current drive methods. In a conventional tokamak with purely inductive start-up, a minimum loop voltage must be maintained for several milliseconds in order to sufficiently energize free electrons to ionize the working gas. This minimum loop voltage depends on the device size and field configuration, and can be up to 30 - 40 Volts for small low-field devices. This constitutes a huge expenditure of ohmic heating system volt-seconds. Additionally, this period of high loop voltage requires a high-voltage OH power supply capable of driving rapid change in the OH solenoid current. In CDX-U this would have entailed using a high-voltage (several thousand volts) OH capacitor bank. Capacitors capable of operating at such voltages would be much more expensive and bulky (much lower stored energy per unit volume) than the lower voltage electrolytic capacitors used to power CDX-U.

Another LART start-up issue is the presence of significant ohmically-induced wall eddy current. Due to the limited size of the structure in the center of the torus, and the fact that the center stack structure and inner vacuum wall is likely to be

a separate component from the rest of the vacuum vessel, toroidal electrical vessel breaks are extremely difficult to design in a LART. Induced wall eddy currents can significantly affect the magnetic structure of the tokamak, therefore proper PF coil programming as well as plasma position diagnostics are necessary to maintain correct field structure and plasma position. For this reason, ohmic induction of wall eddy current is an important motivation to keep the initial voltage spike to a minimum.

The first focus for an attempt to conserve limited OH volt-seconds in a LART is therefore the initial breakdown phase of the discharge, when the plasma resistivity is very high. In CDX-U, auxiliary ECH power is used for breakdown. A small amount of ECH power was sufficient to reduce significantly loop voltage requirements during the plasma start-up, specifically, eliminating the required loop voltage spike necessary for plasma breakdown with purely inductive start-up. CDX-U OH power supplies were designed for the low loop voltage startup possible with ECH preionization. Without a high voltage spike capability, unaided inductive plasma start-up was not possible in CDX-U with the available OH power supply.

4.1 The CDX-U Ohmic Start-up Sequence

The CDX-U start-up sequence for a typical ohmic shot in the experiments in this thesis is shown in Fig. 4.1. Timing of all events during the CDX-U discharge were controlled from a rack of digital time delay generators [see Sec. (3.3.3)]. Vacuum conditions were found to be critical for optimal ohmic performance and discharge reproducibility. Prior to gas puffing, the LaB_6 cathode was heated to emissive temperatures. Titanium gettering was used between runs (overnight). Vacuum base pressure in CDX-U is usually in the low 10^{-7} Torr range, but with the heated cathode on, the pressure rises to $1 - 4 \times 10^{-6}$ Torr during experimental runs. Optimal plasma parameters would be attained after 20 - 40 shots ($\frac{1}{2}$ hour - 1 hour) during which OH and PF power would slowly be brought up to desired levels. The interval between shots was typically 90 seconds.

The start of each discharge sequence was triggered by a pulse from a master clock. In addition to triggering the sequence of gas puffing, rf heating, and magnet coil pulses, this trigger pulse would reset many of the electronics for the diagnostics such as the magnetic diagnostic integrators and the interferometer fringe counter.

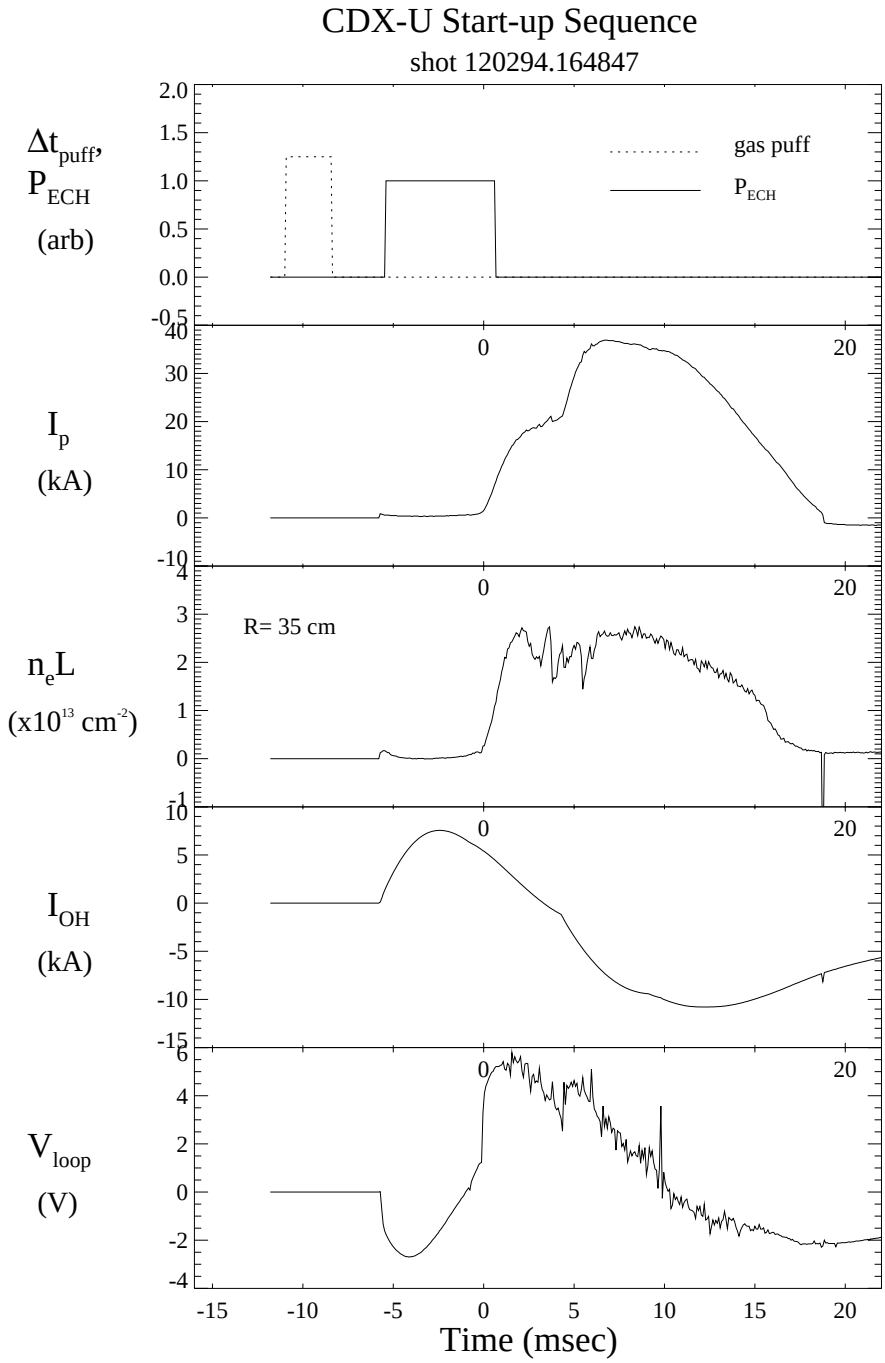

Figure 4.1. The timing of gas puffing and ECH power are shown in relation to plasma current, line-integrated density along the major radius, the ohmic solenoid current, and loop voltage measured at the outer midplane of the vacuum vessel.

The CDX-U start-up sequence began with a puff of the working gas into the chamber which started approximately 11 ms before the start of the plasma current ramp-up (t= -11 ms). The piezoelectric gas puff valve was given a voltage signal sufficient to fully open the valve for 2.5 ms, which is on the order of its characteristic opening time. The gas puff brought the neutral pressure up to the order of $few \times 10^{-5}$ Torr, although this could not be measured accurately since the response time of the ion gauges was slower than the change in fill pressure. Plasma ionization and current ramp-up were highly sensitive to gas puffing time, and therefore neutral gas pressure. In general, the lowest neutral pressure which still allowed breakdown by the ECH system provided the highest ramp-up rate and maximum plasma current.

The DC toroidal field at the plasma major radius was usually 1.0 kG, although ohmic discharges were created with a large range of TF strength. At t= -5.8 ms, the first bank of the OH power supply was fired, and the OH solenoid current began to increase and "charge up" with flux. At t= -5.4 ms, the magnetron ECH source was fired and rf power was transmitted with X-mode polarization into the top of the vessel. Rf transmitted power in the transmission waveguide (see Fig. 3.13) was measured to be 1.2 kW with a Schottky diode detector. The ECH power remained on until just after plasma current ramp-up began.

At t= -2.5 ms the OH primary current reached a maximum and began its downward swing, creating a positive loop voltage in the plasma volume at approximately t= 0 ms, after the resistive time of the vessel. The beginning of positive loop voltage was measured at t= 0 ms at the vessel gap. The first PF coils to be energized were the green and orange/black PF coil sets (see Fig. 3.9) at t= -0.9 ms. As discussed in Sec. (4.3.2), PF coil currents were programmed to provide the proper equilibrium field for the plasma, which in part required the cancellation of much of the eddy-current induced field. At t= -0.2 ms the main vertical field PF set (yellow coil set) was fired, providing radial force balance and stability. After an initial plasma current ramp up to approximately 20 kA, OH bank 2 was fired at 4.2 ms after the start of ramp-up (t= +4.2 ms), driving the OH solenoid current further negative, and supplying a second surge in loop voltage as described in Sec. (3.2.3). Simultaneous with OH bank 2, a second capacitor bank for both the yellow (vertical field) and orange/black coil sets were fired in order to provide proper equilibrium field for the surge in plasma current. Plasma current increased at rates of up to 10 kA/ms, with the maximum rates at times of maximum loop voltage, just after each OH bank was fired. Peak

loop voltages were around 5 V. At t= +9.0 ms OH bank 3 was fired driving a further slow increase in negative OH solenoid current, and providing a relatively long, low loop voltage pulse for maintenance of the plasma current.

The maximum plasma current typically occurred at about 6 ms after the start of ramp-up, giving an averaged ramp-up rate of 6 kA/ms for $I_{p,max} \approx 36$ kA. For peak current shots achieved in CDX-U, $I_{p,max} \approx 60$ kA and the average ramp-up rate is 10 kA/ms.

4.2 ECH Preionization

4.2.1 Electron Cyclotron Resonance Heating

Electron Cyclotron resonance Heating (ECH) involves transmitting rf power to the plasma which is then absorbed where the transmitted frequency is a multiple of the electron cyclotron frequency,

$$f_{ce}(\mathrm{Hz}) = \frac{eB}{2\pi m_e} = 2.8 \times 10^6 B, \qquad \text{(B in Gauss)}. \tag{4.1}$$

A good review of the wave propagation and absorption is given in [Stix, 1992].

In the CDX-U plasma volume, f_{ce} typically ranges between 1-10 GHz, depending on major radius and TF current. The ECH system frequency used was 2.45 GHz. ECH rf breakdown and start-up was first used in low-aspect-ratio in CDX-U, in experiments in which trapped particles in an open-field line configuration were heated solely with ECH [Forest, 1992]. Sufficient pressure-driven toroidal currents were generated to close the flux surfaces and sustain a tokamak configuration. Experiments in this thesis focus on using ECH preionization to assist inductive start-up in low-aspect-ratio .

Several possibilities for ECH rf power absorption exist, depending on the plasma parameters and polarization of the waves. Both X-mode ($\vec{E}_{rf} \perp \vec{B}$) and O-mode ($\vec{E}_{rf} \parallel \vec{B}$) polarizations were launched with equal breakdown efficiencies. Since different absorption coefficients are predicted for the two polarizations, this suggests that the waves undergo multiple reflections within the vacuum vessel before absorption. Waves can be reflected from the vessel walls, as well as the wave cutoffs present in the plasma. Multiple reflections can serve to "scramble" the polarization, so that

both polarizations are present after multiple reflections when only one polarization is launched [COSTLEY *et al.*, 1974]. Also, multiple reflections can allow some of the processes discussed below to occur.

Single-pass absorption at the fundamental and low-harmonic electron cyclotron resonances for nearly perpendicular propagation of the X- and O-modes is theoretically predicted to be weak. The single-pass wave energy transmission, $T = exp(-2\pi\eta)$, of the fundamental and second harmonics of the X- and O-modes can be calculated to lowest order in $\alpha^2 \equiv \frac{\omega_{pe}^2}{\omega^2}$, yielding [MANHEIMER, 1979]:

$$\begin{aligned} \eta_{O1} &\propto \alpha^2 \frac{\omega}{c} \frac{T_e}{m_e c^2}, \\ \eta_{O2} &\propto \alpha^2 \frac{\omega}{c} (\frac{T_e}{m_e c^2})^2, \\ \eta_{X1} &\propto \alpha^2 \frac{\omega}{c} (\frac{T_e}{m_e c^2})^2, \\ \text{and} \quad \eta_{X2} &\propto \alpha^2 \frac{\omega}{c} \frac{T_e}{m_e c^2}. \end{aligned}$$

For the early start-up plasma, $\frac{T_e}{m_e c^2} \ll 1$ and T is nearly 1. Thus, one possibility is that X- and O-mode waves are weakly but directly absorbed at the cyclotron harmonics over multiple passes.

A possibility for strong X-mode absorption is for the wave to first be mode-converted at the upper hybrid (UH) resonance into an Electron Bernstein Wave (EBW) [PENG *et al.*, 1978; CAIRNS, 1991]. This assumes approach from the high-field side, since the X-mode does not propagate between its cutoff at lower density and field, and the UH resonance. Therefore, this absorption process also assumes reflection from the inboard part of the vessel. The EBW is then strongly resonant at the cyclotron harmonics.

Finally, for finite $k_{||}$, the O- and X-modes have coinciding wavenumbers at some point in the plasma, allowing the O-mode to mode-convert to an X-mode and then be mode-converted into an EBW at the UH resonance [CAIRNS, 1991].

4.2.2 Optimal Parameters for ECH Breakdown in CDX-U

Various combinations of vacuum conditioning techniques were used during ohmic operation. Generally, the lowest base pressures attainable, obtained with the help of

the cryo-pump and Ti gettering produced the highest plasma current ramp-up rates.

Transmitted ECH Power

Transmitted ECH power was varied for a given start-up field configuration and fill pressure and found to have a fairly narrow range which allowed breakdown and plasma current ramp-up. At B_0= 0.75 kG, breakdown would not occur for transmitted power $P_{ECH} < 0.9$ kW. Plasma current ramp-up would not occur for $P_{ECH} > 1.5$ kW. In general, a slightly higher P_{ECH} as well as a slightly higher fill pressure (gas puffing duration) was found to be necessary as the toroidal field was increased. This higher fill pressure at higher P_{ECH} may be needed to control the increased influx of impurities from the limiters. Conversely, for a given fill pressure, a P_{ECH} that is too high may cause excessive impurity influx for current ramp-up. The higher P_{ECH} necessary at higher B_0 is consistent with the larger volume of the ECH resonant layer and the increased total absorbed rf energy needed to ionize it.

B_T Operational Range

Startup was achieved within a range of toroidal field variation of a factor of 2.4. Figure 4.2 shows the calculated flux contours in the vessel at start-up. A field null is present on the midplane, just outside the outer limiter radius. The maximum and minimum ECH layer positions are shown as dotted lines, and the position yielding optimum $I_{p,max}$ and $\dot{I}_p$ is shown as a dashed line. The poloidal field configuration at start-up is similar to that found on the outside of a tokamak field configuration, with the field lines at their maximum radial position on the midplane, and moving inward in radius as they extend towards the top and bottom of the vessel. A large fraction of particles in this configuration are likely to be magnetically trapped by the variation in toroidal field strength along the field line, in identical fashion to banana-trapped particles in the tokamak configuration [see Sec. (2.1.2)]. In low-aspect-ratio this field strength variation is especially large [see Eq. (2.8)], and is roughly a factor of 5 in typical CDX-U plasmas. Electrons with large $(\frac{v_\perp}{v_\parallel})$, such as those heated by ECH, are even more deeply trapped than thermalized particles for the same field strength variation. This "trapped particle configuration" is nearly the same as that used for start-up in the previous 100%-bootstrapped tokamak configuration with ECH start-up [Forest, 1992].

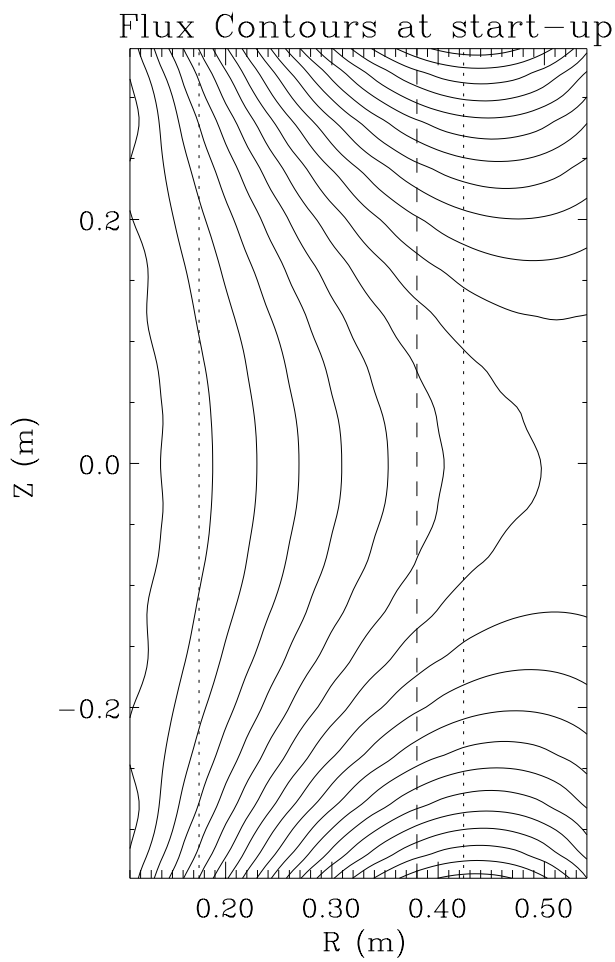

Figure 4.2. The poloidal flux contours at the start of the plasma current ramp-up (t= 0 ms in Fig. 4.1) are shown above. Start-up was possible with a range of B_{T0} between 0.45 kG and 1.1 kG. The maximum and minimum radii of the ECH resonance layer, 18 cm< R_{ECH} <42 cm, for this range of field are shown as dotted lines, while the optimal position is shown as a dashed line. The boundaries of the flux plot coincide with the limiter positions bounding the plasma volume.

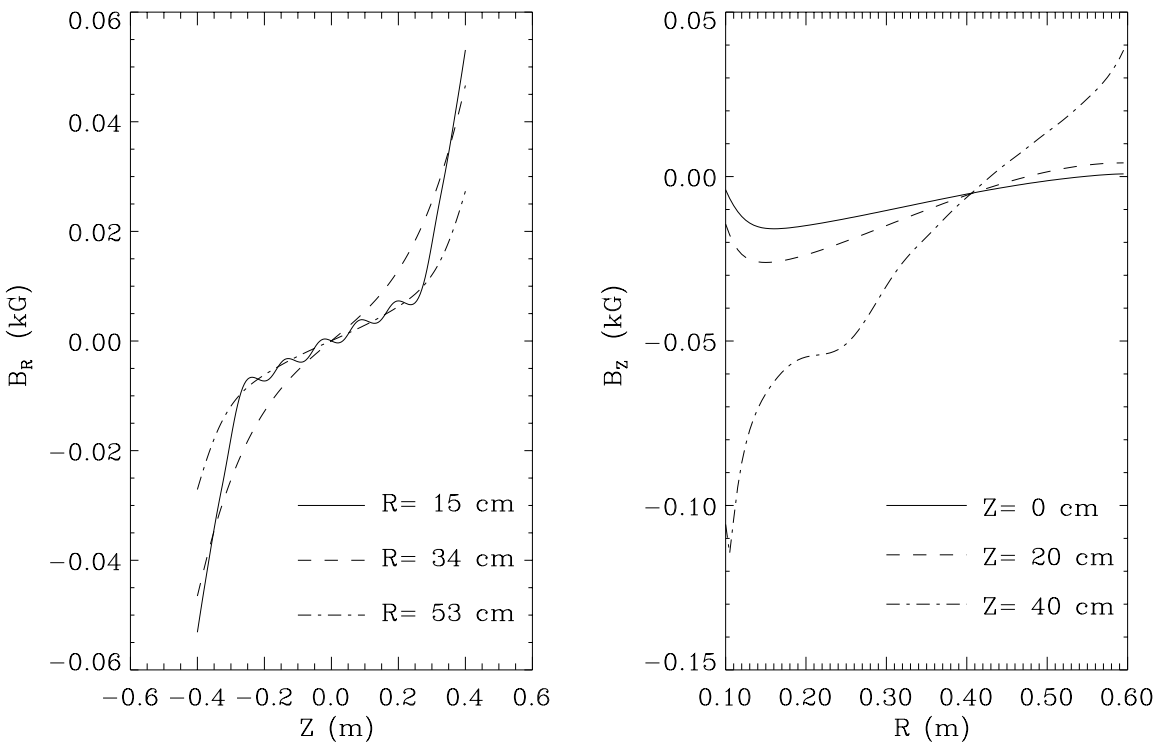

Figure 4.3. Radial and vertical fields at the start of the plasma current ramp-up (t= 0 in Fig. 4.1) are shown above. These field values correspond to the flux configuration shown in Fig. 4.2. These fields include contributions from the PF coils, as well as from OH induced eddy currents, calculated as described in Sec. (4.3.1). These fields were used to estimate typical path lengths to the limiters for loss of particle along the field lines.

The ECH resonance layer occurs where B satisfies the ECH resonance condition, Eq. (4.1). For most tokamaks the vacuum toroidal field, $B_T(R)$, dominates the field and the resonance layer is approximately only a function of major radius, R_{ECH}. The minimum R_{ECH} for start-up is quite close to where field lines intersect the inside limiter, rather than the top and bottom limiters. Path lengths for untrapped charged particles starting on the midplane were estimated using calculated fields from the TF and PF coils, as well as those due to calculated vessel eddy currents [Sec. (4.3.1)]. A plot of the radial and vertical fields at startup is shown in Fig. 4.3, corresponding to the flux configuration at start-up shown in Fig. 4.2. These path lengths ranged from approximately 30 m at $R_{ECH,max}$ to only a few meters for those originating at $R_{ECH,min}$. These path lengths determined particle confinement times in the open field line configuration at breakdown and early start-up stages. As these path lengths and confinement times decreased, there was less time for particles to gain energy from the OH-induced electric field, as well as less time for collisional ionization to take place. In addition, the decreased path length for passing particles could limit plasma start-up by increasing plasma power incident on the limiter and increasing impurity influx into the ECH layer. In addition, the effect of $E_{||}$ from the OH is to tilt the trapped particle orbits, so that one "banana tip" is farther inwards in major radius. This has the effect of reducing the trapped particle population confined within the limiters, especially near the inner limiter. The maximum R_{ECH} for start-up seemed to have been limited simply by the ECH power available for breakdown in the larger ECH-layer volume.

The ECH layer position whose toroidal field yielded the best plasma current, OH efficiency, and shot-to-shot reproducibility is shown as a dashed line in Fig. 4.2, and was slightly outboard of the major radius of the plasma. A balance of several competing factors determined this optimal toroidal field value (optimal R_{ECH}). The most important factor favoring large B_{T0} and R_{ECH} is the existence of a minimum q_a needed to support a high $I_{p,max}$. One factor favoring smaller B_{T0} and R_{ECH} is the reduction in volt-seconds needed to drive a given I_p in a current channel at small R [see Sec. (4.4.2)]. The need to keep the current channel reasonably well centered within the vessel volume and away from the limiters also favored a moderate to small R_{ECH}. In this it is assumed that ECH-resonant trapped particles are heated near a "banana tip" in their orbit, where $v_{||}$ is smallest and the particles spend most of their orbit time.

Electric Field Strength

In addition to particle confinement times, the parallel electric field, $E_{||}$, played an important role in breakdown and start-up. We use the approximation:

$$E_{||} \approx E_{\phi} = \frac{V_{loop}}{2\pi R}. \tag{4.2}$$

Clearly, maximization of $E_{||}$, which drives ionization, is aided by start-up at smaller R. Assuming ionization at the ECH resonance position to the dominant source of ions and electrons in the early plasma, we take R_{ECH} to be the relevant radius for calculation of $E_{||}$. For start-up in CDX-U, 18 cm< R_{ECH} <42 cm, and the parallel electric field was in the range

$$\begin{aligned} 0.4\ \tfrac{V}{m} \ &< \ E_{||} \ < \ 0.9\ \tfrac{V}{m}, \qquad \text{when } V_{loop} = 1 \text{ V}, \\ \text{and } 2.0\ \tfrac{V}{m} \ &< \ E_{||} \ < \ 4.7\ \tfrac{V}{m}, \qquad \text{when } V_{loop} = 5 \text{ V}. \end{aligned}$$

According to the Townsend avalanche model [Engel, 1965], plasma breakdown occurs when the ionization rate exceeds the charged particle loss rate. This condition imposes a minimum limit on $E_{||}$, which must be exceeded to achieve breakdown. Larger values of $E_{||}$ did not provide noticeable improvement in CDX-U start-up reliability or reproducibility. The ionization rate and, therefore, $E_{||,min}$ depend strongly on the neutral fill pressure at breakdown, p_n, as well as the ratio $\frac{E_{||}}{p_n}$. Due to large uncertainties in p_n, $E_{||,min}$ could not be theoretically determined for CDX-U conditions. However, Sec. (4.4.1) compares the $E_{||}$ encountered in CDX-U to that in previous ECH preionization experiments on the DIII-D tokamak [Lloyd *et al.*, 1991], and the implication for operation with large error fields.

4.2.3 Heated Emissive Cathode

Shot to shot reproducibility was found to be improved in the presence of a heated, unbiased emissive cathode. Strong plasma-limiter interactions, discussed in Sec. (4.4.4), were significantly moderated or completely eliminated with the combined effects of heating the CDX-U LaB_6 electron beam injection cathode [see Sec. (3.3.2)] and using Ti gettering. Base neutral pressure was seen to increase as the cathode was heated, probably due to out-gassing from the graphite heating element or the LaB_6 cathode elements. This higher neutral pressure may have helped to moderate the

effect of carbon influx from the limiters during strong plasma-limiter interactions [see Sec. (4.4.4)]. A large impurity flux into the plasma edge can have a major effect on edge temperature and conductivity, and can therefore affect the current profile and MHD stability. This effect is especially important in low q_a plasmas [see Sec. (4.4.3) and Sec. (4.4.4)].

In addition to affecting base pressure, the emissive cathode provides "seed" electrons for ECH breakdown as discussed in Sec. (3.3.2).

4.3 Plasma Current Ramp-up and Control

An especially critical time for maintaining proper field configuration is during breakdown and the early plasma current ramp-up phase of a discharge. When the plasma current is still small compared to the coil currents, the poloidal field configuration and the particle orbits are primarily determined by the external coil currents and induced currents in the vessel.

In a tokamak with purely inductive start-up, maintenance of a poloidal field null is critical for plasma breakdown. A field null allows free electrons near it to complete several circuits around the torus and gain significant energy in the presence of the induced voltage before hitting the vessel. The maximum electron energy can be approximated by:

$$E_{max} \sim eV_{loop}N, \tag{4.3}$$

where N is the number of toroidal circuits traveled before an ionizing collision or before striking a limiter (loss of confinement). As electrons gain more energy than the binding energy of the electrons in the working gas ($E_{max} > E_{ionization} \sim 13.6$ eV in hydrogen), they become able to ionize neutrals. The chances of collisional excitation of the neutral gas by these electrons goes up with their confinement time and accumulated energy. Loss of confinement typically restricts E_{max} in the early period of plasma breakdown. N increases with both field strength and device size. The required V_{loop} spike needed to produce a given E_{max} therefore varies from device to device. Typical breakdown voltage can be reduced to ~ 10 V in a large size tokamak devices with careful field null programming. For smaller, lower field devices such as CDX-U, the required V_{loop} spike must be higher ($V_{loop} > 20$ V) for initial breakdown. Maintenance of the critical field null in this scenario requires precise control of all

poloidal fields, including those produced by the PF coil sets and the OH solenoid. In low-aspect-ratio this task can be especially challenging due to the additional presence of toroidally continuous vacuum vessel sections and significant induced eddy currents.

With ECH-assisted breakdown, however, it is not necessary to accelerate free electrons over several toroidal circuits in order to give them sufficient energy to collisionally ionize a significant fraction of the working gas. Resonant electrons can be accelerated to perpendicular energies of several hundred eV, well above the ionization energy [PENG *et al.*, 1978]. A poloidal field null is therefore not necessary in this case, although a poloidal field configuration should still provide long path lengths to the vessel walls, so that electron confinement times are much longer than electron-neutral collisional ionization times, and also that $E_{max} > E_{ionization}$. As seen in Fig. 4.2, the range of toroidal field allowing ECH-assisted start-up does seem to be affected by the average path lengths between the resonant ECH layer and the limiters.

4.3.1 OH-Induced Wall Eddy Current

Many of the CDX-U vacuum vessel sections are toroidally continuous. These sections include the top and bottom vessel flanges, and flanges and housing structure of the center stack assembly [see Sec. (3.1)]. These sections are well coupled to the OH solenoid, and large eddy currents are induced in them, significantly affecting the magnetic structure and plasma equilibrium.

To assess error fields due to the eddy currents, poloidal fields were measured in the outer array of pickup loops as well as the scanning internal magnetic probe. This set of measurements was used to reconstruct the magnetic field structure. In order to separate eddy current-induced poloidal field from that of the plasma current, a code was written[1] to calculate the induced currents in the vessel. This calculation used measured OH and PF coil current waveforms, then solved the set of circuit equations with a discrete approximation (a set of current filament sources) of the toroidally continuous sections of the vacuum vessel. These toroidally continuous sections of the vacuum vessel were divided into 48 elements, as shown in Fig. 4.4. Together with the PF and OH coil waveforms, these vessel eddy currents were the driving terms in the circuit equations for calculating induced current in the toroidally continuous vessel sections. The resulting poloidal field is then compared with the measured field. The

[1] by Yong-Seok Hwang of the CDX-U group

calculated toroidal eddy current waveform for one sample element is also shown in Fig. 4.4. Most of the induced eddy currents are calculated to be localized in the inner and outer top and bottom vessel corners.

In theory, the toroidal electrical break in the tub prevented any net toroidal currents from flowing. However, perfect electrical isolation between the tub and the top and bottom vessel flanges was not always maintained, allowing the possibility of a toroidal current path from the tub to a top or bottom flange and then back to the tub and around a toroidal circuit. Smaller eddy currents were measured in the outer "tub" section of the vacuum vessel. An effective toroidal current flowed at the midplane. The return path for this current was at the top and bottom edges of the tub. These current waveforms were measured by Rogowski coils [Sec. (3.4.1)] and totaled on the order of one kA. These currents were distributed among another 16 vessel elements (not shown) representing the tub vessel section.

4.3.2 PF Programming

Both measured fields and calculations of vessel eddy currents indicate that induced currents in the vessel were comparable to total current in the PF coils. Careful programming of the PF coil current waveforms was therefore especially critical for maintaining proper field configuration for start-up and equilibrium during ramp-up. Ratios of PF coil currents were roughly determined by the desired field configurations during start-up. Time dependence of PF coil currents primarily supplying vertical field, such as the orange/black pair and the yellow pair were roughly programmed to follow the plasma current as a function of time. The green coil pair was primarily used to compensate for error fields due to the eddy currents, and therefore was programmed to try to follow the loop voltage trace. Fine-tuning of all PF coil currents were performed by changing coil currents between shots while optimizing $\dot{I}_p$ and $I_{p,max}$, and monitoring plasma position to minimize limiter strikes. OH and PF coil current waveforms were controlled by adjusting voltage, timing, and capacitance of the OH and PF capacitor bank power supplies [see Sec. (3.2.3) and Sec. (3.2.2)]. Figure 4.4 shows the programmed waveforms of all PF coil sets, including the OH solenoid. The resulting flux contours at start-up (t= 0 in Fig. 4.1) are shown in Fig. 4.2.

After preionization of a current channel, the resulting poloidal field of the driven PF coil currents and induced vessel eddy currents should provide a vertical field

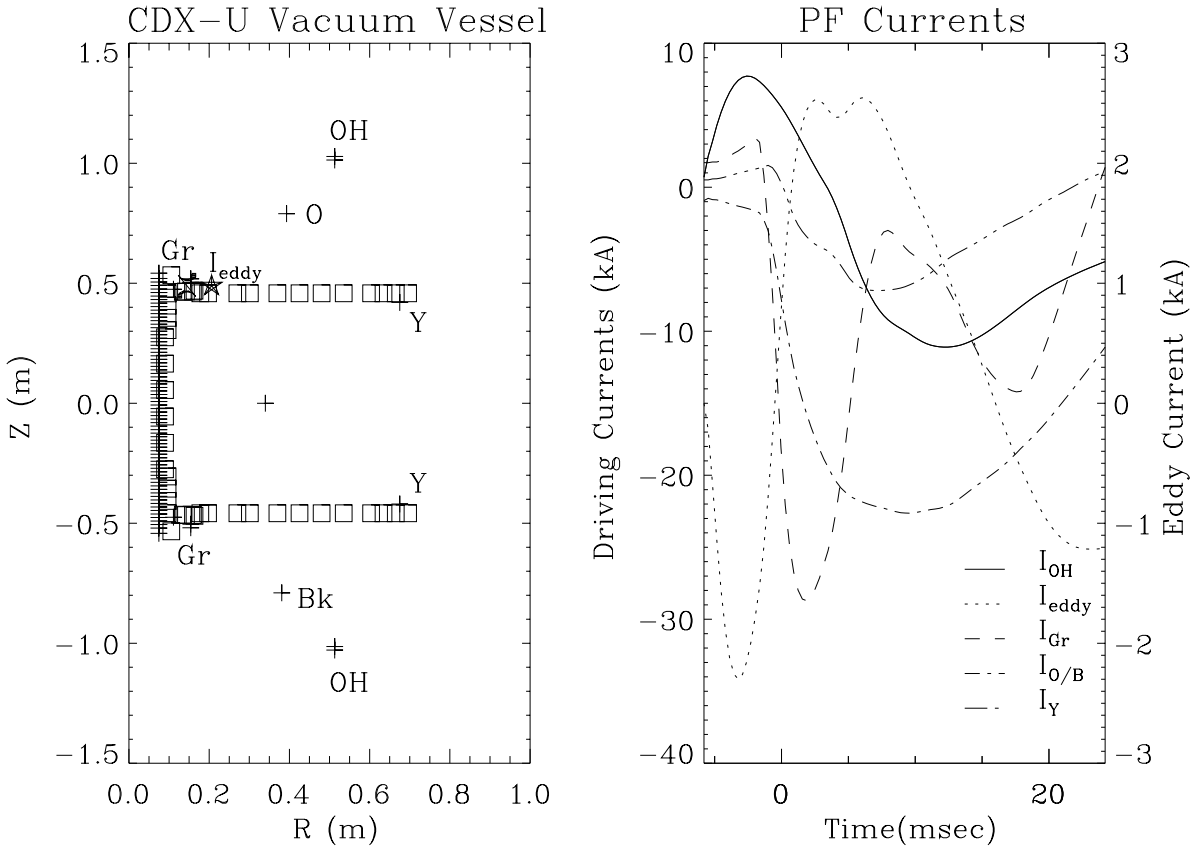

Figure 4.4. Programmed PF coil waveforms for a typical ohmic shot are shown. Positive current is in the direction of plasma current. Units for the OH and PF coil currents are given at left. The plotted PF coil currents are total current (kA-turns), while the OH current is a single-turn current. All positions of the PF coils and the vessel elements are shown in the diagram at left. The calculated eddy current for one element of the vacuum vessel (marked with a star) is shown as a dotted line whose scale is given on the right vertical axis. PF coil current waveforms and their effect on the magnetic configuration and flux consumption are discussed in Sections 4.3.2 and 4.4.2.

which increases proportionately to the plasma current to provide radial force balance. During optimization of the PF configuration for maximum ramp-up and I_p, careful adjustment of the programmed vertical field was most critical. In addition to force balance, stability to bulk motion (n=0, m=1 modes) should be maintained. Figure 4.2 shows that the field at the start of the plasma current ramp-up had the correct curvature for stability against vertical displacement. With the positive swing of the OH current just before plasma start-up, eddy currents in the inside corners of the vacuum vessel (totaling 10 kA, peak) add vertical field in the correct direction for radial equilibrium. However, with the reversal of the loop voltage, the eddy current begins to swing in the opposite direction. In order to maintain the favorable vertical field, the green coil pair begins a pulse just before plasma start-up to maintain the eddy current-produced vertical field, and peaks when $I_p \approx 30$ kA. The orange/black coil pair also provides a large component of the vertical field throughout the shot (0–20 ms) with the yellow coil pair providing local vertical field at the outboard side and a stabilizing $\frac{dB_z}{dR}$ during later periods of the discharge. At the current peak, the elongation is $\kappa \approx 1.5$. This is similar to calculated values of the "natural" elongation (the elongation in the presence of a nearly uniform vertical field) at this aspect ratio of $A \approx 1.6$ [Sykes, 1994].

Optimal I_p ramp-up was found with the plasma riding on the inner limiter during start-up and ramp-up. This can be seen in Fig. 4.8, where the inboard limiter current is relatively large from approximately t= 2 - 5.5 ms. Optimal start-up with the current channel at small major radius can be understood from consideration of flux consumption outside the plasma, and is discussed in terms of L_{ext} in Sec. (4.4.2). From t= 5.5 - 8 ms the plasma detaches from the inner limiter and moves outward. This coincides with the peak plasma current period when the radial equilibrium position is likely to be at a larger major radius. After t= 8 ms the plasma current starts to decay, and the plasma again moves inboard against the inner limiter. Close proximity to the inboard limiter did not seem to affect the discharge as severely as contact with top, bottom, or outside limiters. This may in part be due to the higher field (a factor of five larger than at the outside limiter) on the inboard side.

Plasma Position Monitors

Both magnetic pickup coils and especially currents to the segmented limiter array were used to diagnose plasma motion and position. The limiter array was often crucial to fine-tuning the plasma equilibrium. Figure 4.8 shows an example of the limiter current signal during close contact with the plasma. During operation, the currents in the segmented limiter array were monitored to help determine plasma location. Radial position was reliably monitored by the current to the inside and outside limiters. Figure 4.8 shows the inside and outside limiter signals for two shots. Small corrections were made to the PF capacitor voltages and timing to minimize contact with the limiters. Avoidance of any strong plasma-limiter contact such as that at t= +7 ms in Fig. 4.8 enabled the best current ramp-up results.

4.4 Start-up Results

4.4.1 Low V_{loop} Start-up

The chief goal of ECH preionization, the reduction of required loop voltage in low-aspect-ratio start-up, was achieved. Ohmic start-up with ECH preionization was possible with $V_{loop} \approx 1$ V or slightly less. Typically, peak loop voltage ranged from $V_{loop} \sim 3 - 5$ V in order to achieve desired current ramp-up rates and peak plasma currents. These loop voltages are well below those typically necessary for purely inductive start-up. The higher loop voltages provided the highest ramp-up rates and peak plasma currents. Ramp-up rates and peak currents were limited by available ohmic power until the q_a limits were reached [see Sec. (4.4.3) and Sec. (5.2)].

Recent ECH preionization experiments were performed on DIII-D using ~ 1 MW of ECH at 60 GHz, with $B_{T0} \approx 2$ T, $I_p \sim$ few hundred kA, and in an aspect ratio $A \approx 2.3$ [Lloyd *et al.*, 1991]. Systematic studies of the effects of error fields, variations in $E_{||}$, fill pressure, and ECH power on ECH-assisted and purely inductive tokamak start-up were done. Comparisons between the DIII-D experiments, in which $\frac{P_{ECH}}{P_{OH}} \sim 2$, where P_{OH} is the resistive heating power only (and does not include reactive power necessary to drive $\frac{dI_p}{dt}$), and CDX-U where $\frac{P_{ECH}}{P_{OH}} \leq 0.05$ at much different n_e and B_T, must be treated cautiously. However, comparison of some key parameters can be made.

Due to the small major radius of low-aspect-ratio start-up, $E_{\|}$ for a given V_{loop} is much higher than in conventional aspect ratios. In the DIII-D experiments, start-up was achieved with $E_{\|} \geq 0.25\frac{V}{m}$ using purely inductive start-up, and with $E_{\|} \geq 0.15\frac{V}{m}$ using ECH preionization. Electric fields during breakdown in CDX-U were much larger, with a minimum of $E_{\|} \sim 0.4\frac{V}{m}$ [see Sec. (4.2.2)]. The key to reliable start-up at these low electric field values was careful minimization of error fields at breakdown. In combination with a larger plasma volume, a much larger connection length to the limiters, which we denote as L, and a much longer corresponding confinement time, result. In DIII-D start-up experiments, L was determined to be between 500 m and 2000 m. For reliable, purely inductive start-up in JET, the relation between electric field strength and error fields was found to be [Tanga *et al.*, 1986]:

$$\frac{E_{\|}B_T}{B_{\perp}} > 10^3 \ \frac{V}{m},$$

where $B_{\perp}$ is a typical perpendicular field strength. This limit is consistent with observations in DIII-D purely inductive low-V_{loop} start-up, described in [Lloyd *et al.*, 1991]. With similar fields, ECH preionization in DIII-D permitted start-up with $\frac{E_{\|}B_T}{B_{\perp}}$ approximately 40% smaller than with purely inductive start-up. In contrast, reliable start-up, low-V_{loop} in CDX-U was achieved with:

$$\frac{E_{\|}B_T}{B_{\perp}} \geq 70 \ \frac{V}{m},$$

where $E_{\|} = 0.4\frac{V}{m}$, $B_T = 1.0$ kG, and $B_{\perp} = 0.01$ kG [see Fig. 4.3], corresponding to connection lengths of $L \sim 10$ m. This constitutes a significant improvement in start-up tolerance to error fields over that found in large tokamaks, and even over that observed in the DIII-D ECH-preionization start-up scenario. This result may in part be due to the larger $E_{\|}$ present in low-aspect-ratio. The relatively large error fields in CDX-U were due to both the low $(\frac{I_{TF}}{I_p})$ (i.e. low B_T) operation, and by large OH-induced eddy currents in the toroidally continuous sections of the vacuum vessel. Since such vessel construction may be necessary in low-aspect-ratio where vessel electrical breaks are difficult to engineer, ECH preionization is seen to be especially useful for LART operation. The larger eddy currents associated with a V_{loop} necessary for purely inductive start-up in CDX-U would likely not be possible without more precisely programmed cancellation of error fields by PF coils, or even active feedback control of the error fields.

4.4.2 Volt-second Consumption and Ohmic Efficiency

A plot of maximum plasma current vs. volt-second consumption (flux change at a point near the plasma boundary) for a sample of ohmic shots from operation between Aug. 1994 and Jan. 1995 is shown in Fig. 4.5. These shots include the discharges with the highest ($\frac{I_p}{V \cdot s}$), and were formed in a range of B_{T0} between 0.45 kG and 1.1 kG.

Consumed flux (all of the *poloidal* flux attributed to the plasma current), denoted here as Φ_{tot}, can be decomposed into three components according to their respective magnetic energies [EJIMA *et al.*, 1982]:

$$\Phi_{tot} = \Phi_{ext} + \Phi_{int}^{ind} + \Phi_{int}^{res}, \tag{4.4}$$

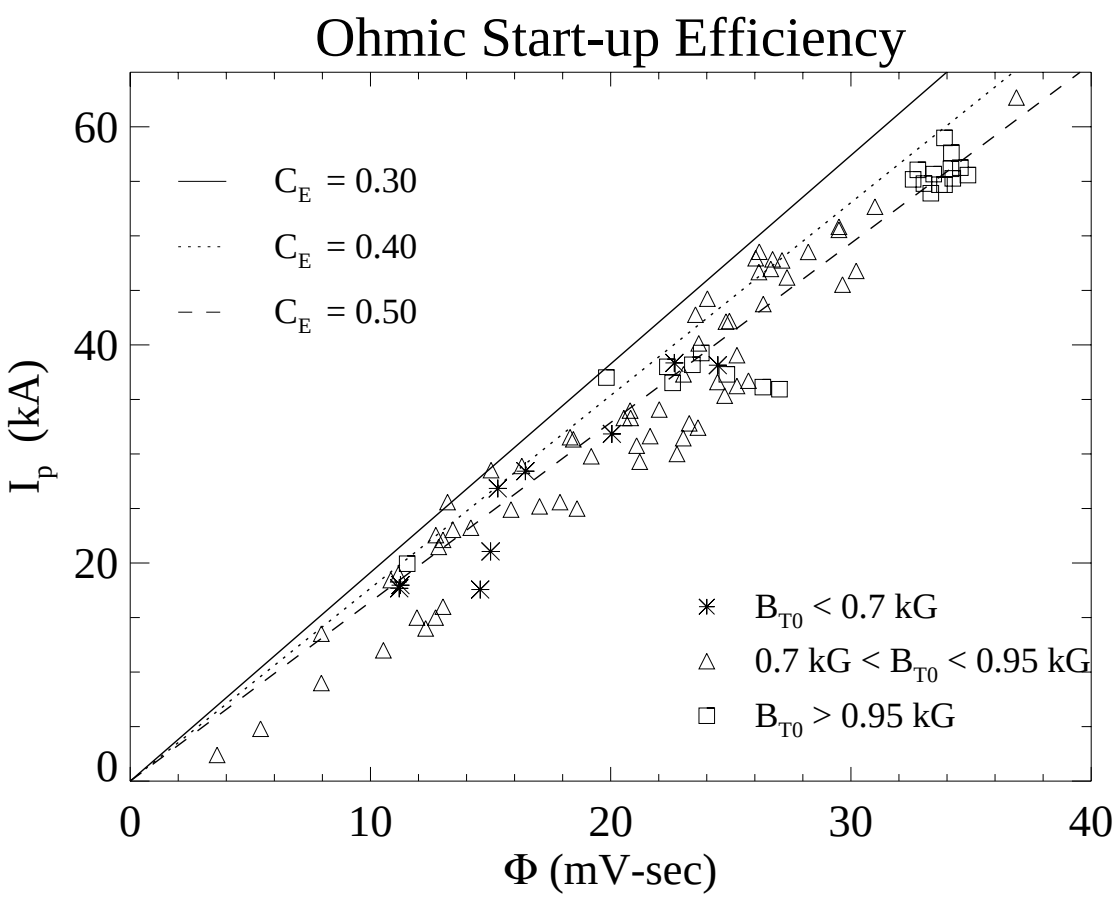

Figure 4.5. Peak plasma current vs. volt-second consumption at peak plasma current for several ohmic shots, including those with the highest ohmic efficiency. Plotted volt-seconds are the flux change in the OH solenoid plus a small correction factor to account for flux change due to vessel eddy currents and PF coil currents (solid line in Fig. 4.6). Toroidal field at the major radius ranged between 0.45 kG and 1.12 kG for these shots.

where

$$\Phi_{ext} = L_{ext} I_p \quad \text{is the flux outside the plasma column,} \tag{4.5}$$

$$\Phi_{int}^{ind} = \frac{\mu_0 R \ell_i}{2} \quad \text{is the flux inside the plasma column,} \tag{4.6}$$

$$\text{and} \quad \Phi_{int}^{res} \equiv C_E \mu_0 R I_p \quad \text{is the resistive flux loss.} \tag{4.7}$$

C_E is the Ejima coefficient and provides a measure of ohmic current drive efficiency. In general, resistive losses are less (smaller C_E) for faster current ramp-up due to the faster temperature and conductivity rise and lower ohmic power dissipation at high temperatures. For large tokamaks $C_E \geq 0.4$ typically, and is limited by skin current effects due to fast ramp-up times.

The external inductance, L_{ext}, accounts for energy stored in the plasma magnetic field outside the plasma boundary. For a plasma with arbitrary aspect ratio and ellipticity, L_{ext} can be approximated by [Hirshman and Neilson, 1986]:

$$\begin{aligned}
L_{ext} &= L_s - \mu_0 R \frac{(M-1)}{4}\left[ln\left(\frac{8}{\epsilon}\right) + \beta_p + \frac{\ell_i}{2} - \frac{3}{2}\right], \\
\text{where} \quad L_s &= \mu_0 R \frac{f_1(\epsilon)(1-\epsilon)}{1-\epsilon+f_2(\epsilon)\kappa}, \\
M &= \frac{(1-\epsilon)^2}{(1-\epsilon)^2 f_3(\epsilon) + f_4(\epsilon)\kappa^{1/2}}, \\
f_1 &= (1+1.81\sqrt{\epsilon}+2.05\epsilon) ln\left(\frac{8}{\epsilon}\right) - (2+9.25\sqrt{\epsilon}-1.21\epsilon), \\
f_2 &= 0.73\sqrt{\epsilon}(1+2\epsilon^4-6\epsilon^5+3.7\epsilon^6), \\
f_3 &= 1+0.98\epsilon^2+0.49\epsilon^4+1.47\epsilon^6, \\
\text{and} \quad f_4 &= 0.25\epsilon(1+0.84\epsilon-1.44\epsilon^2).
\end{aligned}$$

R is the major radius of the plasma, κ is the plasma elongation, and $\epsilon \equiv \frac{a}{R} = \frac{1}{A}$. Of particular note is the well-known linear dependence on the major radius, R, of L_{ext} and thus Φ_{ext}. Therefore Φ_{ext} is minimized at low R. Heuristically, this is due to the small volume in the high-field central column volume, inboard of the plasma. This positive aspect of a small central inboard volume may help mitigate its negative ramifications, namely engineering difficulty and the limited central OH solenoid flux capability. The minimization of Φ_{ext} in a LART can be most effectively utilized by the use of non-inductive current drive, which is not limited by OH solenoid volt-seconds. In CDX-U, the minimization of Φ_{ext} at low R was balanced against the

need to maintain a minimum q_a at $I_{p,max}$ as well as the need to maintain long path lengths to the limiters during breakdown, as discussed in Sec. (4.2.2). Also R should be reasonably well centered within the vessel to maximize plasma volume.

Calculations of C_E were very sensitive to the total consumed flux, inferred from the OH solenoid flux and calculations of the flux contributions from PF coils and vessel eddy currents. Measurement errors of the solenoid flux, and uncertainty in the PF and eddy current flux contributions may limit C_E accuracy to $\sim \pm 0.1$. A few shots achieved $C_E \sim 0.3$, with an average current ramp-up rate of 6 kA/ms. All of the shots with $C_E \sim 0.3$ had a higher field ($B_{T0} > 0.7$ kG). Calculations of C_E for CDX-U shots assumed $R = 35$ cm, $a = 21$ cm, and $\kappa = 1.5$, as found in the equilibrium reconstruction of a 36 kA plasma ≈ 1 ms after the peak current [see Sec. (5.3)]. Conventional large tokamaks are typically limited to $C_E > 0.4$ with average ramp-up rates of around 1 kA/ms.

One possible cause of the low values of C_E in the CDX-U experiments is that faster ramp-up rates in the CDX-U experiments are driving a hollow, unrelaxed current profile. Calculations of consumed flux for the proposed ITER device by [Jardin *et al.*, 1994] have shown that the flux consumption is nearly independent of current ramp-up rate, until the current profile has relaxed (ℓ_i has reached a steady-state value). A hollow current profile could drive some magnetic reconnection (relaxation of the current profile) during ramp-up and near the time of the current peak. Such reconnection is suggested by fluctuations in the plasma current and line-averaged density at the major radius just after periods of rapid current ramp-up. These fluctuations can be seen in Fig. 4.1 at t= 3–4 ms and t= 5–6 ms where $(\frac{\delta I_p}{I_p}) \sim 2$–$5\%$ and $(\frac{\delta(nL)}{nL}) \leq 50\%$. However, these fluctuations are not seen after the current peak, at which time the consumed flux is used for calculating C_E. Also, the magnetic reconstruction just after the current peak shows a peaked current density profile, which may not be far from the profile during the brief flat-top (t= 6–10 ms in Fig. 4.1). If the flux consumed during an extra ms (the time between the current peak and the reconstruction showing a peaked current profile) is included, the lowest calculated C_E values increase to $C_E \sim 0.45$, in agreement with maximum efficiencies in most tokamaks. A more precise calculation of C_E in CDX-U would require precise measurement of the current profile evolution, which at present is not available.

For a CDX-U shot with $C_E \sim 0.3$ ($I_p \sim 38$ kA, $\Phi_{tot} \sim 20$ mV-s), the above

formulas give the following flux consumption breakdown:

$$\begin{aligned} \Phi_{tot} &= 19.9 \text{ mV} \cdot \text{s}, \\ \Phi_{ext} &= 9.9 \text{ mV} \cdot \text{s}, \\ \Phi_{int}^{ind} &= 5.0 \text{ mV} \cdot \text{s}, \\ \text{and} \quad \Phi_{int}^{res} &= 4.9 \text{ mV} \cdot \text{s}. \end{aligned}$$

Shots with $I_{p,max} \approx 20 - 60$ kA had similar fractional composition of internal and external inductive flux consumption and resistively consumed flux.

Figure 4.6 shows the results of a numerical calculation of total flux, and the contribution from each of the OH solenoid, the PF coils, and the induced eddy currents in the vessel. The case shown was calculated without plasma current. T= 0 ms in this plot corresponds to the start of I_p ramp-up, as in Fig. 4.1. Loop voltage and poloidal flux (volt-sec) are shown for a point roughly at the major axis of the plasma (R= 34 cm, Z= 0 cm). The flux at this point represents the total volt-seconds (time-integrated loop voltage) consumed by the plasma for ohmic heating and current drive. The solid line in each plot shows the total loop voltage and flux.

Some general aspects of the magnetic configuration evolution can be seen immediately. One effect of the presence of eddy currents is an effective time delay in the loop voltage (at left, the solid curve is slightly delayed from the dotted curve). This time delay is the current penetration or "resistive time" of the vacuum vessel, and for CDX-U is on the order of 1–2 milliseconds. Data points in Fig. 4.5 were calculated using only the flux change in the OH solenoid (shown as a line with dots and dashes in Fig. 4.6). However, the solenoid flux is the dominant contribution of the total flux as can be seen from the similarity of the solid curve and the solenoid flux (long dashes) at right. The difference between the two is plotted as a dashed curve (short dashes), and represents the combined flux of the programmed PF coils and vessel eddy currents. As discussed in Sec. (4.3.2) a chief function of the PF coils in the presence of significant eddy currents is to cancel unwanted field. The plot of poloidal flux composition shows that the PF coil flux and eddy current flux nearly cancel.

Following the flux as a function of time, we can see that during the initial upward OH current swing between t= -6 ms and t= 0 ms, some of the solenoid flux contribution at the observation point (R= 34 cm, Z= 0 cm) is cancelled by PF coil currents, and especially vessel eddy currents. This is seen as a smaller flux change in the solid

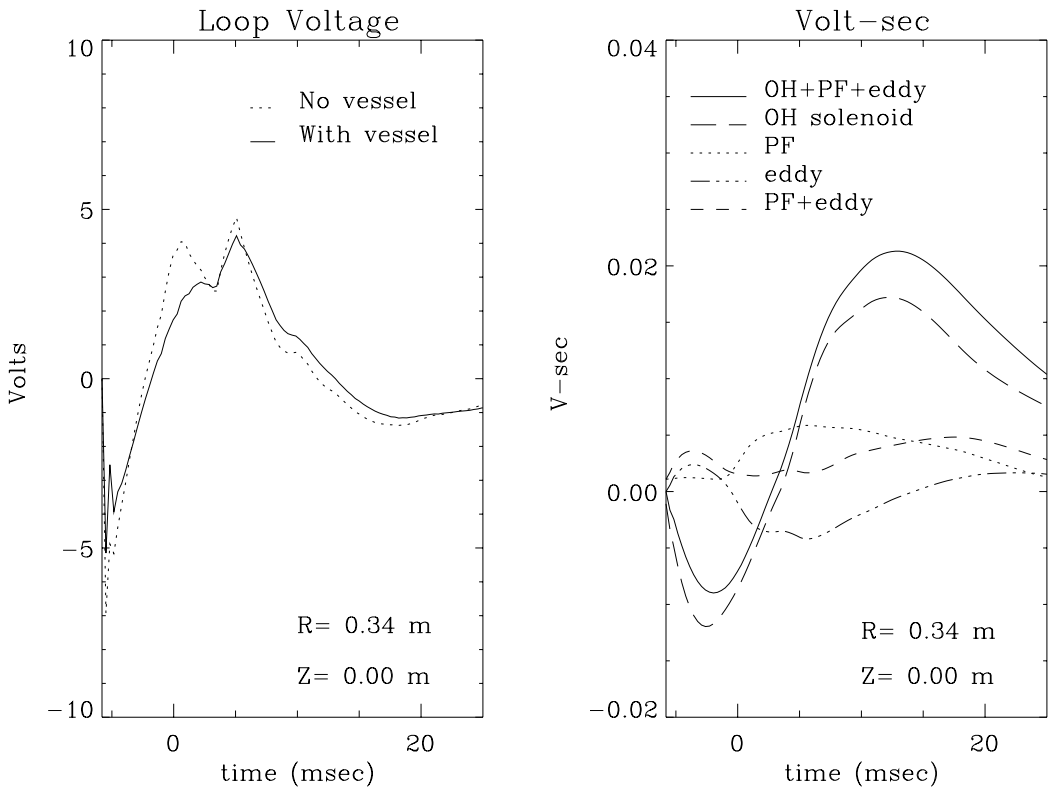

Figure 4.6. Shown above are the results of a calculation of loop voltage which uses a finite element approximation of the vessel, and then solves the set of circuit equations for all field coils and vessel elements, not including plasma current. Loop voltage is then calculated at a point above the major radius. PF and vessel eddy currents, combined, account for < 1 mV-s over the plasma current ramp-up period.

line than the solenoid flux. By the start of the I_p ramp-up at t= 0 ms, the flux at the observation point is again almost all due the solenoid contribution. During the first 8 ms of I_p ramp-up the difference between total flux and the OH solenoid flux is less than 2 mV-s and therefore the consumed flux is nearly all due to OH flux change. This difference only rises to about 4 mV-s by the time of peak current (t= 12 ms). This additional consumed flux is due to contributions from the second pulses of the PF coil currents and especially from the decreasing eddy currents.

4.4.3 Start-up at Low B_T

As discussed in Sec. (1.1.1), plasma performance is optimized at high I_p, while the capital cost of a fusion device is minimized for low B_T. Therefore the factor $(\frac{I_{TF}}{I_p})$, which is proportional to the edge safety factor, q_a, should be minimized. For a given level of ohmic heating power, $I_{p,max}$ is determined by the minimum achievable q_a, or equivalently the minimum B_{T0}. Experiments determining the minimum q_a [and minimum $(\frac{I_{TF}}{I_p})$] are therefore a critical test of the predicted advantage of the LART configuration over conventional aspect ratio.

As shown in Fig. 4.7, ECH-assisted start-up was achieved with a range of toroidal field from 0.45 kG to 1.13 kG on axis, a factor of 2.5 in toroidal field. This corresponds to a range of the ECH fundamental resonance position of 18 cm $< R_{ECH} <$ 42 cm. Also plotted in Fig. 4.7 are corresponding $q(a)$ values, assuming the same R, a and κ. Estimated edge q in CDX-U plasmas seem to have been limited to $\sim$ 3.5. This low limit was only achieved with careful control of the vacuum conditions and the use of Ti-gettering. Edge q in conventional large tokamaks has been found to be limited to 2–3. This limit is determined by MHD stability of the plasma current profile, and can be strongly influenced by impurity influx which can increase resistivity in the plasma edge regions and affect the current profile. The operational q_a-limit in CDX-U is discussed further in Sec. (5.2).

4.4.4 Plasma-Limiter Interaction

One persistent problem encountered in CDX-U ohmic operation, was a strong plasma-limiter interaction. This problem is partly due to the fact that the input power is quite large for LART plasmas, typically exceeding 100 kW of ohmic power

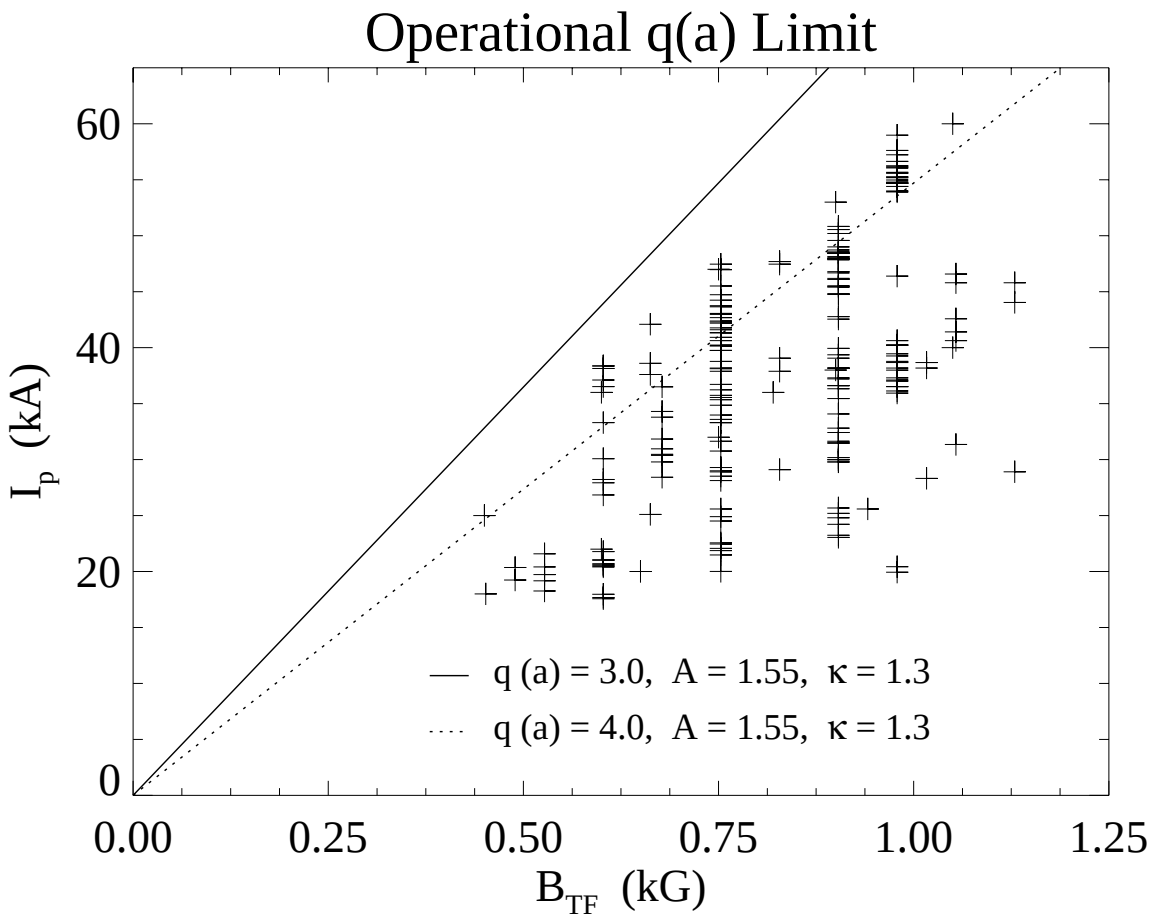

Figure 4.7. Peak plasma current vs. B_{T0} for highest I_p shots at each toroidal field strength. Aspect ratio and elongation are based on limiter placement as well as observed density distribution over range of discharges.

in CDX-U. This power level impinging on a small graphite surface area could result in strong plasma-limiter interactions. In CDX-U the surface area is ≤ 10 cm^2 so that the power flux density can reach 10 kW/cm^2. This power flux on the limiters for several milliseconds is likely to be enough to heat the limiter surfaces to more than 1000 C, at which temperature sputtering from the graphite would be a severe problem. Local hot spots may even have reached the carbon sublimation temperature (≈ 3400 C).

Figure 4.8 illustrates a typical plasma-limiter interaction. This interaction was characterized by a large (often over a factor of 5) increase in the line-averaged electron density throughout the plasma. Simultaneous with this jump in plasma density, a spike in current to one or more of the segmented limiters was observed. C V light,

which was monitored with a metallic film filter and an amplified photomultiplier tube [see Sec. (3.4.5)] also showed a large jump during these events, consistent with a large influx of carbon from the graphite limiters. Finally, magnetic pickup coils on the outside of the vessel detected a sharp drop in poloidal field, simultaneous with a relatively constant or slightly increasing poloidal field on the inboard side of the vessel. This sudden drop in B_p indicated either a rapid inward movement of the plasma or a sudden quenching of the plasma current in the outer flux surfaces, possibly due to rapid cooling. A large influx of carbon impurities would have such a cooling effect.

The frequency of occurrence of these strong plasma-limiter interactions in shots with identical PF and OH programming was greatly affected by vacuum and wall recycling conditions. Gettering with Ti was in combination with the presence of a heated LaB_6 cathode element enabled repeatable ohmic operation free of limiter strikes.

Limiter Material Effects

During most of the experiments in this thesis, graphite limiters were used. Limiters were subsequently changed to molybdenum. The large jump in carbon light observed in the presence of graphite limiters during a limiter strike was substantially reduced after installation of the molybdenum limiters, The line averaged density during relatively quiescent periods of the discharge showed a small increase.

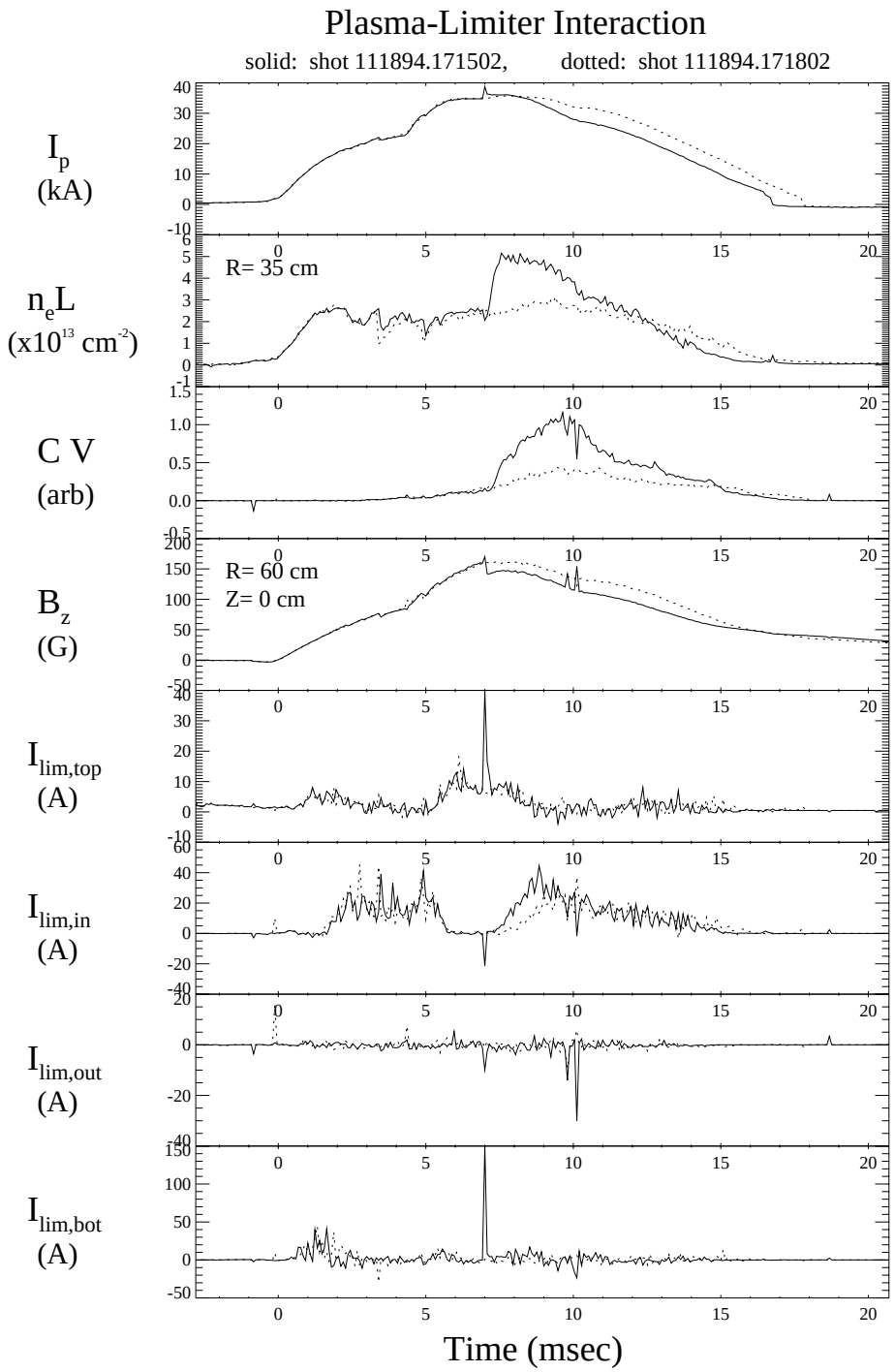

Figure 4.8. An ohmic shot with a plasma-limiter interaction at t= +7 ms is shown (solid lines). For comparison a similar shot without a limiter strike is also shown (dotted lines). The limiter strike results in a large increase in line-averaged density and C V light, most likely from a large influx of carbon from the graphite limiters. The largest jumps in limiter current for this shot were at the top and bottom of the vessel.

Chapter 5

MHD Behavior

AS OUTLINED in Chapter 2, the plasma current limit and pressure limit both depend inversely on the MHD safety factor at the plasma edge, q_a. Determination of the q_a-limit at low aspect ratios is the one of the most important tests of the predicted advantages of the LART configuration. General MHD stability and fluctuation activity at low-aspect-ratio have only begun to be explored experimentally, and need extensive study. In this chapter we discuss MHD behavior in a range of ohmic discharges, and focus on those discharges which were low-q_a and reproducible. Results of fluctuation studies of an MHD mode persistently found in a range of low-aspect-ratio ohmic discharges are presented.

5.1 Ohmic Operations

Ohmic operation in CDX-U covered a range of plasma current up to 60 kA, and a range of toroidal field strength, 0.45 kG $< B_{T0} <$ 1.1 kG. Typical central electron densities were in the range $n_e \sim 0.8 - 5 \times 10^{12}$ cm^{-3}, and core temperatures typically were estimated to be 100–200 eV. The OH pulse and PF were usually programmed to provide a maximum peak plasma current while maintaining reasonable shot-to-shot reproducibility, and producing discharges with 10–20 ms duration.

The loop voltage and PF waveforms available with the present CDX-U power supplies resulted in plasmas which changed shape during the discharge. Equilibria reconstructions were done both at the current peak and 4 ms after the current peak, for a particular non-disrupting reproducible shot. These equilibria are discussed in

detail in Sec. (5.3). For this equilibrium, the plasma filled most of the volume of the vacuum chamber at the time of the current peak: the minor radius was at its maximum and aspect ratio was at a minimum. After the current peak, due to the decreasing loop voltage, the plasma contracted, aspect ratio increased, and therefore q_a *decreased.* Ohmic shots with different peak plasma currents were generally created with PF waveforms proportionally increased with the plasma current, so that *a similar evolution of the plasma shape could be expected.*

5.2 Operational Current Limit

Toroidal Field Scan - Plasma Disruptions

Several of the shots with the lowest values of q_a terminated with hard disruptions. Figure Fig. 5.1 illustrates the disruptive q-limit encountered. In this series of shots, the toroidal field strength was increased from $B_{T0} = 0.60$ kG in shot (a) to $B_{T0} = 1.13$ kG in shot (g). The loop voltage and PF evolution were kept the same. As outlined in Sec. (4.2.2), the working gas fill pressure as well as the ECH power were increased slightly ($\leq 30\%$) with B_{T0} to assist breakdown and start-up. The q_a values at current peak were calculated from Eq. (2.19) and using the plasma boundaries from a reconstruction of a 38 kA plasma at a time corresponding to t= 7 ms in these shots.

Shots (a) through (c) disrupted at or near the time of the plasma current peak, so that $q_a(I_{p,max})$ was the edge-q value at disruption. $q_a(I_{p,max})$ in these shots was just under 4. In shots (d) through (g) disruption occurred several milliseconds after the current peak, during the time when the minor radius, aspect ratio and edge-q were decreasing from their values at $I_{p,max}$. Therefore, these shots are also consistent with an edge-q at disruption of $q_a \leq 4$.

The parameter of interest, q_a, depends only on the ratio $(\frac{I_p}{B_{T0}})$ and the plasma boundary shape. I_p and B_{T0} were known precisely ($< 5\%$ error), so that the largest uncertainty in q_a is from the determination of the plasma shape. Furthermore, the assumption of a plasma shape that nearly fills the volume within the limiters provides an upper bound on q_a, since a smaller plasma (lower a and A) implies a lower q_a.

One issue affecting the kink stability of the discharges during I_p ramp-up and at the current peak, is a possibly broad or even hollow current profile due to the skin

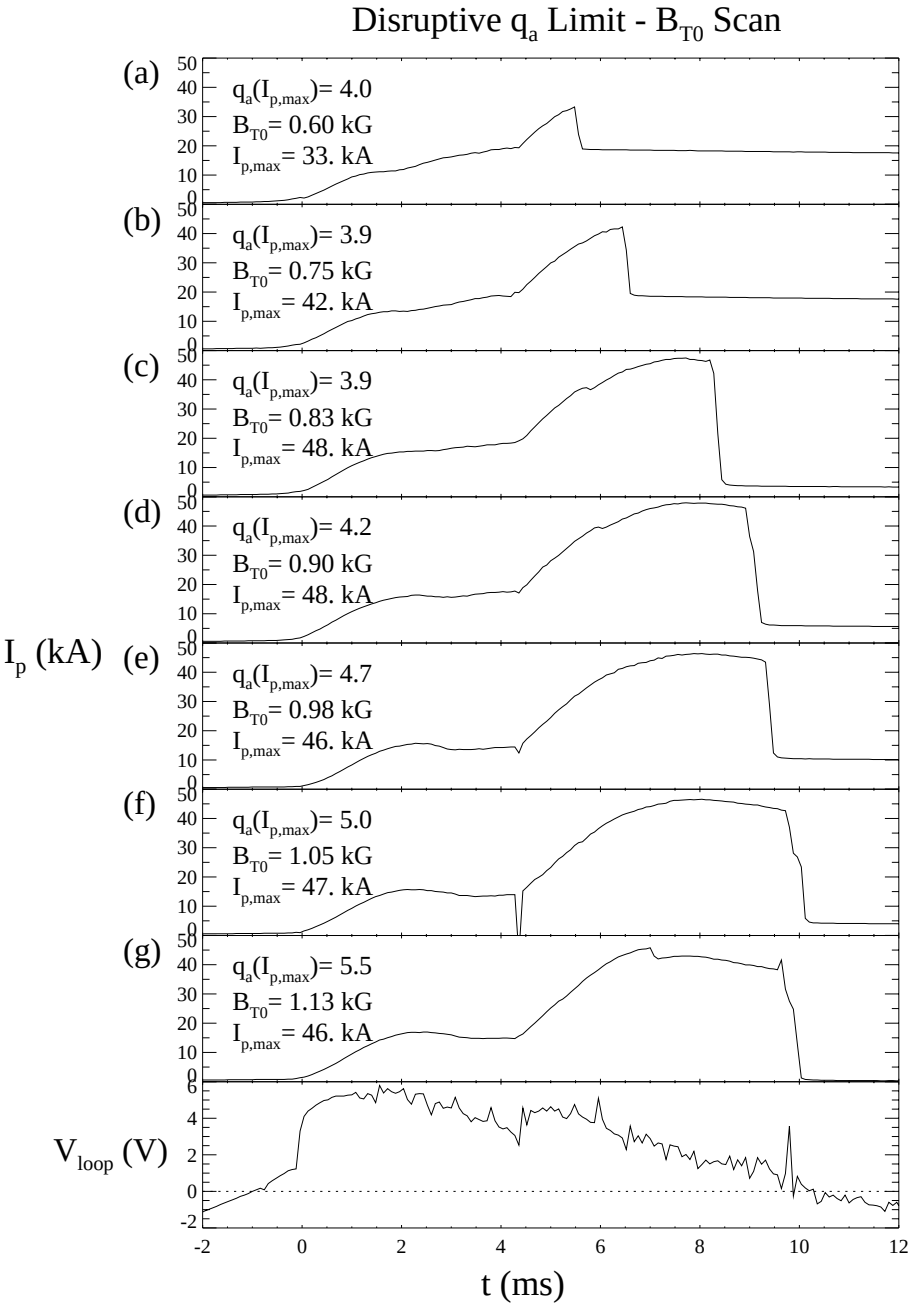

Figure 5.1. Total plasma current as a function of time is shown for a series of shots with equal ohmic power and varying B_{T0}. Plasma shape from an equilibrium reconstruction of a 38 kA plasma was assumed in calculating q_a. Shots (a) through (c) disrupted at maximum I_p or shortly after, so that $q_a(I_{p,max})$ is representative of the minimum q_a during the discharge. Shots (d) through (g) disrupted several milliseconds after the current peak, when A had increased and $q_a < q_a(I_{p,max})$. The q_a limit for this discharge was therefore not greater than 4.

effect of the OH drive. Average ramp-up rates of up to 10 kA/ms were used. This provides a ratio of ramp-up time to resistive diffusion time comparable to that used in most conventional tokamaks, where a skin current effect is often seen which can degrade the kink stability. Even without ideal instability, current profile relaxation-related MHD activity during the rapid I_p ramp-up may have caused limiter strikes by causing sudden plasma displacements or resistive surface tearing accompanying the formation of large island structures.

Shot (g) illustrates a mild example of a limiter strike, which was another possible cause, besides likely MHD activity, of many of the disruptions in CDX-U ohmic plasmas. At t$\approx$ 7 ms, I_p drops sharply by 15%, while the electron density increases sharply (not shown) by a factor of 3–4. These characteristics of strong plasma-limiter interactions are described in Sec. (4.4.4), and may have been caused by improper plasma position control or some sudden plasma movement into the limiters. Equilibrium reconstructions from magnetics data (Fig. 5.6 and Fig. 5.7), density profile data (Fig. 5.4), and typical measured limiter currents (Fig. 4.8) all show the plasma with small major radius and riding on the inside limiter ($R_0 \approx 30$ cm) at the beginning of the discharge. The plasma minor and major radii expand to a maximum at the current peak with $R_0 \approx 40$ cm, then contract with the major radius moving inwards again by the end of the shot. The loop voltage measured at the vacuum vessel toroidal gap is also shown in Fig. 5.1, and can be seen to go negative at about the same time as the plasma terminations in shots (f) and (g). This drop in V_{loop} caused the plasma current to decrease faster than the vertical field, resulting in the inwards radial movement from the radial force imbalance. A sufficiently strong limiter strike could have sputtered enough cold carbon from the limiters into the plasma to quench it and cause the abrupt terminations after the current peak seen in Fig. 5.1. The effects of strong plasma-limiter interactions were found to be minimized by careful programming of the PF evolution, and careful control of the vacuum conditions. Subsequent replacement of graphite limiters with molybdenum further improved performance.

Operational q_a Limit

After surveying over 8,000 CDX-U ohmic discharges from operation between 18 Aug., 1994 and 1 Mar., 1995, several shots with the highest I_p and lowest B_{T0} (i.e. those with the lowest q_a values), were assembled into a database. Also, several other

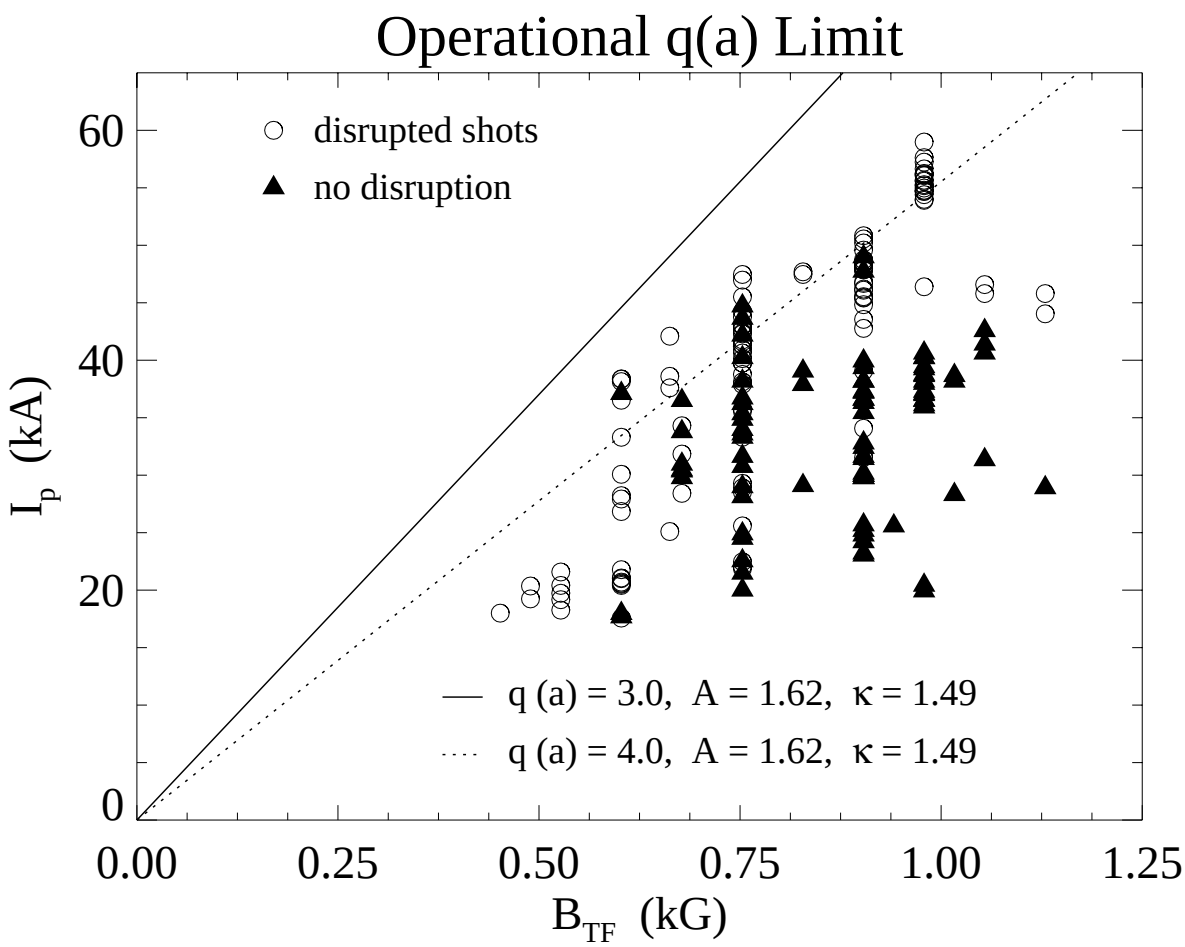

Figure 5.2. Figure 4.7 is shown again, here with disrupted shots and non-disrupting shots distinguished. Peak plasma current vs. B_{T0} for highest I_p shots at each toroidal field strength. Aspect ratio and elongation are based on equilibrium reconstructions from magnetics data, and are consistent with limiter-current measurements of the plasma position as well as with observed density distributions over a range of discharges.

reproducible shots with varying q_a were included. This set of CDX-U ohmic shots is shown in Fig. 5.2.

Again, the lines of constant q_a are calculated using the plasma boundary from an equilibrium reconstruction at maximum current in a 38 kA discharge, in which a and A are nearly maximized for this limiter configuration. These q_a values are therefore a conservative estimate (yielding an upper bound) of the q-limit.

Many shots with the highest ratio of $(\frac{I_p}{B_{T0}})$ terminated with hard disruptions at calculated values of q_a similar to those at disruption for the shots in Fig. 5.1. Again, the operational q-limit in this larger sample of discharges seems to be ~ 3.5. Of particular importance is the presence of non-disruptive shots with $q_a \leq 4$, implying ideal MHD stability (perhaps marginal) at these values of q_a and A, and verifying that $q_a \sim 3.5$ is an *upper bound* of the q-limit. Several of the disruptions in Fig. 5.2 were likely due to plasma control problems, especially those disruptive shots with lower $(\frac{I_p}{B_{T0}})$.

To illustrate again the advantages of low-aspect-ratio in terms of $(\frac{I_{TF}}{I_p})$ and β_c, we compare values at low and moderate aspect ratios, using the observed q_a limit of 3.5, and CDX-U parameter values. After setting the edge-q to 3.5, along with an aspect ratio of $A = 1.6$, an elongation of $\kappa = 1.5$, and a conservative value of $\beta_N = 3.5\%$, Eq. (2.20) and $I_{TF} = \frac{2\pi R B_{T0}}{\mu_0}$ yield:

$$(\frac{I_{TF}}{I_p}) = 2.6,$$

and the Troyon β limit, Eq. (2.21), yields:

$$\beta_c = 11\%.$$

In contrast, the same values of q_a, β_N and κ at aspect ratio of $A = 3.0$ yield:

$$\begin{aligned} (\frac{I_{TF}}{I_p}) &= 15, \quad \text{and} \\ \beta_c &= 3.4\%. \end{aligned}$$

The low-aspect-ratio values are much improved. Since an elongation of $\kappa = 1.5$ at aspect ratio $A = 3.0$ would require active shaping of the plasma and possibly causing vertical instability of the plasma position, the contrast between low and high aspect ratios is even greater. Again, the validity of the Troyon β limit at low-aspect-ratio must be verified experimentally, but recent numerical stability studies, as discussed in Sec. (2.2.1), have been promising, and may even be more favorable at low-aspect-ratio.

5.3 36 kA Discharge - Equilibrium Reconstruction

Equilibrium profile data was not available for ohmic discharges with edge-q values near the operational limit of $q_a \sim 3.5$, largely because of the need for outstanding shot-to-shot reproducibility in collecting such data. Equilibrium magnetics and density profile data for a single discharge configuration in CDX-U were collected over hundreds of shots and several hours of operation. A non-disrupting plasma discharge with a toroidal field on axis of 1.0 kG and a peak current of 36 kA, was found to provide the best shot-to-shot reproducibility. From an equilibrium reconstruction described below, this discharge was determined to have an edge-q value of $q_a \sim 7$ at peak I_p. The poloidal field and plasma shape evolution were similar to CDX-U discharges with the lowest q_a values. Detailed fluctuation studies were facilitated by the excellent reproducibility of the 36 kA discharge, and are described in Sec. (5.5). In addition to the interesting results of the fluctuation studies in the 36 kA plasma, analysis of its MHD behavior can help provide insight into possible destabilizing MHD behavior in the lower q_a shots.

5.3.1 Magnetics Data

Two components ($\hat{R}$ and $\hat{Z}$ components in cylindrical coordinates) of the magnetic field were measured at each of the coils in the CDX-U poloidal array of eleven magnetic

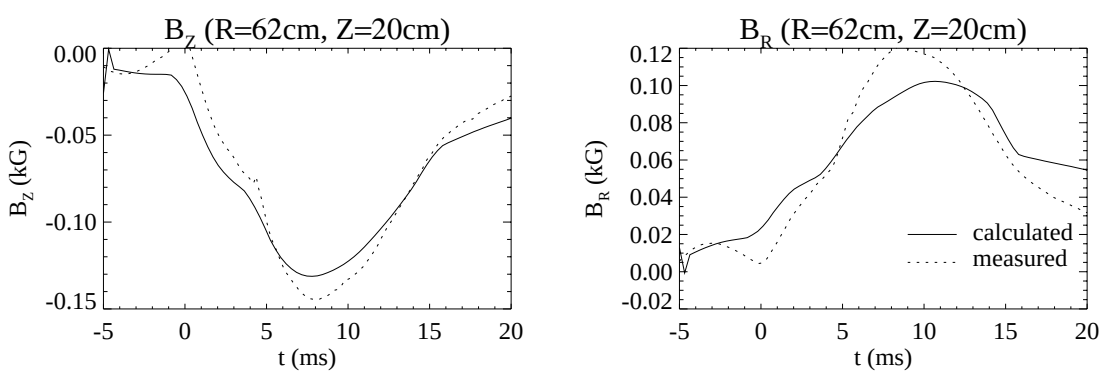

Figure 5.3. This plot shows the evolution of the $\hat{R}$ and $\hat{Z}$ components of the magnetic field in one of fifteen pick-up coils used for external field measurements. The case shown was a shot with a 36 kA peak plasma current. The vacuum field evolution was also measured in order to isolate contributions from the plasma.

pick-up coils located along the top and bottom vessel flanges, and along the outboard tub section of the vessel. Finally, $\hat{R}$ and $\hat{Z}$ field components were recorded with the scannable magnetic probe at 3 cm intervals in $\hat{R}$ and 5 cm intervals in $\hat{Z}$, within its range. In addition, the $\hat{Z}$ field was recorded at three points on the inboard side of the plasma. (The set of CDX-U magnetics diagnostics are reviewed in Sec. (3.4.1) and Table 3.3.) The evolution of each field component was measured both in the presence of a plasma and in a vacuum case, each with an identical PF coil current evolution. The differences between these two signals were the field components due to plasma current, and were used in the magnetic reconstruction of the plasma of the plasma current.

Figure 5.3 shows an example of the magnetic field evolution in one of the magnetic pick-up coils in the array. The measured field is shown as a dotted line. The solid line is calculated from known coil currents, a filament plasma current model, and vessel eddy currents calculated as discussed in Sec. (4.3.1). Separating plasma current and eddy current field contributions was dependent on an accurate determination of the vessel eddy currents. Due to the proximity of the pick-up coils to the eddy currents, the determination of the plasma field, and therefore the reconstructed plasma current profiles, was very sensitive to errors in the eddy current calculation.

5.3.2 Density Profiles

Chord-averaged density data was taken with the 2 mm microwave interferometer system (see Sec. (3.4.4)). Density as a function of time was recorded for both vertical and horizontal views. Time-resolved data was recorded for an entire shot at each position. The results are radial and vertical profiles of the line-averaged density averaged over several shots, shown in Fig. 5.4. Shot-to-shot reproducibility was good, although shot-to-shot variations introduced some noise into the profiles. The peak of the line-averaged plasma density radial profile can be seen to start at $R \approx 30$ cm at t= 0 ms, increase to a maximum of $R \approx 40$ cm at t= 7 ms, and then decrease to $R \approx 30$ cm again by the end of the discharge at t= 12 ms. This is consistent with the equilibrium reconstructions from the magnetics data, where the major radius was calculated to be $R_m = 38$ cm at the current peak (t= 7 ms), and $R_m = 29$ cm, 4 ms after the current peak (t= 11 ms).

The vertical density profile shows a peak $\overline{n_e}L$ slightly below the midplane, starting

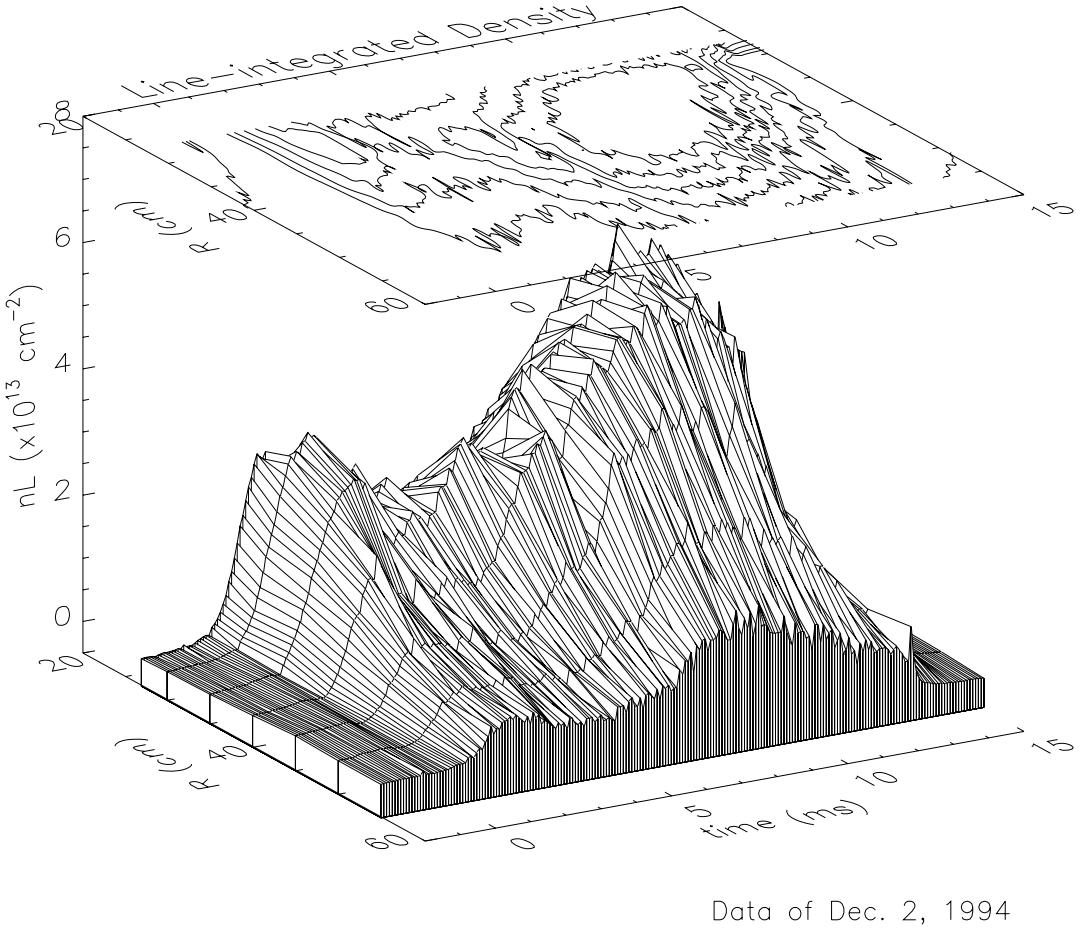

Figure 5.4. The radial line-integrated density profile is shown as a function of time for the 36 kA discharge. Line-integrated density was recorded from a vertical view throughout a shot at each of several radial locations. Contours of constant line-averaged density as a function of time are shown at the top.

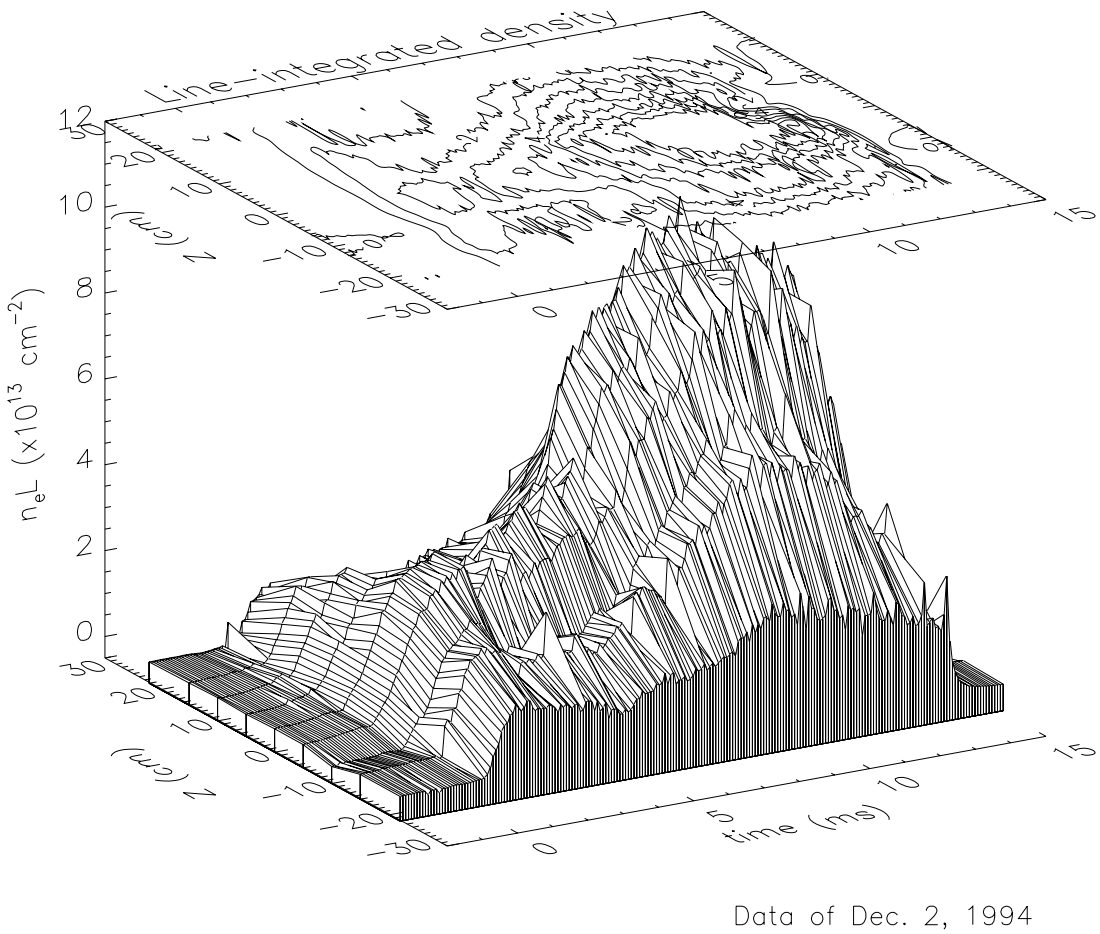

Figure 5.5. The vertical line-integrated density profile is shown as a function of time for the 36 kA discharge. Line-integrated density was recorded from a horizontal view throughout a shot at each of several radial locations. This horizontal interferometer view includes *two* passes through the plasma. Contours of constant line-averaged density as a function of time are shown at the top.

at $Z \approx -5$ cm, then moving downwards to $Z \approx -10$ cm between t= 7 ms and t= 11 ms.

5.3.3 Equilibrium Reconstruction

The EFIT equilibrium code [Lao *et al.*, 1985; Lao *et al.*, 1990] was used to calculate a best fit to magnetic field measurements at two times of paricular interest during the discharge. An equilibrium reconstruction was done just after the current peak, at t= 7 ms in Fig. 4.1, which is within one ms of the current peak for this series of discharges. Another magnetic reconstruction was done 4 ms later, at t= 11 ms, when the dominant 10–15 kHz MHD mode discussed in Sec. (5.5) was observed.

Field measurements around the perimeter of the vacuum vessel, as well as on the midplane between $R \approx 40$ cm and the vessel wall ($R \approx 60$ cm) were used as input for EFIT.[1] Also, measured PF coil waveforms and calculated vessel eddy current waveforms were input into the magnetic reconstructions. Finally, central density from the interferometer data was fed into the code, as well as a specified value of q_0. Internal magnetic measurements were not sufficient to precisely determine the current profile. Equilibrium reconstructions for a range of values of q_0 between 1.0 and 2.5 were performed. Values of $q_0 \approx 1.6$ during the current peak, and $q_0 \approx 1.9$ 4 ms after the current peak yielded the best fit to central pressure, and were used in the final fits in Fig. 5.6 and Fig. 5.7, respectively. Central temperature was based on spectroscopic charge-state analysis of C V and O VI light [see Sec. (3.4.5)], as well as from estimates of the neoclassical resistivity. Central densities were measured with the interferometer, as shown in Fig. 5.4 and Fig. 5.5. The EFIT reconstruction was performed on a 65×65 rectangular numerical grid. The major radius was determined to be $R \approx 35$ cm, the minor radius $a \approx 21$ cm, and the elongation $\kappa = 1.5$, so that the plasma filled most of the volume defined by the limiters. The q_a resulting from the fit was ~ 7.

At this time, the major radius was determined to be $R \approx 28$ cm, the minor radius $a \approx 16$ cm, and the elongation $\kappa = 1.23$. Thus, the plasma contracts after the current peak, while riding on the inside limiter, in agreement with density profile measurements. The q_a resulting from this fit was ~ 4, consistent with similar I_p and B_T0 as during the current peak, but a smaller minor radius and larger aspect ratio.

[1] Equilibrium reconstructions for these equilibria were performed by Yong-Seok Hwang.

```
h EFITD 65x65d 11/19/93  h    k941202.00013
date ran =
shot #    =     941202
t(ms,us) =     13       0
chi2(mag)=  0.140E+05
rout(cm) =      34.63
zout(cm) =     -1.228
a(cm)    =      21.37
elong    =      1.494
utri,ltri=   0.20   0.20
indent   =      0.000
V,A(m3,2)=   0.43  0.205
energy(j)=  2.084E+01
betat(%) =       0.88
betap    =       0.16
betan,In =   0.61   1.44
li,y2    =   0.84  -0.14
error    =  0.840E-02
# iters  =         11
fpols(kA)=        0.0
J0n,J1n  =   1.83   0.00
q1,q95   =   6.96   5.59
dsep(cm) =    -45.000
rm,rc(cm)=   37.5   34.6
zm,zc(cm)=  -0.85  -0.87
betapd   =      -4.42
betatd(%)=     -23.84
wdia(J)  = -5.665E+02
      data used:
ip(ka)   =       38.4
bt0(t)   =     -0.098
 0 flux loops
22 magnetic probes
 1 rogow  2 fc rogows
scrapof(mm)   0.8  1.6  2.4  3.2  4.0
```

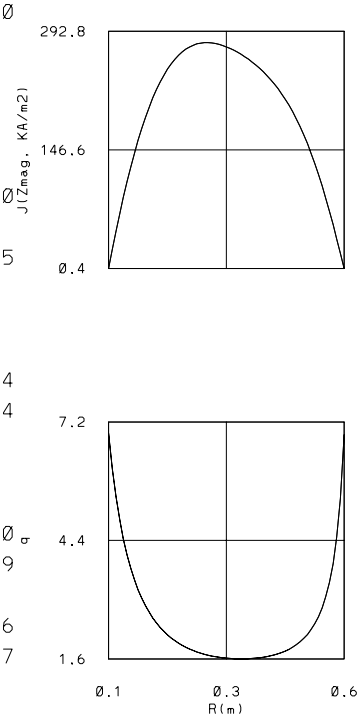

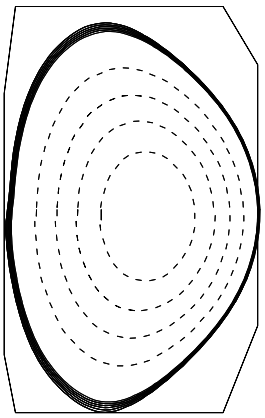

```
icp,  ivs=     0    0
kf,    kp=     2    2
fpd,  pbd=   1.0  1.0
fwbp, fwq=   1.0  1.0
Ze(cm)   =      0.000
```

Figure 5.6. The EFIT equilibrium code was used to reconstruct the equilibrium of the 36 kA discharge just after the time of the plasma current peak. On the right is a plot of the poloidal flux contours. The rectangular boundary around the flux plot denotes the limiter positions. The current density on the midplane is shown at the top left, and the safety factor, q, is shown in the bottom left plot. q ranges from a value of 1.6 on the axis to ~ 7 at the edge.

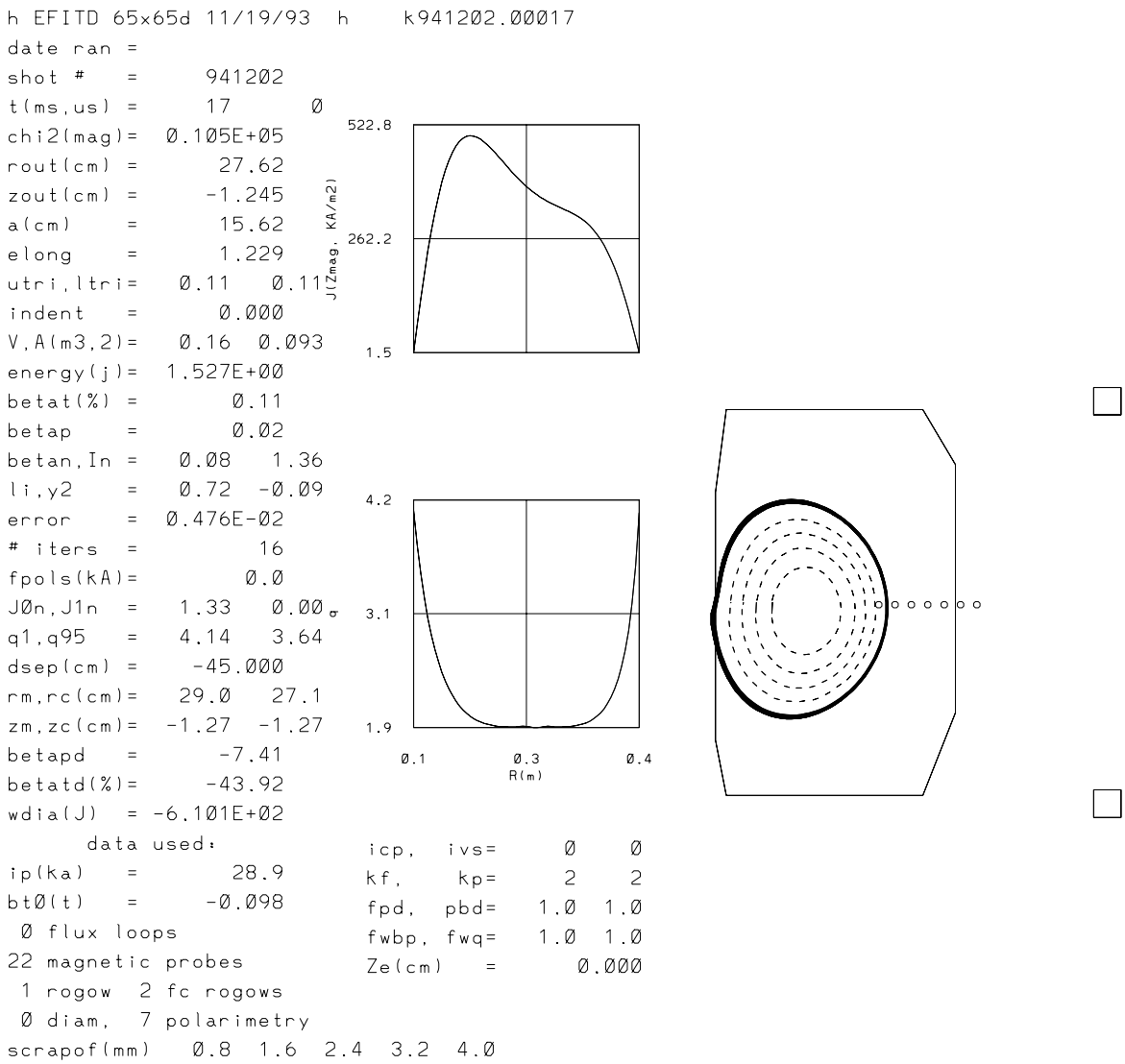

Figure 5.7. The EFIT equilibrium code was used to reconstruct the equilibrium of the 36 kA discharge 4–5 ms after the plasma current peak (t= 11 ms in Fig. 4.1). Again, the flux contours are shown at right, the current density on the midplane at the top left, and the q-profile at bottom left. q ranges from 1.9 on the axis to 4 at the edge.

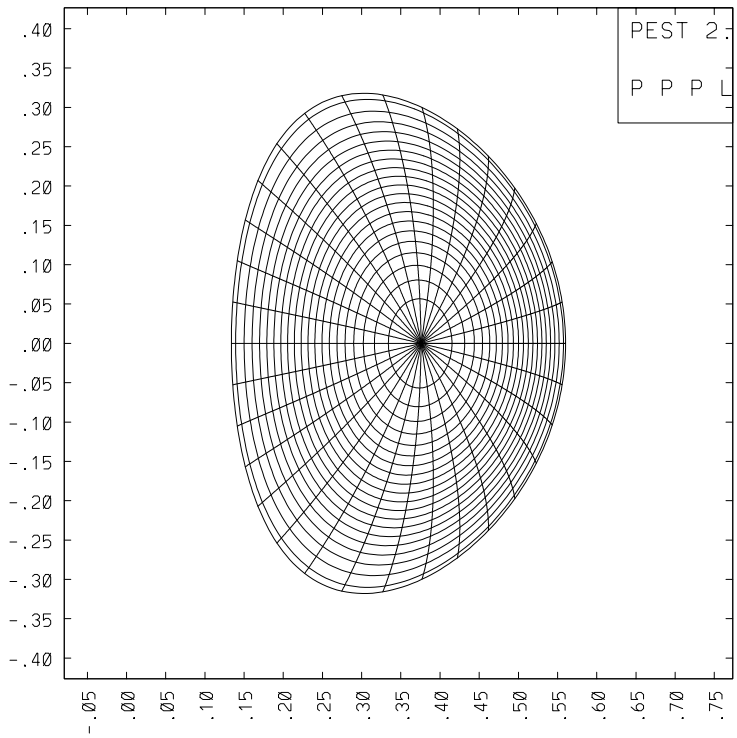

Figure 5.8. The coordinate system used in PEST2 for stability analysis is shown superimposed on the outline of the 36 kA discharge at the time of the plasma current peak. The actual grid used in the stability analysis was much denser than that shown in the figure, with 512 flux surfaces and 256 theta points. The choice of poloidal angle provides for equal arc lengths as θ increases at constant ψ, providing good sampling of the outboard region. In contrast, straight field-line coordinates, often used in PEST stability analysis, the outboard region is sparsely sampled in equilibria with strong toroidicity such as the LART and spheromak configurations.

5.4 36 kA Discharge Stability Analysis - PEST2

The EFIT equilibrium reconstructions of the plasma in Fig. 5.6 and Fig. 5.7 were mapped into a ψ, θ grid used by the equilibrium code JSOLVER.[2] The equilibrium was calculated again by JSOLVER [Chance *et al.*, 1990], which then mapped the equilibrium solution onto a grid used by the PEST2 equilibrium and stability code. Finally, the PEST2 code [Grimm *et al.*, 1983] was used to test for ideal MHD stability.[3]

[2]This mapping code was written by Steve Jardin of PPPL.

[3]Stability analysis for the two tested equilibria was performed by Jon Menard of the CDX-U group.

5.4.1 Stability at Peak Current

Fluctuation data presented in Section 5.5 and 5.6 were dominated by a mode with a clear n=1 toroidal mode number. The equilibrium at current peak was therefore analyzed for stability for n=1 modes with poloidal modes numbers, m=1–36. A toroidal mode number of n=1 was chosen because of the observation of a dominant, saturating mode during fluctuation studies in a wide range of plasmas [see Sec. (5.5)]. Additionally, numerical stability studies for the NSTX LART design equilibria without the presence of a stabilizing wall, generally became unstable for n=1 modes as q_a was lowered. The low plasma β in CDX-U was not expected to produce instability for high n pressure-driven modes, and these were not tested for stability. No stabilizing conducting wall was assumed. The equilibrium was found to be stable to all the n=1, low-m kink modes tested, consistent with the observed ideal stability of the 36 kA, $q_a \sim 7$ discharge phase shown in Fig. 5.6.

In order to explore numerically the kink stability limit of this plasma configuration, the plasma current was increased while maintaining the same plasma boundary and current density profile. The resulting equilibria were also found to be stable to all n=1, m$\leq$ 36 modes, for q_0 (q on axis) down to 1.1 and the edge-q, $q_a \approx 4$. Equilibria with this current profile and q_0 lower than 1 were not tested, since q_0 was not suspected to be less than 1 (no observed sawtoothing). A broadened current profile (lower $\frac{q_a}{q_0}$) was also tested for stability for the same mode numbers. The broadened profile was found to be stable for q profiles down to $q_0 = 1.2$ and $q_a = 3.2$, but unstable for $q_0 = 1.1$ and $q_a = 2.9$. This result is consistent with the known destabilizing effect of finite edge currents and broad current profiles on stability of external kink modes [Wesson, 1978]. Such a broadened, or even hollow current profile may be expected during plasma ramp-up, as in the shots (a)–(c) in Fig. 5.1, and may be a contributing factor for the observed operational q-limit at the even higher value of $q_a \sim 3.5$.

5.4.2 Stability During Current Decay

The equilibrium reconstructed from data approximately 4 ms after the current peak was also tested for stability against n=1, m=1–36 modes. Despite the lower edge-q, this equilibrium was also found to be stable for all modes tested. This was also consistent with the observed ideal stability of the 29 kA, $q_a \sim 4$ discharge phase

shown in Fig. 5.7.

5.5 Fluctuation Studies

Fluctuation studies were conducted on a range of plasma discharges, primarily focused on the 36 kA discharge configuration. Strong fluctuations were found in the poloidal and radial magnetic fields. These magnetic fluctuations were observed using the external array of magnetic pick-up coils [see Sec. (3.4.1)]. The most notable feature was a dominant 10–15 kHz mode present during the current flat-top and especially during the current decay phase of the discharge. These modes saturated in amplitude, and did not cause plasma disruption. Figure 5.9 shows typical magnetic fluctuation signals along with plasma current and line-averaged density waveforms. The fluctuation signal amplitudes, dominated by the 10–15 kHz mode, can be seen to peak during the current decay phase of the plasma. Measurements of the toroidal and poloidal mode numbers were based on cross-power and cross-phase measurements taken between t= 9 ms and t= 12 ms. This mode had a strong ballooning nature: the mode amplitude was seen to be much stronger on the low-field side of the plasma. Also, the amplitude was large enough to cause density fluctuations observable in probe saturation current signals, and even in the line-averaged density signal from the interferometer.

5.5.1 Toroidal and Poloidal Mode Structure

The structure of any perturbation on a toroidal flux surface can be Fourier analyzed in toroidal and poloidal angle, as well as in time. For the poloidal field analyzed in these experiments:

$$\delta B_p = \sum_{n,m,\omega} \delta B_{p\ n,m} e^{i(n\zeta - m\theta - \omega t)}, \tag{5.1}$$

where ζ is the toroidal angle, θ is an angle measuring the poloidal position, (ranging from zero to 2π over one poloidal circuit), and ω is the angular frequency. Measurement of the toroidal and poloidal mode numbers, n and m respectively, then determines the structure of the perturbation. This mode will be resonant at a surface where q is given by:

$$q_{(}\psi_{res}) = \frac{m}{n}. \tag{5.2}$$

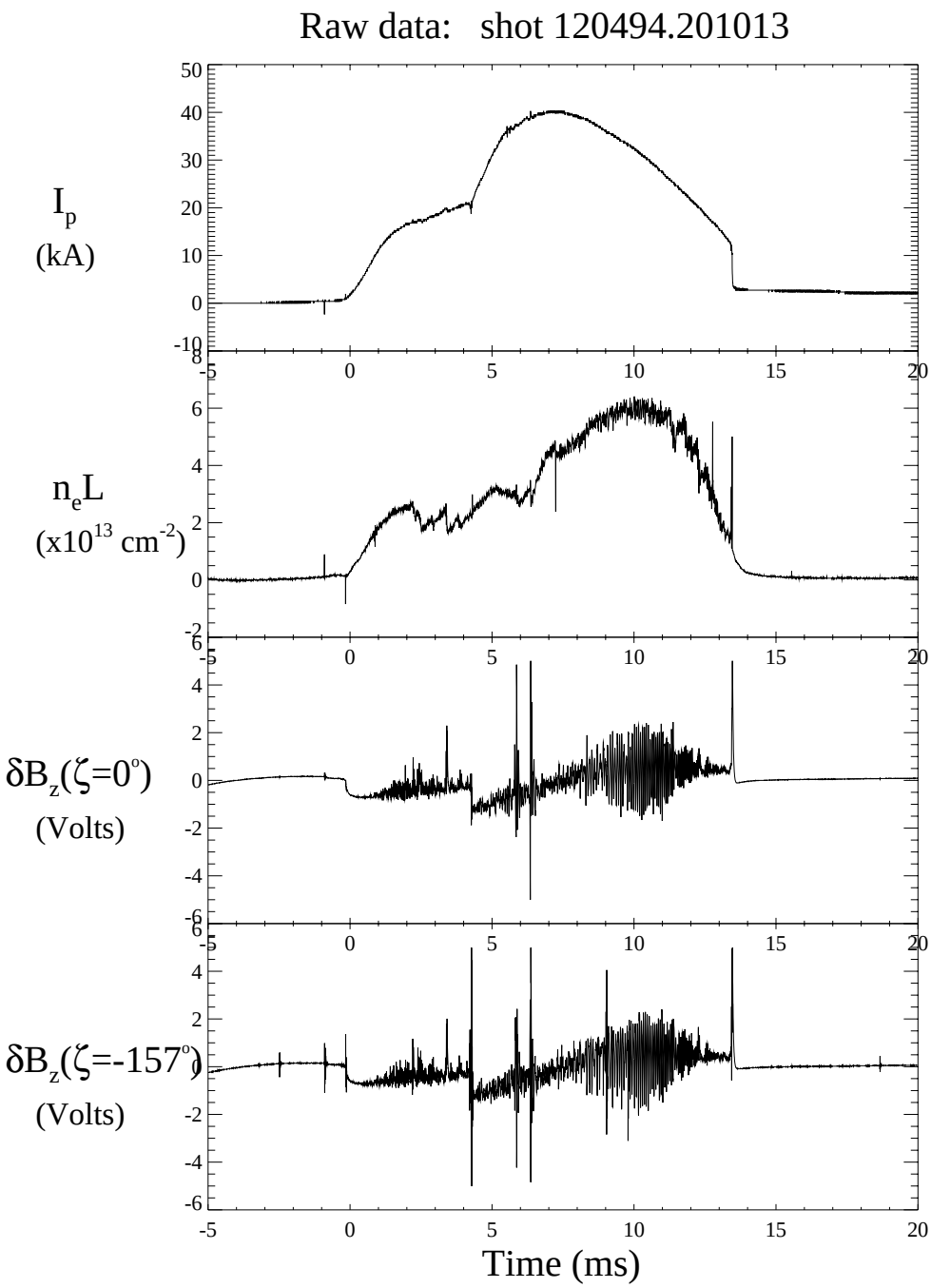

Figure 5.9. Waveforms for a typical shot with the 10–15 kHz mode are shown. The lower two plots show the raw signal from two toroidally separated magnetic pick-up coils on the outboard midplane of the vessel. The fluctuation signals were dominated by a 10–15 kHz frequency component. The mode amplitude can be seen to peak during the plasma current decay.

The toroidal and poloidal mode numbers were determined by using the array of toroidally and poloidally-spaced external magnetic pick-up coils. δB_p signals were recorded throughout a shot for each pair of coils using a sampling frequency of 250 kHz with low-pass filtering at 100 kHz. The cross-power spectrum for both coil signals was calculated, yielding also the cross-phase spectrum.

Let $\delta\tilde{B}_p$ be the discrete Fourier transform of δB_p in frequency (Hz), so that:

$$\delta\tilde{B}_p(f) = \frac{1}{N}\sum_{n=0}^{N-1}\delta B_p(t)e^{\frac{i2\pi ft}{N}}, \quad \text{and} \tag{5.3}$$

$$\delta B_p(t) = \sum_{k=0}^{N-1}\delta\tilde{B}_p(f)e^{\frac{-i2\pi ft}{N}}, \tag{5.4}$$

where $t = n\Delta t$, $f = \frac{k}{\Delta t}$, Δt is the sampling interval, and N is the number of time samples. Then the cross power, CP_{12}, and cross phase, ϕ_{12}, as a function of frequency between signals 1 and 2 are given by:

$$CP_{12} = |S_{12}| \equiv \left|\delta\tilde{B}_{p1}\delta\tilde{B}^*_{p2}\right| \quad \text{for f} = 0 \text{ or } \frac{\text{N}}{2\Delta\text{t}},$$

$$CP_{12} = |S_{12}| \equiv \left|2\delta\tilde{B}_{p1}\delta\tilde{B}^*_{p2}\right| \quad \text{for } \frac{1}{\Delta\text{t}} \leq \text{f} \leq \frac{\text{N}}{2\Delta\text{t}} - 1, \text{ and} \tag{5.5}$$

$$\phi_{12} = tan^{-1}\left(\frac{Im(S_{12})}{Re(S_{12})}\right), \tag{5.6}$$

where S_{12} is the complex cross power, $|x|$ denotes the magnitude, and x^* is the complex conjugate. Note that $S_{12}(f = \frac{n}{\Delta t}) = S_{12}(f = \frac{N-n}{\Delta t})$.

The cross-phase at the dominant mode frequency was then used to determine toroidal and poloidal mode structure. Figure 5.10 shows a typical cross power and cross-phase spectra for two toroidally separated pickup coils on the outer midplane of the device. Notice the dominant frequency component of the cross power centered at 14 kHz. The auto-power spectra of the signals (not shown) show similarly pronounced peaks in frequency. The cross-phase is measured at the peak of the cross power spectrum.

The mode number can be determined from the ratio of the cross-phase between the two signals, ϕ_{12}, and the angular toroidal or poloidal separation between the pick-up coils. Therefore for the toroidal mode number, n:

$$n = \frac{\phi_{12}}{\Delta\zeta}, \tag{5.7}$$

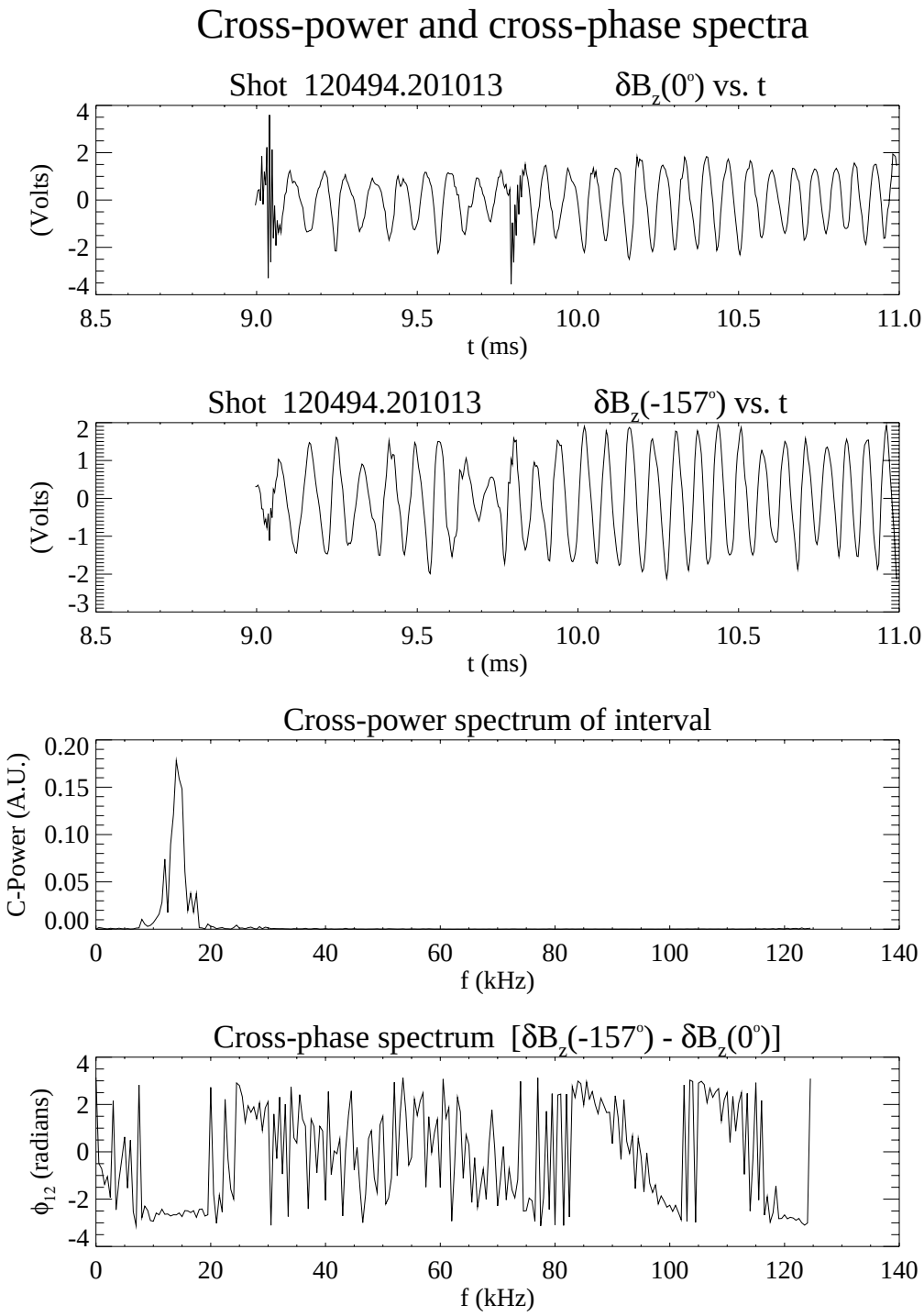

Figure 5.10. Typical cross power and cross-phase spectra for two toroidally separated pick-up coils on the outer midplane of the device are shown. Cross power and cross-phase are measured during an interval where the mode amplitude is strongest, corresponding to the period t= 9 ms to t= 11 ms in Fig. 5.9. For this discharge the mode frequency was peaked at 14 kHz. The cross-phase is measured at the frequency corresponding to peak in cross power (14 kHz).

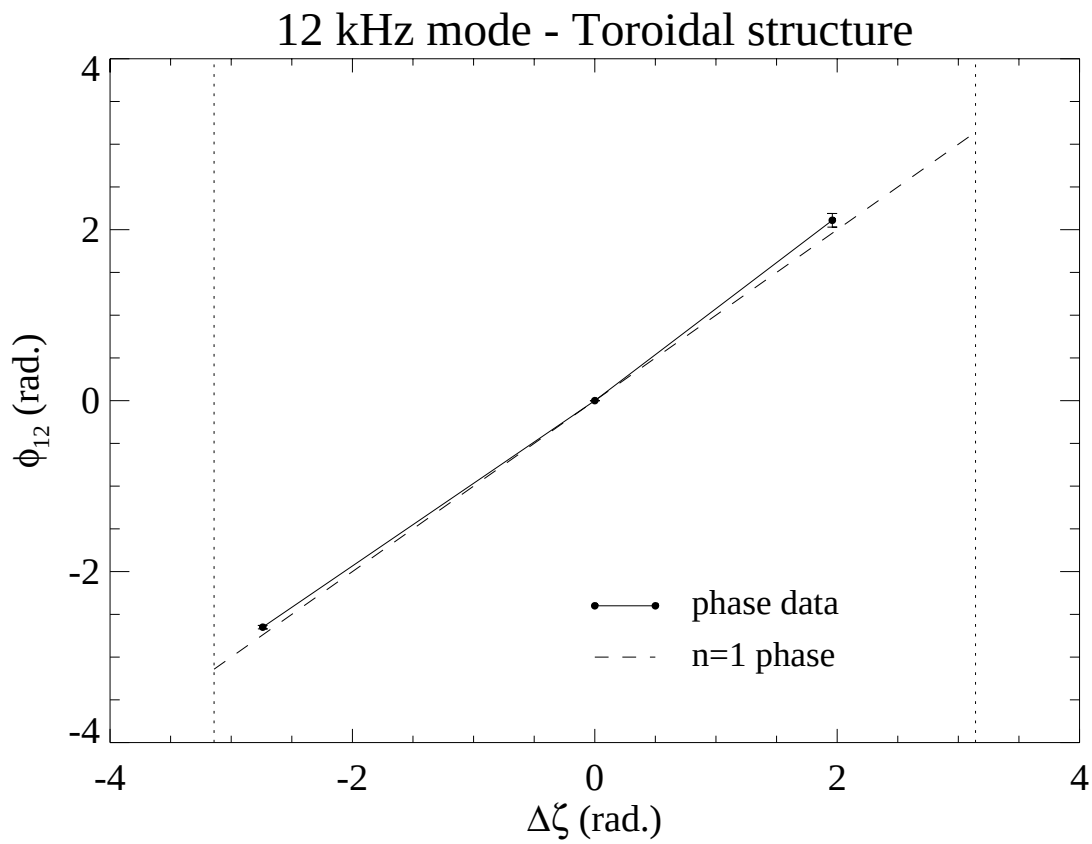

Figure 5.11. Measurements of the 10–15 kHz toroidal mode structure are shown. Each point of phase difference, ϕ_{12}, is an *average* over four shots of the cross-phase of two probe signals. The cross phase for one typical shot is shown in Fig. 5.10. The cross-phase is plotted here as a function of the two probes' toroidal anglular separation, $\Delta\zeta$. Data are shown as triangles connected by a solid line. The error bars show the maximum deviation in the ensemble cross-phase measurements. The phase of a pure n=1 mode is plotted here as a dotted line.

where $\Delta\zeta$ is the toroidal angular separation between the coils (at the same poloidal angle). Figure 5.11 shows the toroidal mode structure data. Three toroidally spaced coils provided rather coarse mode number resolution. However, the excellent fit to n=1 phase structure, over a broad range of conditions in which the 10–15 kHz mode was seen, provides good confidence in the toroidal mode number. Measured phase difference was less than 8% from that expected from a pure n=1 mode.

The poloidal mode number, m, is given by:

$$m = \frac{\phi_{12}}{\Delta\theta}, \tag{5.8}$$

where $\Delta\theta$ is a poloidal angular separation between the coils. The poloidal coordinate,

θ, must be chosen so that its variation is proportional to the local field line pitch, in other words so that it is a straight field line coordinate. For a circular cylindrical plasma, the the field line pitch does not vary around a poloidal circuit, and the cylindrical angle, $\theta_{cyl} \equiv tan^{-1}(\frac{Z}{R-R_0})$ can be used. However, in a non-circular toroidal plasma the proper poloidal angle, which follows the pitch of the field line, is one which is used in the PEST code [GRIMM *et al.*, 1976], and is denoted here as θ_P. θ_P is defined by:

$$\theta_P = \frac{2\pi \int_0^{\theta} f(\theta')d\theta'}{\oint_0^{2\pi} f(\theta')d\theta'}, \quad \text{where} \tag{5.9}$$

$$f(\theta) = [cos(\delta sin\theta) + \frac{\delta}{2} sin2\theta sin(\theta + \delta sin\theta)]/X(\theta). \tag{5.10}$$

$X(\theta)$ can be taken from a parameterization of the plasma surface, given by:

$$X(\theta) = R + acos(\theta + \delta sin\theta), \quad \text{and} \tag{5.11}$$

$$Z(\theta) = -\kappa asin\theta. \tag{5.12}$$

R, a, and κ are as defined as in Sec. (2.1.2). δ is the triangularity of the plasma, and is zero for a circular plasma. For the purposes of determining mode structure from pick-up coil signals, the position of the coil determines the parameterization angle, θ, which can be taken to be the conventional circular cylindrical poloidal angle described above, $\theta_{cyl} = tan^{-1}(\frac{Z}{X})$. Equation 5.9 then provides a mapping to θ_P. The magnetic reconstruction of the plasma at the time of the fluctuation measurements determines the shape parameters, which are as given in Fig. 5.7: $R = 27.6$ cm, $a = 15.6$ cm, $\delta = 0.11$, and $\kappa = 1.23$. For these parameters, the mapping from θ_{cyl} to θ_P is depicted graphically in Fig. 5.12. Notice that $\frac{d\theta_P}{d\theta_{cyl}}$ is small on the low-field side of the plasma ($\theta_{cyl} \sim 0$) where the magnetic field-line pitch is large, and large on the high-field side were the field-line pitch is small. The poloidal position of each pick-up coil in the array is marked by a circle, where the filled circle denotes the position of the coil used as a phase reference.

Figure 5.13 shows the results of analysis of the cross-phase between the δB_p signal from pairs of magnetic pick-up coil array. Each cross-phase measurement can be shifted by 2π radians. The best fit to Eq. (5.8) is shown in the top plot. A mode number of m=3 provides an excellent fit for 9 out of 11 of the cross-phase measurements. If the two poorly-fitting cross-phase measurements (at $\theta_P \approx -1.7$ and -2.7

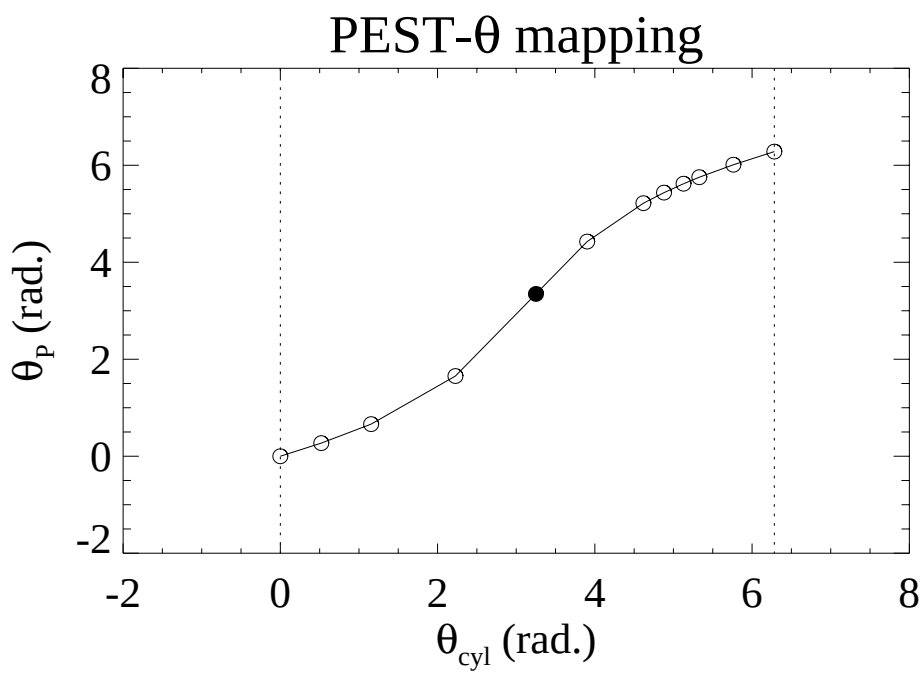

Figure 5.12. The dependence of the PEST straight field line poloidal angle, θ_P, on the cylindrical poloidal angle, θ_{cyl}, is shown. The poloidal position of each pick-up coil in the array is marked by a circle, where the filled circle denotes the position of the coil used as a phase reference. $\theta_{cyl} = 0$ and $\theta_P = 0$ both correspond to the outboard midplane position.

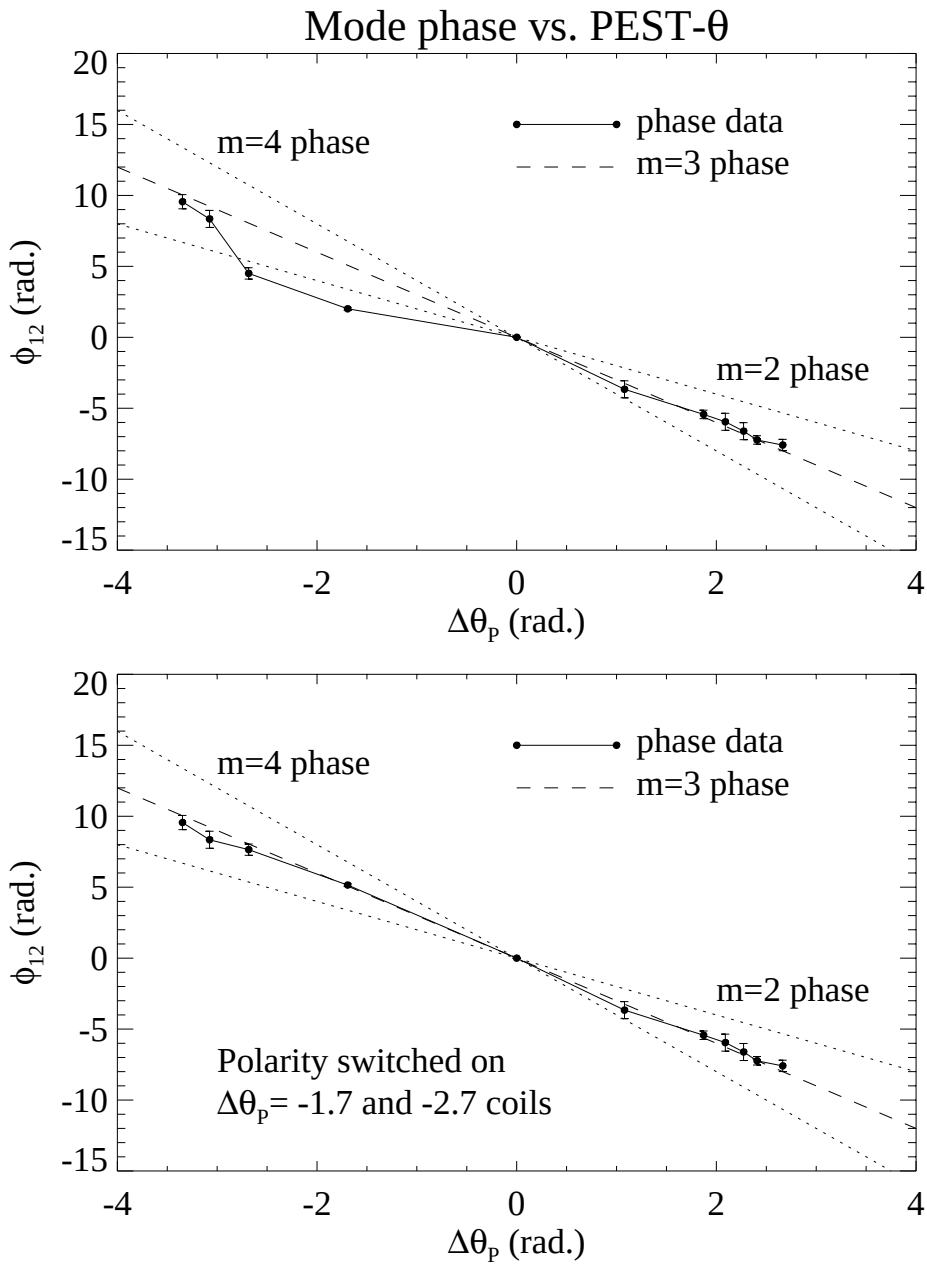

Figure 5.13. Measurements of the 10–15 kHz poloidal mode structure are shown. Each point of phase difference, ϕ_{12}, as a function of straight field line poloidal angle difference, $\Delta\theta_P$, is an average from three shots. Data is shown as a solid line. Each signal phase measurement can be shifted by 2π radians (one wavelength). Shifted data best fits an m=3 phase dependence, shown as triangles connected by a solid line. The error bars show the maximum deviation in the ensemble cross-phase measurements. The phase of a pure m=3 mode is plotted here as a dashed line, and m=2 and m=4 phase are shown as dotted lines for comparison.

radians) are shifted by π radians, as shown in the lower plot the fit is excellent for all data points. Such a switch could have easily happened experimentally by the accidental reversal of the polarity of one of the pick-up coils. The excellent fit of the cross-phase between $\theta_P \approx 1.8$ and 2.3, where poloidal resolution is good, to an m=3 phase, provides extra confidence in the mode number determination.

Finally, the safety factor at the resonant surface for this mode can be determined to be $q_{res} = \frac{m}{n} = 3$. From Fig. 5.7 this surface is located within a few centimeters of the plasma edge. Measurements of the radial structure of the mode were not possible, however, due to excessive perturbation of the plasma by the insertion of the magnetic probe.

5.6 Low-I_p, Low-q_a MHD Activity

A similar MHD mode to that found in the 36 kA discharge was found in low-I_p plasmas ($I_p \sim 15$ kA), and was reported in [Hwang *et al.*, 1994]. The frequency of this mode was also in the 10–15 kHz range. The toroidal mode number was measured to be n=1, while poloidal harmonics with m=1 and 2 were present. The amplitude of this mode was seen to increase with decreasing q_a, as shown in Fig. 5.14(a). The data in this plot constitutes magnetic fluctuation signals from a range of plasma currents and toroidal field strengths. Similar plasma shape as the 36 kA discharge at current peak was assumed in calculating q_a from Eq. (2.19). Plasma shape was not calculated from a reconstruction, although the values in Fig. 5.14 are consistent with limiter current measurements. Of note is the strong increase in the mode amplitude as the edge-q decreases.

The lower plasma temperatures in the low current discharges allowed for the immersion of a the scanning magnetic probe into the plasma without undue perturbation of the plasma. An especially interesting result from the radial fluctuation amplitude profile, is the peaking of the amplitude well inside the plasma surface, as seen in Fig. 5.14(b). Along with the non-disrupting plasma behavior indicating ideal MHD stability of the plasma, this radial mode structure suggests an internal resistive mode and the formation of magnetic islands. The presence of an n=1/m=1 sawtooth-type mode would be consistent with the observed radial mode structure. Coupling of internal modes in low-aspect-ratio may be strong, due to the relatively narrow shear layer

(a)

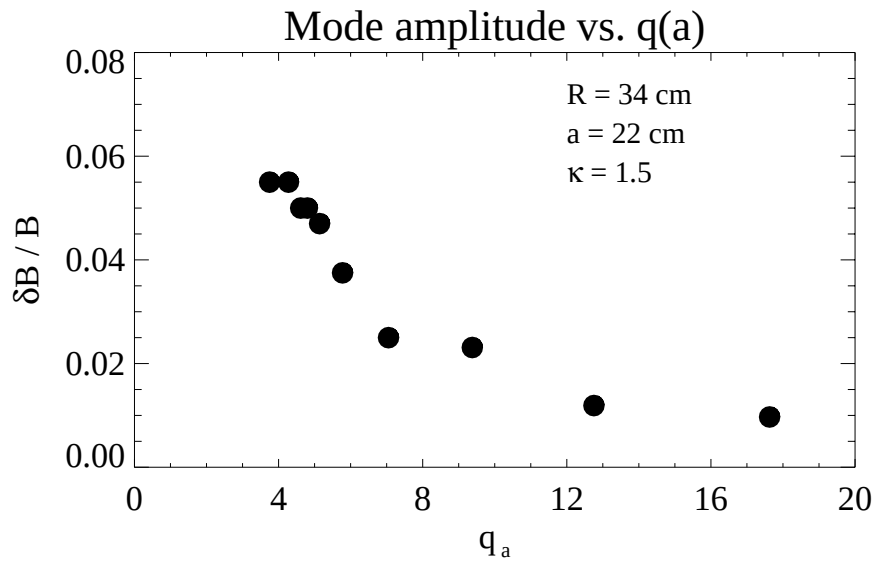

(b)

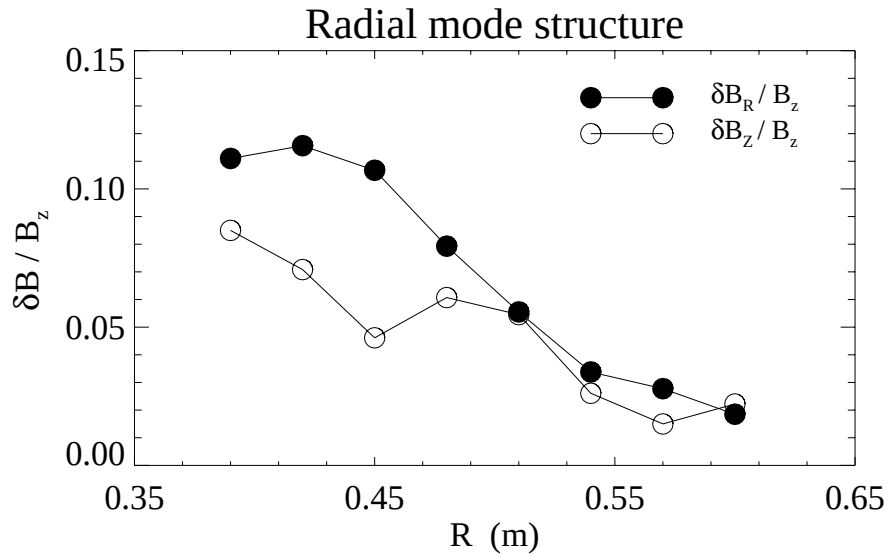

Figure 5.14. Low plasma current ($I_p \sim 15$ kA), 10–15 kHz MHD mode behavior as reported in [HWANG *et al.*, 1994] is shown above. (a) Mode amplitude vs. q_{cyl} for a set of shots with a scan in B_{T0}. (b) Radial mode structure in δB_r and δB_z is shown.

(the layer of plasma surfaces with a significant $\frac{dq}{d\psi}$), and the accompanying likelihood of overlap of magnetic islands on low-order rational surfaces. This may have caused the observed presence of more than one low-order mode harmonic. The 10–15 kHz mode was also observed to have a ballooning nature, with a much stronger amplitude on the low-field side of the plasma.

5.7 Summary

Extended ohmic operation of the CDX-U tokamak with plasma currents up to 60 kA and aspect ratios $A \geq 1.6$ has yielded ideal MHD-stable plasmas with edge safety factors down to $q_a \sim 3.5$. The persistence of this operational q_a limit over a large range of plasma current and toroidal field, suggests an MHD limit has been reached. However, recurring plasma position control problems, and the possibility of very broad or hollow current profiles due to rapid current ramp-up, cannot be ruled out as possible causes of the observed operational q_a limit.

Equilibrium reconstructions from magnetics data were performed for a reproducible discharge configuration with $I_p \leq 36$ kA. Numerical stability analysis of this discharge, with $A \geq 1.6$ and $q_a \leq 7$, indicates ideal MHD stability, in agreement with experimental observations. When the plasma current profile is increased and slightly broadened, and q_a is decreased to 2.9, the plasma ideal MHD instability is encountered.

Fluctuation studies of the magnetic signals revealed the presence of a dominant, coherent, 10–15 kHz mode in a range of discharges, including the 36 kA discharge. The mode structure was measured in the 36 kA discharge, with a resulting toroidal and poloidal mode number of n=1 and m=3, respectively, implying resonance at the $q = 3$ surface. The mode amplitude was observed to have a strong ballooning nature, with a much higher amplitude on the low-field side of the plasma. The saturating, non-disruptive nature of this mode indicates that it is not an ideal instability, but almost certainly a resistive mode.

Fluctuation studies of plasmas with $I_p \sim 15$ kA, reported in [Hwang *et al.*, 1994] revealed an MHD mode in the same frequency range of 10–15 kHz. This mode was measured to have mode numbers of n=1 and m=1 or 2, possibly indicating coupling of resistive modes on nearby rational surfaces. The amplitude of this mode was seen

to increase dramatically in plasmas with q_a approaching the operational q_a limit of 3.5–4.

The presence of similar, dominant, saturating, low-mode number (n=1, m=1–3) modes in a large range of low-aspect-ratio CDX-U plasmas is striking. The observed dramatic increase in the mode amplitude as q_a is decreased in the low I_p shots makes these modes a good candidate for an MHD instability which might be causing the observed operational q_a limit.

Chapter 6

Conclusions

A LARGE PART of this thesis involved a major portion of the design and fielding of a new low-aspect-ratio device, the Current Drive Experiment-Upgrade (CDX-U). This device was designed for the investigation and development of the low-aspect-ratio tokamak (LART) configuration, as well as for the investigation of novel current drive methods. Also as part of this thesis, an ohmic heating system was designed for the CDX-U and subsequently installed, entailing a rebuild of a major portion of the tokamak. This system enabled the ohmic operation and experiments presented in herein.

This thesis has also developed valuable techniques for efficient start-up and operation of a LART, advancing the effort to make the LART a viable, attractive alternative to a conventional tokamak. The use of ECH preionization in low-aspect-ratio has been demonstrated to allow low loop voltage plasma start-up, to allow start-up in the presence of large error fields, and to minimize the large induced vessel eddy currents occurring in toroidally continuous vessels used in LARTs. Plasma current ramp-up and control was successfully demonstrated in the presence of significant ohmically-induced eddy currents ($\sim$ 50% of the final plasma current value). The ECH preionization enabled plasma breakdown and start-up with a range of magnetic field strength, B_{T0}, of a factor of 2.5, from a low of $B_{T0} = 0.45$ kG to a high of $B_{T0} = 1.13$ kG. Ohmic efficiency, in terms of the Ejima coefficient, was measured to be as good as or slightly better than that found in conventional tokamaks, with $C_E \approx 0.3$–0.4 for the best cases.

An operational current limit was found during more than 8,000 ohmic shots in

CDX-U, corresponding to an MHD safety factor, $q_a \sim 3.5$. The creation of non-disrupting plasmas with $q_a \geq 3.5$ demonstrates experimentally the ideal MHD stability at these edge-q values, a new low for these aspect ratios of $A \geq 1.6$. One reproducible, non-disrupting discharge in particular was studied, with a peak plasma current of 36 kA, and $q_a \sim 7$. Analysis of this discharge configuration included a magnetic reconstruction, numerical ideal MHD stability analysis, and magnetic fluctuation measurements. Ideal stability analysis indicated stability for the reconstructed profile, in agreement with experiment. However, a slightly broadened current profile at an increased current level was found to be ideal kink-unstable. Early stages of low-q_a discharges may have had such a current profile, due to the ohmic current drive skin effect, suggesting one possible cause of the observed operational q_a limit. Intermittent plasma positional control problems were observed to cause strong plasma-limiter interaction, resulting in a large impurity influx, and occasional quenching of the plasma, providing a second possible cause of the observed q_a limit.

Fluctuation studies of magnetic signals from the 36 kA discharge revealed a dominant, 10–15 kHz mode. The saturating nature of this mode strongly indicates that it is resistive. This mode was present during the plasma current flat-top, and its amplitude peaked during the plasma current decay phase. Cross-phase calculations of signals detected by the external magnetic pick-up coil array revealed a clear n=1, m=3 mode structure, with significant mode shape effects from the high toroidicity. An equilibrium reconstruction of the plasma during the mode amplitude peak yielded a edge-q of $q_a \approx 4$, so that the resonant $q = 3$ surface was relatively close to the edge. Fluctuation studies of magnetic signals in lower current discharges revealed a similar, dominant, saturating mode with a frequency of 10–15 kHz, and a mode structure of n=1 and m=1 and 2. The measured radial structure of this mode shows an amplitude peaked at approximately $a/2$, consistent with an internal island structure. The amplitude of this mode was also seen to increase dramatically as the edge-q approached the operational limit of $q_a \sim 3.5$–4. The observation of these similar low-order resistive modes over a broad range of low edge-q, low-aspect-ratio plasmas, and the increase in their amplitude with decreasing q_a makes them a good candidate for an MHD instability which the author considers to be the most likely cause of the observed operational q_a limit.

Lastly, the CDX-U device, especially the ohmic heating system, has served as a design prototype for a proposed 1 MA plasma current-sized device, named the Na-

tional Spherical Tokamak Experiment (NSTX). CDX-U has served and will continue to serve as a testbed for new concepts in low-aspect-ratio and advanced tokamak configurations, such as a 100% bootstrap current-driven tokamak [FOREST, 1992] and a planned high-harmonic fast wave heating and current drive experiment [MENARD *et al.*, 1995].

6.1 Future Work

6.1.1 Low-aspect-ratio Start-up

ECH preionization was seen to be of benefit in low-aspect-ratio start-up in the presence of extremely conductive close-fitting walls. More important, however, is the extension of the ECH preionization technique at low-aspect-ratio to application in larger LART devices, and particularly in the proposed NSTX device. Predicted induced vessel eddy currents in the NSTX device are much smaller in proportion to the plasma current than those encountered in the CDX-U vessel. Associated error fields will therefore be much easier to correct, providing a more favorable poloidal field configuration at start-up than that encountered in the CDX-U ECH-assisted ohmic start-up experiments. Since particle confinement time at start-up scales as:

$$\tau \sim \frac{L}{v_{\|}} \sim \frac{1}{v_{\|}} \frac{B_T a}{B_{err}}$$

where $B_{err} = (B_Z^2 + B_R^2)^{\frac{1}{2}}$ is a mean error field due to vessel eddy currents and stray flux from the OH and PF coils, and $v_{\|}$ is determined by $\frac{E_{\|}}{n}$. B_T and a are both larger in NSTX by a factor of 3, and B_{err} and $v_{\|}$ are expected to be similar to those in CDX-U. Therefore the confinement time should be longer, and the associated ohmic acceleration of the particles to ionization energies should be more effective in NSTX. Certainly start-up conditions in NSTX are expected to be more favorable in terms of error fields and their effects, therefore the demonstration of start-up in CDX-U with its larger error fields should strongly indicate successful start-up in NSTX.

Perpendicular energies achieved by electrons resonant with the ECH should be roughly proportional to the rf power density. Since the proposed NSTX device is scaled up by a factor of 2.5 in linear dimension from CDX-U, the volume of the resonance layer should be roughly a factor of $2.5^3 \approx 15$ larger. Therefore the coupled

ECH power should also be scaled up by a factor of approximately 15 in order to achieve similar rf power densities and resultant perpendicular electron energies. With a magnetic field of 0.4 T in NSTX, roughly a factor of four larger than that in CDX-U experiments presented here, an ECH system with modest transmitted power of $P_{ECH} \approx 20$ kW at approximately 10 GHz should be adequate to provide similar benefits of ECH preionization.

6.1.2 Low-aspect-ratio MHD

Experimentally, fluctuation measurements of MHD behavior in disrupting plasmas near the operational q_a limit would be of great interest, and would help clarify the role of the observed low mode number resistive modes in limiting q_a. Fluctuation studies presented in Sec. (5.5) focus on measurements in a discharge phase with $q_a \approx 4.2$ and $A \approx 1.77$. The connection between this mode and the q-limit at $q_a \sim 3.5$ for $A \sim 1.6$ was inferred from the the behavior of the mode amplitude at lower plasma current levels as the edge-q was reduced.

Better measurements of the radial mode structure would also be useful in identifying the observed mode and its connection to the q_a. The localization on the $q = 3$ surface should be verified by observation of island structures. The narrow shear layer in low-aspect-ratio plasmas means that low-order modes are likely to be much more strongly coupled than at conventional aspect ratios. It is possible that several low-order modes are being excited, with an overlap of large magnetic island structures in the plasma core causing disruption. A non-intrusive diagnostic for measuring local fluctuations in the plasma core regions would therefore be most helpful. At present several such diagnostics are being installed on CDX-U, including: a soft x-ray diagnostic for measuring local temperature and density fluctuations with approximately 1 kHz response, a CO_2 laser-based phase-contrast imaging system for local density fluctuations with over 1 MHz response, and a Faraday rotation diagnostic based on the 2 mm interferometer system for line-averaged poloidal field fluctuations, with approximately 1 kHz response.

Certainly, more flexible programmable vertical and poloidal field power supplies would be useful in maintaining proper plasma position and eliminating limiter strikes and early plasma terminations due to improper position control. At least one vertical or radial field coil supply with active feedback control of plasma position would be

most desirable. Poor position control or the possible existence of rapidly changing vessel eddy currents causing sudden plasma motion should be eliminated and ruled out as contributing causes of the observed q_a limit.

Finally, a resistive MHD code for investigating predicted mode behavior in the LART geometry would be extremely valuable. The possible stabilization of these modes with a close fitting conductive wall could also be investigated numerically. Close-fitting passive stabilization plates are planned for the proposed NSTX, where their effect on low mode number resistive kink modes can be tested experimentally.

6.1.3 ULART Experiments in CDX-ST and NSTX

A favorable predicted scaling of the important performance parameters, $(\frac{I_{TF}}{I_p})$, and β_c were seen in comparisons in Sec. (2.2.1) as aspect ratio was reduced from $A = 3.0$ to $A = 1.6$. However, the predicted improvement is much more dramatic as the aspect ratio is reduced to the ultra-low aspect ratio (ULART) regime with $A \sim 1.2$–1.3 and elongation increases to $\kappa \geq 2$. At these values of A and κ, the strong toroidicity causes much greater changes the MHD behavior and neoclassical transport behavior than from that at high aspect ratios.

The proposed MA-sized NSTX device will be capable of plasmas with aspect ratios down to $A = 1.25$ with elongation $\kappa \approx 2.2$. The start of operations is proposed for FY99. In addition to the proposed MA-size NSTX, an upgrade of the CDX-U device, allowing an aspect ratio of $A = 1.3$ with elongation $\kappa \approx 2.2$, is being proposed. The lower aspect ratio will have a higher plasma current limit than the current CDX-U configuration, with the same edge-q and toroidal field, thus allowing investigation of higher current and temperature plasmas, as well as a lower aspect ratio. The start of CDX-ST operations is proposed for FY97. CDX-ST will allow investigation of MHD current limits in the important ULART regime, as well as confinement. NSTX, with proposed high harmonic fast wave heating, would be able to investigate experimentally the plasma confinement and β limit in LART and ULART regimes. Experimental confirmation of the favorable predicted scaling of the β and q_a limits would open the door to an attractive alternative reactor design to the conventional tokamak.

6.1.4 Confinement Studies

Confinement studies at low-aspect-ratio, a vital issue for LART viability, will become feasible in CDX-U with the implementation this calendar year of improved plasma profile diagnostics, such as a Thomson scattering system, improved soft x-ray measurements and bolometry, and a faraday rotation diagnostic.

Recent calculations of trapped electron driven drift wave microinstabilities (TEM), which have been postulated to dominate heat transport in core regions of conventional tokamaks, have shown a predicted stabilization with lower aspect ratio [Rewoldt and Tang, 1989; Rewoldt *et al.*, 1994]. Calculated linear growth rates for these modes for a D-shaped plasma show stabilization at aspect ratios of approximately 1.5 [Rewoldt *et al.*, 1994], where CDX-U plasmas lie. Studies of the plasma confinement and TEM mode dynamics as these modes approach marginal stability would provide important insight into transport in both low-aspect-ratio and conventional geometry tokamaks. Studies of plasma transport in CDX-U, however, will depend on the ability to stabilize MHD activity. Somewhat higher safety factors than the observed limit of $q_a \sim 3.5$ may be desirable to minimize MHD activity. The addition of a phase-contrast imaging system for density fluctuations will be a valuable for studying microinstabilities.

Appendix A

PPPL-TM-396: OH System

CDX-U New Center Stack with Ohmic Heating Solenoid

T. G. Jones, D. S. Darrow, M. Ono

Technical Memo 396 issued by
Princeton Plasma Physics Laboratory
Princeton University
Princeton, NJ 08543

May 1992

Abstract

The present CDX-U device is capable of aspect ratios as low as 1.4. Plasma currents of ten kiloamps have been achieved using DC helicity injection. In order to extend the machine's plasma current capability to the several tens of kiloamps, a new center TF stack is being built with an ohmic heating coil. The new OH coil should be capable of up to 0.15 V-sec, and will not appreciably change the lowest achievable aspect ratio. Breakdown and initial current drive will still be accomplished with DC helicity injection, reducing peak loop voltage required. Computer simulations have

been run using the Tokamak Simulation Code with: ne = 10^{12} cm^{-3}, Te = Ti = up to 0.5 keV, and final I_p = 100 kA. Central ν_{*e} would be $\sim 10^{-3}$ compared to $\nu_{*e} \sim 10$ with present parameters. This would benefit studies of low aspect ratio physics such as bootstrap current and trapped electron modes (TEM's), both of which are driven by banana-trapped electrons.

PPPL-TM-396 Outline

I. Introduction and Motivation
- Mission of Current Drive Experiment-Upgrade
- Physics Goals of Ohmic Heating Experiments
- Performance Required of Center Stack

II. Housing
- Description of Structure
- Method of Fabrication
- Sealing to Other Vacuum Vessel Components
- Mechanical Stresses Due to Vacuum

III. Toroidal Field Conductors
- Conductor Specification and Arrangement
- Operating Limits
- Experience with Present Center Stack
- Connections to Outer Coil Sections
- Heat Generation and Removal
- Method of Fabrication
- Insulation and Sealing

IV. Ohmic Heating Solenoid
- Conductor Specification and Arrangement
- Operating Scenario and Limits
- Method of Fabrication
- Electrical Connections
- Heat Generation and Removal
- Mechanical Stresses in Solenoid

Acknowledgments
References
Tables
Appendix: Supporting Calculations for OH System

Figures

List of Tables

Table 1 Center Stack Housing Parameters Table 2 Toroidal Field Conductor Parameters Table 3 Ohmic Heating Solenoid Parameters

List of Figures

(Please refer to PPPL Drafting Dept. for updated, master drawings.)

Figure 1 Cross section of CDX-U device (Dwg. D-CCL100-1)
Figure 2 Vertical Cross section of OH Center Stack (Dwg. D-CCL100-2)
Figure 3 Center Stack Housing (Dwg. D-CCL101-1)
Figure 4 9 1/2" Flange (Dwg. D-CCL101-2)
Figure 5 Housing Gusset (Dwg. D-CCL101-3)
Figure 6 14" Flange with O-ring (Dwg. D-CCL102-1)
Figure 7 14" Flange without O-ring (Dwg. D-CCL102-2)
Figure 8 Full size Assembly Section (Dwg. D-CCL103)
Figure 9 Horizontal Cross section of Top of OH Center Stack, Showing OH Connections (Dwg. D-CCL104-1)
Figure 10 Horizontal Cross section of Top of OH Center Stack, Showing TF Connections (Dwg. D-CCL104-2)
Figure 11 Horizontal Cross section of OH Center Stack (Dwg. D-CCL104-3)
Figure 12 Vert. Cross sec. of Top of OH Center Stack-45° (Dwg. D-CCL105-1)
Figure 13 Vert. Cross sec. of Top of OH Center Stack-68° (Dwg. D-CCL105-2)
Figure 14 Vert. Cross sec. of Top of OH Center Stack-110° (Dwg. D-CCL105-3)
Figure 15 Phenolic Casing - Layer 6 (Dwg. D-CCL106-1)
Figure 16 Phenolic Casing (Dwg. D-CCL106-2)
Figure 17 OH Solenoid Clamp (Side View) (Dwg. D-CCL107-1)
Figure 18 OH Solenoid Clamp (Top View) (Dwg. D-CCL107-2)
Figure 19 OH Solenoid Clamp Brace (Dwg. D-CCL107-3)
Figure 20 OH Solenoid Clamping Shoe (Top) (Dwg. D-CCL107-4)
Figure 21 OH Solenoid Clamping Shoe (Bottom) (Dwg. D-CCL107-5)
Figure 22 G-10 for Clamping Shoe (Dwg. D-CCL107-6)
Figure 23 G-10 for Clamp Brace (Dwg. D-CCL107-7)
Figure 24 Phenolic Clamp Hold-Down (Dwg. D-CCL107-8)
Figure 25 OH Return Conductor with Slots (flat) (Dwg. D-CCL108-1)

Figure 26 OH Return Conductor (rolled) (Dwg. D-CCL108-2)
Figure 27 OH Solenoid Inner Connector (Dwg. D-CCL109-1)
Figure 28 OH Return Inner Connector (Dwg. D-CCL109-2)
Figure 29 Details of TF Joints (Dwg. D-CCL109-3)
Figure 30 OH Jumper Bus (Dwg. D-CCL109-4)
Figure 31 OH Return Bus Connector (Dwg. D-CCL110-1)
Figure 32 OH Solenoid Bus Connector (Dwg. D-CCL110-2)

I Introduction and Motivation

The Current Drive Experiment-Upgrade (CDX-U) is a small, toroidal, magnetized plasma device located on the second floor of the Laboratory wing at C-site of the Princeton Plasma Physics Laboratory. CDX-U is a facility in which advanced concepts with potential application to tokamaks are developed and tested, and a facility in which basic plasma physics experiments can be performed. Present areas of research are in current drive for tokamaks by means of electron beams (dc helicity injection), properties of low-aspect-ratio tokamaks, and the physics of low-aspect-ratio plasmas. The parameters of the device are: R=33 cm, a=25 cm, (hence a minimum aspect ratio of R/a≈1.4), κ=1.5 (vertical elongation), and $B_T \leq 1.5$ kG. Average plasma parameters, at present, are $n_e \approx 5 \times 10^{12}$ cm^{-3}, $T_e \approx 20$ eV, and $I_p \approx 10$ kA.

Low-aspect-ratio tokamaks are expected, on theoretical grounds, to have a number of advantages over present day tokamaks. Among the most important are the ability to operate at higher β and a magnetic structure which may improve energy confinement. CDX-U, with dc helicity injection as the current drive method, has produced plasmas with currents as large as 10 kA. This current drive technique is under investigation in hopes of making power- efficient steady-state operation of a tokamak reactor possible. This current drive research will be continue in the future, with the objective of driving larger plasma currents. In parallel, however, we desire to add an ohmic heating (OH) system for the following physics goals: (1) With the OH system, low-aspect-ratio tokamak discharges can be formed for comparison to known scaling laws determined at higher aspect ratios. CDX-U is the only ohmic current drive device in the US with the capability of testing such scalings in the near future. (2) The OH system will permit comparisons in the same device between ohmic and helicity-injected discharges, a process important to testing the viability of the helicity injection technique. (3) With the OH transformer, synergistic effects involving dc helicity injection and ohmic current drive can be investigated. These may be useful in improving tokamak startup and current profile control capabilities. (4) The OH system would increase the overall flexibility of the CDX-U device, and could be used diagnostically to measure plasma resistivity.

Technically speaking, the CDX-U center stack is an innovation in TF coil design (see the CDX-U device proposal). The first center stack for the device was successfully built and installed 18 months ago. After an initial period of operation, arcing

occurred within the center stack, due to accumulation of water in the insulation. This problem was diagnosed and corrected by drying the center stack, disconnecting the damaged turns, and sealing the top of the assembly. The center stack has operated reliably since then but, since it is a critical assembly for CDX-U, the idea of constructing a replacement was considered at length. This process led us to develop a number of improvements which are incorporated into the design described herein. Our conclusion was that an OH coil could be incorporated into a new center stack relatively straightforwardly, without sacrificing machine performance, especially the lowest achievable aspect ratio (1.4). The enhanced physics capability provided by the OH coil definitely makes it worth constructing.

From the experimental and theoretical point of view, tokamak plasmas in the CDX-U vessel would be most interesting with plasma currents in the 30 to 100 kA range. The goal of this effort, then, is to design and construct a center stack with toroidal field and ohmic heating coils such that a plasma carrying 100 kA can be formed in CDX-U.

Figures 2 and 11 depict the proposed new center stack in cross section. The principal components are the housing, the ohmic heating solenoid, the toroidal field conductors, and the insulation. The remaining sections of this document describe these components in more detail and justify the various choices made in the design process.

II Housing

The housing of the center stack is depicted in Fig. 3. It will serve both as packaging for the coils, and as part of the vacuum wall of the CDX-U vessel. As seen in Fig. 3, the housing consists of a number of components. The first of these is an Inconel 625 tube, of 6.875 inches (17.2 cm) outside diameter, 42 inches (106.7 cm) in height, with a wall thickness of 1/16 inch. At both ends, where several flanges will be attached, short sections of 1/8 inch wall Inconel tube (close-fitting to the outside of the long tube) will be attached by nichrobrazing. These short sections of tube will be 8 inches in length, and will serve to stiffen the ends of the tube where four flanges will be attached, two at each end. The flanges at the absolute ends of the tube will be Inconel 625, 9 1/2 inches OD and 1/4 inch thick, to serve as a support for a set of

phenolic rings in which are fastened electrical connections for the toroidal field (TF) and ohmic heating (OH) coils. A second pair of flanges (also Inconel 625), a few inches in from each end, are to be 3/8 inch thick, and will be sealed with O-rings to the top and bottom plates of the vessel (refer to Fig. 1). These vacuum-sealing flanges will be subject to significant forces, and therefore will be braced to the thickened tube wall by eight triangular gussets each. The gussets and the flanges will also be nichrobrazed to the tube. Along the outside of the tube wall, between the two thickened sections, will be tack-welded 16 square stainless steel bars, each 1/4 by 1/4 inch by 33 inches long, tapped to receive 6-32 screws at intervals. These bars will serve as fixtures on which to mount diagnostics, and as stiffening bars for the tubular housing. Parameters of the housing are summarized in Table 1.

Inconel was chosen for the housing material because it is non-magnetic, resistive, and quite strong. Grade 625 is reportedly in common use at PPPL, and it exhibits slightly greater strength than some other alloys. The wall thickness of the tube was chosen to be as thin as possible so that its electrical resistance would be maximized. This is of importance because the tube has a large mutual inductance to the OH solenoid. The high resistance minimizes induced currents and energy dissipation in the tube, both of which are undesirable. The flanges have also been designed to be as thin as possible for the same reason. The short sections of 1/8 inch thick tube have been added to provide the tube wall with greater rigidity where the flanges and the gussets are fastened. The inclusion of these tube sections does not significantly increase the eddy currents which flow in the tube wall.

The 1/16 inch wall tube will be fabricated by rolling and seam-welding a sheet of Inconel, as such a size tube could not be found as a standard production item from any US supplier. The rolling and welding will be done in facilities here at PPPL: the rolling at the Forrestal machine shop, and the welding at the Vacuum Shop. Following the welding, it is expected that the tube will not be exactly circular in cross section, and that the diameter in the middle will be slightly smaller than the diameter at either end. To counteract this effect, the tube will be rerolled after welding, until the deviation from circular cross section and the variation of diameter along the length are both less than 1/16 inch.The short sections of 1/8 inch wall tube will be fabricated in a similar fashion. The various other parts can be cut from Inconel plate stock.

The entire assembly will be assembled, joined, and sealed by nichrobrazing in an oven in the Vacuum Shop. It should be possible to braze the entire assembly in one

heating.[1]

Because the housing will be a part of the CDX-U vacuum vessel, atmospheric pressure will exert significant forces upon it. From the geometry of the top and bottom plates (52 inches OD), 40% of the total atmospheric loading will be applied to the center stack housing. That will produce a compressional stress in the tube wall of 18,600 psi. This stress can be easily accommodated by the Inconel. (Note that susceptibility of the tube to buckling has not been estimated. It is thought that buckling will not occur because of the conductors and potting which act to stiffen the column.) The atmospheric force on the top and bottom flanges will be transferred to the vacuum sealing flanges on the center stack. These flanges will be 14 inches in diameter, 3/8 inch thick, and will be supported by the gussets mentioned above. The gussets will extend to a point directly under the bolts which will attach the flanges to the top and bottom plates. Hence, stresses in the flanges will be minimal, and negligible deformation is estimated. The sections of 1/8 inch wall tube are included to ensure that the tube wall does not deform under the radial forces that the gussets tend to apply.

III Toroidal Field Conductors

The toroidal field coil of CDX-U consists of 128 turns, each carrying a maximum current of 2000 A DC. The maximum toroidal field at the machine centerline (R=33 cm) is, therefore, B_T=1.5 kG. All 128 turns must pass through the center stack. The TF current is limited by the motor-generator system which, additionally, has a maximum voltage output of 300 V. Parameters of the TF conductors are listed in Table 2.

Figure 11 shows the cross section of the center stack, and the arrangement of the TF conductors. In order to minimize the space occupied by the TF conductors, 1/4-inch- square, Oxygen-Free copper conductors will be utilized, with a center cooling passage 0.140 inches in diameter. These conductors will be wrapped in half-lapped fiberglass tape, overwrapped with Fusafab tape, then assembled in the arrangement shown, and bonded together by heating in a suitably-configured jig. The assembly will then be epoxy-potted inside a G-10 tube. In the final assembly process, the

[1] R. Walls, PPPL, private communication

OH solenoid and the TF conductor assembly will be placed concentrically inside the housing, and potted to bond the entire package together. It is proposed to contract with a qualified organization[2] to tape, cut, package and pot the coil assemblies. The TF conductor assembly will be roughly square, with a dimension of 3.2 inches (8.1 cm) along a side.

The existing center stack in the CDX-U device consists of an assembly of 160 TF conductors, each 1/4-inch-square. This TF system has been operated at currents up to 1600 A, and now uses only 128 of the existing 160 conductors. At the maximum current noted above, the outlet water cooling hoses from the center stack are only warm to the touch (~40 °C).

Each conductor in the new center stack will produce heat at a rate of 2.8 kW, at maximum current. The conductors will be cooled by the L-wing deionized water system at a minimum flow rate of 0.375 gpm per conductor (if flow falls below 0.75 gpm for any flow meter on the CDX-U water system, each of which monitors two cooling paths, the generator power will be interrupted). The water flow will be arranged so that the TF conductors comprise 64 loops of two conductors each. Under these worst case conditions, the maximum temperature rise of the water flowing through the conductors will be 53 °C. The inlet water temperature rarely exceeds 30 °C, meaning that the outlet temperature of the cooling water should not exceed 83 °C. Observations of the existing center stack, noted above, bear this prediction out. In the present configuration, a pressure difference of about 200 psi exists between the inlet and outlet of the cooling loop, providing a flow of 1.2 gpm, or 25 ft/sec, and yielding a temperature rise about three times smaller. This latter flow rate may be large enough to cause cavitation inside the cooling passages.[3] For the new center stack, we plan to install pressure-regulating valves on the inlets which feed the center stack toroidal field conductors, in order to reduce the flow rate to a safe level of about 15 ft/sec (0.68 gpm). Under these conditions, the temperature rise in the cooling water, at maximum coil current, would be 29 °C.

The means of connecting the 1/4-inch-square conductors to the TF coil joints is shown in Figs. 12-14 and 29. The joints allow the outer sections of the TF coils to be removed for maintenance and disassembly of the machine. The joints consist of 1/2

[2] e.g., Stonite Coil Corporation in Robbinsville, NJ or Everson Electric of Allentown, PA

[3] P. Heitzenroeder, CDX-U OH Upgrade Preliminary Design Review chit

inch wide copper blocks, 1 3/8 inches high, with two screw holes for connection to the outer section of the TF conductor. These copper blocks have a silver-plated face, and are mounted in a phenolic ring, 1/2 inch thick. The blocks are brazed to 3/32 inch thick copper flat stock which is, in turn, soft-soldered to the 1/4-inch-square conductor. Figures 12-14 show that there are four layers to the TF coil connections, each layer containing 32 conductors. The connections on one layer must be completed before work on the next layer can be started. It should be emphasized that this connection technique has worked satisfactorily on the existing CDX-U center stack, and sufficient experience has been gained that no problems are foreseen in using the same method again.

In order to prevent recurrence of the insulation damage experienced in the existing center stack, the top of the assembly will be potted with epoxy once all the connections between the 1/4-inch-square conductors and the joint blocks are made. It is intended that this potting extend to the top of the phenolic ring assembly and be somewhat domed or conical, in order to shed any spilled water away from the center stack. The top of the potting will be sealed with a silicone rubber conformal coating of the type used for sealing printed circuit boards.[4] The potting will also prevent portions of the TF conductors from moving when the OH solenoid is pulsed (see Sec. IV), and for this reason both the top and bottom ends will be potted, though only the top will be sealed. Since the currents in the toroidal field conductors are parallel, only attractive forces act between them, and these are readily supported by the potting material.

IV Ohmic Heating Solenoid

The ohmic heating solenoid is shown in Figs. 2 and 11. The dimensions of the coil are listed in Table 3. Numerical simulations of the CDX-U plasma, done with the Tokamak Simulation Code (TSC) [Jardin *et al.*, 1986], indicate that a minimum flux of 0.1 V-sec is required in order to achieve a plasma current of 100 kA from a starting current of 30 kA. This latter current can be supplied by dc helicity injection. This coil is designed to provide 0.15 V-sec of flux when operated in a double-swing mode, allowing some margin for unforeseen losses or for maintaining a short flattop at maximum plasma current.

[4]Dow Corning Conformal Coating Compound 1-2577

The coil will be a tightly-wound, single-layer solenoid, formed of 1/2-inch-square OF copper conductor with an internal water cooling passage 1/4 inch in diameter. The coil conductor will be a single piece of copper, to avoid brazes in the interior of the coil which would soften it. Bus connections will be made at the top of the center stack, and a split copper tube 3/16 inch thick will carry the return current to the top of the center stack again (see Figs. 2,12,13,25, and 26). The coil will be powered by a capacitor-bank supply capable of providing the required 47 kA (with a maximum voltage of 1000 V.), assumed to be a sinusoidal form with a period of 60 ms. Over-voltage protection at a maximum of 2000 V. will be provided on the OH power supply. There should be a 50% margin in tensile stress in the coil conductor, before the recommended operating limit of two-thirds of the yield strength is reached. The margin is intended to allow for possible stress concentrations at the ends of the coil, and other contingencies.[5] The maximum OH current creates a tensile stress of 7,800 psi, requiring a yield strength of at least 17,500 psi. Of the two tempers available in the necessary length, fully-hardened copper conductor was chosen, with a yield strength of 35,000 psi.

The return current from the OH solenoid would be carried through the center stack along a copper sheet, which is depicted in Figs. 25 and 26. This sheet will be slotted along its length to ensure that current flows predominantly in the vertical direction and, therefore, does not create any non-axisymmetric error fields. Each vertical leg in the return conductor will have a resistance equal to that of its neighbors, ensuring that equal currents flow in each leg. The sheet will be rolled into a cylindrical shape, and will be potted into the center stack assembly just inside the solenoid and just outside the TF conductor bundle (with appropriate insulation from each). It is intended that the return conductor be attached to the ground side of the OH power supply which, among other things, will minimize its propensity to arc to the TF circuit. Tabs extending from each end of the return conductor will be bent to form contact surfaces at the phenolic ring where all attachments will be made (see Fig. 9).

Fabrication of the OH solenoid would be contracted either separately or together with the assembly of the TF conductor array. The OH conductor would be wrapped before winding with two layers of half-lapped mylar tape. Additional insulation would be provided by winding the coil onto a mandrel which had previously been wrapped with resin- impregnated fiberglass cloth to a thickness of 3/16 inch. After the resin

[5] upon the advice of Y-K. M. Peng of Oak Ridge National Laboratory

cured, a lathe cut would be taken across its surface to provide a cylindrical form upon which to wind the coil. The conductor would then be brushed with epoxy during winding in order to bond it to the fiberglas layer. A similar fiberglass and resin outer jacket would be applied, and another lathe cut would be taken to provide a uniform exterior to the assembly. This technique should ensure a well-insulated and rigid solenoid.

To take up the tension at the ends of the solenoid, insulated clamps which secure the conductor will be affixed to the end flanges of the housing. These clamps are depicted in Figs. 17 and 18; the faces of the clamping shoes will be knurled to better grasp the conductor. The tension, at peak current, is 1560 lbs.

The electrical and water cooling connections to the solenoid are depicted in Fig. 9. The water connection is provided at the end of the conductor, and beyond the clamps mentioned above. It will be recessed into the phenolic housing in order to avoid protruding beyond the 9 1/2 inch OD, which is required so that the top and bottom plates of the vessel can be mounted and dismounted. The electrical connection consists of a block soldered to the solenoid just before the clamping arrangement. This block will have a contact area of about 2.5 square inches (16 cm^2), its surface will be silver plated, and the attaching conductor will be mounted with a force of 1000 psi to ensure good electrical contact and low joint resistance.

Assuming a maximum OH coil current of 47 kA, and a discharge duration of 30 msec, then the total energy dissipated in the solenoid during one pulse is 328 kJ (79 kcal). This will raise the temperature of the coil by 21 °C. Given reasonable water flow rates, it would be possible to remove this quantity of heat in about 120 seconds, which is an acceptable interval between shots.

The return conductor will, in one shot, rise in temperature by no more than 0.25 °C. This temperature rise is quite modest, and so the return conductor will only be cooled passively by transfer of heat to other components. The tabs at each end, which serve as electrical contacts, provide about 4 square inches of contact area. These surfaces will, as with the solenoid contacts, be silver plated, and the contacting conductors will be tightened to 1000 psi contact pressure.

The OH coil produces forces on a number of components of the center stack, including itself. As noted above, the tendency of the OH coil to expand when current flows causes a tensile stress of 7,800 psi in the conductor, a value which can be

adequately supported by the conductor itself.

The magnetic field from the OH coil will exert some force on the toroidal field conductors when they are near the center stack. A simple computer calculation (see Appendix 2) indicates that the total force will be less than 200 N (44 lbs.). Most of this force is borne at the inside ends. This force can be sustained by the existing TF coil connectors and supports.

Acknowledgments

The authors would like to thank the members of the CDX-U New Center Stack Design Review Committee, P. Heitzenroeder, P. Bonanos, C. Bushnell, L. Dudek, R. Parsells, and R. Walls, for their helpful suggestions and advice for improving the design and for manufacturing critical components. The authors thank P. DePeter for checking the drawings, and especially W. Choe for many hours of work in producing many of the necessary drawings.

This work was supported by U. S. Department of Energy contract No. DE-AC02-76- CHO-3073.

PPPL-TM-396 Tables

Table 1: Center Stack Housing Parameters

Tube outside diameter	6.875 inches (17.5 cm)
Tube wall thickness	0.062 inch (1.6 mm)
Tube length	42.0 inches (107 cm)
End flange outside diameter	9.5 inches (24.1 cm)
End flange thickness	0.25 inch (6 mm)
Sealing flange outside diameter	14 inches (35.6 cm)
Sealing flange thickness	0.375 inch (1.0 cm)
Separation between sealing flanges	35.375 inches (90.0 cm)
Gusset size	3.0 $\times$ 4.0 inches (7.6 $\times$ 10.0 cm)
Stiffening tube thickness	0.125 inch (3.2 mm)
Stiffening tube length	8 inches (20.3 cm)
Stiffening tube outside diameter	7.125 inches (18.1 cm)

Table 2: Toroidal Field Conductor Parameters

Number of Conductors	128
Conductor size	0.250 $\times$ 0.250 inch (6 $\times$ 6 mm)
Average length of conductor	49.25 inches (125 cm)
Cross sectional area of conductor	0.047 square inch (0.30 square cm)
Single conductor resistance	0.69 mΩ

Table 3: Ohmic Heating Solenoid Parameters

Solenoid Radius	2.94 inches (7.5 cm)
Number of Turns	76
Height	42 inches (106.7 cm)
Conductor Size	0.50×0.50 inch (1.3×1.3 cm)
Cross sectional area of conductor	0.201 square inch (1.30 square cm)
Length of Conductor	116.9 feet (35.6 m)
Resistance of solenoid	4.88 mΩ
Inductance of solenoid	113 μH
L/R time of solenoid	23.2 msec

Appendix: Supporting Calculations for OH System

Tensile stress in OH solenoid conductor

Tensile stress in solenoid wall due to magnetic pressure:

$$\sigma = \frac{P_{mag} r}{t}$$

where:

σ = tensile stress
P_{mag} = Magnetic pressure = $\frac{B^2}{2\mu_o}$
r = mean solenoid radius = 0.0746 m
t = effective solenoid conductor thickness = A/w = 0.0102 m
(A is conductor cross-sectional area, w is width of square conductor).

The OH solenoid is designed to provide a maximum of 0.150 $V \cdot s$. The magnetic flux change for a double swing transformer is $\Phi = 2B_{max}\pi r^2$. The pressure may then be written in terms of the flux swing:

$$P_{mag} = \frac{\Phi^2}{8\pi^2 \mu_o r^4},$$

so that the maximum tensile stress in the solenoid conductor is:

$$\sigma_{max} = \frac{\Phi^2}{8\pi^2 \mu_o r^3 t}.$$

Substituting values into the formula:

$$\begin{aligned} \sigma_{max} &= \frac{(0.150\ V \cdot s)^2}{8\pi^2 (4\pi \times 10^{-7})(0.0746\ m)^3 (0.0102\ m)} \\ &= 53.6\ MPa \\ &= 7,770\ psi. \end{aligned}$$

A good safety margin allowing for concentrated stresses in the solenoid is 50% below a standard maximum working stress of two-thirds of the conductor yield strength. The conductor selected for the OH solenoid has a yield strength of 35,000 psi, so that a safe maximum stress would be 15,550 psi. The maximum expected stress of 7,770 psi is well below this value.

The magnetic field of a solenoid is: $B_{sol} = \frac{\mu_o N I}{h}$, where:

N = number of turns in solenoid = 76
I = solenoid current
h = solenoid height = 1.067 m.

Combining this with the expression for Φ yields an expression for the maximum current in the solenoid:

$$I_{max} = \frac{\Phi h}{2\pi \mu_o r^2 N}.$$

Substituting values into the formula:

$$\begin{aligned} I_{max} &= \frac{(0.150\ V \cdot s)(1.067\ m)}{2\pi(4\pi \times 10^{-7})(0.0746\ m)^2(76\ turns)} \\ &= 47,930\ Amps. \end{aligned}$$

The load sustained by the end clamps due to tension in the solenoid is:

$$F = \sigma_{max} A$$

where:

$\sigma_{max} = 7,770$ psi = 53.6 MPa
A = cross-sectional area of conductor = 0.2009 sq. in. = 1.296 cm^2.

Substituting values into the formula:

$$\begin{aligned} F &= (53.6 \times 10^6\ Pa)(1.296 \times 10^{-4}\ m^2) \\ &= 6,940\ N \\ &= 1560\ lbs. \end{aligned}$$

Stress on solenoid end clamp assembly bolts

1. Stress on end clamp shoe bolts

There will be six 1/4-28 bolts holding the clamping shoes together, each of which may be tightened to a yield strength of 36,000 psi. The total force from each bolt is then:

$$F = \sigma A$$

where:

F = total force of the bolt
σ = final tightened bolt stress = $36,000$ psi
A = thread root area of the bolt = 0.0364 sq. in.

Substituting values:

$$\begin{aligned} F &= (36,000\ psi)(0.0364\ sq.\ in.) \\ &= 1310\ lbs/bolt. \end{aligned}$$

For the six bolts holding the clamping shoes together, this will result in 7,860 lbs. of clamping force, which with knurled faces shoud be sufficient to hold the 1560 lbs. of pull from the conductor.

2. Frictional force holding end clamp brace

There will be six 1/4-28 bolts holding the brace to the housing flange. If bolts are torqued to yield point, there will be again be a force of 7,860 lbs. The coefficient of friction for clean steel on steel is $\mu = 0.58$ (CRC Handbook of Chem. & Phys., 61st ed.), so that the brace will not slip with a pull of:

$$F_{max.pull} = \mu F_{\perp} = (0.58)(7860\ lbs.) = 4560\ lbs.,$$

which is more than the calculated maximum of 3120 lbs. This means there should be no shear forces on the bolts holding the clamp brace.

Temperature Rise in Center TF Conductors

There are two center TF conductors in each cooling path, for a total power dissipation of $P = I^2R$ where:

$$\begin{aligned} R &= \frac{\rho L}{A} \\ &= \frac{(1.724 \times 10^{-6}\ \Omega \cdot cm)(244\ cm)}{(0.304\ cm^2)} \\ &= 1.38 \times 10^{-3}\ \Omega, \end{aligned}$$

so that:

$$P = (2000\ A)^2(1.38 \times 10^{-3}\ \Omega) = 5530\ W$$

for two conductors. Then the temperature rise of the cooling water is:

$$\Delta T = \frac{P}{fC_p}$$

where:

P = ohmic power dissipated as heat
f = minimum cooling water flow = $0.375\ \frac{gal}{min} = 25.0\ g/s$
$C_p = 4.18 \frac{J}{g \cdot {}^\circ C}$.

Substituting values:

$$\begin{aligned} \Delta T &= \frac{(5530\ W)}{(25.0\ \frac{g}{s})(4.18\ \frac{J}{g \cdot {}^\circ C})} \\ &= 53\ {}^\circ C. \end{aligned}$$

Since incoming cooling water does not tend to rise above 30 $^\circ C$, this means cooling water should not rise above 83 $^\circ C$.

Temperature Rise in OH Conductors

1. Temperature Rise in Solenoid Conductor

$$\Delta T = \frac{P_{avg} t}{M C_p}$$

where:

t = period of sinusoidal OH current pulse = 0.06 sec
M = mass of solenoid conductor = $\rho_m LA$ = 41.2 kg
C_p = specific heat of copper = 0.38 $\frac{J}{g \cdot {}^\circ C}$
P_{avg} = average power during sinusoidal pulse = $\frac{I_{max}^2 R}{2}$
$R = \frac{\rho L}{A}$.

Substituting values:

$$\begin{aligned}
R &= \frac{(1.724 \times 10^{-6}\ \Omega \cdot cm)(3560\ cm)}{1.296\ cm^2} \\
&= 4.74 \times 10^{-3}\ \Omega \\
P_{avg} &= \frac{(48000\ A)^2 (4.74 \times 10^{-3}\ \Omega)}{2} \\
&= 5.46\ MW \\
\Delta T &= \frac{(5.46 \times 10^6\ W)(0.06\ sec)}{(41.2 \times 10^3\ g)(0.38\ \frac{J}{g \cdot {}^\circ C})} \\
&= 21\ {}^\circ C.
\end{aligned}$$

2. Temperature Rise in Return Conductor

$$\begin{aligned}
M &= \rho_m LA = (8.92\ g/cm^3)(113.7\ cm)(11.89\ cm^2) \\
&= 12.1\ kg \\
R &= \frac{(1.724 \times 10^{-6}\ \Omega)(113.7\ cm)}{(11.89\ cm^2)} \\
&= 1.65 \times 10^{-5}\ \Omega \\
P_{avg} &= \frac{(48000\ A)^2 (1.65 \times 10^{-5})}{2} \\
&= 19.1 kW
\end{aligned}$$

$$\begin{aligned}\Delta T &= \frac{(19.1 \times 10^3\ W)(0.06\ sec)}{(12.1 \times 10^3\ g)(0.38\ \frac{J}{g \cdot {}^\circ C})} \\ &= 0.25\ {}^\circ C.\end{aligned}$$

$\vec{J} \times \vec{B_{OH}}$ Forces on TF Conductors

Force per unit length is $\vec{I} \times \vec{B} = I_{TF} B_{ZOH}$. The lowest TF coil (in the strongest B_{OH} field) is at $Z = 63.4$ cm and runs from $R = 13$ cm to 77 cm. Below is a tabulation of B_{ZOH} at $Z = 63.4$ cm due to the OH solenoid and PF coil currents during an OH pulse at maximum flux swing. These values were calculated using the Green's function for the Grad-Shafranov equation, and are consistent with values calculated by Mr. Charles Bushnell of PPPL due solely to the solenoid.

$R(cm)$	$B_{ZOH}(T)$
1	0.748
5	0.652
9	0.479
13	0.320
17	0.217
21	0.160
25	0.127
29	0.103
33	0.078
37	0.051
41	0.025
45	0.005
49	-0.006
53	-0.011
57	-0.013
61	-0.013
65	-0.012
69	-0.011
73	-0.010
77	-0.009

From the table, a conservative estimate of B_{ZOH} falloff is that it is linear with radius, falling to zero at 45 cm. Therefore, take:

$$\begin{aligned}(B_{ZOH})_{avg} &= \frac{1}{2}(B_{ZOH}(13\ cm) + (B_{ZOH}(45\ cm)) \\ &= \frac{1}{2}(0.320 - 0.005)\ T \\ &= 0.158\ T.\end{aligned}$$

For each TF conductor:

$$\begin{aligned}F &= I_{TF}(B_{ZOH})_{avg}L \\ &= (2000\ A)(0.158\ T)(0.32\ m) \\ &= 101\ N \\ &= 23\ lbs.\end{aligned}$$

This can easily be supported by the two 10-24 bolts connecting each TF conductor to the phenolic section of the center stack.

PPPL-TM-396 Figures

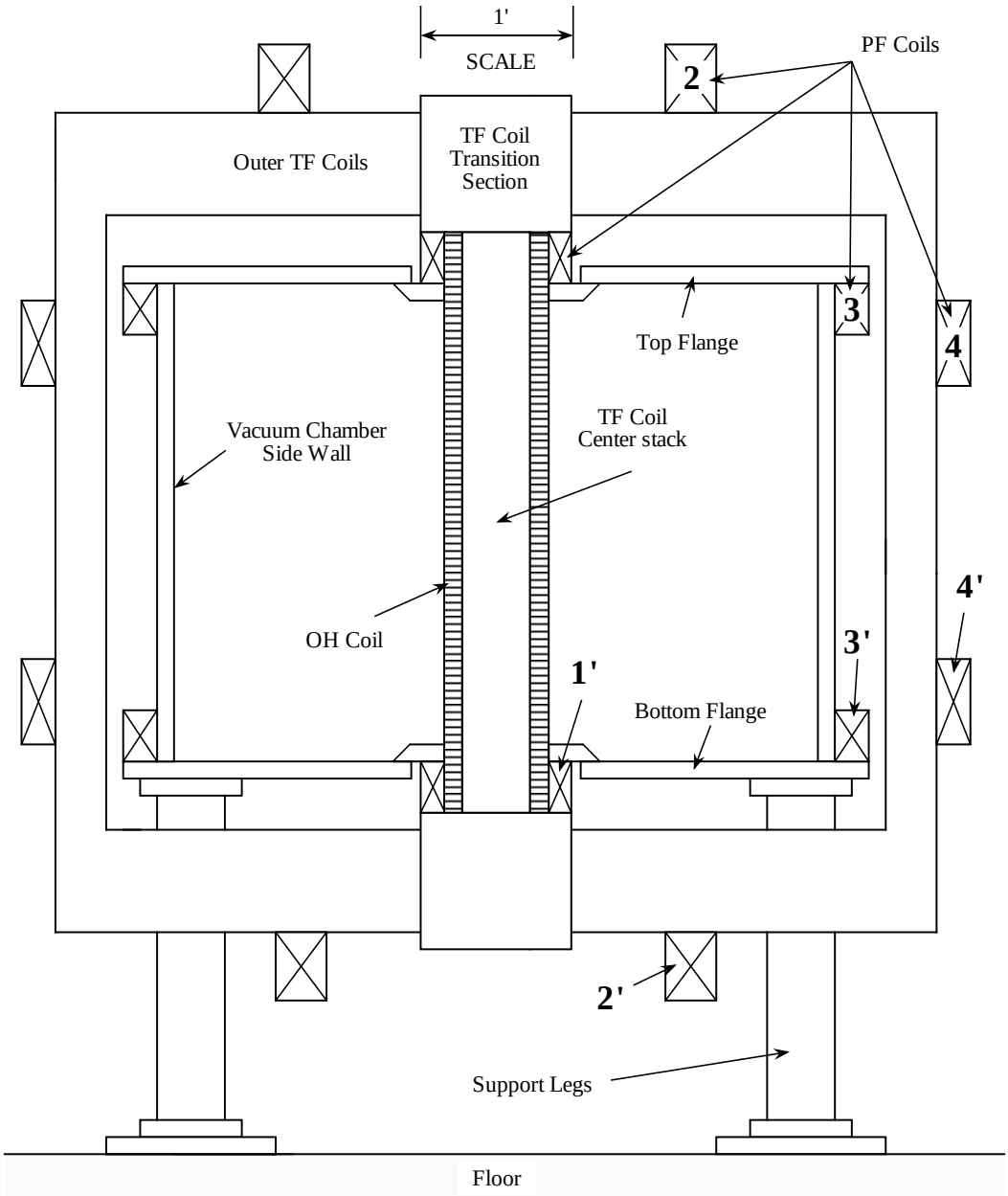

Figure A.1. Cross section of CDX-U device (Dwg. D-CCL100-1)

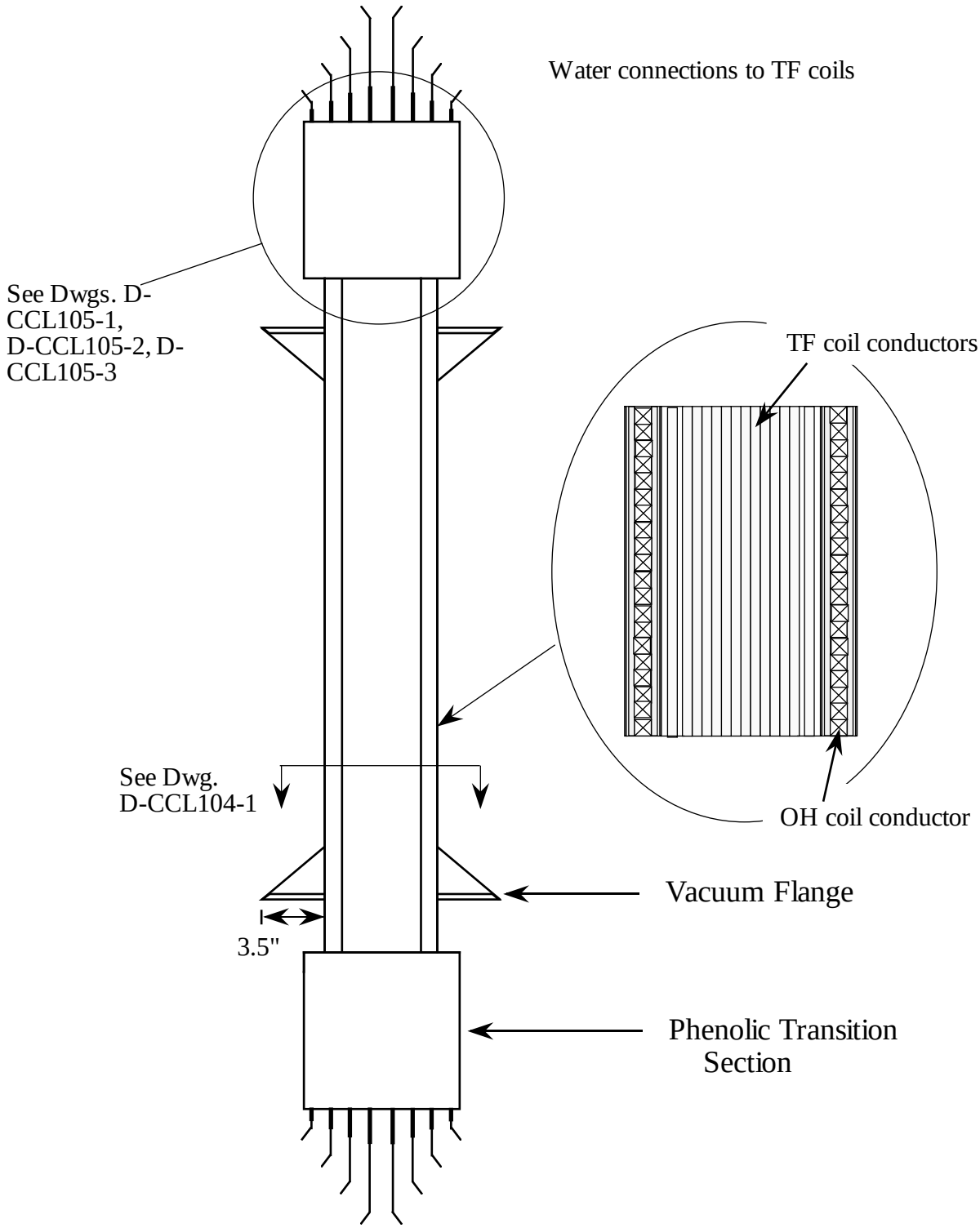

Figure A.2. Vertical Cross section of OH Center Stack (Dwg. D-CCL100-2)

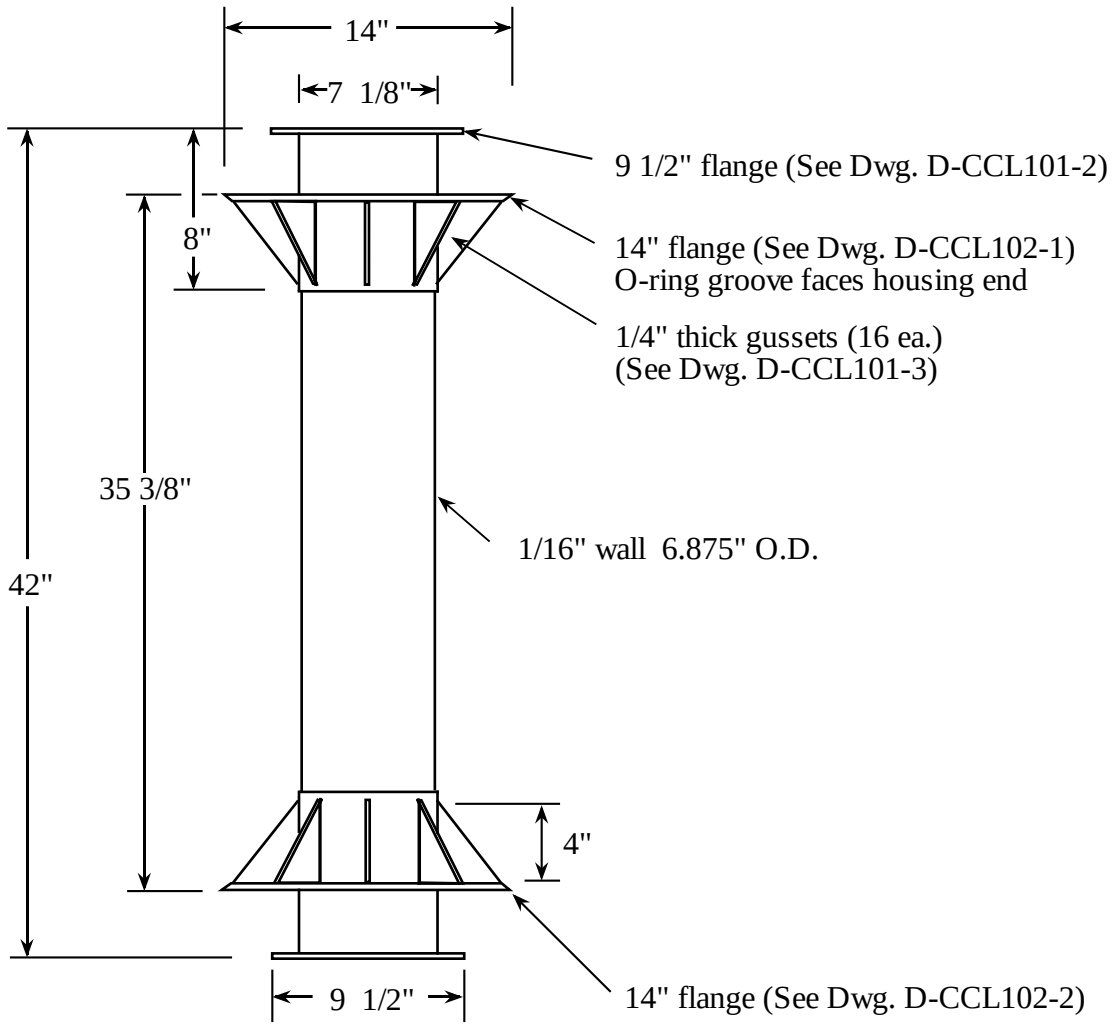

Notes)

i) All material is Inconel 625.

ii) All joints are to be brazed, including vacuum seal between 1/8" thick reinforcing collars at ends and 1/16" main tube.

Figure A.3. Center Stack Housing (Dwg. D-CCL101-1)

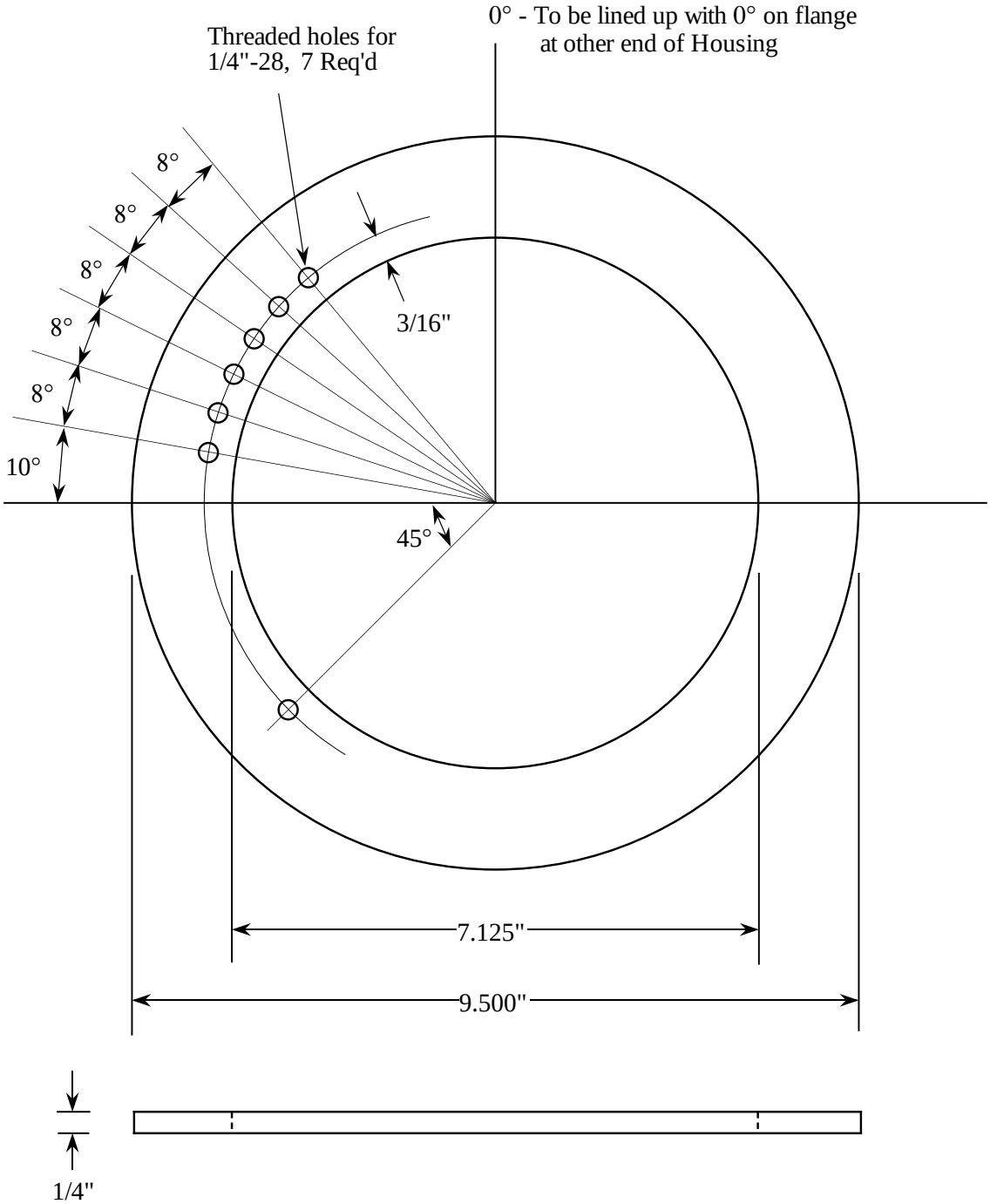

Material : 304 S.S.

Figure A.4. 9 1/2" Flange (Dwg. D-CCL101-2)

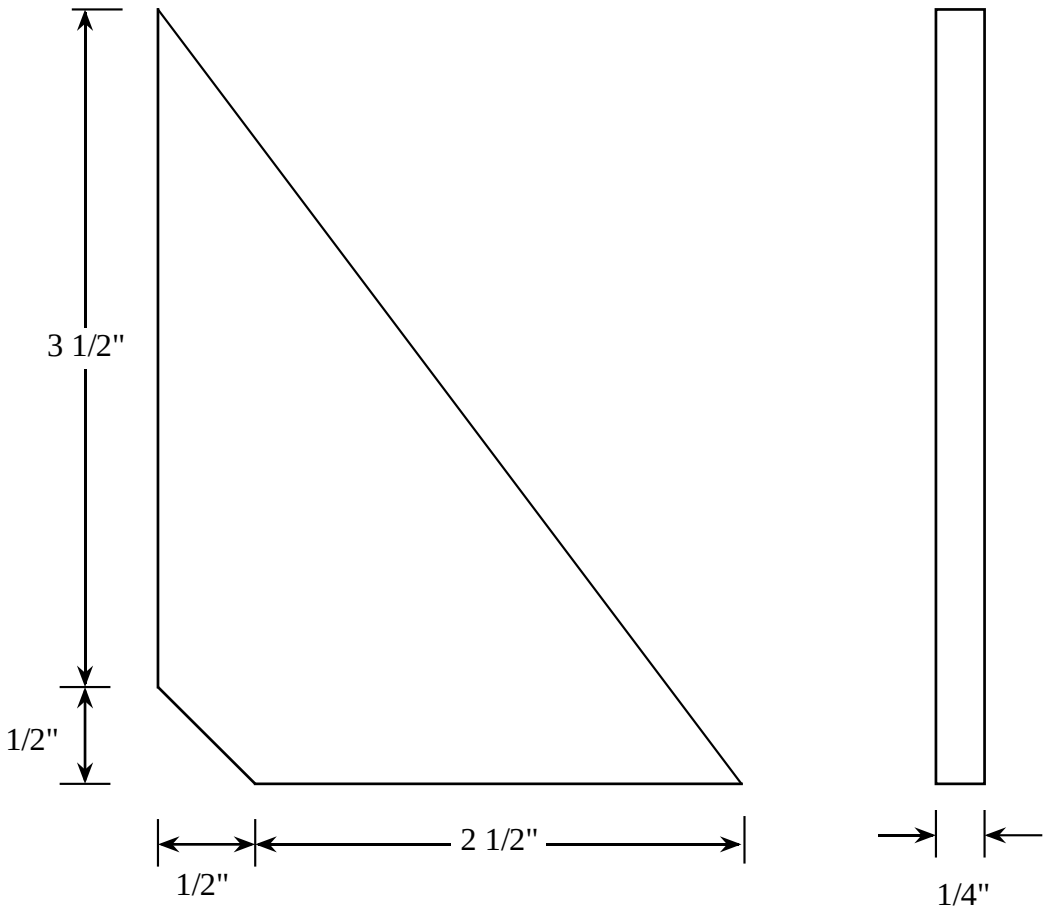

Material : Inconel 625, 16 Req'd

Figure A.5. Housing Gusset (Dwg. D-CCL101-3)

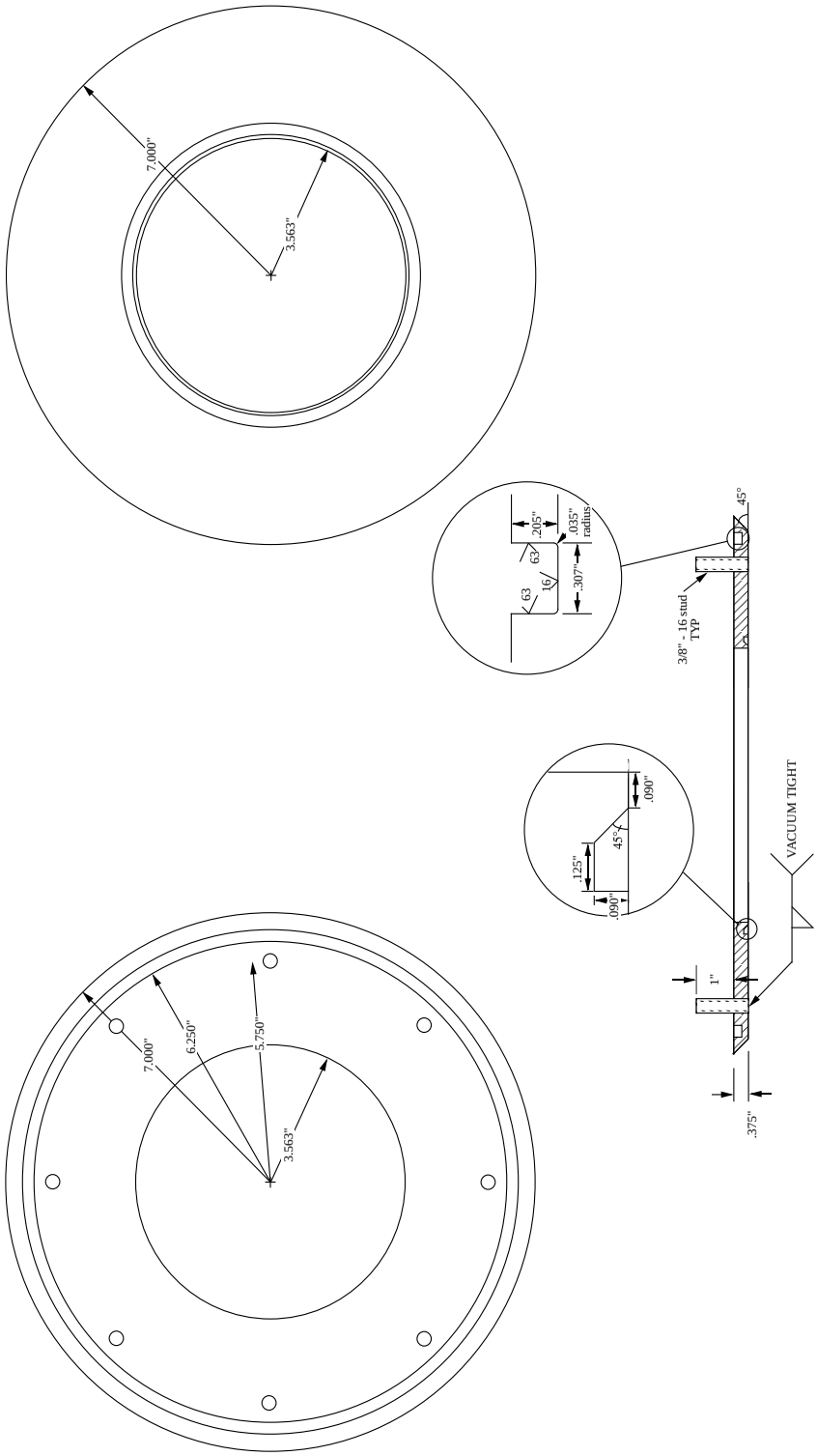

Figure A.6. 14" Flange with O-ring (Dwg. D-CCL102-1)

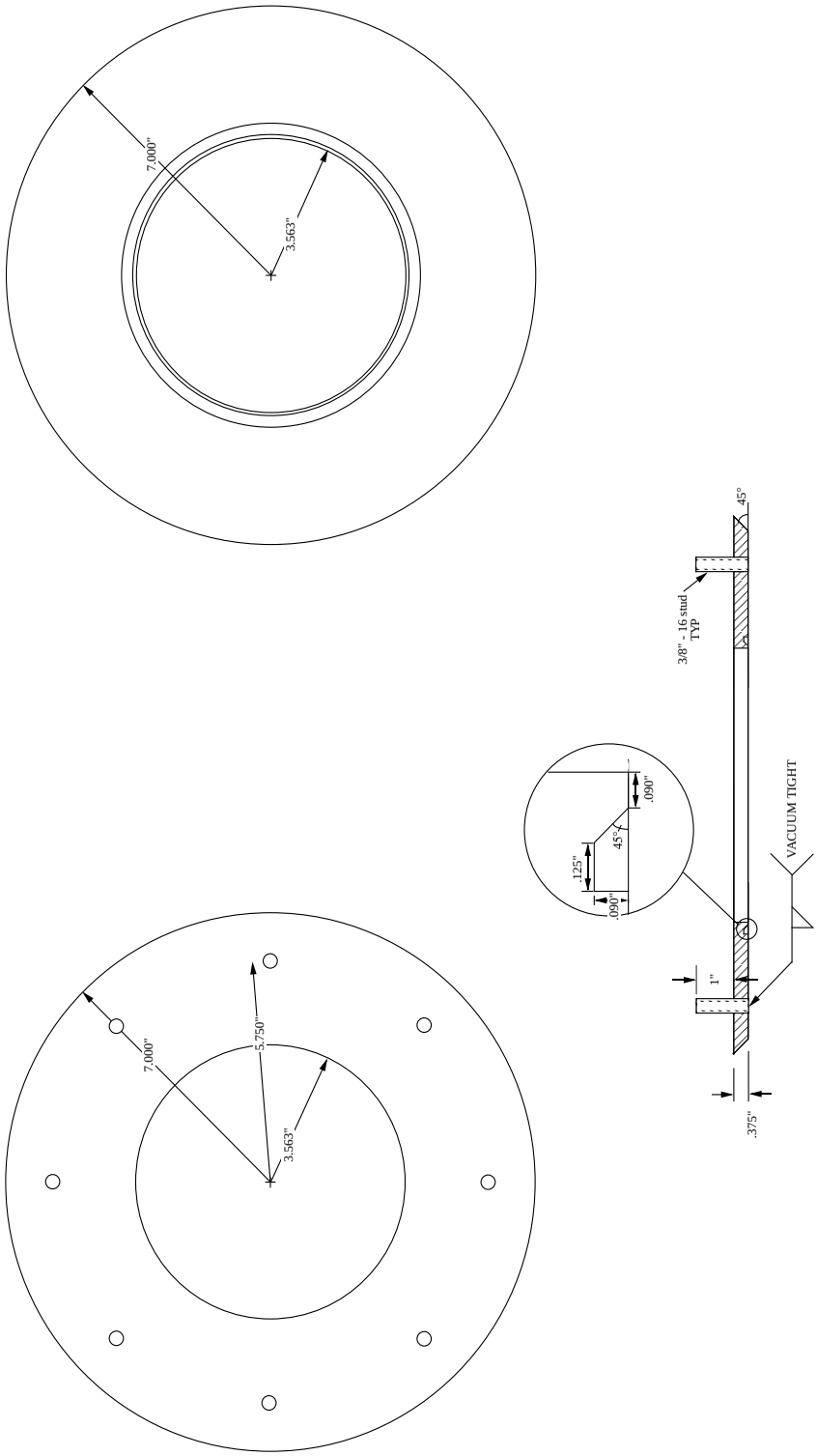

Figure A.7. 14" Flange without O-ring (Dwg. D-CCL102-2)

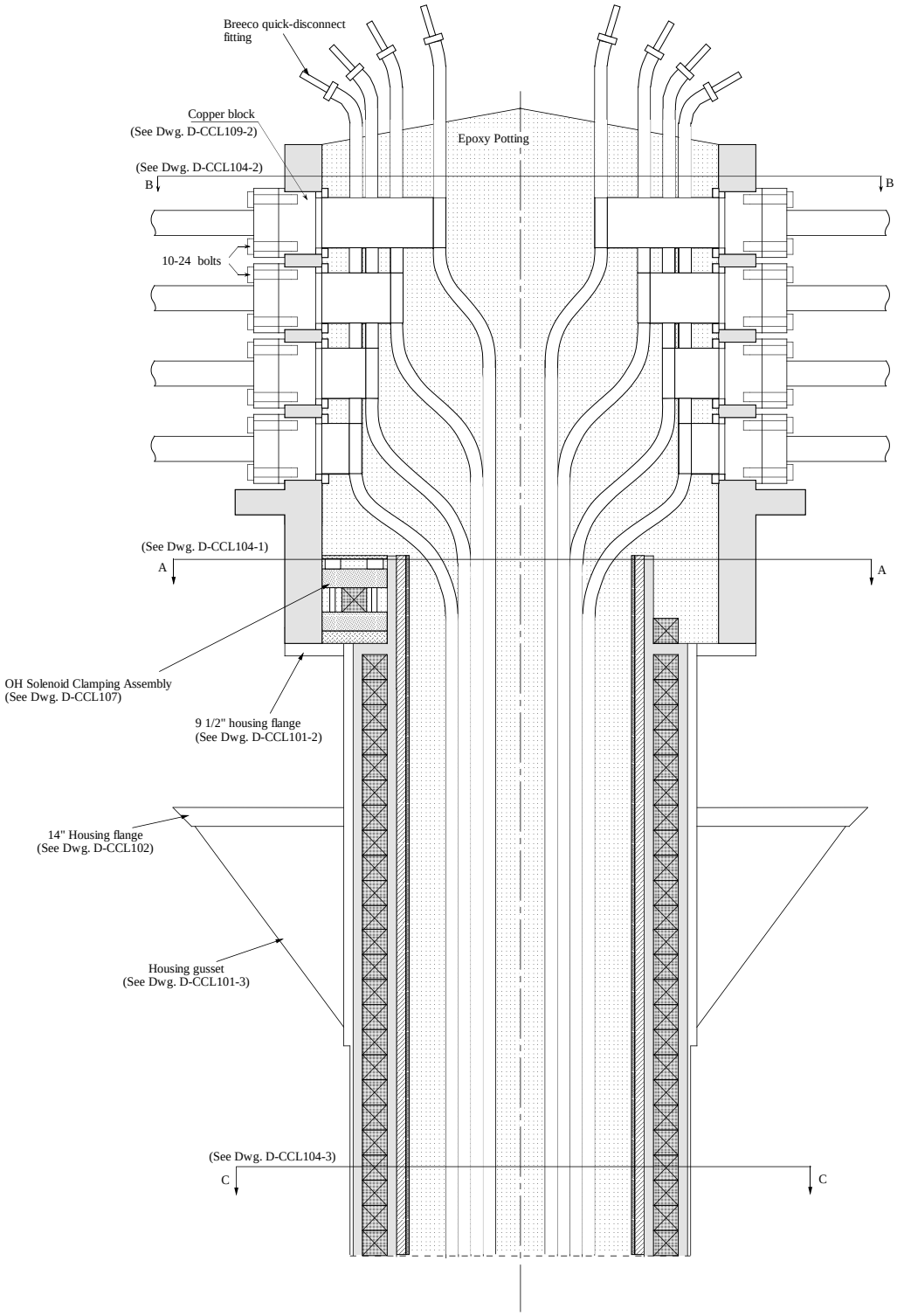

Figure A.8. Full size Assembly Section (Dwg. D-CCL103)

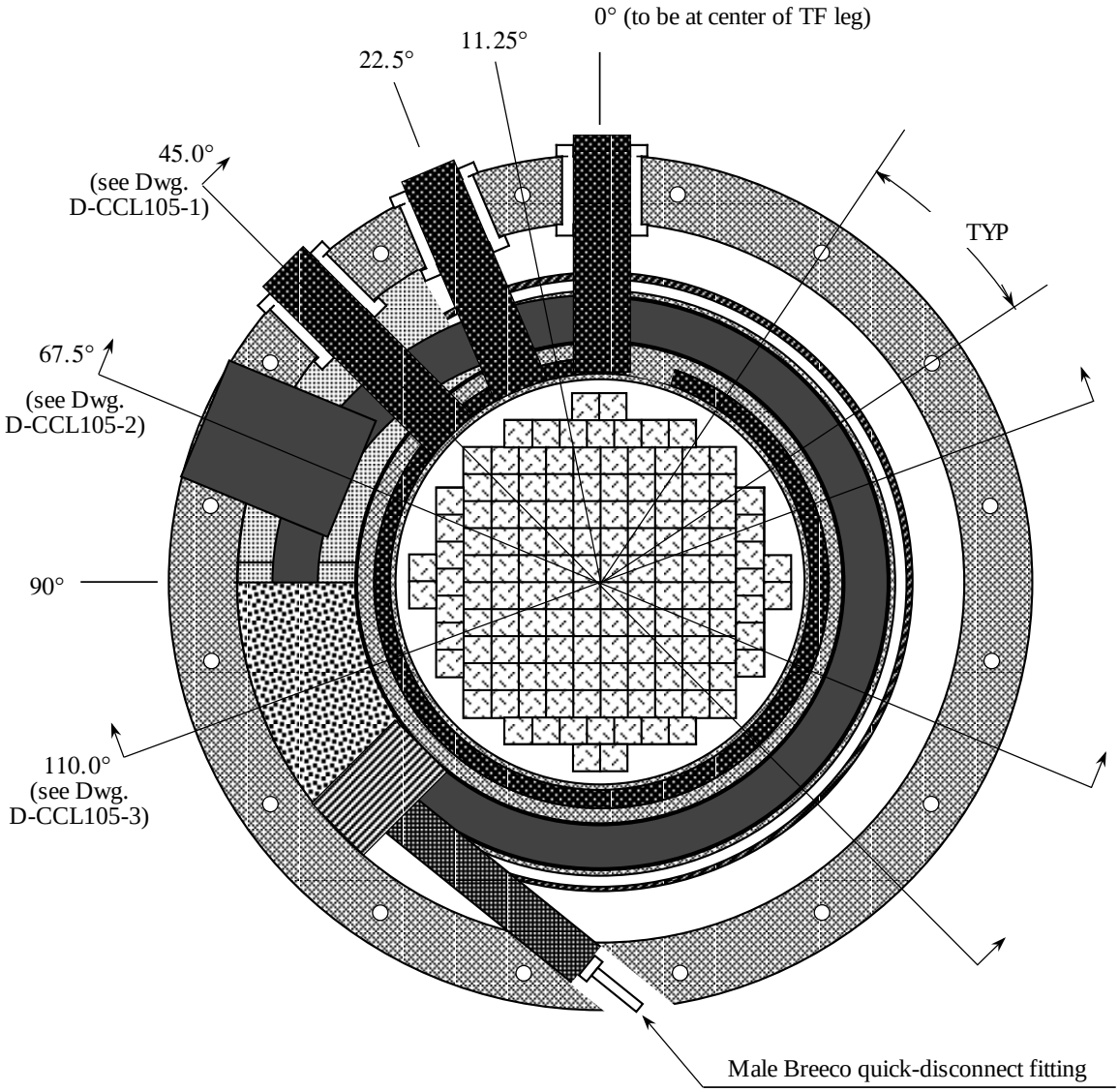

Figure A.9. Horizontal Cross section of Top of OH Center Stack, Showing OH Connections (Dwg. D-CCL104-1)

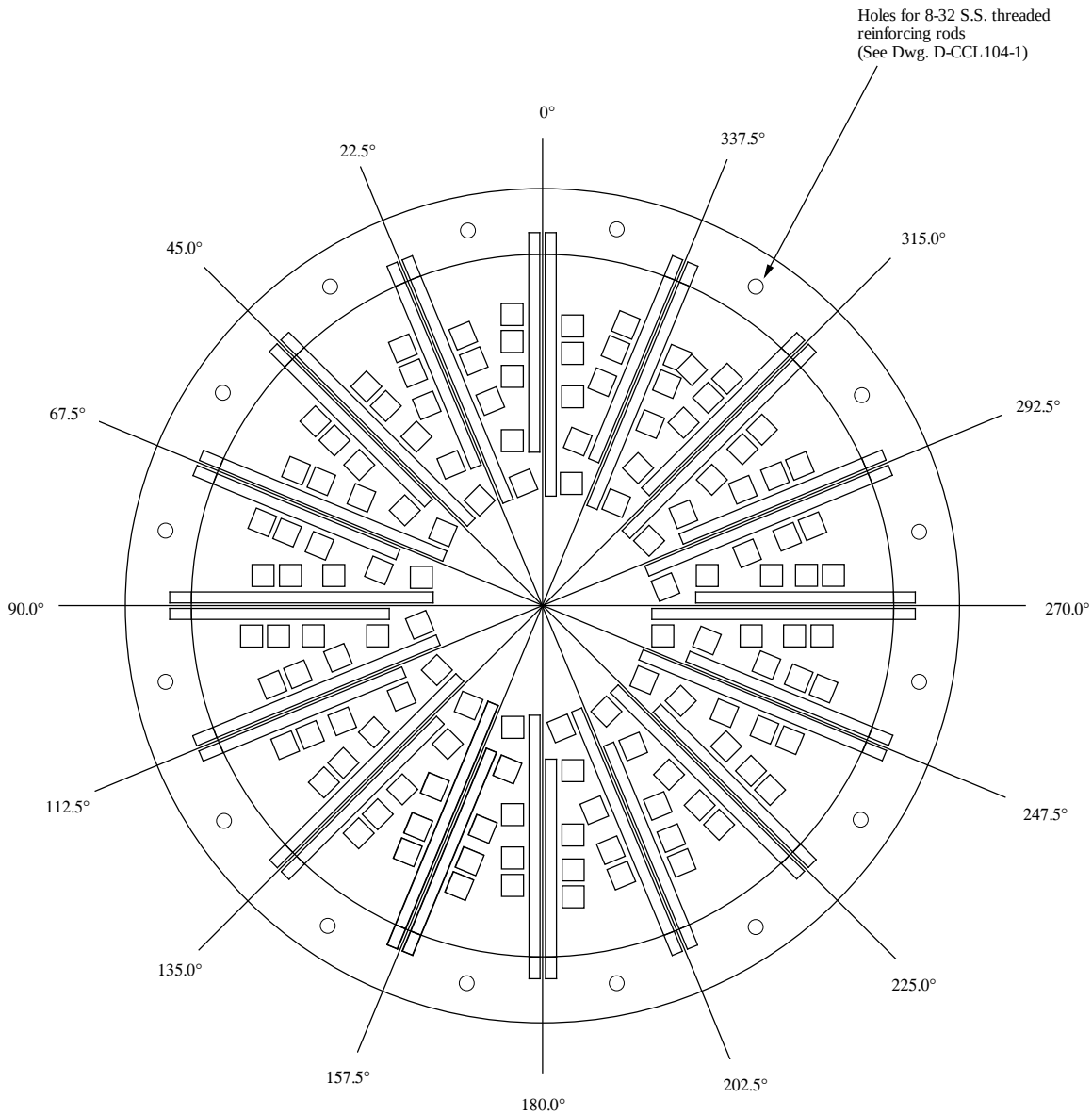

Figure A.10. Horizontal Cross section of Top of OH Center Stack, Showing TF Connections (Dwg. D-CCL104-2)

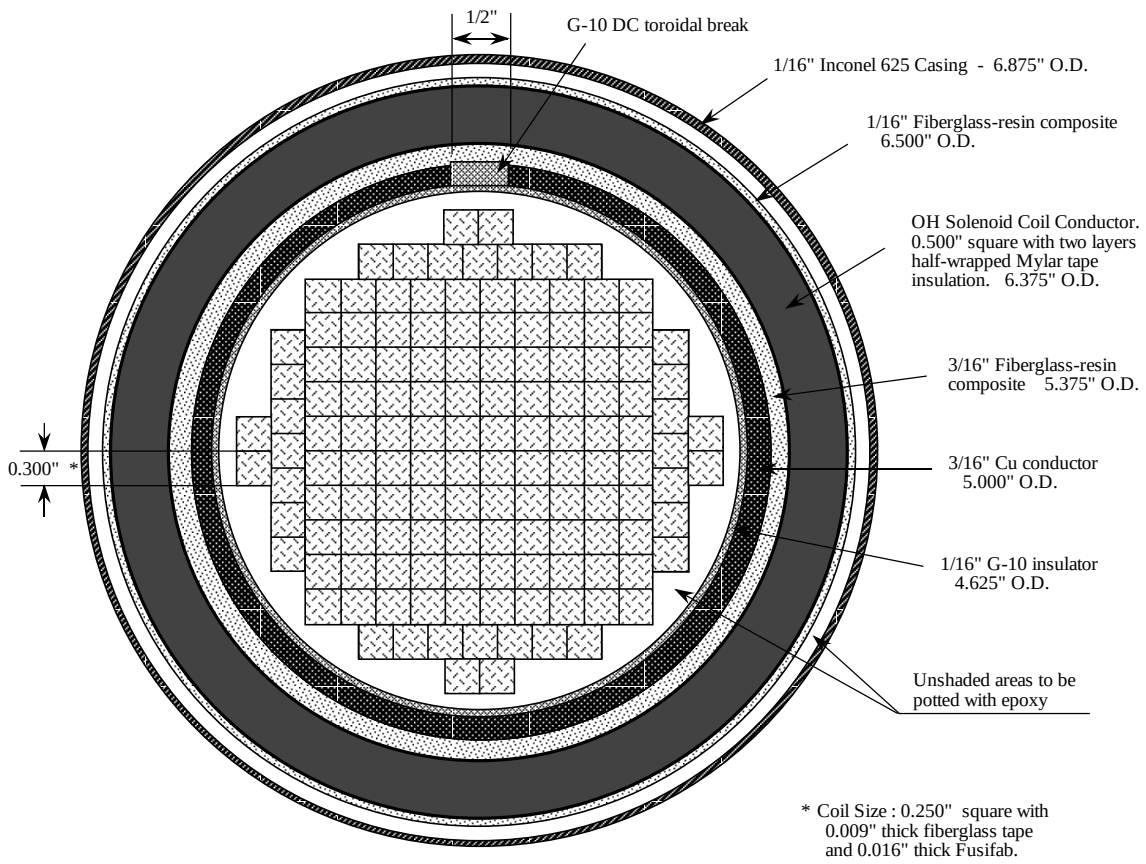

Figure A.11. Horizontal Cross section of OH Center Stack (Dwg. D-CCL104-3)

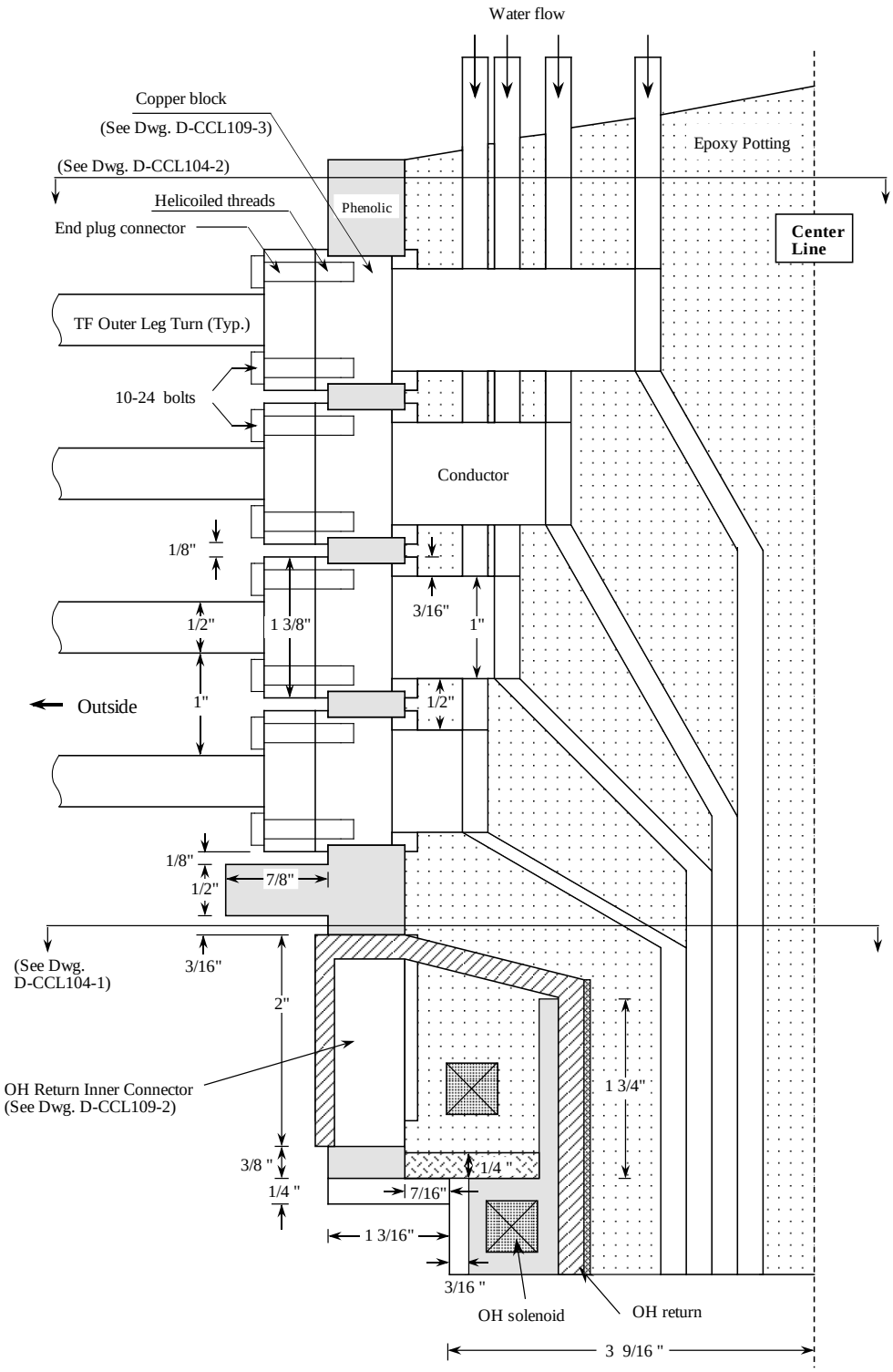

Figure A.12. Vertical Cross section of Top of OH Center Stack-45° (Dwg. D-CCL105-1)

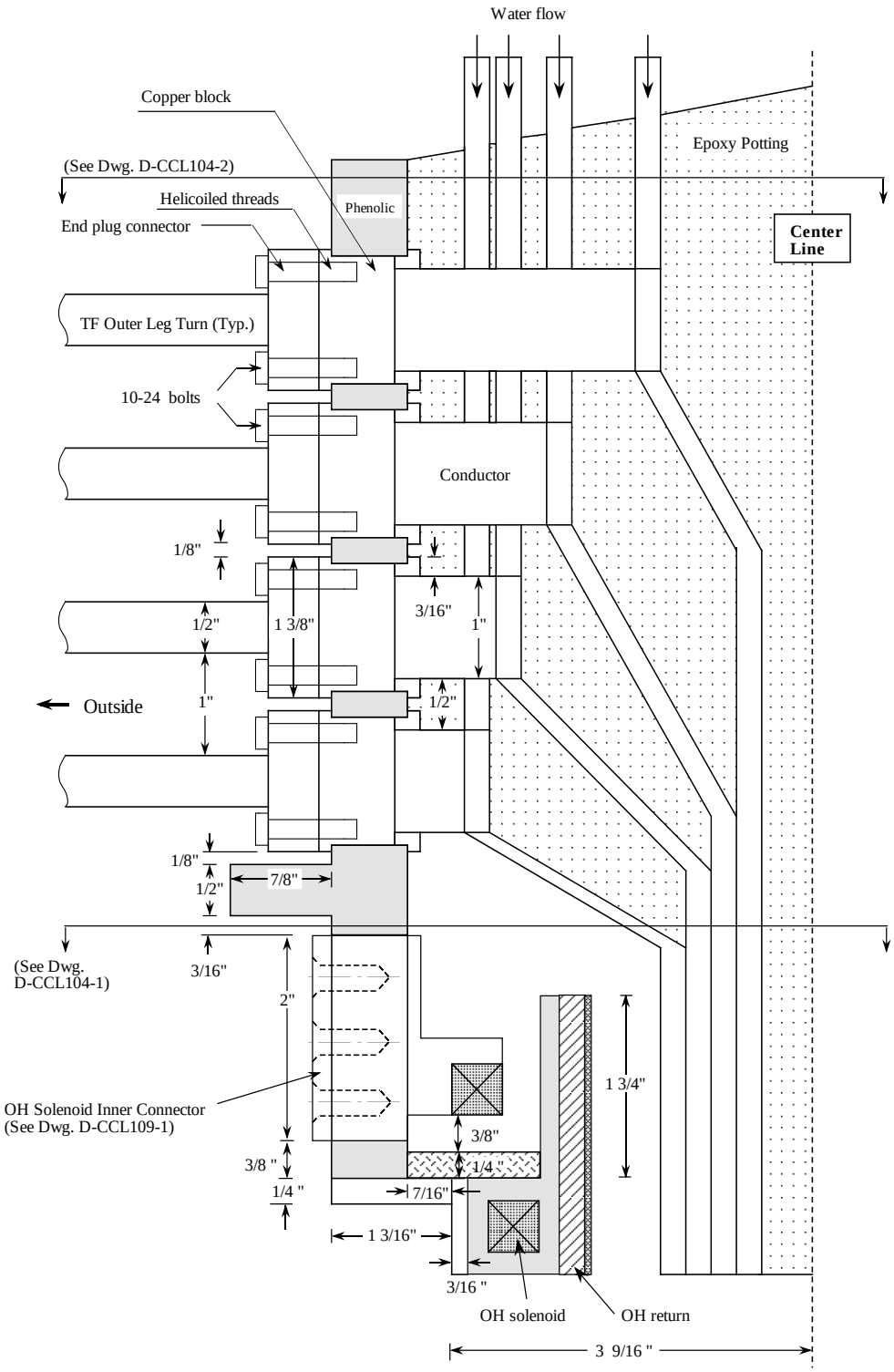

Figure A.13. Vertical Cross section of Top of OH Center Stack-68° (Dwg. D-CCL105-2)

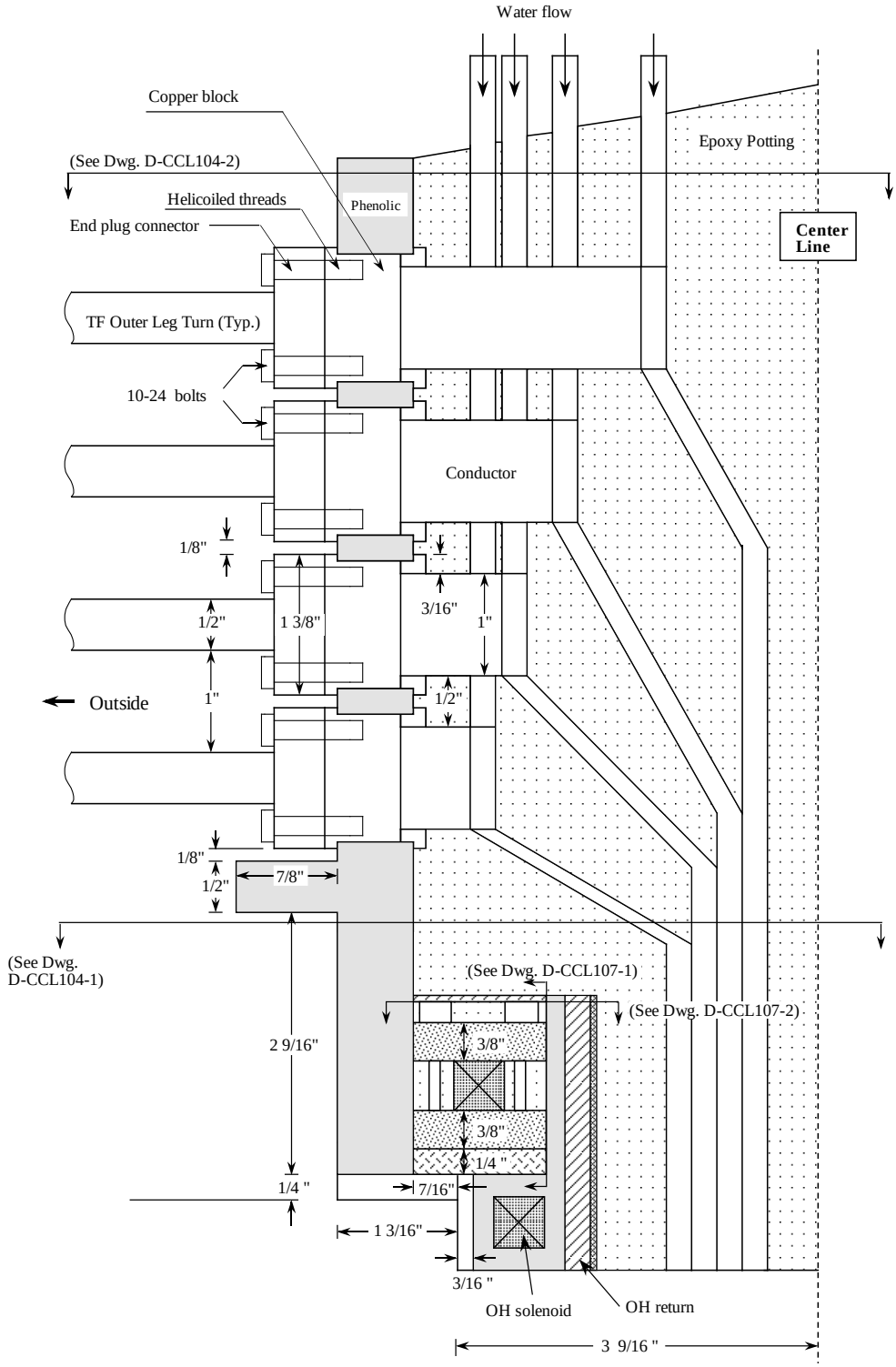

Figure A.14. Vertical Cross section of Top of OH Center Stack-110° (Dwg. D-CCL105-3)

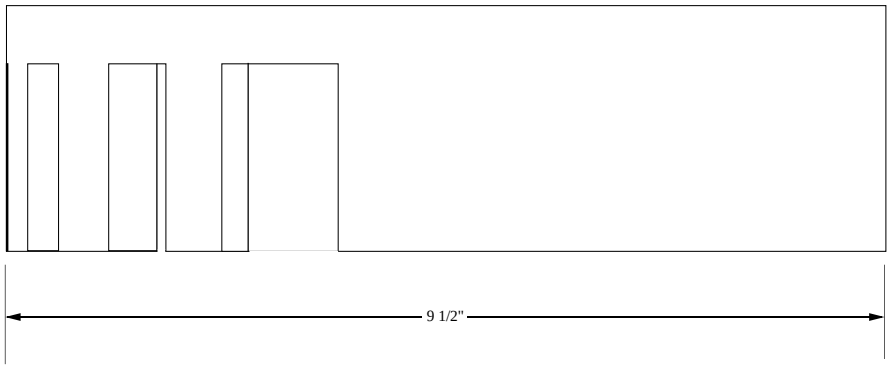

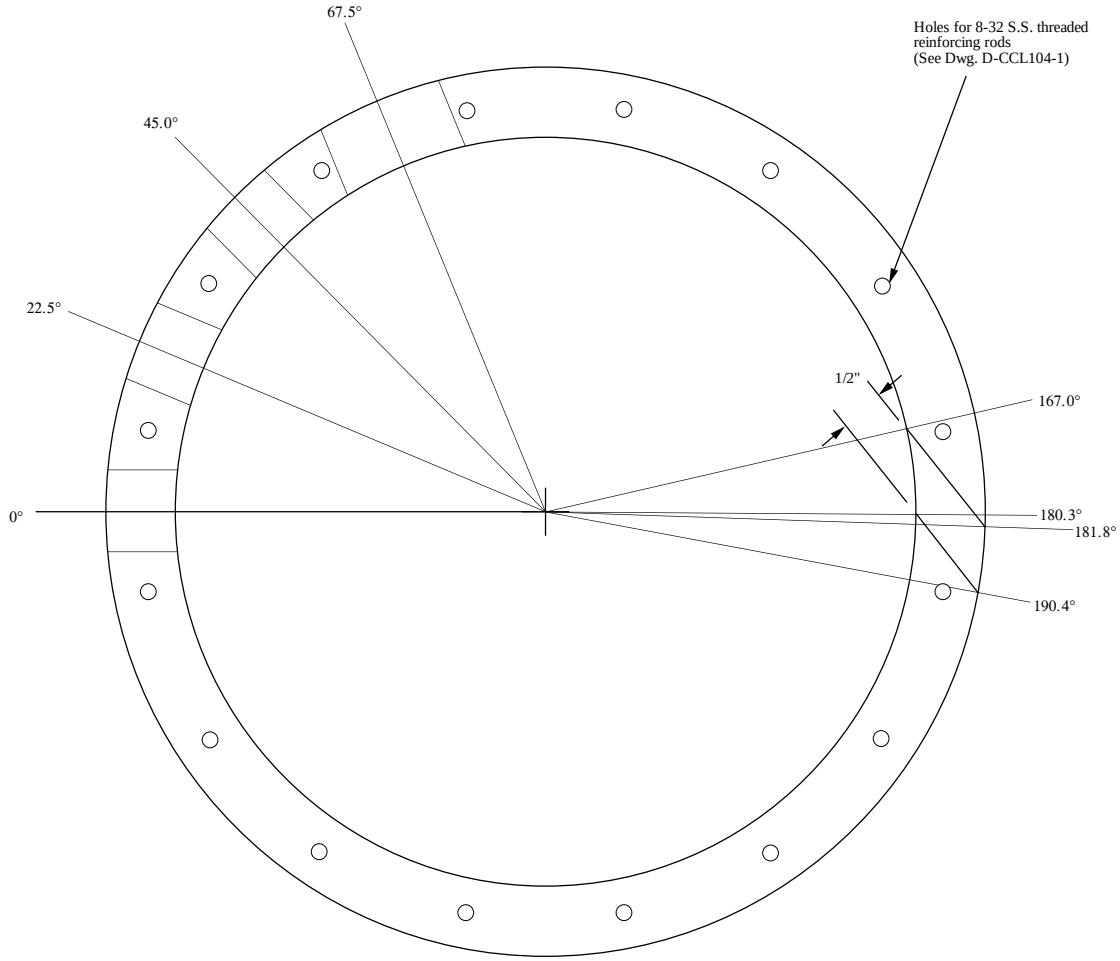

Figure A.15. Phenolic Casing - Layer 6 (Dwg. D-CCL106-1)

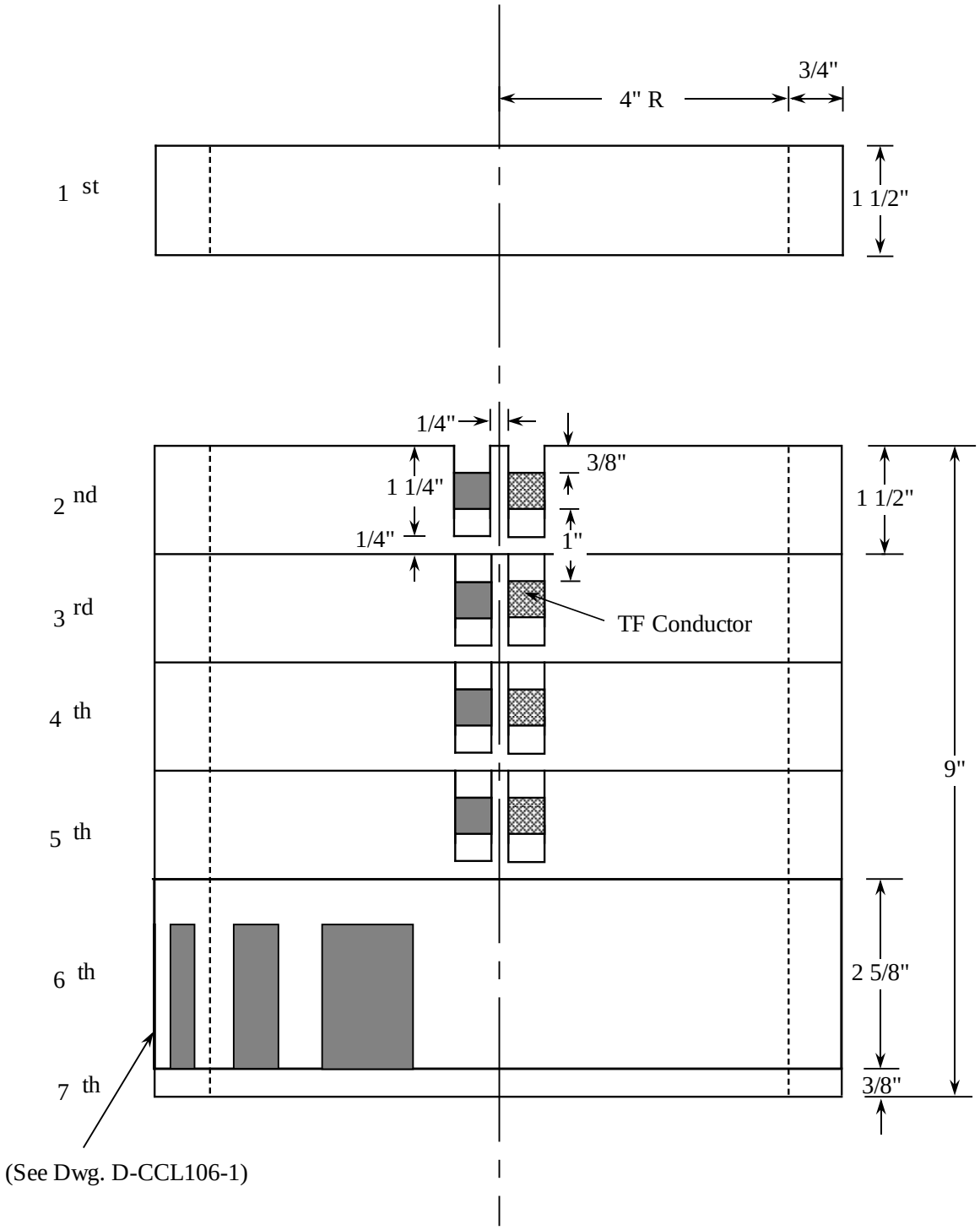

Figure A.16. Phenolic Casing (Dwg. D-CCL106-2)

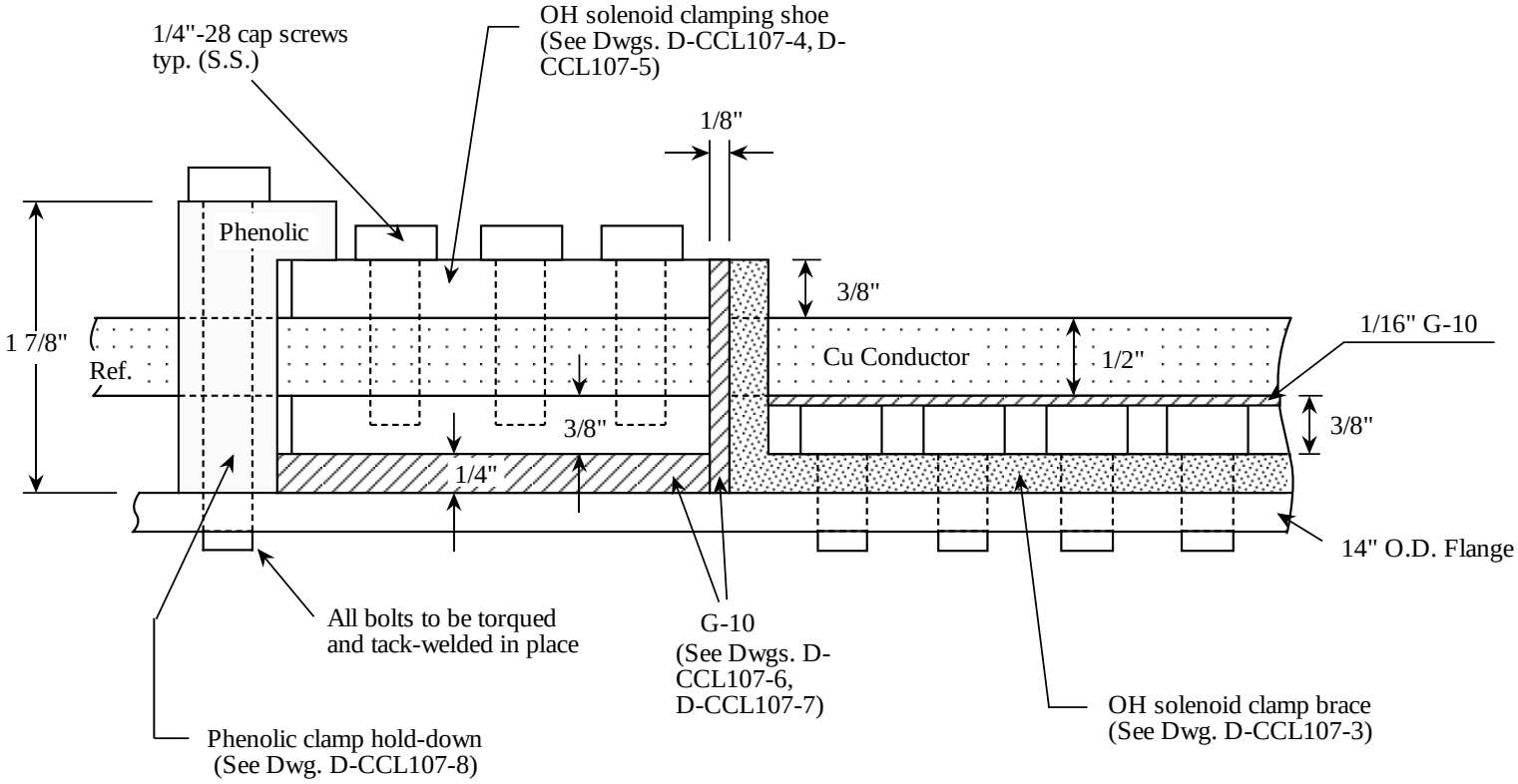

Figure A.17. OH Solenoid Clamp (Side View) (Dwg. D-CCL107-1)

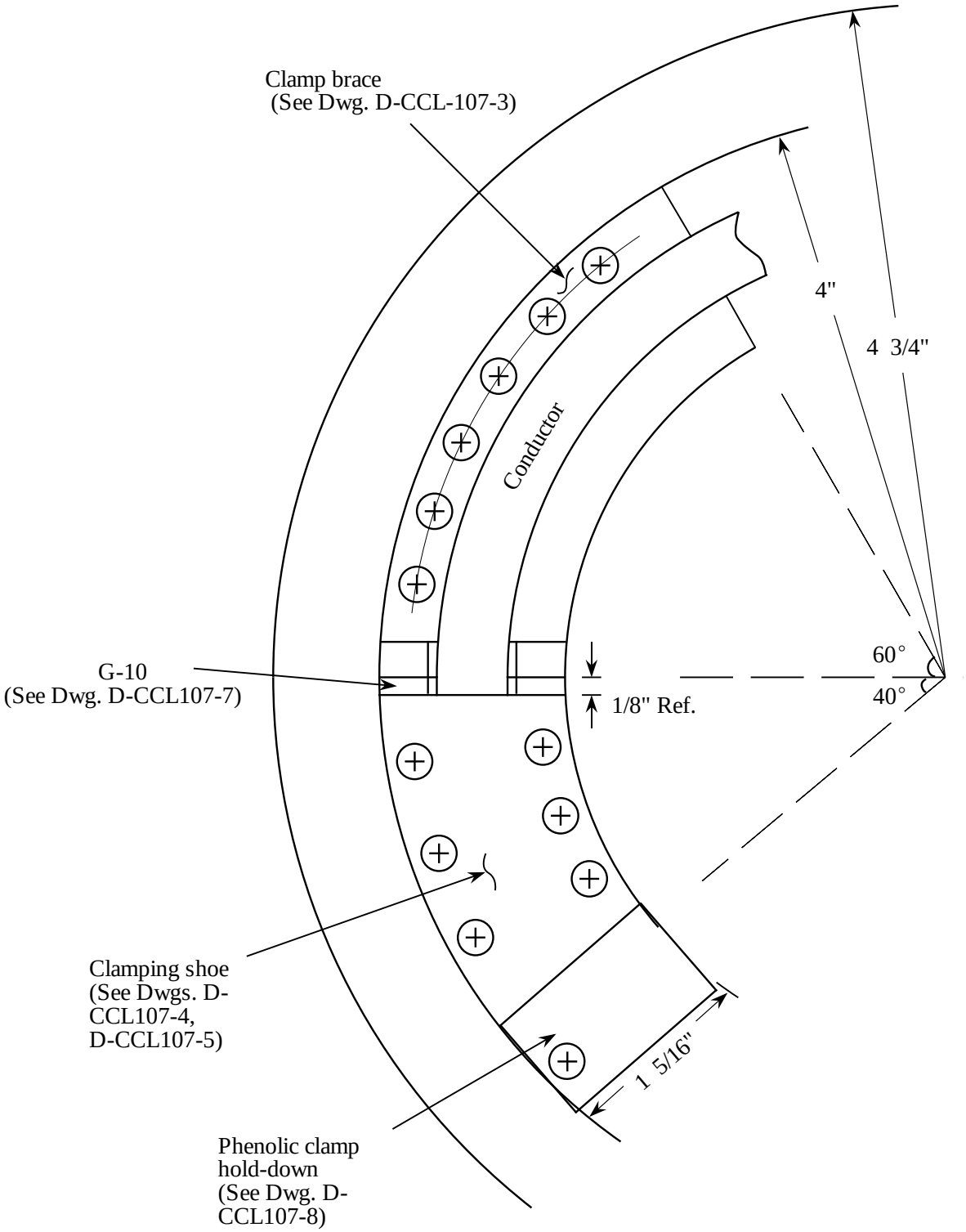

Figure A.18. OH Solenoid Clamp (Top View) (Dwg. D-CCL107-2)

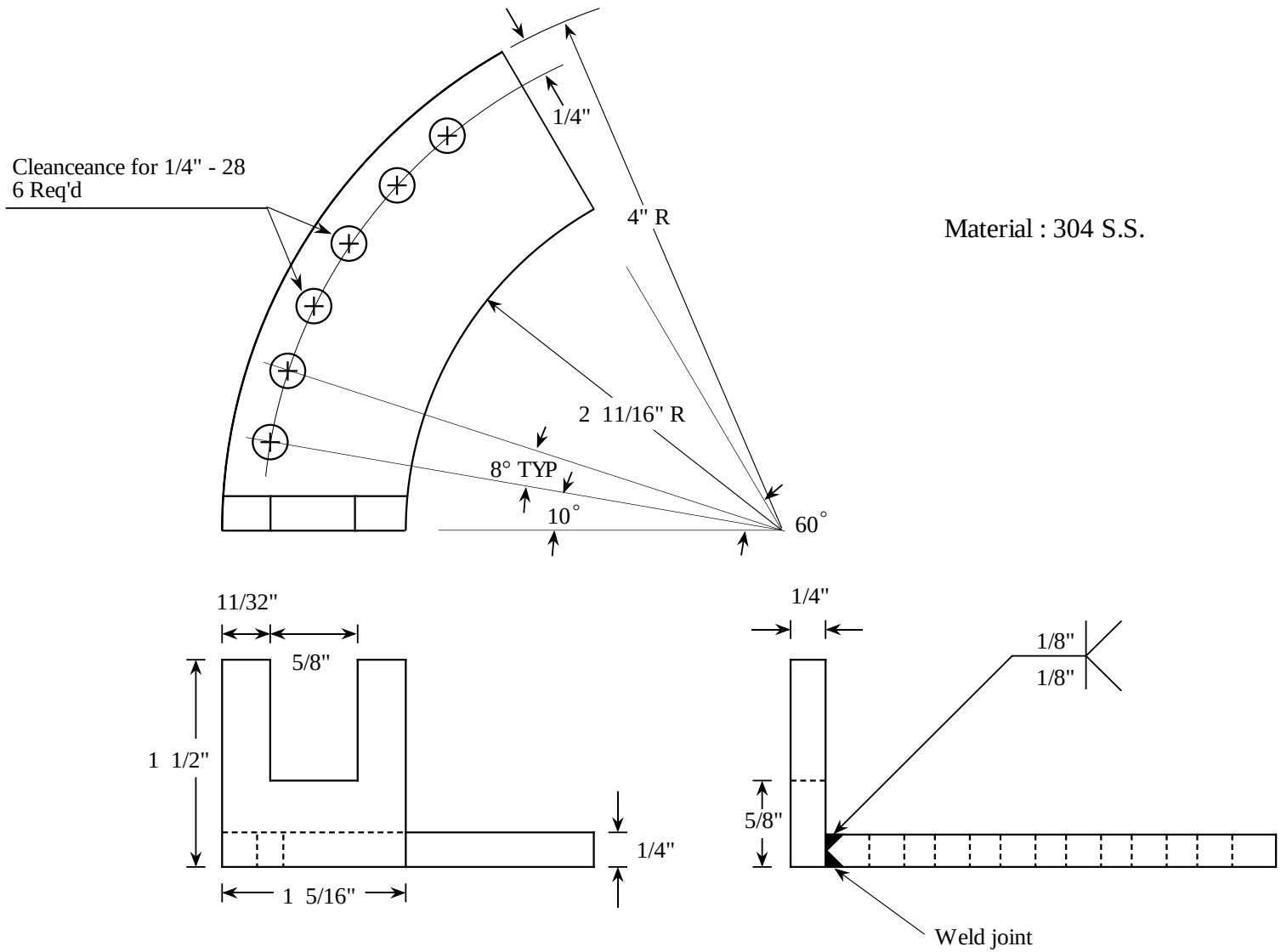

Figure A.19. OH Solenoid Clamp Brace (Dwg. D-CCL107-3)

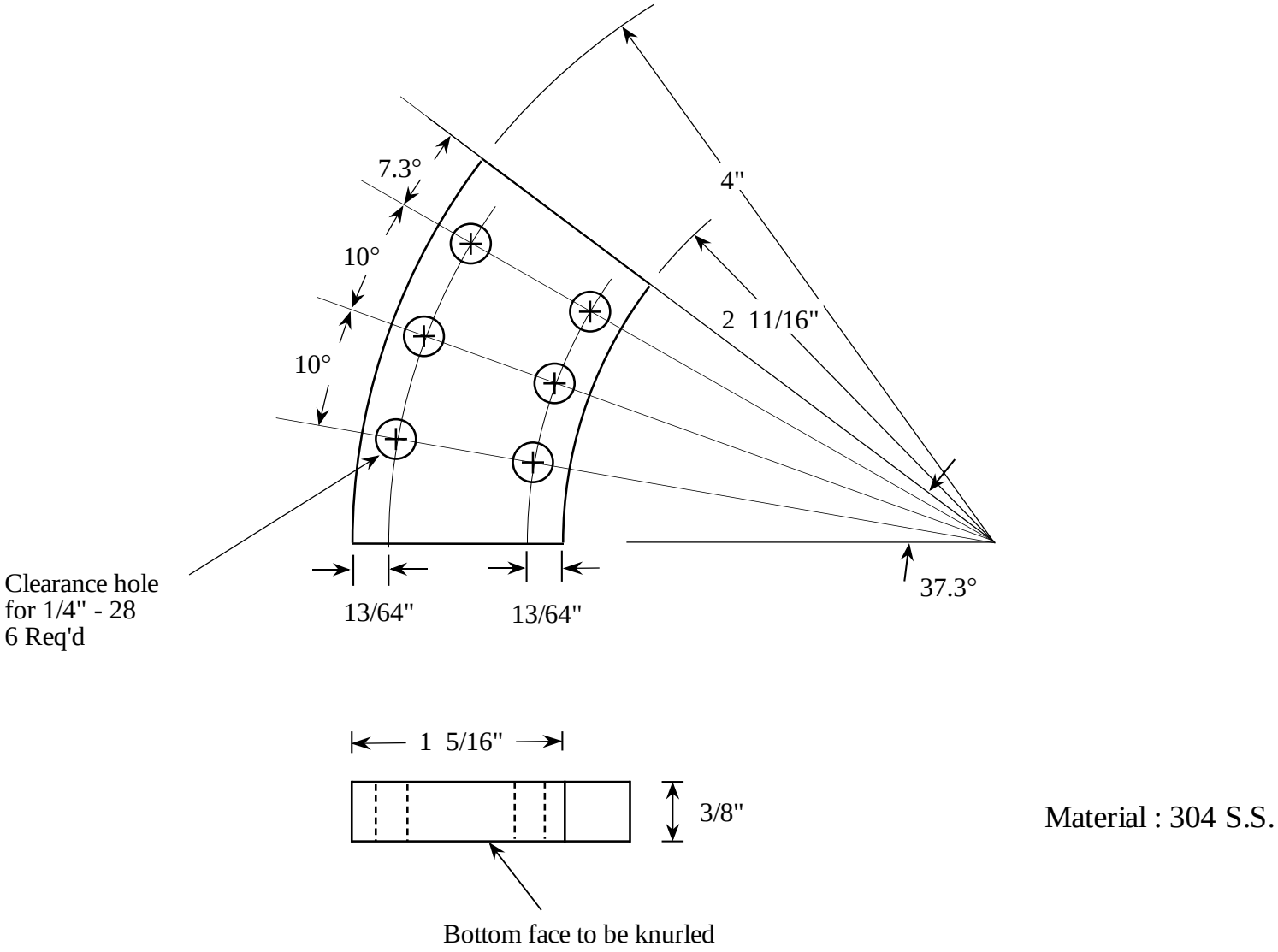

Figure A.20. OH Solenoid Clamping Shoe (Top) (Dwg. D-CCL107-4)

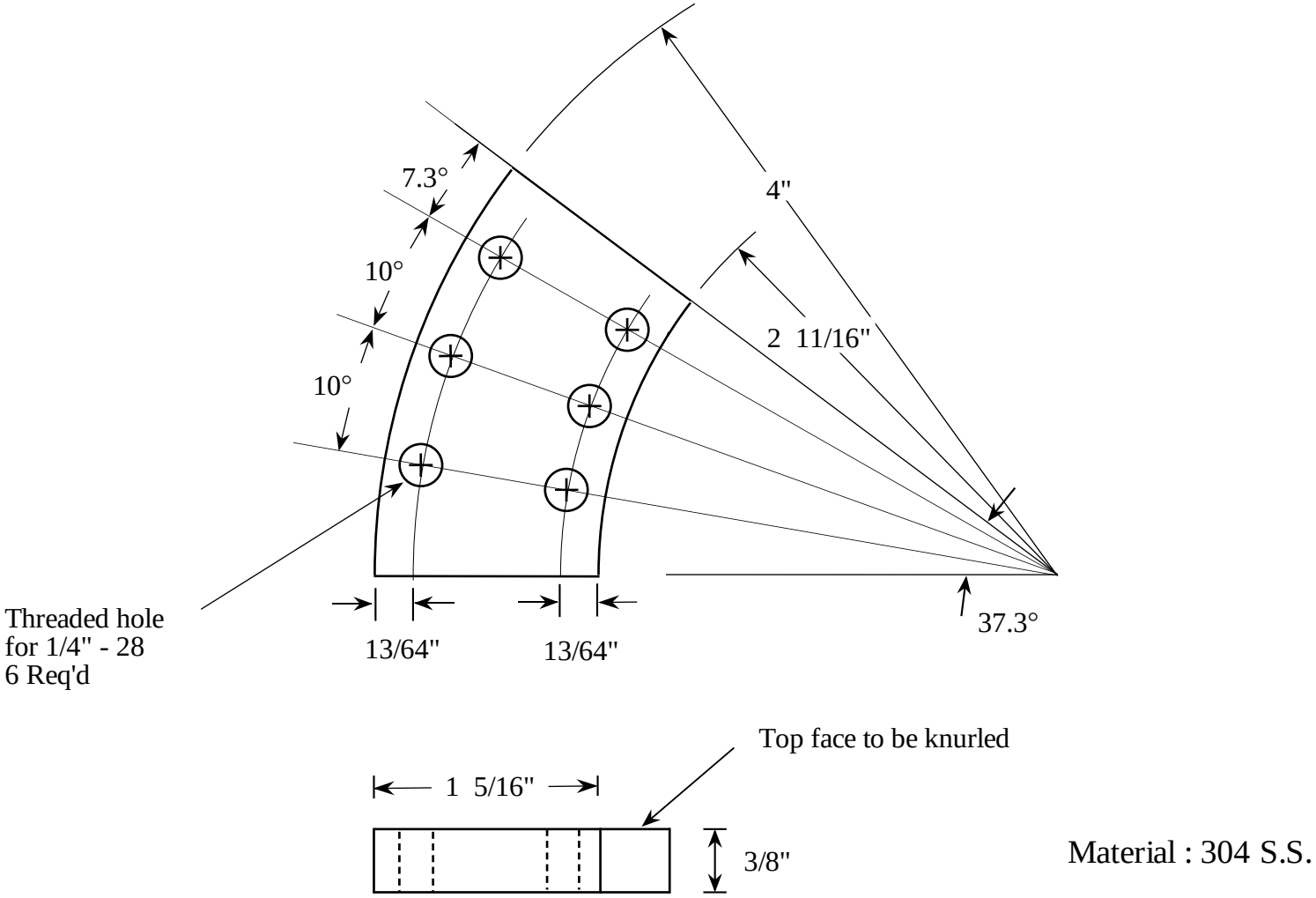

Figure A.21. OH Solenoid Clamping Shoe (Bottom) (Dwg. D-CCL107-5)

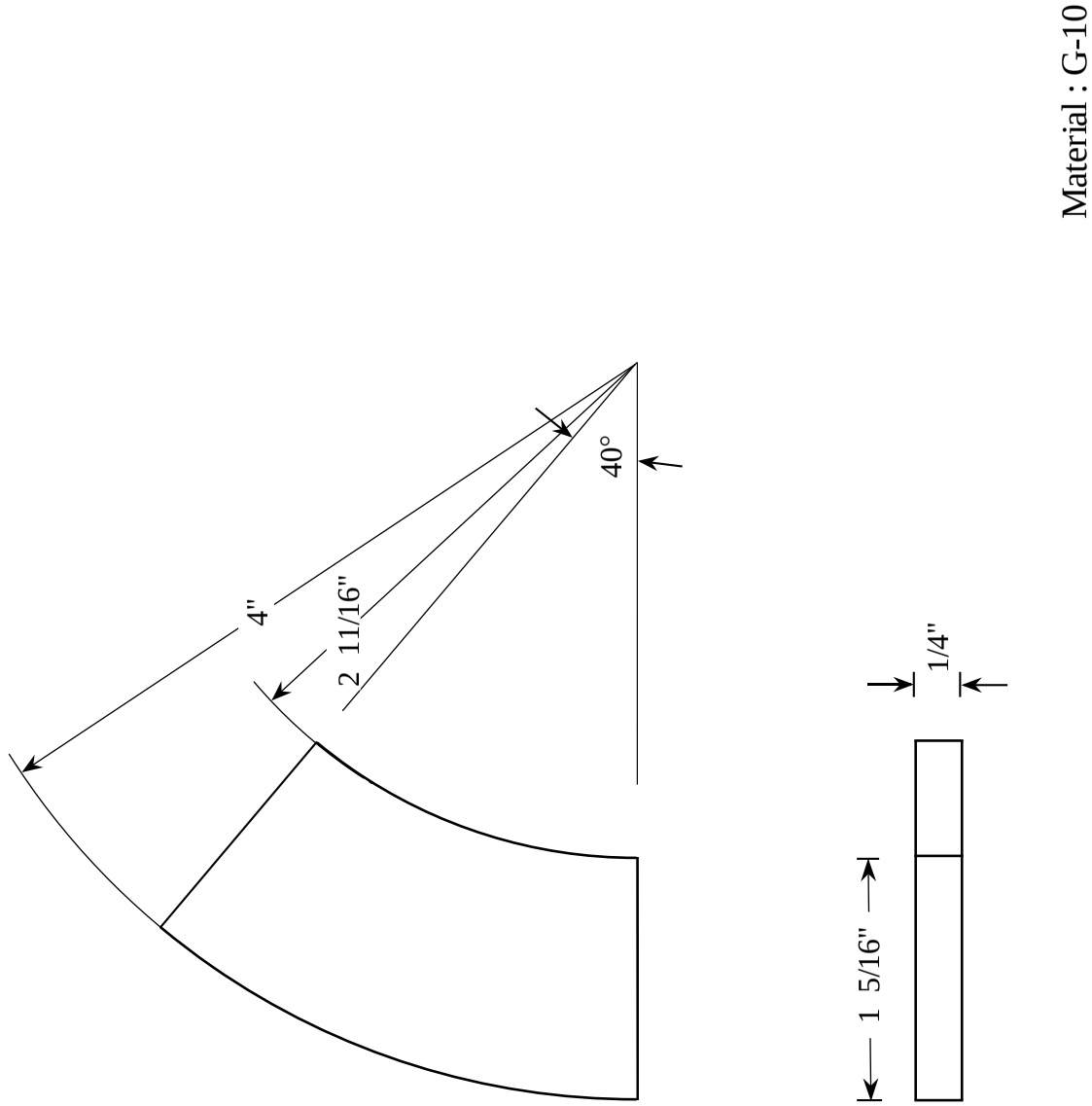

Figure A.22. G-10 for Clamping Shoe (Dwg. D-CCL107-6)

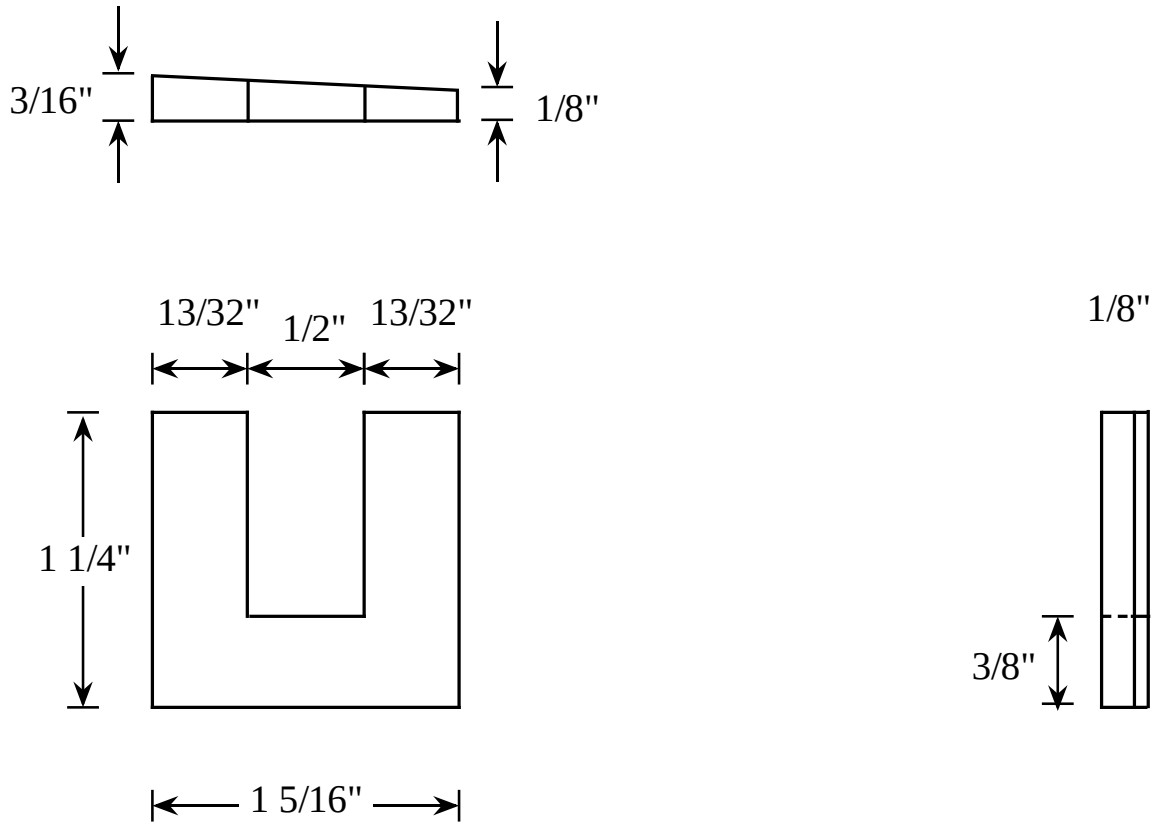

Material : G-10

Figure A.23. G-10 for Clamp Brace (Dwg. D-CCL107-7)

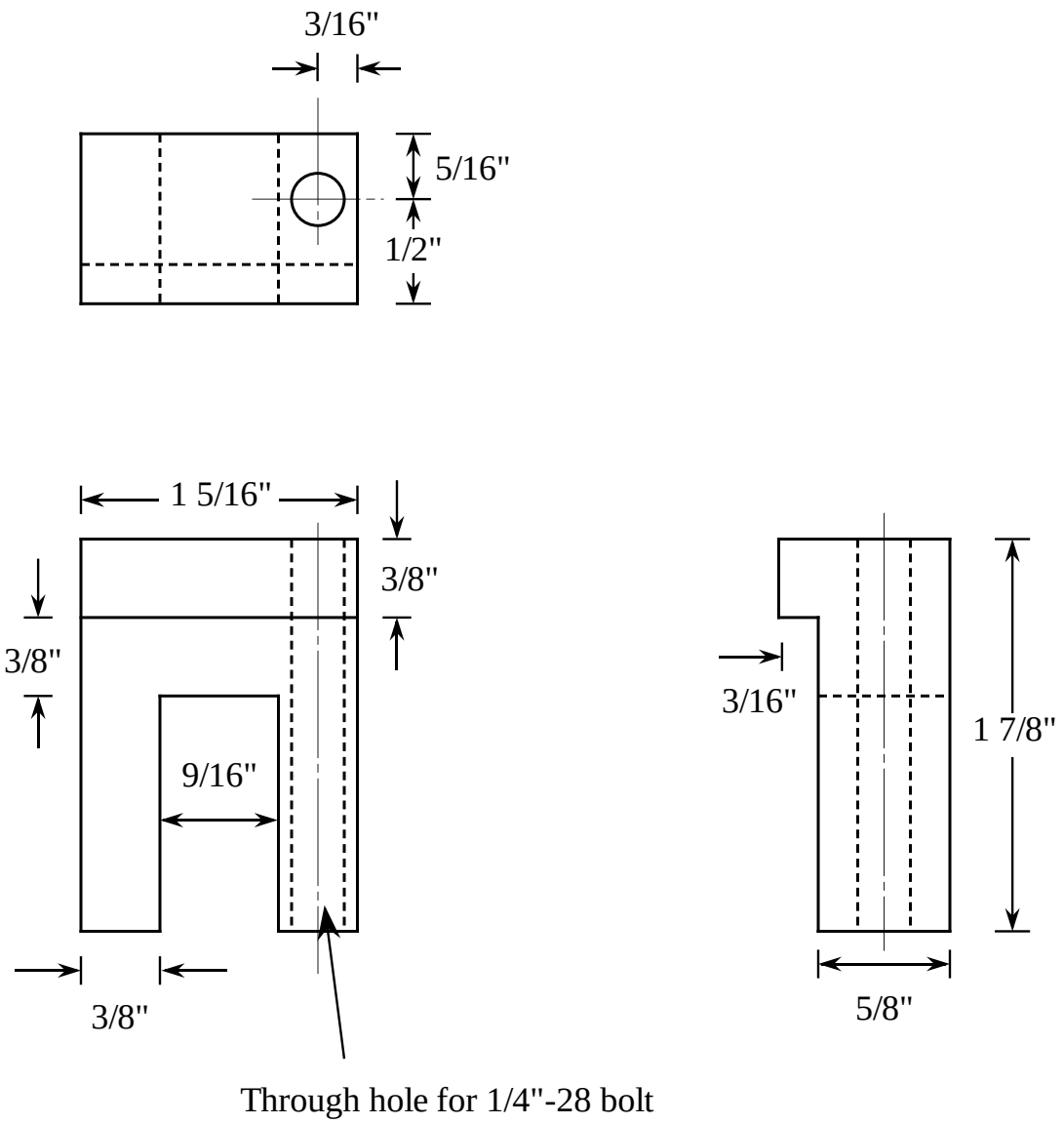

Figure A.24. Phenolic Clamp Hold-Down (Dwg. D-CCL107-8)

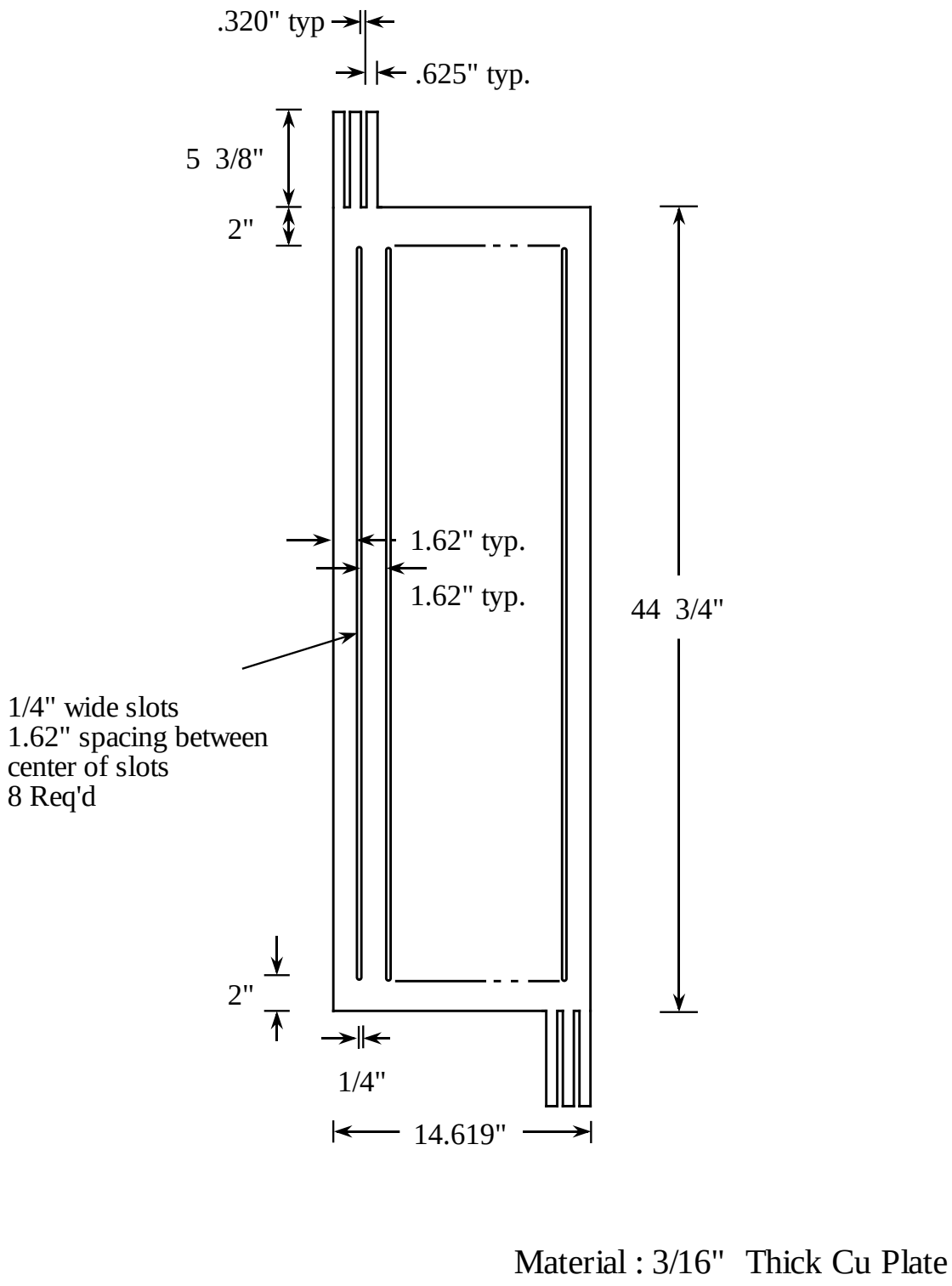

Figure A.25. OH Return Conductor with Slots (flat) (Dwg. D-CCL108-1)

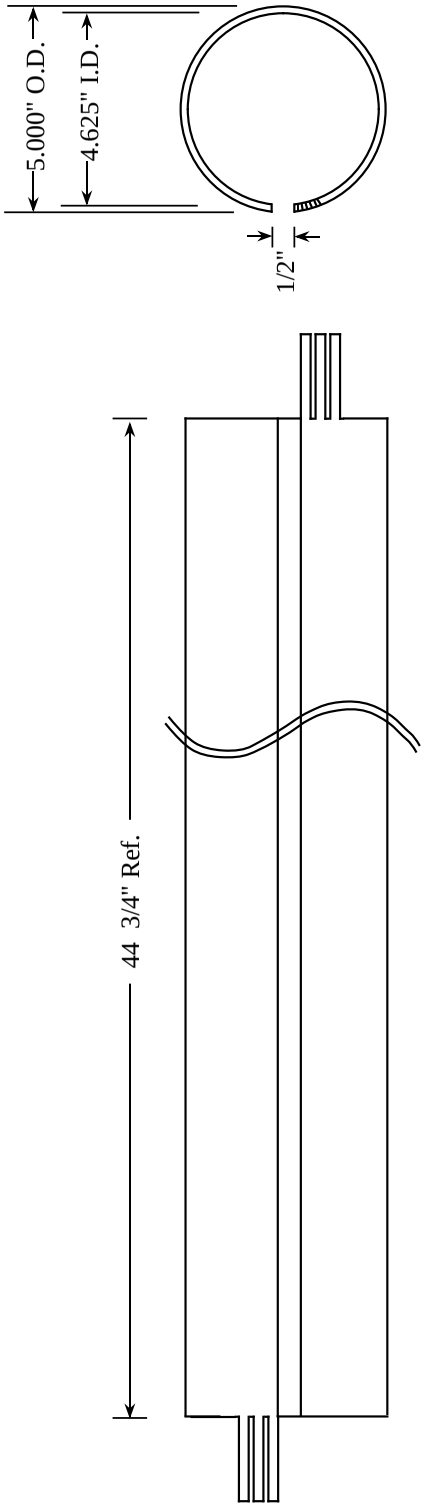

Figure A.26. OH Return Conductor (rolled) (Dwg. D-CCL108-2)

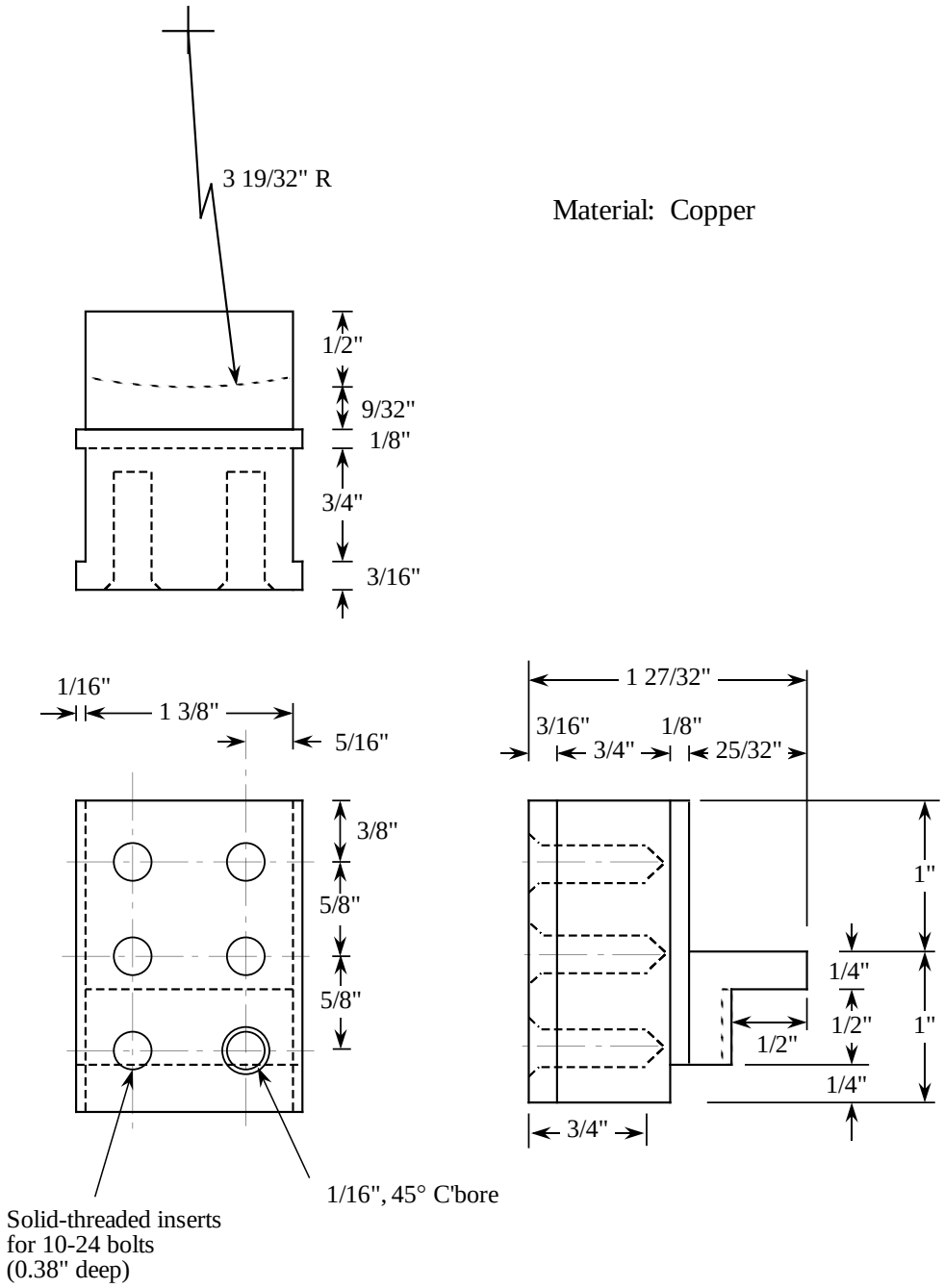

Figure A.27. OH Solenoid Inner Connector (Dwg. D-CCL109-1)

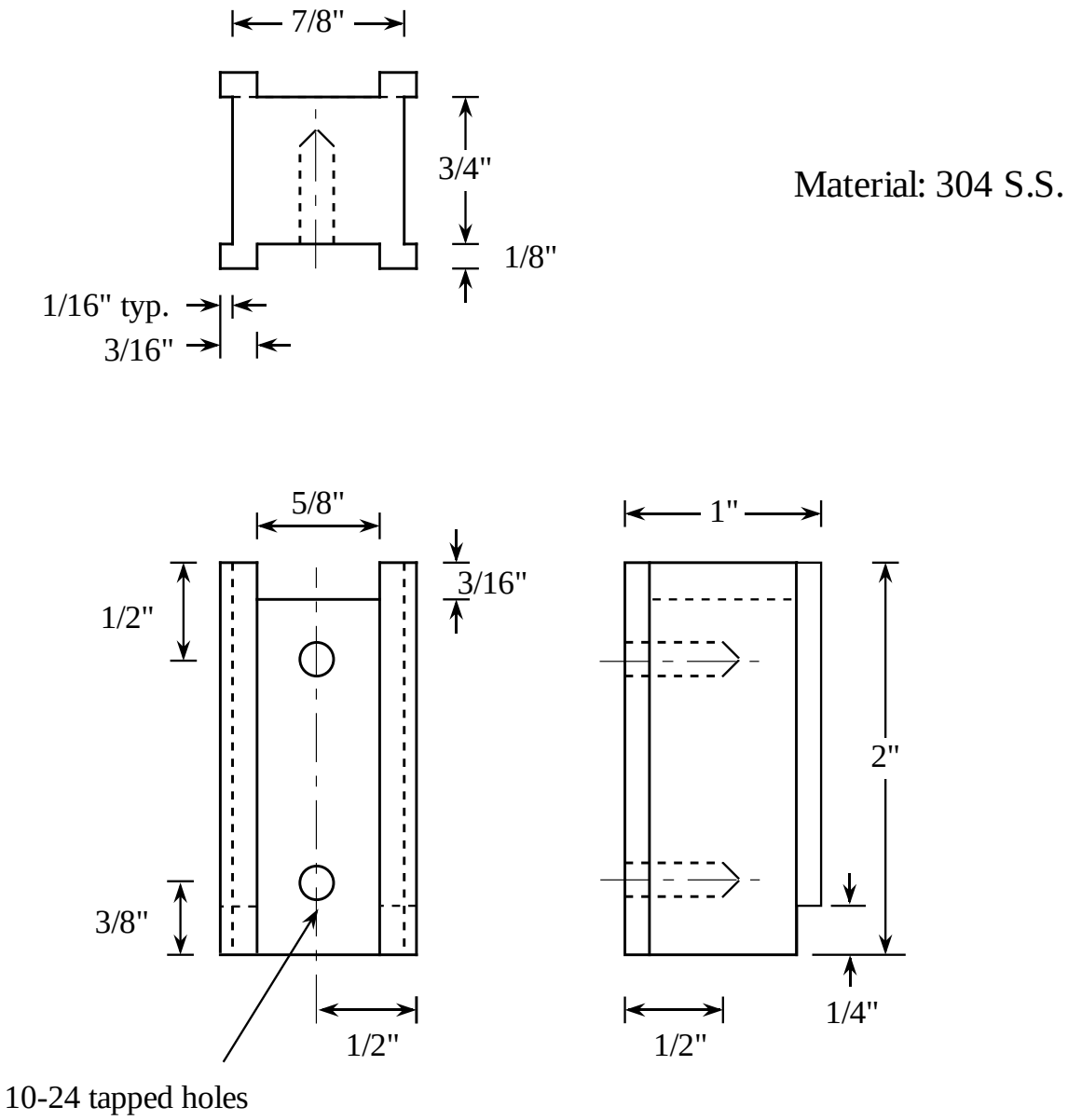

Figure A.28. OH Return Inner Connector (Dwg. D-CCL109-2)

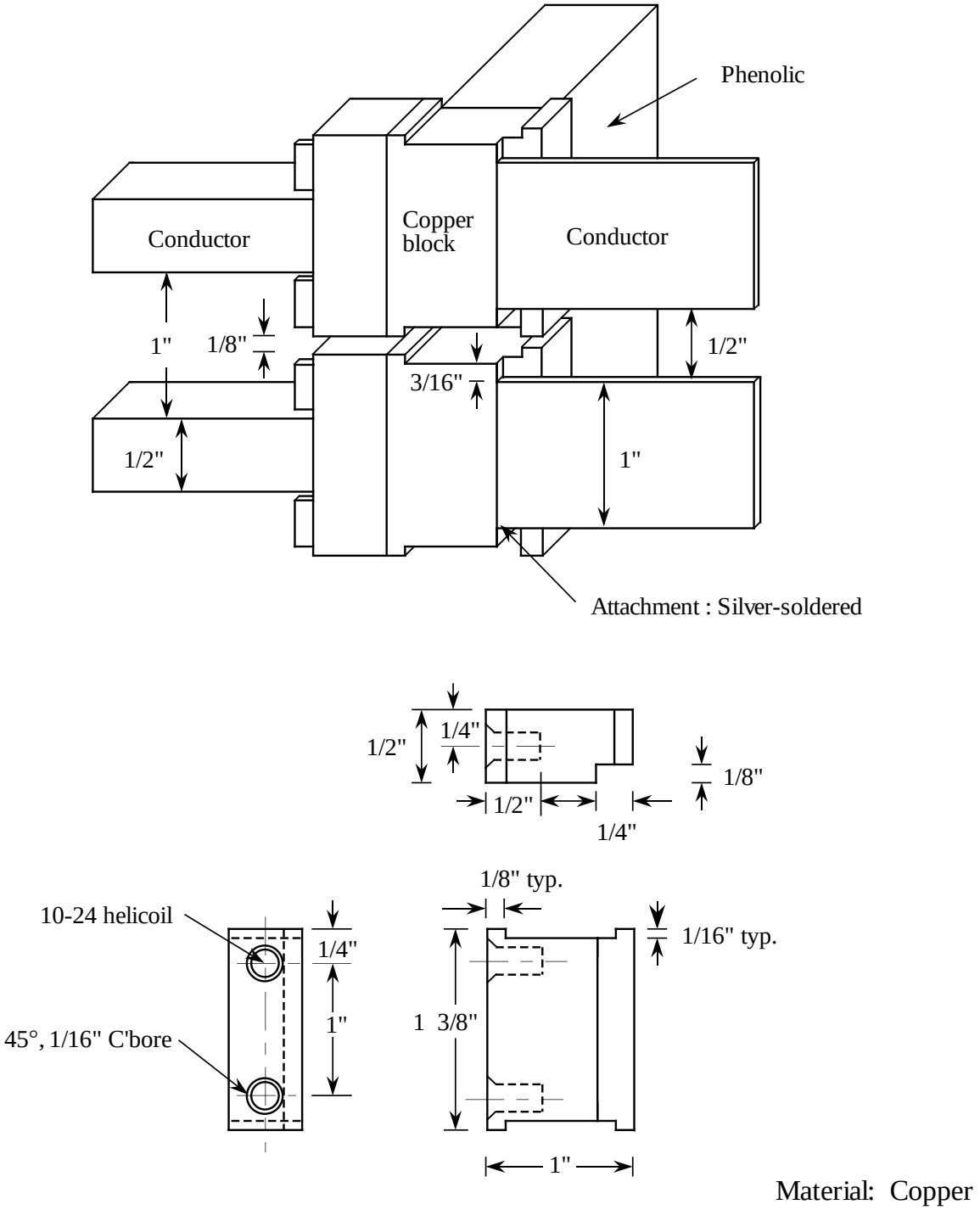

Figure A.29. Details of TF Joints (Dwg. D-CCL109-3)

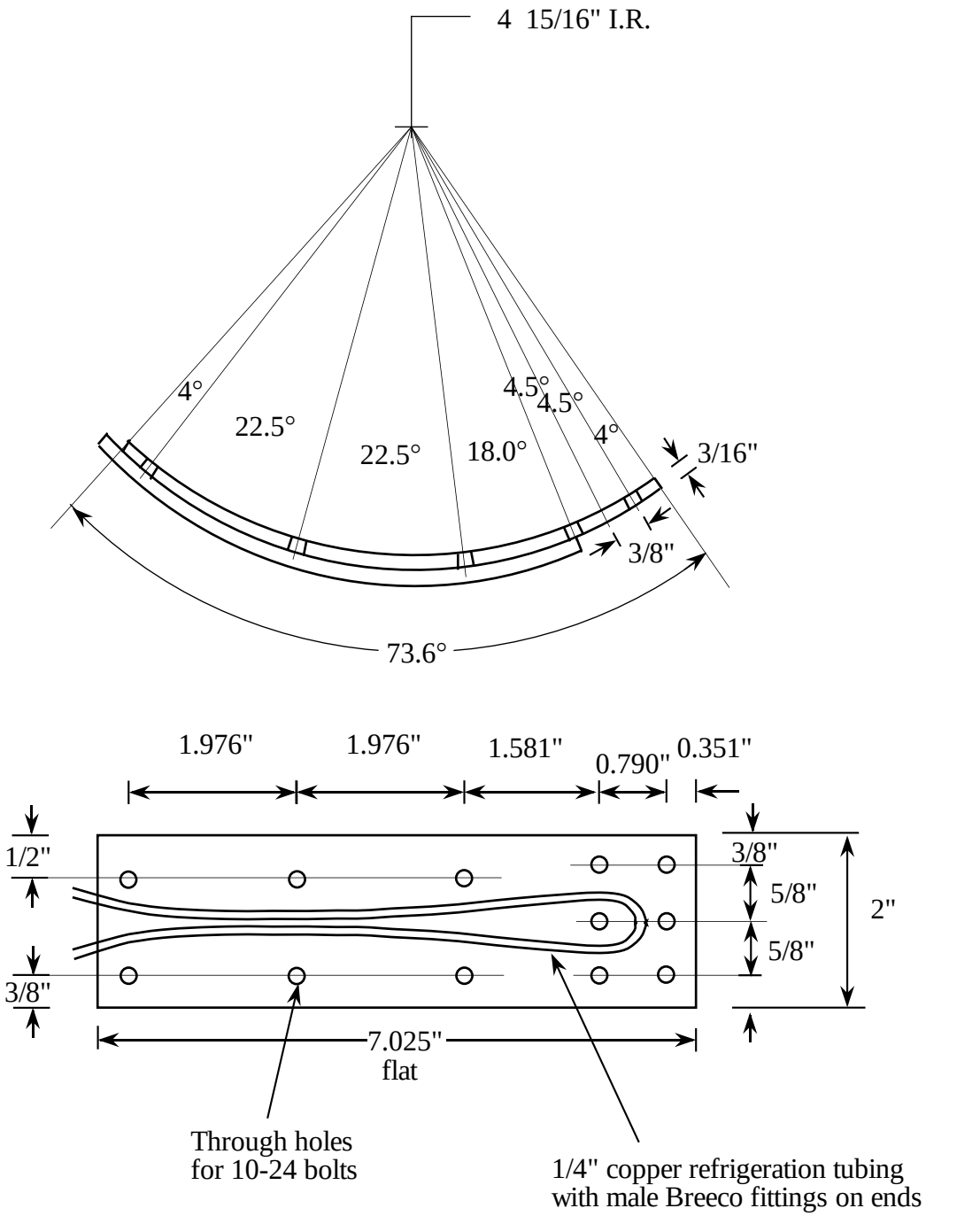

Material : Copper

Figure A.30. OH Jumper Bus (Dwg. D-CCL109-4)

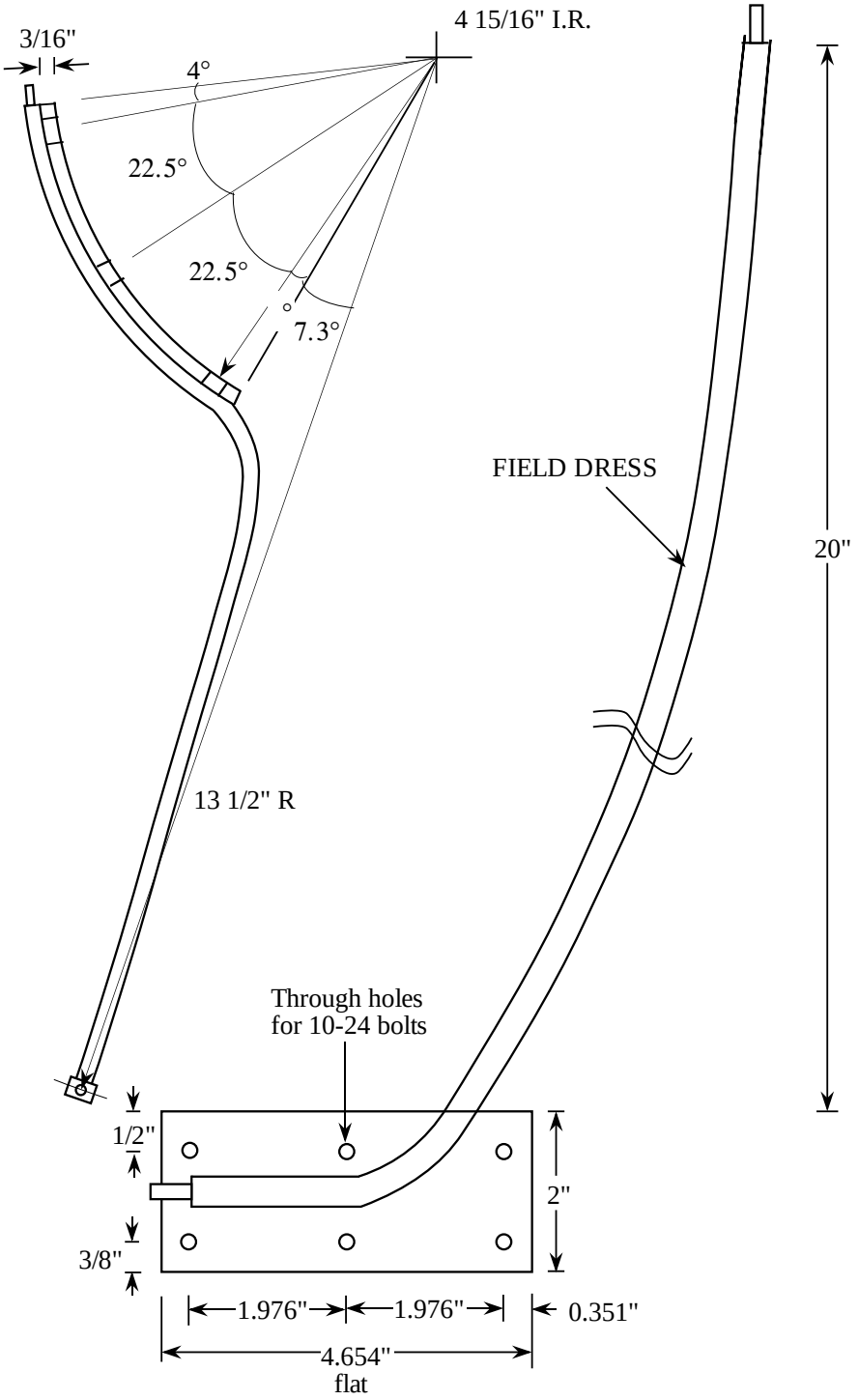

Figure A.31. OH Return Bus Connector (Dwg. D-CCL110-1)

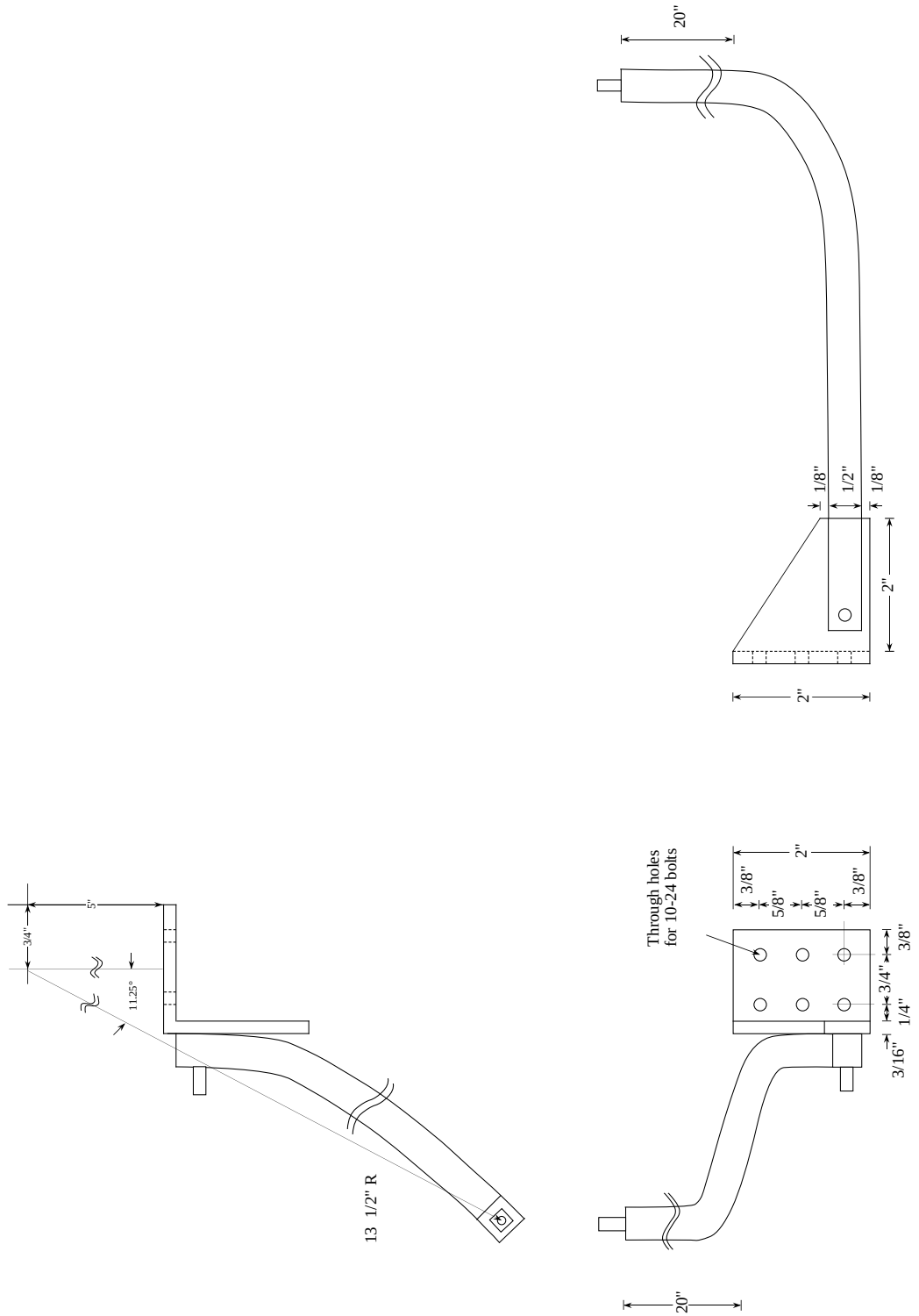

Figure A.32. OH Solenoid Bus Connector (Dwg. D-CCL110-2)

Bibliography

Appel, L. C., Duck, R., Fielding, S. J., Gibson, K. J., Hugill, J., Li, J., Manhood, S. J., Morris, A. W., Robinson, D. C., Sykes, A., Turner, M. F., Valovic, M., and Walsh, M. J. (1992). Energy Confinement in the Tight Aspect Ratio Tokamak, START. In *Proc. 19th European Conf. on Controlled Fusion and Plasma Physics, Innsbruck*, page 31.

Bickerton, R. J., Connor, J. W., and Taylor, J. B. (1971). Diffusion Driven Plasma Currents and Bootstrap Tokamak. *Nature (London) Physical Society* **229**, 110.

Brown, M. and Bellan, P. M. (1990). Spheromak Injection Into a Tokamak. *Phys. Fluids B* **2**, 1306.

Bruhns, H., Brendel, R., Raupp, G., and Steiger, J. (1987). Study of the Low Aspect Ratio Limit Tokamak in the Heidelberg Spheromak Experiment. *Nuclear Fusion* **27**, 2178.

Cairns, R. A. (1991). *Radiofrequency Heating of Plasmas.* The Adam Hilger Series on Plasma Physics. Adam Hilger, New York.

Chance, M. S. *et al.* (1990). Ideal MHD Stability of Very High Beta Tokamaks. In *Proc. Thirteenth International Conference on Plasma Physics and Controlled Nuclear Fusion Research - Washington, DC*, Vienna. International Atomic Energy Agency.

Costley, A. E., Hastie, R. J., Paul, J. W. M., and Chamberlain, J. (1974). Electron Cyclotron Emission from a Tokamak Plasma: Experiment and Theory. *Phys. Rev. Lett.* **33**, 758.

CUTSOGEORGE, G. (1980). Amplitude and Phase Detector for Radio-frequency Measurements. Technical Report PPPL-1623, Princeton Plasma Physics Laboratory.

DARROW, D. (1988). *DC Helicity Injection Studies on the Current Drive Experiment.* PhD thesis, Princeton University.

DOANE, J. (1980). Broadband Superheterodyne Tracking Circuit for Millimeter Wave Measurements. *Rev. Sci. Instrum.* **51**, 317.

DUANE, B. H. (1972). Fusion Cross Section Theory. Technical Report BNWL-1685, Brookhaven National Laboratory.

EJIMA, S., CALLIS, R. W., LUXON, J. L., STAMBAUGH, R. D., TAYLOR, T. S., and WESLEY, J. C. (1982). Volt-second Analysis and Consumption in Doublet III Plasmas. *Nuclear Fusion* **22**, 1313.

ENGEL, A. V. (1965). *Ionized Gases.* Clarendon Press, Oxford, 2nd edition.

FOREST, C. B. (1992). *Pressure Driven Currents in the CDX-U Trapped Particle Configuration.* PhD thesis, Princeton University.

FOREST, C. B., GREENE, G., and ONO, M. (1990). CDX-U Two-dimensional Scanning Microwave System. *Rev. Sci. Instrm.* **61**, 2888.

FOREST, C. B., HWANG, Y. S., ONO, M., and DARROW, D. (1992). Internally Generated Currents in a Small-Aspect-Ratio Tokamak Geometry. *Phys. Rev. Lett.* **68**, 3559.

GARSTKA, G. D., BASKEN, J., DANIELSON, J. R., DETTMERS, D., FOUCHER, B., KRESS, L., LEWICKI, B., MAYER, D., SPRINGER, M., TRITZ, K., and FONCK, R. J. (1994). First Results from the Low-Aspect-Ratio MEDUSA Tokamak. *Bull. Am. Phys. Soc.* **39**, 1574. Poster 2T36, 1994 APS-DPP conference, Minneapolis.

GOLDSTON, R. (1994). TPX: What, When, and How. Seminar in Astrophysical Sciences 558, Princeton University, Nov. 1, 1994.

GOREE, J. A. (1985). *The Backward Electrostatic Ion-Cyclotron Wave, Fast Wave Current Drive, and FIR Laser Scattering.* PhD thesis, Princeton University.

GREENE, G. J. and ONO, M. (1989). Magnetic Field Structure and Current Transport in the CDX Plasma. *Bull. Am. Phys. Soc.* **34**, 1993.

GRIMM, R. C., DEWAR, R. L., and MANICKAM, J. (1983). Ideal MHD Stability Calculations in Axisymmetric Toroidal Coordinate Systems. *J. Comput. Phys.* **49**, 94.

GRIMM, R. C., GREENE, J. M., and JOHNSON, J. L. (1976). Computation of the Magnetohydrodynamic Spectrum in Axisymmetric Toroidal Confinement Systems. *J. Comput. Phys.* **16**, 253.

GUSEV, V. (1994). GLOBUS-M Program - Motivation, Background, Plan. In *Workshop on Establishing the Physics Basis Needed to Access the Potential of Compact Toroidal Reactors - Oak Ridge 1994*. Oak Ridge National Laboratory.

HIRSHMAN, S. P. and NEILSON, G. H. (1986). External Inductance of an Axisymmetric Plasma. *Phys. Fluids* **29**, 790.

HUTCHINSON, I. H. (1990). *Plasma Diagnostics*. Cambridge University Press, New York.

HWANG, Y., FOREST, C., DARROW, D. S., GREENE, G., and ONO, M. (1992). Reconstruction of Current Density Distributions in the CDX-U Tokamak. *Rev. Sci. Instrum.* **63**, 4747.

HWANG, Y.-S. (1993). *Studies of Non-inductive Current Drive in the CDX-U Tokamak*. PhD thesis, Princeton University.

HWANG, Y. S., YAMADA, M., JONES, T. G., ONO, M., CHOE, W., JARDIN, S., LO, E., LUDWIG, G., MENARD, J., FREDRIKSEN, A., NAZIKIAN, R., POMPHREY, N., YOSHIKAWA, S., MORITA, A., ONO, Y., ITAGAKI, T., KATSURAI, M., and TOKIMATSU, K. (1994). Exploration of Low-aspect-ratio Tokamak Regimes in CDX-U and TS-3 Devices. In *Proc. Fifteenth International Conference on Plasma Physics and Controlled Nuclear Fusion Research - Seville, Spain*. International Atomic Energy Agency. Paper IAEA-CN-60/A5-II6.

JARBOE, T. R. *et al.* (1992). Formation and Sustainment of a Very Low Aspect Ratio Tokamak Using Coaxial Helicity Injection (the Helicity Injection Tokamak

[HIT] Experiment). Technical Report DOE/ER 54095-2, University of Washington, Aerospace and Energetics Research Program, Seattle, WA.

JARDIN, S. C., KESSEL, C. E., and POMPHREY, N. (1994). Poloidal Flux Linkage Requirements for the International Thermonuclear Experimental Reactor. *Nuclear Fusion* **34**, 1145.

JARDIN, S. C., POMPHREY, N., and DELUCIA, J. (1986). Dynamic Modeling of Transport and Positional Control of Tokamaks. *J. Comput. Phys.* **66**, 481.

JASSBY, D. L. (1977). SMARTOR - A Small-aspect-ratio Torus for Demonstrating Thermonuclear Ignition. Technical Report PPPL-1371, Princeton Plasma Physics Laboratory.

JONES, T. G., ONO, M., DARROW, D. S., TAYLOR, J., and KINEYKO, W. (1988). Current Drive Experiment on Small Aspect Ratio Torus. *Bull. Am. Phys. Soc.* **33**, 1933. Poster 3U5, 1988 APS-DPP conference, Hollywood.

KAYE, S., THE ITER JOINT CENTRAL TEAM, and THE ITER HOME TEAMS (1994). Projection of ITER Performance Using the Multi-Machine L and H-Mode Databases. In *Fifteenth International Conference on Plasma Physics and Controlled Nuclear Fusion Research - Seville, Spain.* International Atomic Energy Agency. paper IAEA-CN-60/E-P-3.

KRALL, N. A. and TRIVELPIECE, A. W. (1973). *The Principles of Plasma Physics.* McGraw-Hill Book Company, New York.

LAFFERTY, J. M. (1951). LaB_6 as a High-current Cathode. *J. Appl. Phys.* **22**, 299.

LAFRAMBOISE, J. (1966). Theory of Spherical and Cylindrical Langmuir Probes in a Collisionless, Maxwellian Plasma at Rest. Technical Report UTIAS-100, University of Toronto Institute for Aerospace Studies.

LAO, L. L., FERRON, J. R., GROEBNER, R. J., HOWL, W., JOHN, H. S., STRAIT, E. J., and TAYLOR, T. S. (1990). Equilibrium Analysis of Current Profiles in Tokamaks. *Nuclear Fusion* **30**, 1035.

LAO, L. L., JOHN, H. S., STAMBAUGH, R. D., KELLMAN, A. G., and PFEIFFER, W. (1985). Reconstruction of Current Profile Parameters and Plasma Shapes in Tokamaks. *Nuclear Fusion* **25**, 1611.

LAZARUS, E. A. *et al.* (1985). A Feasibility Study for the Spherical Torus Experiment. Technical Report ORNL/TM-9786, Oak Ridge National Laboratory.

LLOYD, B., JACKSON, G. L., TAYLOR, T. S., LAZARUS, E. A., LUCE, T. C., and PRATER, R. (1991). Low Voltage Ohmic and Electron Cyclotron Heating Assisted Startup in DIII-D. *Nuclear Fusion* **31**, 2031.

MANHEIMER, W. M. (1979). Electron Cyclotron Heating of Tokamaks. In BUTTON, K., editor, *Infrared and Millimeter Waves, Vol. II*, page 299. Academic Press.

MENARD, J., MAJESKI, R., ONO, M., and WILSON, J. R. (1995). High Ion-Harmonics Fast Wave Heating in NSTX and CDX-U. In *Proc. Eleventh Topical Conference on Radio Frequency Power in Plasmas, Palm Springs, CA*. AIP. to be published.

MILEY, G. H., TOWNER, H., and IVICH, N. (1974). Fusion Cross Section and Reactivities. Technical Report COO-2218-17, Univ. of Illinois, Urbana.

MILLER, R. L. *et al.* (1986). Advanced Tokamak Reactors Based on the Spherical Torus (ATR/ST). Technical Report LA-10740-MS, Los Alamos National Laboratory.

MILLER, R. L. and THE ARIES TEAM (1989). The ARIES-I High-Field-Tokamak Reactor: Design-Point Determination and Parametric Studies. In *Proc. Thirteenth Symposium on Fusion Engineering - Knoxville, TN*, volume 2. IEEE.

NASCIMENTO, I. C., LUDWIG, G. O., *et al.* (1991). The TBR-E Project - Basic Engineering Design. Technical report, Institute of Physics of University of São Paolo, Brazil and State University of Campinas, Brazil and Brazil National Institute for Space Research.

OHKAWA, T. (1970). New Method of Driving Plasma Current in Fusion Devices. *Nuclear Fusion* **10**, 185.

Ono, M. (1978). *Experimental and Theoretical Studies of Parametric Instabilities in the Ion Cyclotron Range of Frequencies.* PhD thesis, Princeton University.

Ono, M., Greene, G., Darrow, D., Forest, C., Park, H., and Stix, T. (1987). Steady State Tokamak Formation via DC Helicity Injection. *Phys. Rev. Lett.* **59**, 2165.

Ono, M., Kaye, S., and the NSTX Team (1994). PPPL Laboratory Development Activities for Fiscal Year 1994 - Spherical Tokamak Experiment. Technical Report PPPL/LPDA-2, Princeton Plasma Physics Laboratory.

Ono, M., Kaye, S., and the NSTX Team (1995). National Spherical Tokamak - Status Report. Technical report, collaboration of Princeton Plasma Physics Laboratory, Oak Ridge National Laboratory, University of Washington, and General Atomics D-IIID Group.

Ono, M. and the CDX group (1988). Current Drive Experiment - An Upgrade Proposal (CDX-U). Proposal to Experimental Plasma Research Branch, Div. of Applied Plasma Physics, Office of Fusion Energy, U.S. Dept. of Energy. Submitted by Office of the Associate Director for Program and Research, Princeton University, Plasma Physics Laboratory.

Peng, Y.-K. and Strickler, D. J. (1986). Features of Spherical Torus Plasmas. *Nuclear Fusion* **26**, 769.

Peng, Y.-K. M., Borowski, S. K., and Kammash, T. (1978). Microwave Start-up of Tokamak Plasmas Near Electron Cyclotron and Upper Hybrid Resonances. *Nuclear Fusion* **18**, 1489.

Peng, Y.-K. M. and Dory, R. A. (1978). Very Small Aspect Ratio Tokamaks. Technical Report ORNL/TM-6535, Oak Ridge National Laboratory.

Rewoldt, G. and Tang, W. M. (1989). Effects of Finite Aspect Ratio on High-n Instabilities in Tokamaks. In *1989 Sherwood conference, San Antonio.* Poster 1C26.

Rewoldt, G., Tang, W. M., and Kaye, S. (1994). Microinstability Studies of Small-Aspect-Ratio Tokamaks. *Bull. Am. Phys. Soc.* **39**, 1573. Poster 2T28, 1994 APS-DPP conference, Minneapolis.

Skiff, F. (1985). *Linear and Non-Linear Excitation of Slow Waves in the Ion Cyclotron Frequency Range*. PhD thesis, Princeton University.

Stambaugh, R. D., Moore, R. D., Bernard, R. W., Kellman, L. C., Strait, E. J., Lao, L., Overskei, D. O., *et al.* (1985). Tests of Beta Limits as a Function of Plasma Shape in Doublet III. In *Plasma Physics and Controlled Nuclear Fusion Research (Proc. 10th Int. Conf., London, 1984)*, page 217.

Stix, T. H. (1992). *Waves in Plasmas*. American Institute of Physics, New York.

Sykes, A. (1994). MHD in START. In *1994 Spherical Tokamak Workshop, Oak Ridge*. Oak Ridge National Laboratory. Presentation at the 1994 Spherical Tokamak Workshop.

Sykes, A., Bevir, M., Bamford, R., Colchin, R. J., Duck, R., Erents, S. K., Ferreira, J., Gibson, K., Gimblett, C., Goodall, D. H. J., Gryaznevich, M., Hender, T. C., Hugill, J., Jenkins, I., Martin, R., Parry, S., Ribeiro, C., Robinson, D. C., Sakharov, N., Tomas, J., Turner, M. F., Walsh, M. J., and Wilson, H. R. (1994). The START Spherical Tokamak. In *Proc. Fifteenth International Conference on Plasma Physics and Controlled Nuclear Fusion Research - Seville, Spain*. International Atomic Energy Agency. Paper IAEA-CN-60/A5-II5.

Sykes, A., DelBosco, E., Colchin, R. J., Cunningham, G., Duck, R., Edlington, T., Goodall, D. H. J., Gryaznevich, M. P., Holt, J., Hugill, J., Li, J., Manhood, S. J., and Turner, M. F. (1992). First Results from the START Experiment. *Nuclear Fusion* **32**, 694.

Sykes, A., Turner, M. F., and Patel, S. (1983). Beta Limits in Tokamaks due to High-n Ballooning Modes. In *Controlled Fusion and Plasma Physics (11th European Conference, Aachen, European Physical Society)*, volume 7D, page 363.

Tanga, A., Thomas, P. R., Cordey, J. G., *et al.* (1986). *Tokamak Start-up*. Plenum Press, New York. p. 159.

Troyon, F., Gruber, T., Sauremann, H., Semenzato, S., and Succi, S. (1984). MHD Limits to Plasma Confinement. In *Plasma Physics and Controlled*

Fusion (11th European Conference, Aachen, European Physical Society), volume 26, 1A, page 209.

WALSH, M. J. (1994). START- the Small Tight Aspect Ratio Tokamak. Presentation at Princeton Plasma Physics Laboratory, Nov. 1994.

WEISSLER, G. L. and CARLSON, R. W. (1979). *Vacuum Physics and Technology*, volume 14 of *Methods of Experimental Physics*. Academic Press, New York.

WESSON, J. (1987). *Tokamaks*. Clarendon Press, London.

WESSON, J. A. (1978). Hydromagnetic Stability of Tokamaks. *Nuclear Fusion* **18**, 87.

WILSON, J. R. (1980). *Ponderomotive Force Effects on Resonance Cones and Slow-Wave Coupling above the Lower Hybrid Frequency*. PhD thesis, Princeton University.

WURDEN, G. A. (1982). *CO_2 Laser Scattering on RF Waves in ACT-1*. PhD thesis, Princeton University.

YUSHMANOV, P., TAKIZUKA, T., and REIDEL, K. (1990). Tokamak Energy Scaling Expressions and Their Uncertainty. *Nuclear Fusion* **23**, 3.